Data, Models and Transitions in Computational Neuroscience

Bottom-up and Top-down Approaches

Manu Kalia

DATA, MODELS AND TRANSITIONS IN COMPUTATIONAL NEUROSCIENCE

Bottom-up and Top-down Approaches

Manu Kalia

Graduation committee:

Chairman:

prof. dr. J. N. Kok	University of Twente

Supervisors:

prof. dr. ir. C. Brune	University of Twente
prof. dr. ir. M. J. A. M. van Putten	University of Twente

Co-supervisor:

dr. H. G. E. Meijer	University of Twente

Other members:

prof. dr. A. J. Schmidt-Hieber	University of Twente
dr. ir. B. C. Schwab	University of Twente
prof. dr. J. N. Kutz	University of Washington
prof. dr. R. B. Jolivet	Maastricht University
prof. dr. C. R. Rose	Heinrich Heine University Düsseldorf

The work in this thesis was carried out at Mathematics of Imaging and AI (formerly Applied Analysis), Faculty of Electrical Engineering, Mathematics and Computer Science, University of Twente, Drienerlolaan 5, 7522NB, The Netherlands.

This work was funded by the Deutsche Forschungsgemeinschaft project (FOR 2795) 'Synapses under stress', see `www.for2795.hhu.de/en`.

Cover design:	Arjun Yadav and Manu Kalia
Lay-out:	Manu Kalia
Printed by:	Ipskamp Printing
ISBN:	978-90-365-5409-1
DOI:	10.3990/1.9789036554091

Data, models and transitions in computational neuroscience

Bottom-up and top-down approaches

DISSERTATION

to obtain
the degree of doctor at the University of Twente,
on the authority of the rector magnificus,
prof. dr. ir. A. Veldkamp,
on account of the decision of the Doctorate Board
to be publicly defended
on Thursday, July 14 2022 at 14.45 hours

by

Manu Kalia

born on December 24, 1994
in New Delhi, India

This thesis has been approved by the supervisors:

prof. dr. ir. C. Brune
prof. dr. ir. M. J. A. M. van Putten

and the cosupervisor:

dr. H. G. E. Meijer

Η Ιθάκη σ' έδωσε τ' ωραίο ταξείδι.
Χωρίς αυτήν δεν θάβγαινες στον δρόμο.
Άλλα δεν έχει να σε δώσει πια.

Ithaka gave you the marvelous journey.
Without her you would not have set out.
She has nothing left to give you now.

- From Ιθάκη *(Ithaka) by C.P. Cavafy.*
Translation by E. Keeley and P. Sherrard.

Contents

1 Introduction **1**
- 1.1 Challenges and motivation . . . 2
- 1.2 Aims of the thesis . . . 4

2 Background **7**
- 2.1 Energy dependence in the brain and ischemic stroke . . . 7
- 2.2 Modeling in computational neuroscience . . . 12
- 2.3 Transitions in models: bifurcation theory . . . 21

3 Ion dynamics of the energy-deprived tripartite synapse **27**
- 3.1 Introduction . . . 28
- 3.2 A model for ion homeostasis at the tripartite synapse . . . 30
- 3.3 Results . . . 36
- 3.4 Discussion . . . 51
- 3.5 Materials and methods . . . 55

4 A neural mass model for EEG in ischemia **79**
- 4.1 Introduction . . . 80
- 4.2 Model description . . . 82
- 4.3 Results . . . 90
- 4.4 Discussion . . . 96
- 4.5 Appendix . . . 98

5 Normal form autoencoders for data-driven model discovery **103**
- 5.1 Introduction . . . 104
- 5.2 Results . . . 109
- 5.3 Conclusion . . . 113
- 5.4 Appendix . . . 114

6 Homoclinic saddle to saddle-focus transitions in 4D systems **129**
- 6.1 Introduction . . . 129
- 6.2 Derivation of the model maps . . . 133

6.3 Analysis of the scalar model map . . . 140
6.4 Analysing the 3D model map . . . 148
6.5 Interpretation for the original ODE system . . . 156
6.6 Examples . . . 158
6.7 Discussion . . . 162

7 General Discussion **167**
7.1 Consequences of biophysical modeling . . . 167
7.2 Parameter-dependency in models . . . 169
7.3 Future work and outlook . . . 170

Summary **175**

References **177**

List of publications **202**

Chapter 1

Introduction

The broad goal of computational neuroscience is to understand and predict the behavior of neural phenomena using *in silico* techniques - or mathematical models - which are designed *bottom-up* using physical principles and often manifest in a set of equations. Experimental observations and pathophysiological behavior are then explained rigorously by mathematical analysis of the equations' qualitative features. The surge in measurements and data in neuroscience has propelled the *top-down* perspective of data-driven modeling - models and insight are derived directly from sufficiently large datasets. This thesis addresses challenges in the understanding of cerebral ischemia caused by stroke, a leading cause of disability or even death, by introducing bottom-up models. On the other hand, this thesis also discusses the use of top-down techniques to construct such models and the novel unfolding of qualitative features that they describe.

In neuroscience, complex phenomena arise in the interaction of several mechanisms that regulate healthy behavior in the brain. These phenomena range over several spatiotemporal scales - generation of action potentials in a single neuron occurs on the timescale of milliseconds and electroencephalographic rhythms on a neural population level can vary on the timescale of hours or days. Neuroscientists use a variety of techniques to record and explain these phenomena, which output an assortment of *data* to work with. The 21st-century data boom has amplified the cycle of experiments and theoretical insight via computational neuroscience. This practice began in the 1950s with Hodgkin and Huxley describing dynamics of the giant squid neuron [1], and has now evolved into a plethora of phenomenological and biophysical models that describe the brain's complex phenomena across diverse spatiotemporal scales [2].

These models are often described by a set of evolutionary equations that explain several qualitative features underlying the neural phenomena. The transitions between these features are controlled by one or many parameters in the model, that are tuned to experimental data. Model parameters allow for

several experimental conditions to be explained by a single model describing the physical phenomena. Mathematically, the exhaustive study of qualitative transitions in features exhibited by such models is called *bifurcation analysis* [3, 4]. Within the domain of dynamical systems, there is a list of canonical transitions - or bifurcations - possible in mathematical models described by differential equations. They are key in explaining the origins of rhythms, tipping points and points-of-no-return in computational neuroscience. Bifurcations thus play a key role in predictive modeling, and continuing the cycle of insight between experimental and theoretical neuroscience.

The recent boom in data has also propagated a top-down approach to modeling. In a bottom-up approach, biophysical principles or phenomenological approximations are used to construct governing equations. On the flip side, the abundance of experimental data is used to directly construct equations, usually via some optimization procedure, saving significant time and effort. Combined with machine learning and *a priori* insight into the underlying biophysics, the data-driven approach to modeling is a powerful tool and is a mainstay of today's cutting-edge research.

This thesis explores the interaction of these three elements: **data, models** and **transitions**, in the context of computational neuroscience. Biophysical models to describe neural pathologies are constructed - in particular, cerebral ischemia. Data-driven approaches are also introduced, to construct simplified models from high-dimensional data. Lastly, newly observed transitions are analyzed to derive their canonical behavior. Throughout the thesis, transitions in qualitative behavior are analyzed via bifurcation analysis: to provide insight, to derive canonical behavior of previously unobserved transitions, and as an inspiration for data-driven modeling.

1.1 Challenges and motivation

Stroke is characterized by a reduction of blood flow to the brain, and is one of the leading causes of death in the world [5]. About 87% of all stroke cases are of *ischemic* type - where an occlusion in a blood vessel leaves areas in the brain exposed to low-energy conditions. This manifests in a multitude of neural pathologies, which can be studied at a cellular and global level, and on time scales of minutes to days. Clinically, low cerebral blood flow results in communication breakdown and subsequent that may result in, for instance, loss of cognition, motor abilities and sensory behavior. This can be accompanied by tissue swelling, that spreads outwards from the *core* area [6]. On a cellular level, lack of energy may cause the breakdown of ion gradients leading to synaptic failure and cellular swelling. A variety of techniques are used to study these dynamics - magnetic resonance imaging (MRI), computer tomography (CT) and electroencephalography (EEG) in the clinic [7, 8], and flourescence microscopy and electrophysiological recordings to study more local

events [9, 10]. Nevertheless, several questions regarding the breakdown of physiology remain open today - from a biological and clinical standpoint.

At a biological level, today's research provides significant insight into the dynamics of specific ion gradients at the synapse, such as those of Na^+, K^+ and Cl^-, and their breakdown [11, 12]. These ion gradients are co-dependent via several complex regulatory mechanisms such as ion channels and cotransporters. It is thus difficult to ascertain their interaction at the breakdown of energy-dependent processes. For instance, it remains unclear how exactly rising Na^+ levels in the neuron trigger neurotransmitter accumulation in the extracellular space. This has consequences on understanding how synaptic communication may fail and what therapeutic measures can be introduced.

From a global viewpoint, it is well known that functional failure in the brain precedes tissue swelling and cell death during stroke [13]. One clinical approach to measuring functional failure during stroke is by detecting favorable and unfavorable EEG rhythms [14]. However, the link between cellular ion gradient breakdown, functional failure and consequent brain rhythm generation remains unclear despite a variety of data from diverse modalities on multiple spatiotemporal scales. Another challenge is the presence of several isolated experiments in literature today, that deal with the same pathophysiological phenomenon. Many papers study single phenomena, while it is well known that several interacting processes are disturbed. For instance, *in vitro* stroke experiments with animal models collect isolated experimental data, such as Ca^{2+}, Na^+ and K^+ transients [11] and spreading depolarizations [15]. Capturing the essentials of the multifaceted changes involved in stroke ini a single framework is challenging.

This thesis focuses on mathematical models that provide a sandbox approach to answering the questions above. Modeling allows the collection of several interacting pathophysiological processes in a single formulation to test hypotheses and formulate predictions. Several experimental conditions can thus be lumped together in a single dynamical description, which is usually done via model parameters. Another reason to consider this approach is to extract the most significant representations from provided neural data.

Since the advent of Hodgkin and Huxley's work, numerous other formulations have spurred in computational neuroscience. These include spatial models [16, 17], population averaging [18, 19, 20] and single-cell extensions of the Hodgkin-Huxley approach itself [21, 22]. In particular, this thesis proposes the use of biophysical descriptions as a working principle for building computational models across different spatiotemporal scales. Biophysical models naturally incorporate physical rules such as conservation laws and limiting principles such as the Donnan equilibrium [23]. Moreover, they provide a generalized framework to corroborate with several isolated experiments.

As mentioned before, neural data comes in various spatiotemporal modalities. Given the volume of experimental data available and the growing use of data-driven approaches in applied sciences, a flip-side to modeling can be

proposed: can feasible computational models be derived directly from data? This question has already been addressed in several data-driven approaches used in neuroscience today [24]. These methods also include *machine learning*-based approaches which grow in synergy with neuroscience - advances in computational neuroscience in turn also improve machine learning methods [25]. This thesis focuses on the following question: can machine learning and data-driven approaches uncover governing equations directly from data, similar to those obtained from bottom-up approaches? Recent works have shown that this perspective is promising [26, 27].
In bottom-up and top-down approaches, computational models are required to be feature-rich - it is often desirable to express several experimental conditions within the same formulation. This is characterized by model parameters. For instance, consider a neural model with a parameter describing available energy in the system. Changing this parameter value results in a transition from healthy activity to pathological behavior such as swelling, depolarization and synaptic arrest. This thesis addresses the characterization and quantification of such transitions via bifurcation analysis. These transitions - or bifurcations - are characterized by *normal form* equations, which are universal equations describing generic behavior in models upon varying parameters [3, 4].

1.2 Aims of the thesis

This thesis has three overarching goals, outlined as follows.

1. From a *bottom-up* perspective, the goal of this thesis is to construct explainable and extendable neural models that corroborate several isolated experiments, and reconcile clinical and biological events, specifically in ischemia.
2. From a *top-down* perspective, the goal is to obtain feasible models directly from neural data. These methods are applied when bottom-up approaches are unfeasible - such as when datasets are high-dimensional.
3. Bottom-up and top-down models are required to be feature rich with the help of parameters. Thus the third goal in this thesis is to quantify and qualify parameter variance in top-down and bottom-up approaches with bifurcation analysis.

The thesis begins with a background on cerebral ischemia, and bottom-up and top-down modeling in **Chapter 2**.
In **Chapter 3**, a detailed biophysical model of the tripartite synapse is constructed to examine ion dysregulation in low-energy conditions. The model is inspired by several different modeling efforts and describes the dynamics of Na^+, K^+, Cl^-, Ca^{2+} and glutamate at the synapse during ischemic conditions. Using bifurcation analysis, crucial tipping points and points-of-no-return are

quantified, to explain the path to recovery from transient ischemia. Moreover, blocking specific ion channels is suggested as therapeutic measures.
In **Chapter 4**, the effort in Chapter 3 is extended to a neural population level using a detailed neural mass model. Here, the aim is to reconcile EEG rhythmic behavior during stroke with the effects of ischemia on synapses using differential sensitivity analyses. These effects include suppression of healthy EEG rhythms and the functional reorganization of inter-population networks.
In **Chapter 5**, data-driven model discovery is studied from the perspective of parameter variance. High-dimensional datasets are collected from physical phenomena that contain a transition in pattern-forming behavior. Machine learning is used to discover underlying low-dimensional representations in the form of characteristic normal form equations of the bifurcation involved. The technique serves as a first approach for building parameter-dependent models directly from data by using normal forms as building blocks.
In **Chapter 6**, a new bifurcation observed in a neural field equation is explored. In the travelling wave formulation of the neural field, the problem reduces to explaining the unfolding of a new codimension 2 homoclinic bifurcation. The bifurcation is characterized by a saddle to saddle-focus transition, where the critical point is characterized by a 3-dimensional stable leading eigenspace. The unfolding is constructed using a Poincaré map technique and analyzed for its asymptotic behavior in the wild case.
Chapter 7 concludes the thesis with a general discussion and an outlook towards future work.

Chapter 2

Background

This chapter lays out the scientific setting of the thesis. In Section 2.1, biological events surrounding ischemic stroke in the brain are summarized, from a local and global view. Section 2.2 briefly explains how mathematical models for such phenomena may be constructed, from a bottom-up and top-down perspective. In Section 2.3, fundamentals of bifurcation analysis are explained.

2.1 Energy dependence in the brain and ischemic stroke

The human brain consumes about 20% of the body's energy supply [28]. The heavy cost is paid for maintaining healthy signaling using adenosine triphosphate (ATP) as the currency [29]. ATP is produced all over the body to meet energy needs via two processes of different efficiencies: glycolysis in the cytosol and oxidative phosphorylation in the mitochondria. The former produces 2 mol of ATP for every mole of glucose, and the latter 36 mol of ATP per mol of glucose. Neurons take advantage of both these processes to meet their demands [30, 31, 32].

Supply of glucose and oxygen to the brain is mediated by a rich network of blood capillaries that interact with brain cells at the blood-brain barrier. These cells include neurons and glial cells. Restriction of blood flow to this junction can result in *stroke* that triggers a cascade of pathological events at the cellular and brain network level [5]. Ischemic stroke in particular counts for 87% of all stroke cases, characterized by the blockages in arteries carrying oxygen rich blood, often due to blood clots. This leaves areas in the brain exposed to metabolic stress and has immediate and possible long-term consequences. Deprivation of energy can result in cell death and loss of synaptic communication within minutes. On a longer timesclae, stroke can lead to chronic issues such as

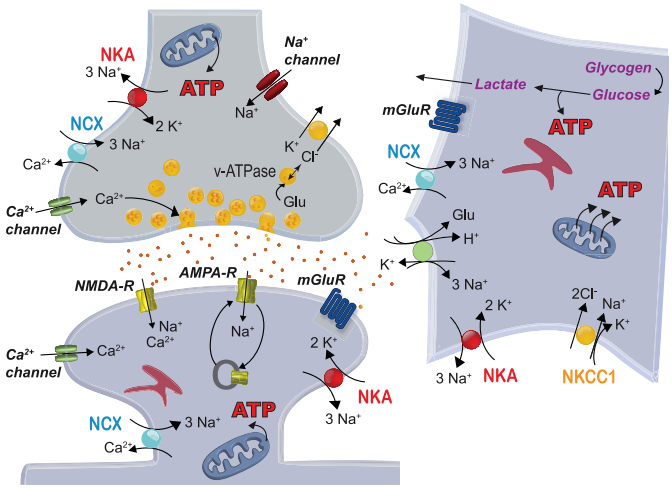

Figure 2.1: Summary of energy dependent processes at the tripartite synapse and the affected ion transport mechanisms. The tripartite synapse is composed of four major compartments, the presynaptic terminal (left top), the perisynaptic astrocyte process (right), the postsynaptic terminal (left bottom) and the synaptic cleft. Several ion transport mechanisms of Na^+, K^+, Cl^-, Ca^{2+} and glutamate are shown, with critical ATP-dependent processes marked in red. Reprinted from ref. [33] with permission.

paralysis and loss of cognition [6].
In the *core* area of stroke, cells irreversibly swell and lyse within minutes in a process called cytotoxic edema, resulting from significant changes in ion concentrations and increased osmotic pressure across the cell membrane. The area of interest as a therapeutic target is the stroke *penumbra*, where metabolic stress is mild and reversible. Here, the cascade of pathologies may possibly be reversed, but the dynamics in mild ischemic conditions are not well understood. Understanding these dynamics may hold the key to identifying mechanisms underlying stroke pathophysiology and the prevention of its spreading into neighboring areas [5].

2.1.1 Biological consequences: ion homeostasis

To understand stroke dynamics it is vital to first examine energy dependence at a cellular level and the consequences of low-energy conditions. The blood-brain barrier comprises endothelial cells at the capillary wall that selectively exchange glucose with the brain via glucose transporters. The capillaries are wrapped to a large extent by the endfeet of *astroyctes* [34] - a specific type of glial cells - which store glucose in the form of glycogen, for eventual conversion to lactate for neuronal use via the astrocyte-to-neuron-lactate-shuttle (ANLS) [35, 36]. Astrocytes have star-like soma and big surface area, and play an immense role in ion homeostasis and regulating neuronal energy supply. Thin

perisynaptic astrocyte processes protrude into neighboring synapses away from the astrocyte soma and clear away excess ions in the synaptic cleft, thereby maintaining healthy synaptic transmission [37, 38, 39].

The critical meeting point of the perisynaptic process, a presynaptic and postsynaptic terminal is called the *tripartite synapse* [40], and is one of the key topics studied in this thesis. At this juncture several ATP-dependent processes in the form of ion channels and exchangers are responsible for mediating healthy neuronal communication. A summary of these processes is shown in Fig. 2.1. The vast majority of ATP is consumed by the Na^+/K^+-ATPase (NKA), found in astrocytes and neurons [29, 41]. The NKA consumes 1 molecule of ATP to drive 3 Na^+ ions and 2 K^+ ions against their concentration gradient across the cellular membrane. By doing so, the NKA helps to maintain a hyperpolarized resting membrane potential.

The gradients of Na^+ and K^+ are regulated by several ion channels, cotransporters and exchangers active across the membrane. For instance, voltage-gated Na^+ and K^+ channels in the neuron allow the respective ions to flow across the membrane along their concentration gradient in response to depolarization. They are also regulated by the bulk movement of anions, namely Cl^- via cotransporters such as the KCC cotransporter [42], that pushes one Cl^- ion into the cell, along the concentration gradient of K^+. The ions Na^+, K^+ and Cl^- are the only ions that exist in large millimolar concentration intracellularly and extracellularly, and hence largely mediate cellular volume regulation via osmotic diffusion of water, aquaporins and volume-regulated channels [43, 44, 45]. The bulk movement of these ions also interact with the homeostasis of other critical ions, such as Ca^{2+} and neurotransmitters, that exist in smaller intracellular and extracellular concentrations. Action potential mediated depolarization allows the influx of Ca^{2+} in the neuronal presynaptic terminal. This in turn catalyses neurotransmitter endocytosis and exocytosis into the synaptic cleft [46]. Ca^{2+} gradients are also mediated by ion exchangers such as the Na^+/Ca^{2+}-exchanger (NCX), which exchanges 3 Na^+ ions for 2 Ca^{2+} ions across the membrane [47].

The excess release of ions in the extracellular space and synaptic cleft by the neuron is readily cleared by the astroycte [37]. The astroycte maintains a resting membrane potential close to the reversal potential of K^+ and is highly sensitive to the extracellular concentration of K^+. Ion channels like the inwardly-rectifying K^+ channel (Kir) [48] and the Na^+-K^+-$2Cl^-$ cotransporter [49] clear away excess extracellular K^+ released during an action potential and allow the neuronal membrane potential to recover. Coupled with astrocyte Na^+ and K^+ gradients, the excitatory amino acid transporters (EAATs) clear excess glutamate from the cleft at glutamatergic synapse post neuronal exocytosis [50, 51, 52]. The astrocytes at the tripartite synapse thus function as a sponge - absorbing excess extracellular ions - to prevent irreversible neuronal depolarization and postsynaptic excitotoxicity [53], and allow the smooth signalling between neurons.

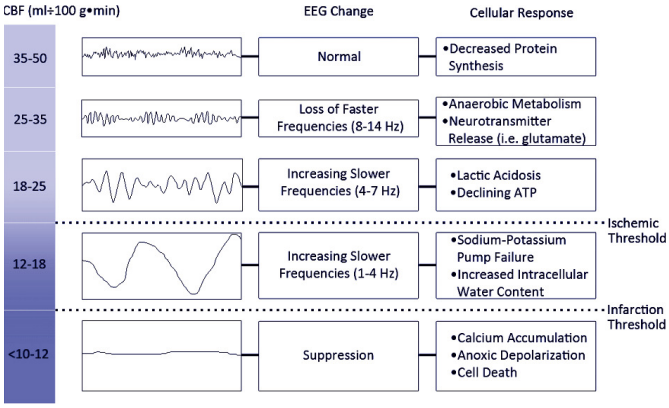

Figure 2.2: Changes in electroencephalography (EEG) rhythms as a function of cerebral bloodflow. Cerebral ischemia during stroke is characterized by loss of cerebral blood flow (CBF) which results in a progressive loss of faster frequencies in electroencephalography (EEG). This is accompanied by ion dysregulation, compartmental swelling, depolarization and death at a cellular level. Reprinted from ref. [62] with permission.

Under low-energy conditions, the NKA breaks down and ions move more freely across their concentration gradient [54]. Accumulation of Na^+ and K^+ follows immediately after the inhibition of NKA activity, inside and outside neurons and astrocytes [55, 56, 11], which triggers further accumulation of these ions via voltage-gated channels and other transporters with nonlinear behavior, driving strong depolarization which may be irreversible [57, 58]. Astrocytes become incapacitated to manage the changing extracellular gradients, further exacerbating the situation [59]. Massive intracellular ion accumulation results in osmosis-driven cell swelling and possible lysing. At the synaptic level, rising presynaptic Ca^{2+} and excess cleft glutamate cause excitotoxicity in postsynaptic receptors [60, 11], and may manifest in apoptosis-induced cell death [61].
Today's research provides insight into these processes more than ever before. However, it is still unclear exactly how all these processes contribute to efficient synaptic communication. Moreover, the key players and the effect of their breakdown on other ion homeostatic processes are not completely understood. What are the consequences of Na^+, K^+ and Cl^- dysregulation on other ions such as Ca^{2+} or glutamate? What are the crucial tipping points and points-of-no-return? How can isolated experiments be assimilated to realize therapeutic measures for homeostatic recovery? Many of these questions are addressed in this thesis with computational modeling, which is the subject of Section 2.2.

2.1.2 Clinical consequences: rhythms and networks

Stroke patients exhibit a range of symptoms following stroke, such as cognitive damage or possibly paralysis. In the clinic, several techniques such as magnetic resonance imaging (MRI), computer tomography (CT) and

electroencephalography (EEG) are used to diagnose, monitor and assist in the treatment of stroke patients. CT scans distinguish between ischemic or hemorrhagic stroke. MRI analysis, though slower, provides more detail and is used to observe changes in stroke lesion volume following acute stroke [63, 7]. In acute stroke, the role of EEG is limited. However, EEG finds increasing application in monitoring comatose patients with a postanoxic encephalopathy after cardiac arrest for prognostication. For instance, in carotid arterectomy, the EEG has an established role to to assist in the decision of temporary shunting is needed [64, 65, 66].

EEG is an important diagnostic tool for many other clinical applications such as neurodegenerative disorders and epilepsy. It is obtained by recording electrical activity from a grid of electrodes placed on a patient's scalp. The activity is generated by cortical columns that serve as large current dipoles. The cortical columns are composed of interneurons, glia and most importantly, several aligned pyramidal cells that receive synchronous input [8, 67]. Pyramidal cells are neurons that are found ubiquitously, and are characterized by a conical soma and rich dendritic branching, that play an important role in signaling and computation [68].

The brain generates distinct rhythms and patterns in the form of signal intensity and frequency that can be noninvasively measured with scalp EEG recordings, as shown in Fig. 2.2. Faster rhythms such as β (14-20 Hz) and α (8-13 Hz) are regarded as normal rhythms and dominant in 'awake' patients. Slower rhythms such as θ (3-8 Hz) are normal in children and young adults, and are also the dominant rhythms during sleep. δ (<3 Hz) rhythms are also normal during sleep, but are associated with pathology when awake. Suppression of fast and emergence of slow rhythms are common in patients with acute and subacute ischemic stroke [14, 69, 70]. Moreover, isoelectric, low voltage and burst-suppression patterns are associated with poor neurological outcome following global cerebral ischemia [71, 72, 73].

Stroke also affects circuitry and may result in functional reorganization and plasticity with long-term effects [74]. Axonal sprouting [75] and dendritic spine turnover [76] are associated with damage and recovery in the penumbra. Cortical stroke can also impair motor function by disrupting thalamocortical connectivity [77, 78, 79]. These impairments are associated with chronic behavioral changes and require techniques such as neurorehabilitation for recovery.

It is well known that synaptic failure precedes edema, spreading depolarization and cell death in stroke [41]. At a cellular level, this may be alluded to diminishing neurotransmitter loading and release in low-energy conditions [13]. However, the relation between complex ischemic pathophysiology at the synaptic level and stroke mediated functional damage at the neuronal population level remains unclear. How does ion dysregulation at the tripartite synapse manifest in pathological EEG rhythms? How does synaptic arrest occur before cell swelling and spreading depolarizations? The answers to

these questions should be addressed by understanding the multi-scale impact of stroke. In the next section, mathematical modeling is presented as a way to address this viewpoint and put into perspective the multitude of interactions occurring at cellular and tissue level.

2.2 Modeling in computational neuroscience

Since the 1950s, computational modeling has offered an alternative view to neuroscience. Models describe neurophysiological processes - biophysically or phenomenologically - with the aim to reproduce experimental results, provide novel insight and make consistent predictions. This approach began with the seminal work of Hodgkin and Huxley in 1952 [1], who described the genesis of action potentials in the giant squid axon with a set of equations, famously known as the Hodgkin-Huxley model. It can be said that the Hodgkin-Huxley model serves as a basis for nearly all of today's diverse range of models in computational neuroscience. This section explores some of the essential ideas in computational neuroscience today with context to providing insight to some of the issues discussed in the previous section. In particular, single-cell, spatial and data-driven approaches are discussed.

2.2.1 Single-cell approaches

Single-cell modeling focuses on describing ion homeostasis and membrane potentials of a single neural compartment. The selective permeability of the compartmental membrane allows ions to be exchanged with the extracellular space, subject to two driving forces: diffusion and electrical forces. These two balance out at the Nernst potential, which is the solution to disappearing current in the Nernst-Planck equation [2]. The Nernst potential E_X is associated with the 'reversal' in movement of an ion X, and is used to model the associated current I_X given the membrane potential V as follows,

$$I_X = g_X(V - E_X), \tag{2.1}$$

where g_X is a constant conductance. The Nernst potential is given by,

$$E_X = \frac{RT}{zF} \log\left(\frac{[X]_e}{[X]_i}\right), \tag{2.2}$$

where $[X]_i$ and $[X]_e$ are intracellular and extracellular concentrations of ion X respectively. The constants R and F are the universal gas constant and Faraday's constant, respectively. The absolute temperature T is usually set to body temperature and z is the valency of the ion X.
The Hodgkin-Huxley model describes the formation of an action potential, based on the opening and closing of voltage-gated Na^+ and K^+ channels. In

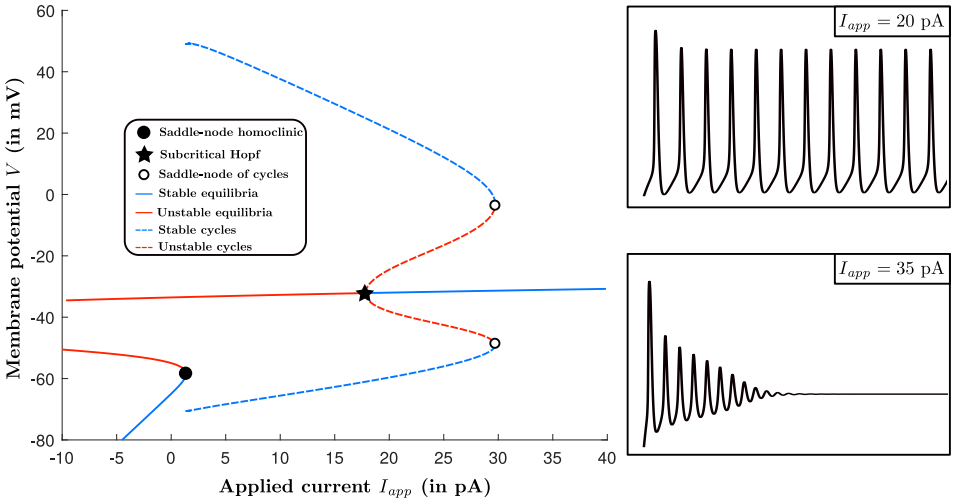

Figure 2.3: Diverse behaviour exhibited by the Hodgkin-Huxley model Eq. 2.3. (Left) Plot of the bifurcation diagram of the model with respect to input current I_{app}. (Right) Plots of membrane potential V against time for two values of parameter I_{app} using $V = -65$ mV as initial condition. The following parameters are fixed: $E_{\text{Na}^+} = 55$ mV, $E_{\text{K}^+} = -77$ mV, $E_L = -65$ mV, $\bar{g}_{\text{Na}^+} = 40$ mS/cm^2, $\bar{g}_{\text{K}^+} = 35$ mS/cm^2, $g_L = 40$ mS/cm^2 and $C = 1$ µF/cm^2. The following bifurcations are shown: limit point (saddle-node) of cycles (LPC), subcritical Hopf (H) and the saddle-node homoclinic bifurcation (SNH). Bifurcation analysis is performed with Matcont [80].

this case the conductances g_X are nonlinear functions of the membrane potential V. The reader is referred to [2, 81] for a detailed discussion and derivation. The model is composed of a set of four differential equations that describe the membrane potential V of a neuron as follows,

$$\begin{cases} C\dfrac{dV}{dt} = -\bar{g}_{\mathrm{Na}^+} m^3 h (V - E_{\mathrm{Na}^+}) - \bar{g}_{\mathrm{K}^+} n^4 (V - E_{\mathrm{K}^+}) - g_L (V - E_L) + I_{\mathrm{app}}, \\ \dfrac{dm}{dt} = \alpha_m (1 - m) - \beta_m m, \\ \dfrac{dh}{dt} = \alpha_h (1 - h) - \beta_h h, \\ \dfrac{dn}{dt} = \alpha_n (1 - n) - \beta_n n, \end{cases} \tag{2.3}$$

where m, h, n are voltage-dependent gating variables, $\bar{g}_X$ are maximal conductances, E_X are reversal potentials and I_{app} is constant applied current. The terms α_X and β_X model the opening and closing of the gating variables respectively. They are described by nonlinear terms dependent on the membrane potential V and are given by,

$$\begin{aligned} \alpha_m &= \frac{0.32(V+52)}{1-\exp(-(V+52)/4)}, \ \beta_m = \frac{0.28(V+25)}{\exp((V+25)/5)-1}, \\ \alpha_h &= 0.128\exp(-(V+53)/18), \ \beta_h = \frac{4}{1+\exp(-(V+30)/5)}, \\ \alpha_n &= \frac{0.016(V+35)}{1-\exp(-(V+35)/5)}, \ \beta_n = 0.25\exp\left(-(V+50)/40\right). \end{aligned} \tag{2.4}$$

Typical traces of V against time for nonzero I_{app} are shown in Fig. 2.3 (right). For a range of the parameter I_{app}, the Hodgkin-Huxley model is *bistable* - varying I_{app} results in multiple invariant sets that are simultaneously stable. The system contains two stable equilibria (one healthy, one depolarized) and a stable periodic orbit (action potentials). This property is exploited in single-cell approaches to design models that inherently contain bistability which provides the basis to qualify tipping points and points-of-no-return via bifurcation analysis.

The dynamics of other ion channels are also modeled as ohmic currents, identical to Eq. 2.1. Alternatively, the Goldman-Hodgkin-Katz (GHK) current was formulated to model unequal ion distribution on either side of a membrane [82, 83, 84]. While the ohmic current as in Eq. 2.1 has a linear dependence, the GHK current is nonlinear in V and is given by,

$$I_{\mathrm{GHK}} = \frac{\mathrm{F}^2 V}{z^2 \mathrm{RT}} \frac{[X]_i - [X]_e \exp\left(-\frac{\mathrm{F}V}{z\mathrm{RT}}\right)}{1 - \exp\left(-\frac{\mathrm{F}V}{z\mathrm{RT}}\right)}. \tag{2.5}$$

Computational models developed since the 1950s have continuously used these two types of currents to model ion fluxes, along with nonlinear gating variables and Michealis-Menten type kinetics within the Hodgkin-Huxley setting. Given GHK or ohmic formulations of ion channel currents I_Y^X of type Y corresponding to ion X, the evolution of intracellular ion concentrations $[X]$ is given by,

$$\frac{d}{dt}[X] = -\frac{1}{zF \cdot W} \sum_Y I_Y^X, \tag{2.6}$$

where W is the intracellular volume.

Early works modeled astrocyte-mediated ion homeostasis using glial buffers [85, 86] that modeled K^+ buffering [37]. The buffers were described as a bath of constant K^+ concentration and were allowed to exchange K^+ exclusively with the extracellular space. This exchange was modeled by linear diffusion. For several models that study spreading depolarization in the context of ischemia or epilepsy, glial buffers remain the norm [87, 88, 89]. Explicit ion dynamics in the astrocyte were first constructed in the context of cytosolic Ca^{2+}-oscillations, that depended on inositol 1,4,5-trisphosphate (IP_3) concentrations [90, 91]. These models evolved to explicitly explain the Ca^{2+}-induced-Ca^{2+}-response phenomenon that is mediated by metabotropic glutamate receptors on the astrocyte membrane [92, 93, 94].

During this time, astrocytes came to be recognized increasingly with neurotransmission and *gliotransmission* [95, 96] - the release of neurotransmitter glutamate back into the synaptic cleft by astrocytes. This creates a positive feedback mechanism for glutamate at the *tripartite synapse*. Modeling efforts in this context focused on this cycle, and its effect on synaptic transmission [97, 98, 99, 100, 101]. Similar to previous work, these models focused on astrocyte Ca^{2+}-signaling with novel coupling of presynaptic and postsynaptic function.

As discussed in the previous section, it is essential to understand Na^+, K^+ and Cl^- dynamics at neuron-astrocyte interactions in the context of ischemia and stroke. Several such models have been proposed over the years to study spreading depolarizations and epilepsy [86, 85, 88, 87]. The addition of the anion Cl^- makes the system electroneutral - allowing an almost equal exchange of charge across the membrane without completely relying on leak channels. Such formulations have also been proposed to investigate the specific roles of astrocyte channels such as the bicarbonate cotransporter, Na^+-K^+-$2Cl^-$transporter (NKCC1) and the inwardly rectifying Kir channel on healthy neuronal function [102, 103, 104]. Ischemia is modeled by transiently inhibiting Na^+/K^+-ATPase activity. In this regard, modeling work has focused on qualifying irreversible depolarization and the mechanistic nature of cell swelling [89, 105, 43, 106].

Nevertheless, the insight provided by single-cell models regarding the link between transmission failure, cell swelling and ion dysregulation remains limited. The challenge lies in the highly complex nature of the tripartite synapse - it is feasible to model certain processes phenomenologically, such

as glutamate recycling [107] or anion movement [105]. Moreover, it is difficult to reconcile conservation of mass and volume, electroneutrality and physical limiting principles like the Donnan equilibrium, with biophysical ion gradients [43]. With growing experimental insight on specific ion channel behavior, the volume of detailed models today and increasing computational power, there is a silver lining. Given such detailed models of the tripartite synapse, several questions arise. What are the key parameters underlying ischemic pathologies and differential sensitivity? What astrocyte processes contribute to the preservation of healthy neuronal behavior in low-energy conditions? What therapeutic measures, if any, can assist in successful recovery of the synapse upon restoration of energy?
This section provided a very brief outline of single-cell approaches today. An overview of early neuronal modeling can be found in the classic books by Hille (1984) [108], and Koch and Segev (1989) [21]. Reviews on state of the art astrocyte modeling are presented in [109, 22, 110].

2.2.2 Spatial models

Examples of some global pathologies of ischemia and stroke are the enlarging of the core area, global synaptic failure and spreading waves of depolarization and ion accumulation. These events occur on a broader spatial scale - such as cortical columns, tissues and brain regions - where the number of neurons could vary from thousands to millions. In this scenario, single-cell models become computationally expensive, and difficult to accurately describe and infer from. Spatial models overcome this by coarse graining and describing the averaged activity of a neuronal population instead. They are designed to be compared with clinical measurements such as EEG and spatial imaging data such as MRI, and are mathematically tractable. This section covers two such formulations - *neural masses* and *neural fields*.
The foundational work in neural mass modeling was laid by Lopes da Silva and colleagues [18] to explain physiological α-rhythms. The work was further popularized by the Jansen-Rit formulation [19, 111] which contains three interacting neuronal populations - pyramidal neurons, and *inhibitory* and *excitatory* interneurons. Neural mass models contain two essential components underlying coarse-graining - the synaptic response and firing rate. The simplest model corresponds to that of a single population. Given an incoming firing rate or spike density $Q_{in}(t)$ (in units of frequency), the neural mass model computes the average postsynaptic potential $V(t)$. The resulting EEG is assumed to be directly proportional to the pyramidal postsynaptic potential. $V(t)$ is simply given by the linear convolution,

$$V(t) = h(t) * Q_{in}(t), \tag{2.7}$$

where $h(t)$ is the synaptic impulse response (in volts) usually normalized to unity and ν is the mean synaptic efficacy. The convolution collects effects of

incoming firing rates $Q_{in}(t)$ via the opening and closing of the synapse, as described by the impulse response. They are usually modeled after postsynaptic potential profiles. For instance, the impulse response used in the Jansen-Rit formulation is the following,

$$h(t) = \nu t \tau_1 \exp(-t\tau_2), \tag{2.8}$$

where ν is the maximum postsynaptic potential, and τ_is are positive time constants. The populations are *excitatory* for $\nu > 0$ and *inhibitory* when $\nu < 0$. Next, potential $V(t)$ is converted to a population firing rate $Q(t)$ via a sigmoidal firing rate $S(x)$ as follows,

$$Q(t) = S(V(t)), \tag{2.9}$$

where

$$S(x) = \frac{Q_{\max}}{1 + \exp(\beta(x_{th} - x))}, \tag{2.10}$$

with slope β, threshold x_{th} and maximal firing rate $Q_{\max}$. The firing rate $Q(t)$ can then be fed into other populations or to itself (self excitation/inhibition). The evolution equations are constructed by taking the Laplace transform of Eq. 2.7, which gives,

$$\ddot{V} + 2\tau_2 \dot{V} + \tau_2^2 V = \nu \tau_1 Q_{in}(t), \tag{2.11}$$

where the dot indicates a time derivative. By introducing more populations and adding connections, the term Q_{in} is replaced by firing rates from connected populations, which forms the basis for *coupled* neural masses. Extensions of the Jansen-Rit model are used frequently in coarse-grained neuronal modeling today. For instance, coupled neural masses are used widely to study epileptic seizure activity [112, 113, 114, 115]. They are also popular in the clinic and are essential components in virtual epileptic surgery [116, 117].

The idea of population firing rate in Eq. 2.10 can be leveraged to construct spatiotemporal models of neural activity. This is precisely the working principle in neural field equations, first conceived by Beurle [118], and popularized by the works of Wilson and Cowan [119, 16], Amari [17, 120] and Nunez [121]. They are characterized by spatiotemporal integrodifferential equations and contain two major components - a synaptic component and a spatial connectivity kernel supported by the firing rate function. The popular Amari formulation models the activity $u(x,t)$ corresponding to a neuron at point $x \in \Omega$ and time t as follows,

$$\dot{u}(x,t) = -u(x,t) + \int_\Omega w(x,y) S(u(y,t)) dy, \tag{2.12}$$

where the dot indicates time derivative. The term $w(x,y)$ is the connectivity kernel and $S(u)$ is the firing rate Eq. 2.10 from before. The kernel $w(x,y)$ is usually chosen to be homogeneous such that $w(x,y) \equiv w(x-y)$ which makes the integral term a convolution,

$$\dot{u}(x,t) = -u(x,t) + w * S. \tag{2.13}$$

Diverse variants of neural field equations are studied for their rich pattern-forming dynamics - bump solutions, traveling waves and breather solutions [122, 123]. Modeling efforts in neural fields focus on finding these patterns using bifurcation analysis, which is covered in the next section. These spatiotemporal patterns are linked with a variety of neurological phenomena, such as EEG rhythms [124], working memory [125], hallucinations [126], microelectrode array data [127], evoked response potentials [128] and epileptic seizures [129]. In the chapters ahead, a new transition in traveling wave behavior emerging from a neural field equation is theoretically analyzed for nearby behavior.

This thesis also focuses on building models that bridge single-ion approaches and spatial models in the context of stroke. Neural mass models are chosen for coarse graining for two reasons. First, spatial dependence is absent in neural masses. Second, biophysical descriptions of synaptic currents can be efficiently extended to the population-averaged setting. Adaptations to the Jansen-Rit formulation have been used to extend the pool of describable EEG rhythms. The Wendling model [130] in particular uses slow-fast synaptic dynamics to explain rapid activity in addition to normal activity, spike discharges and slow rhythmic activity. Slow-fast dynamics govern the presence of burst-suppression behavior [20] and mixed-mode oscillations [131, 132], which are clinically unfavorable EEG phenomena.

Slow characteristics at the synapse are derived from plasticity and ion dynamics. The Liley model [133] is the first to introduce reversal potentials in the neural mass formulation, resulting in chaotic dynamics - a property considered vital for modeling perception and cognition [134, 135]. Extensions of the Liley model have successfully modeled burst suppression behavior [136, 137].

In the context of stroke and ischemia, there is a dearth of neural mass approaches to explain EEG dynamics. Ion dynamics play a crucial role in providing the slow transients needed to model behavior such as physiological rhythms, slow δ activity and burst suppression in a single model. The challenge lies in the detail required to model energy dependence, and to reconcile the effect of low ATP at synapses with population-averaged activity. To this end, Fokker-Planck approaches have been used to derive spatially homogeneous coarse-grained activity from populations of Hodgkin-Huxley and FitzHugh-Nagumo neurons [138]. However, applying this approach to detailed single-cell models - such as those discussed in the previous subsection - quickly becomes mathematically intractable. Moreover, changing ion dynamics also make the firing-rate assumption in Eq. 2.10 unfeasible [139] and requires a reworking of the reversal potentials in the Liley model, which are kept constant. In chapters ahead, bridging ion dynamics and population activity in the context of ischemia is addressed by using a hybrid neural mass model that includes explicit ion dynamics, a detailed firing rate function and realistic synaptic currents.

2.2.3 Data-driven modeling

So far, *bottom-up* approaches have been discussed - physical principles and approximations are used to construct equations that constitute computational models. However, the bounty of experimental data today warrants a fresh perspective on modeling. Can data reinforce a biophysical description? Can underlying physical principles be derived directly from data itself? This view - the so-called *top-down* approach - forms the modern arm of modeling, and has tremendous scope in computational neuroscience. *Data-driven* modeling thus focuses on building generalizable approaches for analyzing sufficiently large datasets - with the goal of performing predictive modeling.

A key problem associated with detailed biophysical models is that of parameter estimation. Extensions of the Hodgkin-Huxley model contain several parameters that are required to be inferred or estimated from data, which is tedious. Data assimilation methods are widely used in computational neuroscience to do so, and also assimilate unobserved states. Particle filters such as Kalman filter methods have been used to estimate unobserved Hodgkin-Huxley gating variables [140], and unknown parameters in neuronal models [141, 142].

Classical optimization approaches are also used in data assimilation. Assuming data $\hat{X} \equiv \hat{X}(t)$ and of state $X \equiv X(t)$ described by a parameter-dependent model $\dot{X} = f(X, \alpha)$, the goal is to compute unknown parameter α by optimizing a cost function, usually chosen as the least-squares difference between state and observation,

$$\min_{\alpha} \sum_{t} \|\hat{X} - X\|^2. \tag{2.14}$$

Synchronization methods - where data is fed back as control into the model itself - are used to estimate parameters in domains with periodicity and chaos [143, 144]. In ref. [145], parameter sensitivity equations were computed to perform the optimization steps. The reader is referred to ref. [146] for a review of data assimilation and other statistical approaches in computational neuroscience.

In data assimilation approaches, the underlying biophysical principles are already known. Data-driven approaches such as Bayesian inference methods, modal decomposition techniques and machine learning approaches extract causal information directly from datasets. From a Bayesian viewpoint, perception in the brain is represented probabilistically [147]. Inference methods are thus used widely in behavioral studies to understand decision making [147, 148, 149]. Lately, they have also been theorized as a way to understand learning [150] by viewing synaptic weights as random variables.

On the other hand, modal decomposition techniques use spectral methods to identify the most significant spatiotemporal patterns from high dimensional datasets. This reduces the analysis to just a few significant *modes*. Such information is leveraged to capture low-dimensional representations from data and is suitable for classification tasks. Popular methods include principle

component analysis (PCA) and empirical mode decomposition (EMD) [151, 152]; they are however not particularly suited to time-varying nonlinear data. A new modal decomposition technique, called dynamic mode decomposition (DMD) [153] overcomes this issue by approximating the underlying linear Koopman operator. DMD and Koopman operator methods have been recently applied in neural data to characterize mismatch negativity [154] and spindle networks [155] in electrocorticography (ECoG) data and detect seizures in EEG [156].
Alternatively, one may consider extracting evolution equations directly from data - a perspective called data-driven model discovery. This view is the principle behind the Sparse Identification of Nonlinear Dynamics (SINDy), introduced in [157]. Given observations $\hat{X}$, a prospective model is introduced,

$$\dot{X} = \Theta^T W(x), \tag{2.15}$$

for a library of candidate functions $W(x)$ and a list of interpolation constants Θ. Next, a cost function identical to the one used in data assimilation is introduced, which is optimized over the interpolation constants with a sparsity constraint,

$$\min_{\Theta} \|\hat{X} - X\| + R(\Theta). \tag{2.16}$$

where the regularization $R(\Theta)$ is used to define a sparsity constraint on the interpolation constants. This yields a parsimonious representation of dynamics and has been used in modeling biological networks [158], chemical reaction dynamics [159], fluid flows [160] and control [161].
This thesis particularly focuses on low-dimensional, or *latent* representations of complex behavior, which may manifest in the form of high-dimensional datasets. Machine learning, or deep learning [162, 163], is a widely used technique to achieve this, and has been successfully applied across several disciplines. The building block in machine learning is a neural network, which is canonically an interconnected, feed-forward network of perceptrons [164]. For a large dataset $X \in \mathbb{R}^d$, the underlying low-dimensional representation $Y \in \mathbb{R}^m$, $m \ll d$ is computed via a neural network $\phi_\theta : \mathbb{R}^d \mapsto \mathbb{R}^m$, parametrized by θ,

$$Y = \phi_\theta X. \tag{2.17}$$

The neural network ϕ_θ is a composition of nonlinear functions f_i such that,

$$\phi_\theta = f_1 \circ f_2 \circ f_3 \cdots \tag{2.18}$$

The usual representation of f_i's are

$$f_i(x) = \sigma(W_i x + b_i), \tag{2.19}$$

where *weights* W_i and *biases* b_i are matrices and vectors respectively. The *activation* σ is usually a monotonously increasing functional, acting component-wise. The weights and biases make up the set θ. To learn the parameters

θ, another neural network $\psi_\alpha : \mathbb{R}^m \mapsto \mathbb{R}^d$ is introduced and the following minimization problem is solved for a suitable chosen norm (usually l_2),

$$\min_{\alpha,\theta} \|\psi\phi X - X\| + R(X, \alpha, \theta), \tag{2.20}$$

where $R(\alpha, \theta)$ is a suitable regularization. Choices of network architecture, activations, and cost function change depending on the problem at hand. The architecture introduced above, characterized by the pair $(\phi_\theta, \psi_\alpha)$, is called an *autoencoder*. Machine learning methods have been used in the context of computational neuroscience to characterize latent representations in data, categorize behavior from neural data and infer cortical perception by extracting feature maps. The reader is referred to [165, 166] for reviews on these applications.

Data-driven techniques today provide a variety of fresh perspectives on predictive modeling in neuroscience. The field of model discovery is fresh with not many applications to neuroscience, but is suited to the long-standing goal of extracting parsimony and tangible models from high-dimensional data. Lately, neural networks have been used to perform model discovery in the latent space. Underlying models are characterized by the SINDy [26] approach or the approximate Koopman operator [27, 167]. However, one of the key obstructions here is the absence of parameter-dependent models. In the context of neural pathologies like seizures and stroke, the modeling goal is to represent essential qualitative features in one single formulation, using parameters. Recently, parameter-varying data was used to construct a data-driven bifurcation diagram, however without constructing a tangible model [168]. In chapters ahead, parameter-variance in the context of model discovery is addressed using neural networks in conjunction with *normal forms* - canonical, parameter-dependent model building blocks - which are subjects of the next section.

2.3 Transitions in models: bifurcation theory

Steady-state objects such as equilibria and periodic orbits are called *invariant sets*. The transition points in between are examples of *bifurcations*. Quantifying the location and unfolding of such transitions between invariant sets forms the domain of bifurcation analysis [1]. Consider a nonlinear dynamical system,

$$\dot{x} = f(x, \alpha), \quad x \in \mathbb{R}^n, \ \alpha \in \mathbb{R}. \tag{2.21}$$

The invariant set $\omega(x_0)$ corresponding to an initial condition $x = x_0$ is given by,

$$\omega(x_0) = \{x \mid \exists \{t_j\} \text{ s.t. } \varphi_{x_0}^{t_j} \to x \text{ when } j \to \infty\}, \tag{2.22}$$

[1] This section covers some of the essentials of bifurcation analysis. The reader is referred to [3, 4] for comprehensive text on the matter.

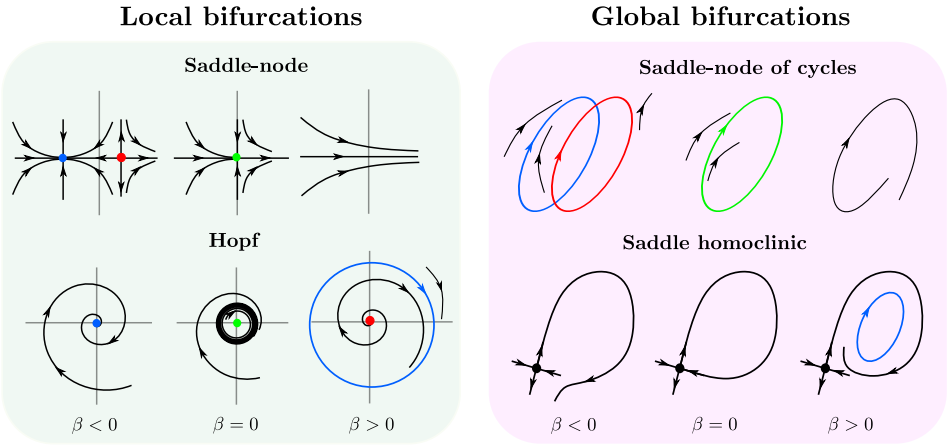

Figure 2.4: Canonical transitions corresponding to a few codimension one bifurcations. Saddle-node and Hopf are canonical bifurcations of equilibria (local), while saddle-node of cycles and saddle homoclinic orbits correspond to global bifurcations. Blue, red and green equilibria or cycles correspond to stable, unstable and center invariant sets respectively. The black circle corresponds to a hyperbolic saddle.

where φ_y^t is the corresponding time trajectory at time t with initial condition y, and is called an *orbit*. A steady state would simply correspond to a single point in $\omega(x_0)$, while a periodic orbit would be a closed curve. The notion of a qualitative change in invariant set behavior is captured by topological equivalence - two instances of the dynamical system $f(x, \alpha_1)$ and $f(x, \alpha_2)$ are topologically equivalent if orbits from both systems can be mapped onto each other by continuous, invertible transformations called homeomorphisms. The Grobman-Hartman theorem ensures that two dynamical systems are topologically equivalent close to an equilibrium if the eigenvalues of their linearizations at corresponding equilibria have the same sign.
A bifurcation is the breakdown of topological equivalence. A parameter $\alpha = \alpha_0$ is a bifurcation point when the systems corresponding to $\alpha = \alpha_0 + \epsilon$ and $\alpha = \alpha_0 - \epsilon$ yield topologically inequivalent dynamical systems, for small $\epsilon > 0$. Bifurcations manifest a change in the type and stability of limit sets $\omega(x_0)$. For instance in the Hodgkin-Huxley model, the applied current parameter I_{app} controls the transition between inactive (equilibrium) and active (spiking) states. This is illustrated in Fig. 2.3 (left). At $I_{\text{app}} = 0$ pA and $I_{\text{app}} = 35$ pA , time trajectories of the model approach a stable equilibrium. In between, for $I_{\text{app}} = 20$ pA, the trajectories quickly approach a stead-state spiking behavior, which is a periodic orbit. The transition between inactive and spiking state in the Hodgkin-Huxley model that occurs at $I_{\text{app}} \approx 1.37$ is a form of saddle-node bifurcation[2]. There are several canonical bifurcations that have been studied over the years,

[2]The bifurcation is a saddle-node of homoclinic orbits, or a saddle-node on invariant curve (SNIC) bifurcation.

that depend on the dimension and nonlinearity of the system. A few of them are shown in Fig. 2.4.

For bifurcations of equilibria, their behavioral transition is described by a *normal form* equation. These equations are polynomial vector fields with a finite number of terms that are locally topologically equivalent to any system that satisfies the bifurcation conditions. The Hopf normal form for instance is simply,

$$\dot{z} = (\alpha + i)z \pm z|z|^2,\ z \in \mathbb{C}, \tag{2.23}$$

where $\alpha \in \mathbb{R}$ is the bifurcation parameter which is sufficiently small. In Euclidean terms, the above normal form is in $\mathbb{R}^2$. However, a large n-dimensional dynamical system may also satisfy Hopf bifurcation conditions. In that case, *center manifold theory* guarantees the existence of a restriction onto a linearly attracting/repelling two-dimensional manifold - a center manifold - where the Hopf normal form describes the flow. This idea is critical to the projection of high-dimensional datasets onto low-dimensional spaces for model discovery, which is studied in chapters ahead.

In the case of periodic orbits, bifurcations are described by assessing the map formed by the action of the dynamical system on a local cross-section - called a Poincaré map. In this case, bifurcations of the map and their respective normal forms describe generic behavior. For other invariant sets such as homoclinic orbits [169] - trajectories that approach an equilibrium both in reverse and forward time - the bifurcations do not have corresponding normal forms. Generic behavior in this case is described by means of a model map on a Poincaré section.

Bifurcation analysis is widely used to determine the onset of behavioral regimes, quantify points-of-no-return and assimilate the full range of dynamics in neural modeling. In the Hodgkin-Huxley example, the saddle-node homoclinic bifurcation at $I_{\text{app}} \approx 1.37$ and the saddle-node of cycles bifurcation at $I_{\text{app}} \approx 29.72$ are the two respective thresholds of spiking behavior. One is often concerned with *bistable* regimes - parameter domains where two stable states coexist for a fixed parameter value - as seen in [170, 171, 172]. In the context of ion dynamics, this could occur when equilibria corresponding to baseline resting conditions and the depolarized state coexist and are stable [173, 43]. In this case, therapeutic measures are aimed at moving away from the bistable regime, so that the baseline resting condition is the only stable equilibrium. In a bistable regime, the study of critical switching from one stable state to another is called *tipping*, see [174, 175] for reviews on the topic.

In spatial and population-based models, periodic orbits and their bifurcations characterize the onset of spatiotemporal patterns, rhythms and even chaos [176, 177, 178]. Hyperbolic homoclinic orbits are particularly interesting, as their parametric perturbation yields at least one periodic orbit. As a result, homoclinics form boundaries of periodic behavior in models. Zero-Hopf and saddle-node homoclinic bifurcations control the onset of seizure-like activity in neural mass models for epilepsy [179, 180, 181, 182]. Homoclinic orbits can also

determine the onset of bursting behavior for instance, in Morris-Lecar neurons, see [183, 2] for detailed discussions on bursting. In neural field equations, travelling pulse solutions are represented by homoclinic orbits in the traveling wave frame [184, 185, 186]. As Shilnikov chaos revolves around homoclinic orbits, their existence is associated with rich periodic dynamics in the vicinity.
Bifurcations are an integral part of every chapter ahead. In particular, tipping phenomena in bistable regimes, slow-fast dynamics in the context of EEG rhythms, normal forms in data-driven model discovery, and the unfolding of a new homoclinic bifurcation are discussed.

Chapter 3

A biophysical model of the ion dynamics at the energy-deprived tripartite synapse

M. Kalia, H.G.E. Meijer, S.A. van Gils, M.J.A.M. van Putten and C.R. Rose, *PLOS Computational Biology 17(6): e1009019*, 2021.
M. Engels, M. Kalia, S. Rahmati, L. Petersilie, P. Kovermann, M.J.A.M. van Putten, C.R. Rose, H.G.E. Meijer, T. Gensch and C. Fahlke, *Front. Cell. Neurosci. 15:735300*, 2021.

Abstract

The anatomical and functional organization of neurons and astrocytes at 'tripartite synapses' is essential for reliable neurotransmission, which critically depends on ATP. In low energy conditions, synaptic transmission fails, accompanied by a breakdown of ion gradients, changes in membrane potentials and cell swelling. The resulting cellular damage and cell death are causal to the often devastating consequences of an ischemic stroke. The severity of ischemic damage depends on the age and the brain region in which a stroke occurs, but the reasons for this differential vulnerability are far from understood. In this chapter, we address this question by developing a comprehensive biophysical model of a glutamatergic synapse to identify key determinants of synaptic failure during energy deprivation. Our model is based on fundamental biophysical principles, includes dynamics of the most relevant ions, i.e., Na^+, K^+, Ca^{2+}, Cl^- and glutamate, and is calibrated with experimental data. It confirms the critical role of the Na^+/K^+-ATPase in maintaining ion gradients, membrane potentials and cell volumes. Our simulations demonstrate that the system exhibits two stable states, one physiological and one pathological. During energy deprivation, the physiological state may disappear, forcing a

transit to the pathological state, which can be reverted when blocking voltage-gated Na^+ and K^+ channels. Our model predicts that the transition to the pathological state is favoured if the extracellular space fraction is small. A reduction in the extracellular space volume fraction, as, e.g. observed with ageing, will thus promote the brain's susceptibility to ischemic damage. This chapter provides new insights into the brain's ability to recover from energy deprivation, with translational relevance for diagnosis and treatment of ischemic strokes.

3.1 Introduction

Information transfer at synapses [40] critically depends on the cellular availability of adenosine triphosphate (ATP), the main energy-carrying molecule in the body. Most of the energy consumption results from the activity of various ATP-dependent ion pumps, including the Na^+/K^+-ATPase (NKA). This pump transports Na^+ and K^+ ions to maintain physiological ion gradients across the cell membranes and various other ATPases involved in the release and vesicular reuptake of neurotransmitters like glutamate [187, 188].

Insufficient availability of ATP quickly results in synaptic transmission failure [189, 41, 190, 187, 188]. Depending on the depth and duration of energy deprivation (ED), this is accompanied by a loss of membrane potentials, cell swelling, and, ultimately, cell death [187, 41, 173, 190]. Several of these processes are well understood at a phenomenological level. For instance, if NKA activity is insufficient to counteract cellular Na^+ influx, the concentration of Na^+ increases within the neuronal and astrocyte compartments [191, 190, 192], and membrane potentials change. At glutamatergic synapses, the depolarization of presynaptic terminals causes the opening of voltage-gated Ca^{2+} channels, resulting in Ca^{2+} influx and subsequent glutamate exocytosis into the synaptic cleft. In addition, lack of ATP causes failure of plasma membrane Ca^{2+}-ATPases, while Na^+/Ca^{2+}- exchangers (NCX) may aggravate intracellular accumulation of Ca^{2+} due to their reversal [191, 193, 192]. At the same time, the increase in neuronal Na^+ is accompanied by an increase in intracellular Cl^- to maintain electroneutrality [43], resulting in cell swelling [44]. If NKA activity is completely absent such as in the core region of an ischemic stroke, ion gradients evolve to the Gibbs-Donnan potential [194]. All active transport fluxes have disappeared at this equilibrium, and the membrane potential equals the individual ions' Nernst potentials. This cascade of events is accompanied by failure of cellular glutamate uptake through excitatory amino acid transporters (EAATs), which are mainly expressed by astrocytes [50, 195]. The resulting toxic accumulation of glutamate in the extracellular space (ECS), coupled with intracellular Ca^{2+} accumulation, triggers neuronal cell death via multiple pathways [196].

Despite these recent experimental advances in understanding the phenomenology of energy failure in the brain, there is only limited understanding of the

interplay of the distinct transporters and ion fluxes of both neurons and surrounding astrocytes under these conditions. The tight anatomical and functional inter-relationship between pre- and postsynaptic compartments and surrounding astrocytes, established about 20 years ago as the tripartite synapse [40], adds to the challenging complexity of the biological system. The numerous dynamical and nonlinear interdependencies between different transport processes in the cellular compartments involved can eventually only be elucidated with biophysical models, calibrated with experimental data [197]. Motivated by these considerations, various biophysical models of the tripartite synapse have been introduced [198, 109, 110]. Some models focus on glutamate release and uptake in the extracellular space and Ca^{2+} release from IP_3-sensitive Ca^{2+} stores in astrocytes [199, 200, 201]. Other works have addressed mechanisms of gliotransmission via vesicular release [101, 100].

A few models describe neuron-glia interactions in pathological conditions, e.g., to identify mechanisms involved in cell swelling or spreading depression [43, 105, 202, 203, 204]. Several key questions, however, remain. For example, the temporal aspects remain mostly unexplored, whereas experimental data shows that the duration of ED is a crucial parameter. Short durations allow neurons to recover [191]. Longer, even infinite, durations of ATP depletion lead to the Gibbs-Donnan potential [43].

A clinically highly significant finding is that the vulnerability to ischemia differs between brain regions. Here, the differential sensitivity of the cellular and biophysical determinants is not evident [205, 206, 15]. The age-dependence of the brain's cellular vulnerability to ischemic conditions is another highly relevant phenomenon that is not understood in detail [207]. The expression of many ion transporters changes significantly during postnatal development and maturation of neuronal networks. Ageing is associated with down-regulation of NKA and weakening pump activity [208] and is accompanied by structural changes such as the fine morphology of astrocytes [209]. However, it is unclear to what extent this contributes to the age-dependent sensitivity to ischemia. In addition, the relative size of the ECS changes significantly during life. Whereas the ECS volume fraction is about 20% of total tissue volume in adult rodents' forebrain, it is around 40% in neonates and shrinks to about 15% in aged animals [210]. The consequences of these changes for the functional interplay between the different compartments of the tripartite synapse and their relevance for the vulnerability of tripartite synapses to energy depletion are not understood.

Taken together, we hypothesize that there are a critical duration and depth of ATP depletion to induce a pathological state. This duration and depth depend on ion kinetics and geometry. To address this question, we study how the bulk ion species, i.e., Na^+, K^+, and Cl^-, react to switching off NKA for a specific duration and depth. Our model also includes Ca^{2+} and glutamate. Although we report on their dynamics, we do not study these in detail as they do not represent the bulk of ions. Nevertheless, it is necessary to include both as they mitigate large Na^+- and K^+-currents during energy depletion.

We propose a novel model combining elements from existing models into a comprehensive, biologically realistic description. The model includes a neuron and an astrocyte within a finite extracellular space. For the active transporters and glutamate release, we formulate a correct electrodiffusive, ion conserving model. All ion fluxes included in this chapter have been studied and validated in simpler setups. For most models, it suffices to model K^+. For instance, Kager et al. [211] proposed a microdomain model accounting for all fluxes with glial behaviour modelled with a K^+ bath to study spreading depression. Later, other researchers [43, 212, 213, 102, 214] have proposed electrodiffusively correct models. Building on these submodels, we use parameter values from the literature where possible. We calibrate the remaining ones using recent experimental data [191].
In this chapter, we first briefly describe the layout of our biophysical model of the synapse under normal conditions. We show that including the astrocyte is essential for preserving synaptic transmission. Next, we simulate energy depletion by switching off NKA. Depending on the duration and depth of ATP depletion, the system's state either recovers or ends up in a pathological equilibrium. We explain these results using bifurcation analysis, allowing us to identify critical factors determining vulnerability, including the size of the extracellular volume and NKA pump strength. Finally, our simulation results agree with experimental data regarding recovery [15], enabling us to explore how to promote the recovery to the physiological state. Our results aid in our understanding of the early events following energy depletion. Most notably, our simulations shed new light on the cellular basis of differential vulnerability of neurons to ischemic damage.

3.2 A model for ion homeostasis at the tripartite synapse

We introduce a novel biophysical model, extending our previous work on a single cell [43] by incorporating more biological detail. The model in [43] contained a single neuronal compartment in an infinite extracellular space, whose volume is regulated by changes in osmolarity. Here, we model a neuronal and astrocytic soma, a presynaptic terminal, the perisynaptic astrocyte process, the synaptic cleft and a global extracellular space (ECS), illustrated in Fig 3.1. The volumes of the somatic compartments and ECS can change; the cleft, the presynaptic terminal and the perisynaptic astrocyte process have fixed volumes. In each of these compartments, we describe the energy-dependent dynamics of the ions Na^+, K^+, Cl^-, Ca^{2+} and glutamate, including vesicle recycling, by ordinary differential equations (ODEs). We further assume that Ca^{2+} and glutamate are confined to the presynaptic terminal, the perisynaptic astrocyte process and cleft. The concentrations of Na^+, $K^+$and Cl^- are assumed to be the same in the synaptic as well as in the somatic compartments. This allows

us to work with both small molar changes of Ca^{2+} and glutamate and large Na^+, $K^+$and Cl^-gradients across the somatic membranes, within the same compartmental framework.

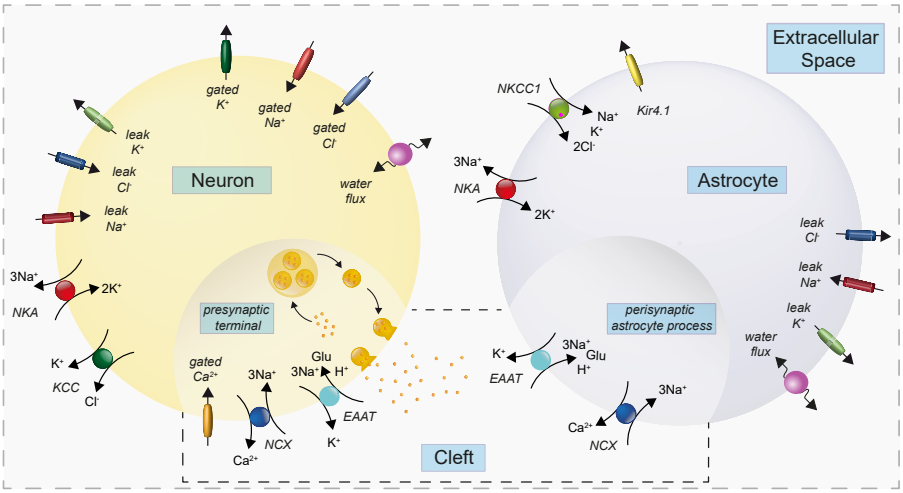

Figure 3.1: Compartments, ion channels and transporters included in the modelling of the glutamatergic synapse. Shown are the three main components representing a presynaptic neuron, an astrocyte and the extracellular space (ECS). Each of these compartments also contains a synaptic compartment as indicated by the different shading and the additional box (presynaptic terminal, perisynaptic process and synaptic cleft, respectively). The largest ATP consumption in the presynaptic neuron and the astrocyte is by the Na^+/K^+-ATPase (NKA). At the presynaptic terminal, ATP is also needed to energize glutamate uptake into vesicles. The key transporters at the cleft are the Na^+/Ca^{2+}-exchanger (NCX) and the Excitatory Acid Amino Transporter (EAAT). NKCC1: Na^+-K^+-Cl^--cotransporter. KCC: K^+-Cl^--cotransporter. Kir4.1: K^+ inward rectifier channel 4.1.

3.2.1 Model equations

For an ion X in compartment i, we describe the dynamics of the number of moles N_X^i and volumes W_i by introducing ion channels and cotransporters Y. Their currents and fluxes I are given by $I_Y^{X,i}$. The currents/fluxes I may depend on gating variables q that describe the nonlinear opening and closing of the channels/cotransporters. We define concentration $[X]_i$ of ion X in compartment i by $[X]_i = N_X^i/W_i$. A summary of the notation used is shown in Table 3.1. Thus we obtain the following system of differential equations that describe the

dynamics of N_X^i and W_i

$$\begin{cases} \frac{d}{dt}N_X^i = -\frac{1}{z_X F}\sum_j I_j^{X,i}, \\ \frac{d}{dt}W_i = \lambda_i \sum_X ([X]_i - [X]_e), \\ \frac{d}{dt}q = \alpha_q(1-q) - \beta_q q, \end{cases} \tag{3.1}$$

where F is Faraday's constant, z_X is the valence of ion X, λ_i is the osmotic flux rate for compartment i, and q denotes the Hodgkin-Huxley gating variables. To model glutamate dynamics in the cleft, we combine existing models of vesicle recycling from Tsodyks and Markram [215] and Walter et al. [216], as illustrated in Fig 3.2. Non-releasable glutamate pool (N) is made readily-releasable through four Ca^{2+}-dependent intermediate steps (R, R_1, R_2, R_3). After release into the cleft from a fused vesicle, (F), glutamate is removed by presynaptic and astroglial EAATs and enters the 'inactive (I)' state. As a final step, glutamate is again stored in a vesicle depot (D) and enters the non-releasable pool (N) again. The rate equations of these states are given by

$$\frac{d}{dt}N_Y = \sum_X \nu_X([Ca^{2+}]_n)N_X, \tag{3.2}$$

where Y and X span over $\{N, R, R_1, R_2, R_3, I, D, F\}$. The rate constants ν_X depend on Ca^{2+} concentrations in the neuronal synaptic compartment. Eqs. (3.1) and (3.2) describe ion and volume dynamics in the neuronal and astrocyte compartments. To obtain extracellular dynamics, we use three conservation laws, i.e.,

$$\begin{cases} \sum_{X,i} z_X N_X^i = 0, \\ \sum_i W_i = C_W = \text{constant}, \\ \sum_i N_X^i = C_X = \text{constant}, \end{cases} \tag{3.3}$$

for the preservation of charge, volume, and mass, respectively. Our model is essentially described by Equations (3.1), (3.2) and (3.3). Here, the constants C_W and C_X are the total volume and total molar amount of ions present in the system, respectively. We present further details in the section **Materials and Methods**.

3.2.2 Simulations and model calibration

In the following sections, we present and discuss *in silico* experiments simulating ED. We simulate ED by temporary blocking and subsequently restoring of the

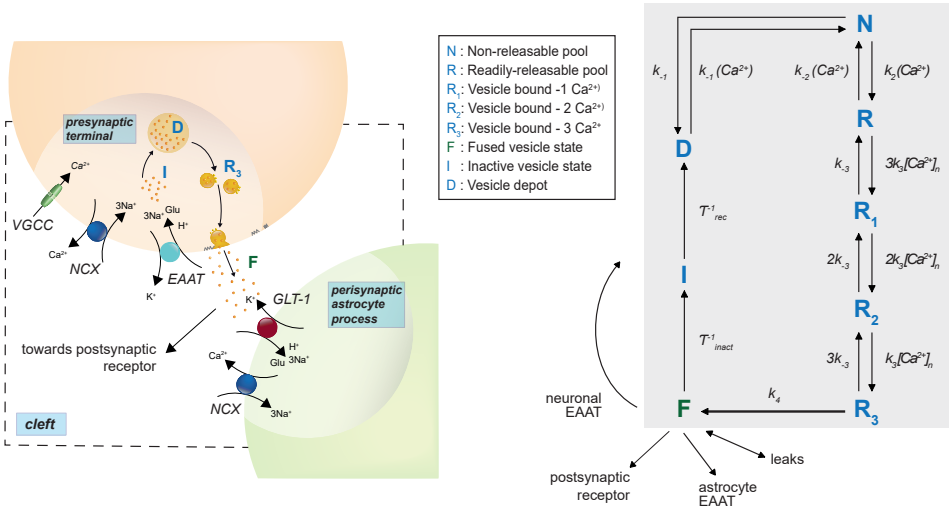

Figure 3.2: Glutamate recycling scheme, inspired by combining vesicle-based models from [215] and [216]. (Left) Closer view of the model scheme at the synapse and (Right) the glutamate recycling scheme. Inactive neuronal intracellular glutamate (I) moves to the depot (D) from where it is packed into vesicles which pass through five stages (N,R, $R_{1,2,3}$) before they are released into the synaptic cleft (F). These stages have fast time-constants that depend on intracellular Ca^{2+} concentration. The stages R_i correspond to vesicles that are bound by i Ca^{2+} ions. The time-constants change when there is influx of Ca^{2+} in the presynaptic terminal in response to membrane depolarization. Released glutamate in the cleft can be taken up by astrocytes or back to neurons using excitatory amino acid transporters (EAATs) or leak channels, thereby recycling the released neurotransmitter.

NKA current in the neuronal and astrocyte compartment. The expression for the NKA current is given by,

$$I^i_{\mathrm{NKA}} = \left(\frac{I^{\max}_{\mathrm{NKA}}(t)}{100}\right) P^{\mathrm{scale}}_{\mathrm{NKA}} f^i_{\mathrm{NKA}}. \tag{3.4}$$

The expression f^i_{NKA} describes the inward NKA current. It depends on neuronal Na^+ concentration and extracellular K^+concentration. Details can be found in **Materials and Methods**. ED is simulated by manipulating the function $I^{\max}_{\mathrm{NKA}}(t)$, which is the amount of energy available (in %). The function $I^{\max}_{\mathrm{NKA}}(t)$ is implemented as

$$I^{\max}_{\mathrm{NKA}}(t) = P_{\min} + (1 - P_{\min}) I_{\mathrm{block}}(t), \tag{3.5}$$

where we have the U-shaped function

$$I_{\mathrm{block}}(t) = (1 + \exp(\beta(t - t_1)))^{-1} + (1 + \exp(-\beta(t - t_2)))^{-1}, \tag{3.6}$$

Table 3.1: **Notation used in the model equations.**

Notation	Description
N_X^i	Molar amount of ion X in compartment i.
$[X]_i$	Concentration of ion X in compartment i.
W_i	Volume of compartment i.
$I_Y^{X,i}$	Current/flux contribution of ion channel/transporter Y with respect to ion X in compartment i.
V_i	Membrane potential with respect to compartment i.
z_X	Valence of ion X.
$P_X^{X,i}$	Permeability/strength/conductance of ion channel/transporter Y with respect to ion X in compartment i.
	Choices for i, X, Y
i	n (neuronal soma), a (astrocyte soma), e (extracellular space), ps (presynaptic terminal), pap (astrocyte process) or c (cleft).
X	Na^+, K^+, Cl^-, Ca^{2+} or glutamate.
Y	EAAT, NCX, NKA, KCl, NKCC1, Kir, G (Gated) or L (Leak).

such that

$$t_1 = t_{\text{start}} - \frac{1}{\beta}\log(1/P_{\min} - 1),$$
$$t_2 = t_{\text{end}} + \frac{1}{\beta}\log(1/P_{\min} - 1). \tag{3.7}$$

The parameter β controls the steepness, t_{start} denotes the onset time, and t_{end} denotes the offset time. The parameter $P_{\min}$ is the minimum available energy when ED is induced. Fig 3.3A shows how this is implemented.
All the parameters in this model have been sourced from previously published work. However, we set the parameters α_e, $P_{\min}$, $P_{NKA}^n (= P_{NKA}^a)$ to fit the experimental traces in [191] using an empirical parameter search. In these experiments, metabolism is inhibited by exposing cells to 'chemical ischemia' for 2 minutes. Recordings are made before, during and after the event. Of note, the transient drop in ATP levels is not abrupt and lasts longer than 2 minutes. To account for this, we simulate ED for 5 minutes and compare to compartmental Na^+ and extracellular K^+ concentrations, see Fig 3.3. As details about the change of NKA activity resulting from chemical ischemia used in the experiments are not completely known, we observe some differences in neuronal and astrocytic Na^+ gradients during the onset of ED. In neurons, the presence of voltage-gated Na^+ channels that are activated upon membrane depolarisation causes a fast and strong Na^+ influx. In contrast, the model for astrocytes does not have any fast, channel-mediated Na^+ influx pathway, resulting in lower Na^+ rise. Thus, we characterize the chemical ischemia experiments from [191] with the parameter values $\alpha_e = 80\%$, $P_{\min} = 50\%$ and $P_{NKA}^n = 86.4$ pA, and use them

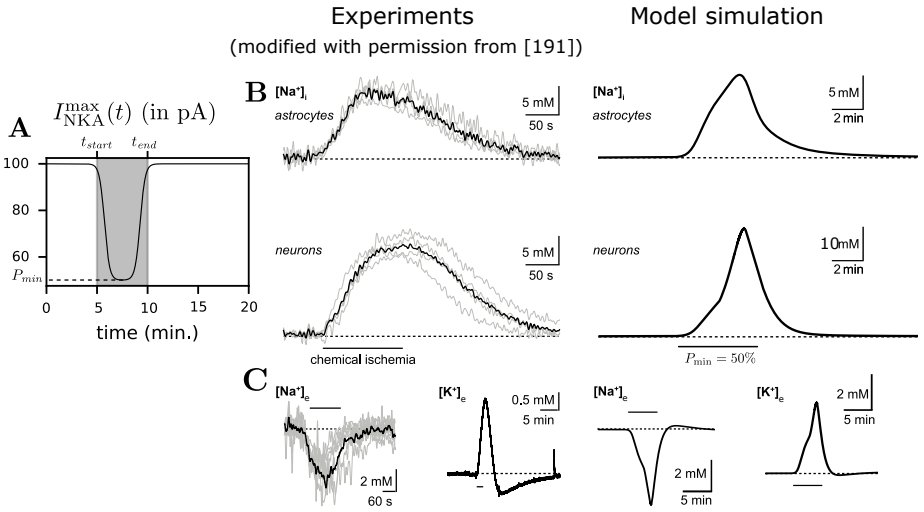

Figure 3.3: Model calibrations reproduce experimental data. (A) Plot of $I^{\max}_{NKA}(t)$ versus time t. ED begins at $t = t_{start}$ min. and ends at $t = t_{end}$ min. while being reduced to a minimum of $P_{\min}$. (B,C) Experimental traces from [191] (left) and the corresponding model simulations (right) with (B) showing intracellular sodium for neurons and astrocytes and (C) showing extracellular sodium and potassium. Empirically adjusted parameters: $P_{\min}$ and α_e^0 (initial extracellular volume fraction) were chosen by fitting model dynamics qualitatively to Na^+ and K^+ concentration time-traces. Here, $P_{\min} = 50\%$ and $\alpha_e^0 = 80\%$. The difference in Na^+ increase between neurons and astrocytes is attributed to the presence of fast Na^+ influx through voltage-gated Na^+ channels in neurons, which are lacking in astrocytes. Please note that scaling axis in panels B and C may slightly differ between experiments and simulations for optimal display purposes.

for further simulations presented in this chapter.

We summarize the various simulations performed ahead in Table 3.2. Apart from finite-time ED, we also perform simulations for different values of P_{scale} and α_e. This can have consequences on other parameters. P_{scale} scales the baseline NKA strength P^i_{NKA}, making it stronger ($P_{\text{scale}} > 1$) or weaker ($P_{\text{scale}} < 1$). Upon changing P_{scale} from its default value of 1, the equilibrium corresponding to the initial (baseline) conditions disappears. To fix this equilibrium, we recompute all leak permeabilities $P_L^{X,i}$ whenever P_{scale} is changed.

The parameter α_e is the initial extracellular volume ratio and is given by

$$\alpha_e = \frac{W_e^0}{W_{\text{tot}}}. \tag{3.8}$$

We fix the initial volumes W_n^0 and W_a^0, and choose the extracellular volume to

Table 3.2: **Parameter values for all simulations performed.** Units are presented in the same manner as they are implemented in the Python code.

Simulation	Parameter values	Description
Calibration	$P_{\min} = 50\%$ $\alpha_e = 80\%$ $P_{scale} = 1$ $t_{start} = 5$ min. $t_{end} = 10$ min.	Parameters used to calibrate to the two-minute *in vitro* chemical ischemia experiments performed in [191].
Excitation	$P_{\min} = 100\%$ $\alpha_e = 80\%$ $P_{scale} = 1$ $\max(I_{excite}) = 20$ pA (4 times, 10s)	Exciting the neuron in the presence and absence of the astrocyte.
ED	$P_{\min} = 50\%$ $\alpha_e = 20\%$ (Small ECS) $\alpha_e = 80\%$ (Large ECS) $P_{scale} = 1$ (normal) $P_{scale} = 2$ (strong) $t_{start} = 5$ min. $t_{end} = 10$ min. (short) $t_{end} = 20$ min. (long)	Transient ED for a) long and short duration, b) small and large surrounding extracellular volume and c) normal and stronger NKA pump strength.

be

$$W_e^0 = \alpha_e (W_n^0 + W_a^0)(1 - \alpha_e)^{-1},$$
$$W_{\text{tot}} = W_n^0 + W_a^0 + W_e^0. \tag{3.9}$$

3.3 Results

3.3.1 Astrocytes and ion homeostasis

We first assess the contribution of the astrocyte to the extra- and intracellular ion homeostasis under physiological conditions. For this, we stimulate our neuron with a 10-second long pulse of square wave input with magnitude 25 pA, both with and without a functional astrocyte (Fig 3.4). Simulations are performed with a realistic initial extracellular volume fraction for mature rodent cortex [210] by setting $\alpha_e = 20\%$ and full ATP availability ($P_{\min}$=100%). When the astrocyte is functional, the current injection (black trace) induces a burst of neuronal action potentials (in total 475 during 10 s) and transient depolarizations of the

astrocyte. The burst firing of neurons is accompanied by a transient decrease in extracellular Na^+, while neuronal Na^+ increases, consistent with experimental data [217]. On the other hand, in our simulation, astrocytic Na^+ slightly decreases in response to neuronal burst firing. After stimulation subsides, both membrane potentials and ion concentrations return to baseline, see Fig 3.4A. Profiles of Ca^{2+} and other ion fluxes are presented in Fig 3.12.
When the astrocyte is non-functional (simulated by blocking all astrocyte ion transport), the neuron irreversibly depolarizes during the burst (Fig 3.4B). This new state is accompanied by a significant accumulation of Na^+ in the neuronal soma following Na^+ entry via voltage-gated Na^+ channels. As astrocytic K^+ uptake via Kir4.1, NKA and NKCC1, is blocked, K^+ accumulates in the extracellular space, resulting in a sustained depolarization block of the neuron. As the continued Na^+ influx is higher than NKA-mediated Na^+ efflux, the neuron accumulates even more Na^+ and does not recover even after excitation ends. This irreversibly depolarized state is accompanied by an increased volume of the intracellular compartments resulting from an increase in intracellular Na^+ and Cl^-.
Upon restoring astrocytic function, the neuron and astrocyte do not return to their initial resting membrane voltage (Fig 3.4B). Membrane potentials remain at approximately -30 mV, and input currents can no longer trigger action potentials. From the two simulations performed Fig 3.4A and 3.4B, we see that two stable resting states are possible, i.e., the system displays *bistability*. The first state corresponds to membrane potentials of approximately -65 mV (neuron) and -80 mV (astrocyte), respectively, with functional synaptic transmission, i.e. the physiological state. The second corresponds to a pathological state with non-functional neurons and astrocytes, and impaired synaptic transmission.

3.3.2 Dynamics after varying periods of ED

We know from experimental observations that energy depletion results in accumulation of Na^+ in neurons and astrocytes while extracellular K^+ increases see, e.g. [44, 191]. At the (thermodynamic) equilibrium, the Nernst potentials of Na^+ and K^+ reach equal values. During this evolution towards equilibrium, neurons can generate oscillatory depolarizations, known as anoxic oscillations [189, 173]. These drive Ca^{2+} into the presynaptic terminal by activating of voltage-gated Ca^{2+} channels (VGCCs) which triggers the release of glutamate into the cleft. The efflux of K^+ does not fully compensate the increase in intracellular Na^+. Thus, intracellular Cl^- increases to preserve electroneutrality [218]. The resulting osmotic imbalance leads to water influx, i.e., cell swelling [44].
We first simulate such dynamics by setting the available energy $P_{\min}$ to 50% of baseline activity at an initial extracellular volume ratio $\alpha_e = 80\%$ for 5 minutes, shown in Fig 3.5A. Similar to experimental observations, reduced NKA activity leads to an increase in intracellular Na^+ and extracellular K^+. Reactivated NKA

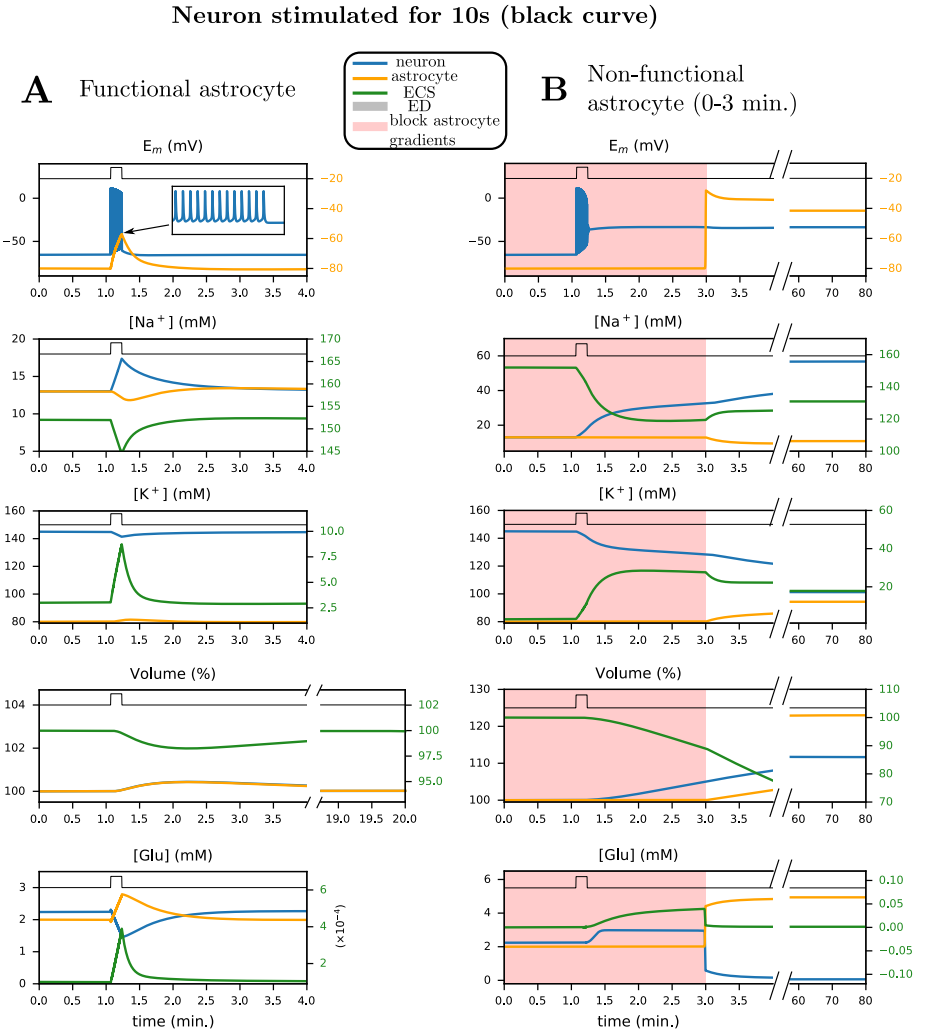

Figure 3.4: Shown are the time courses of the membrane potential, sodium and potassium concentrations, cell volume and glutamate in response to a current pulse (25 pA, 10 s, black trace) with (A) and without (B) a functional astrocyte. (A) In response to the pulse, there is a burst of action potentials and return to baseline of all quantities. (B) Without a functional astrocyte, the neuron depolarizes after the burst, and remains in this state, even if the astrocyte function is restored. Here, we plot neuronal (blue), astrocyte (orange) and extracellular (green) traces against time for several quantities. The initial extracellular volume ratio is $\alpha_e = 20\%$. The shaded red area corresponds to periods during which ion transport across the astrocytic plasma membrane is blocked.

restores the Na^+ and K^+ gradients, so membrane potentials recover to baseline in agreement with experiments [191, 15]. Changes in cell volume are below 5%, i.e., they are negligible for this simulation.

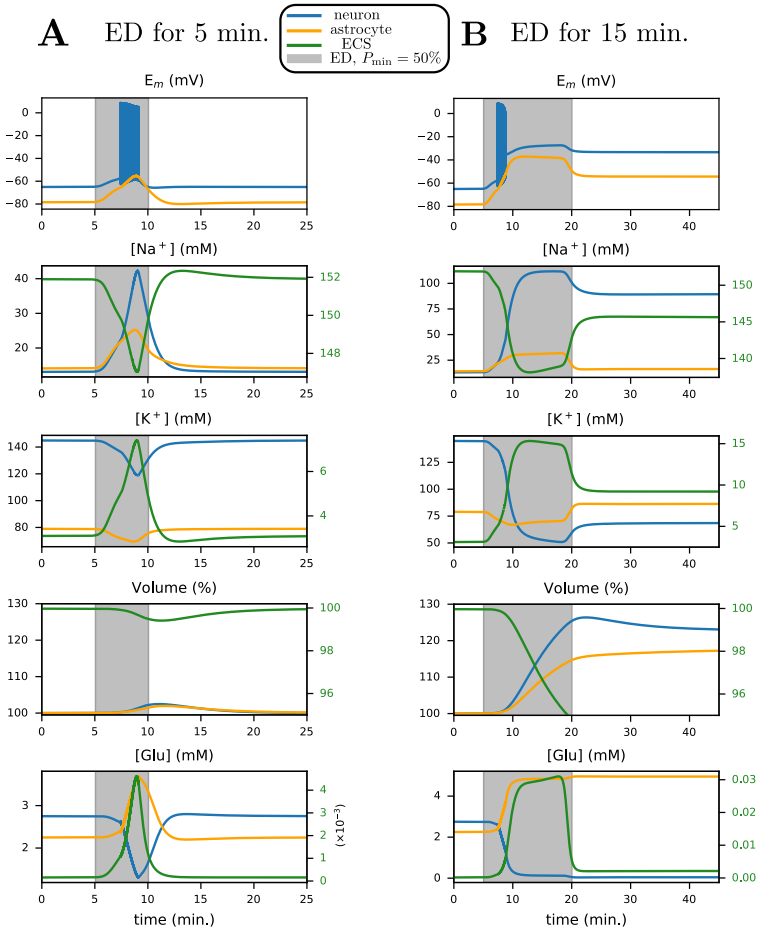

Figure 3.5: ED for 5 minutes (A) and 15 minutes (B) demonstrates the existence of two stable states: 1) before ED (baseline resting state) and 2) after prolonged ED of 15 minutes (stable depolarized state). Here, we plot neuronal (blue), astrocyte (orange) and extracellular (green) traces against time for several quantities. The initial extracellular volume ratio $\alpha_e = 80\%$ and minimal energy available $P_{\text{min}} = 50\%$. Shaded grey areas correspond to the period where Na^+/K^+-ATPase (NKA) activity is gradually reduced to P_{min} and restored to baseline, identical to Fig 3.3A.

However, when we extend the duration of ED from 5 to 15 minutes, Na^+ accumulation in the neuron is much larger than in the previous scenario. A depolarization block results, where the membrane potential approaches a stable pathological state of about -35 mV. As shown in Fig 3.5B, the increase in intracellular Na^+ and Cl^- (see Fig 3.13) causes an osmotic imbalance resulting in cell swelling. Na^+ accumulation in the astrocyte reduces EAAT activity, preventing successful clearance of excess cleft glutamate. Upon restoring energy,

astrocytic Na^+ recovers and enables EAAT to drive glutamate into the astrocyte. At the same time, in contrast, neuronal EAAT activity weakens, which prevents sufficient reuptake of glutamate into the presynaptic terminal. As a result, during ATP depletion, transport of glutamate into presynaptic vesicles is initially diminished, see neuronal EAAT current in Fig 3.13. Further, ion gradients do not return to physiological values, and permanent cell swelling is observed (approximately 20% increase in neuronal, and 10% in astrocytic volume). This occurs once again due to bistability. After a sufficiently long, but transient, period of ED resulting in both neuron and astrocytic reduction of NKA activity, the physiological state is not restored, as reflected by persistent membrane depolarization and increased cell volume. This contrasts with the scenario presented in Fig 3.5A, where the physiological state is restored for a shorter duration of ED. Time-traces for concentrations of Cl^- and Ca^{2+} are presented in Fig 3.13.

3.3.3 Determinants for recovery

Various determinants other than the depth and duration of ED have been proposed to be critical for recovery of synaptic transmission failure after ED, including the size of ECS, pump strength, and the role of the gating variables. Using our model, we explore their importance in the potential of neuronal recovery after (transient) ED.

Size of the extracellular volume

Recovery from a depolarization block after energy restoration was addressed experimentally in [15]. Neurons from two different brain regions were subjected to 15 minutes of zero energy conditions. Magnocellular neuroendocrine cells recovered, while pyramidal cells remained depolarized post energy restoration (see also Fig 3.8). As argued in [219], this may result from different ECS volume fractions. We now explore this hypothesis in our model by changing the baseline value of the parameter α_e (the extracellular volume fraction in %). In Fig 3.6A, we simulate ED for 5 minutes for $\alpha_e = 80\%$ (large ECS) and $\alpha_e = 20\%$ (small, realistic ECS) and plot the relative neuronal volume change after 30 minutes of energy restoration. The parameter P_{min} is set to 50%. For $\alpha_e = 80\%$, we observe no volume increase, which corresponds to a successful recovery after energy restoration, and vice-versa for $\alpha_e = 80\%$. Further, we simulate ED during 5 minutes for different values of α_e and P_{min} and plot the relative neuronal volume change after 30 minutes of energy restoration. We find that compartmental volumes (and thus, membrane potentials and ion concentrations) recover for larger values of α_e. This result implies that neurons and astrocytes surrounded by smaller extracellular spaces exhibit a relatively higher vulnerability to transient ED.

We provide further insight into the selective sensitivity to ECS size using

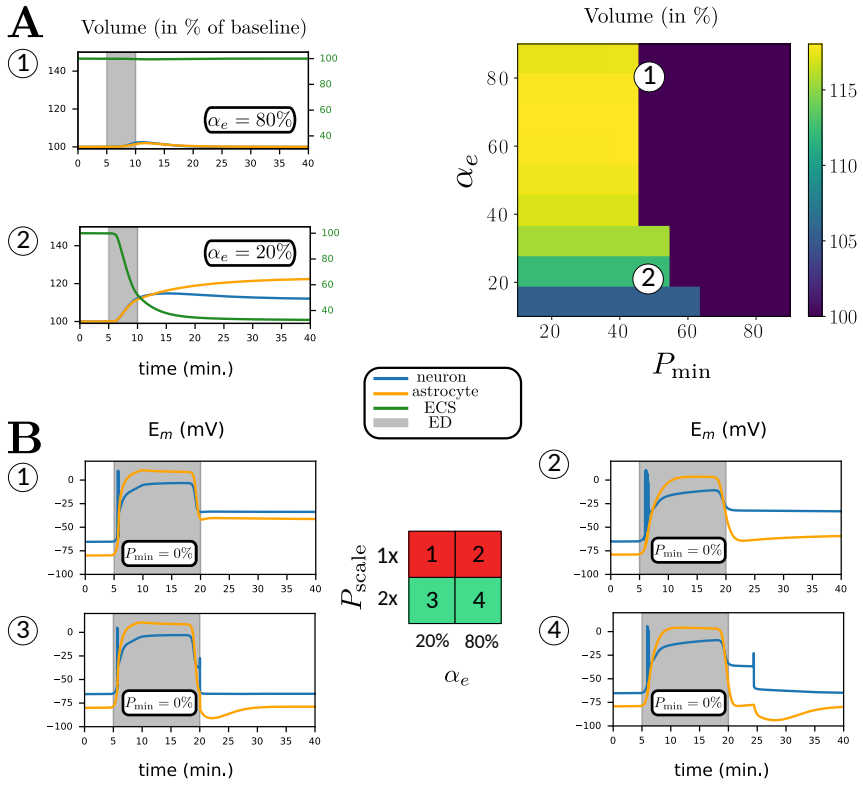

Figure 3.6: Differential sensitivity of ED to initial extracellular volume ratio α_e (A) and to baseline Na^+/K^+-ATPase strength factor P_{scale} (B). (A) We deprive the neuron and astrocyte of energy for 5 minutes before restoring it to baseline and report the relative volume 30 minutes after restoration. We show two examples, (A.1) for large ECS ($\alpha_e = 80\%$) and (A.2) for realistic ECS ($\alpha_e = 20\%$). Here, we plot neuronal (blue), astrocyte (orange) and extracellular (green) traces against time for compartmental volume change. (B) We deprive the neuron and astrocyte of energy for 15 minutes before restoring it to baseline, for two different values of P_{scale} and α_e. We show neuronal and astrocyte membrane potentials against time. The grey area in (B.1-4) illustrates the period of ED. The table in the middle indicates whether the system recovers (green) post energy restoration or not (red).

bifurcation diagrams shown in Fig 3.7A. We show diagrams for both $\alpha_e = 20\%$ and $\alpha_e = 80\%$ as a function of the available energy $P_{\min}$. We plot initial neuronal volume (in %) against $P_{\min}$, after setting $I_{\text{NKA}}^{\max}(t) = P_{\min}$ as constant. We obtain two branches of resting states. Solid (red/blue) lines correspond to stable resting states, while the dashed blue branches correspond to unstable resting states.
The bifurcation diagram can be interpreted by following the stable resting states. We start at the blue line at $P_{\min} = 100\%$, which corresponds to the baseline physiological state. As we lower NKA activity in the neuron and

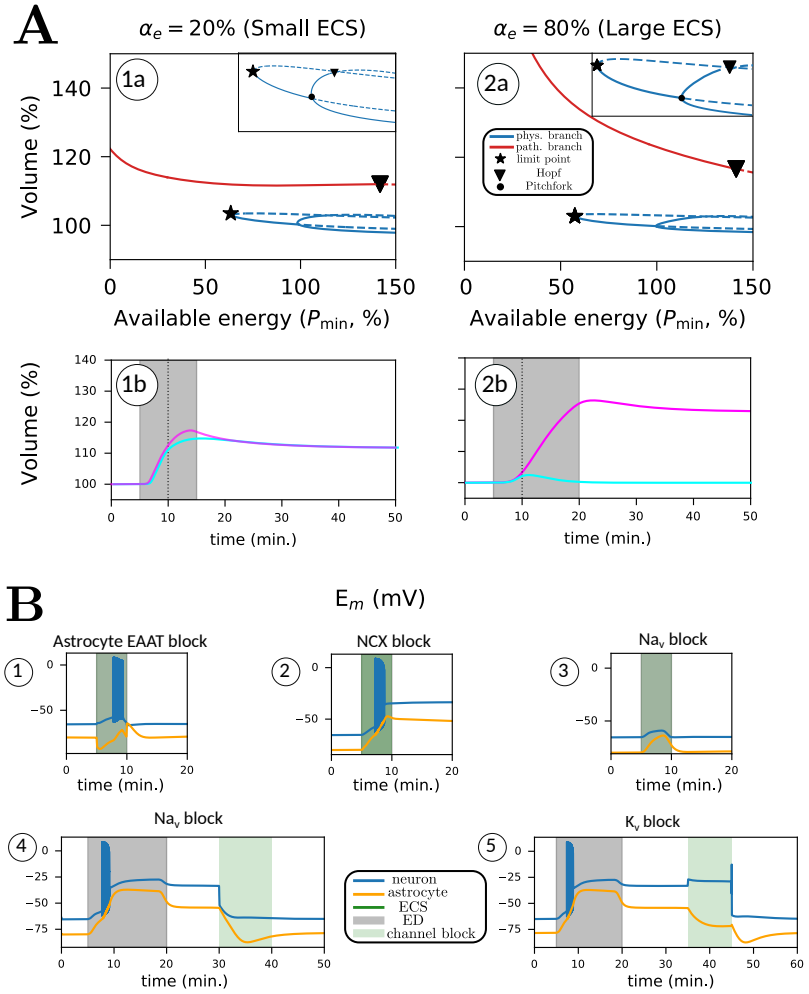

Figure 3.7: Tipping in a *bistable* regime (A) and the change in tipping behavior by introducing pharmacological blockers (B). In (A.1a and A.2a), we plot bifurcation diagrams with respect to P_{min} for $\alpha_e = 20\%$ (realistic ECS) and $\alpha_e = 80\%$ (large ECS). Red curves are pathological branches, and blue curves are physiological branches. Dashed lines represent unstable parts. The only two relevant local bifurcations are limit point (star) and Hopf (inverted triangle). The inset shows two additional bifurcations, a pitchfork (dot) and a Hopf. We show two simulations (A.1b and A.2b), short ED (5 minutes, cyan curve) and long ED (15 minutes, pink curve), both for $P_{\text{min}} = 50\%$. In (B), we block different pathways during ED (green area, B.1, B.2 and B.3) and after restoration (green area, B.4). For (B.1-3), energy is deprived for 5 minutes for parameters $\alpha_e = 80\%$ and $P_{\text{min}} = 50\%$. In (B.4), energy is deprived for 15 minutes for parameters $\alpha_e = 80\%$ and $P_{\text{min}} = 50\%$.

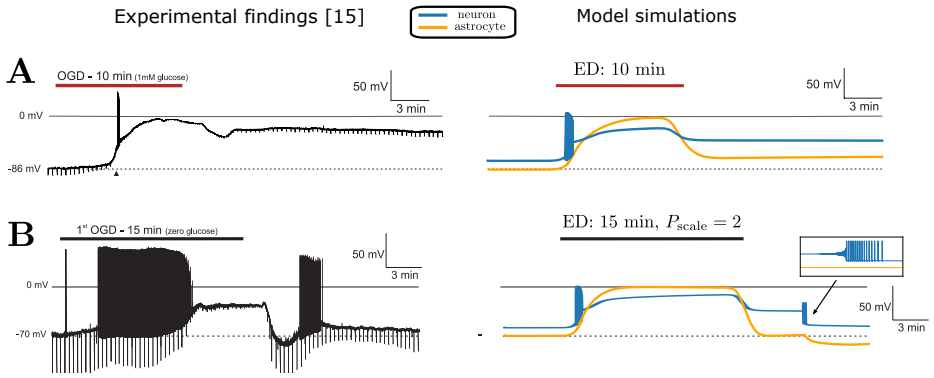

Figure 3.8: Experimental findings from Brisson and Andrew [15] (reproduced with permission) and our model simulations. (A) (Left) Membrane depolarization of a pyramidal neuron during 10 minutes of oxygen glucose deprivation (OGD), that persists after restoring energy. (Right) Model simulations on the right show the neuronal(blue) and astrocyte membrane potentials. ED (OGD) is introduced for 15 minutes (red line). Here, $\alpha_e = 80\%$ and $P_{\text{min}} = 0\%$. The dynamics are faithfully reproduced, including anoxic oscillations at the initial phase of depolarization. (B) (Left) Membrane potential of a magnocellular neuroendocrine cell, showing a similar depolarization during 15 minutes oxygen glucose deprivation and full recovery after this period. Both at the start of the depolarization and during recovery action potentials are generated. (Right) Model simulations. ED (OGD) is introduced for 15 minutes (black line). Here, $\alpha_e = 80\%, P_{\text{min}} = 0\%$ and $P_{\text{scale}} = 2$. With these parameter settings, the membrane potential recovers to baseline conditions after the period with ED. Note that during recovery, the experimentally observed oscillations are also faithfully simulated.

astrocyte, we move to the left, along the solid blue curve. For values lower than $P_{\text{min}} = 63.93\%$, the blue curve does not exist. Decreasing P_{min}, the physiological branch disappears via a limit point bifurcation (star). For $\alpha_e = 80\%$, the limit point occurs at $P_{\text{min}} = 57.4\%$. At this bifurcation point, unstable (dashed blue line) and stable (solid blue line) resting states merge. For lower values of P_{min}, to the left of the limit point, the pathological state is the only stable resting state. The loss of bistability here explains the transition to the pathological state during ED.

This is further illustrated with two simulations where energy is deprived for 5 (turquoise trace) and 15 minutes (magenta trace) for $P_{\text{min}} = 50\%$. These simulations are presented simultaneously in the bifurcation diagram (Fig 3.7A.1a and 3.7A.2a) and the time traces (Fig 3.7A.1b and 3.7A.2b). When energy is deprived for 5 minutes, the system transits to the pathological state for $\alpha_e = 20\%$ and does not recover to the physiological state. For $\alpha_e = 80\%$, the same simulation results in recovery. However, upon restoring energy later (15 minutes, orange trace), the synapse transits to the pathological resting state for both values of α_e. During energy restoration, the system's state slides along the

red curve. When we return to $P_{\text{min}} = 100\%$, the pathological state is still stable, implying that recovery is impossible without further intervention. As the pump is already fully activated, this resting state would become unstable only if its maximal strength P_{min} is increased above 145% of its initial value, at which a Hopf bifurcation occurs (inverted triangle), which is biophysically unrealistic. The pathological and physiological resting state curves are much farther apart for $\alpha_e = 80\%$ than for $\alpha_e = 20\%$. Moreover, for $\alpha_e = 80\%$, the limit point bifurcation (star) is further to the left (i.e. more severe ED). This shows that the transition to the pathological state occurs at larger values of P_{min} for synapses with a small ECS (small α_e).

Pump strength

Next, we explored the consequences of different pump strengths on the recovery of membrane potentials and ion dynamics after transient ED. We mimic this behaviour by changing the baseline maximum NKA current. We thus change the parameter $P_{\text{NKA}}^{\text{scale}}$. At baseline, $P_{\text{NKA}}^{\text{scale}} = 1$. When $P_{\text{NKA}}^{\text{scale}} > 1$, NKA becomes stronger by a factor $P_{\text{NKA}}^{\text{scale}}$. We keep the baseline conditions (ion concentrations, volumes and membrane potentials) fixed by changing the leak permeabilities of K^+ and Na^+ in neurons and astrocytes.

We first simulate ED for 15 minutes in large ECS ($\alpha_e = 80\%$) and realistic ECS ($\alpha_e = 20\%$), shown in Fig 3.6B.1 and 3.6B.2. Here, we set $P_{\text{NKA}}^{\text{scale}}$ to 1 and P_{min} to 0%. In both cases, neuronal and astrocyte membranes depolarize and do not recover after energy is restored. Note that it takes longer to reach the peak depolarization for neurons in large ECS, in agreement with observations in the bifurcation diagram (Fig 3.7A). In Fig 3.6B.3 and 3.6B.4, we show results of the simulations with $P_{\text{NKA}}^{\text{scale}} = 2$. This corresponds to NKA being twice as strong. In both cases, the membrane potentials transit to a stable depolarization block during the period of ED. In both cases, the synapse now returns to the physiological resting state after energy restoration. In the case of $\alpha_e = 80\%$, the neuronal membrane potential closely mimics experimental findings for magnocellular neuroendocrine cells [15] (see Fig 3.8B). We also observe that the neuron undergoes transient spiking immediately before recovery. This spiking results from a Hopf bifurcation, shown in the corresponding bifurcation diagram (Fig 3.7A). When $P_{\text{NKA}}^{\text{scale}} > 1$, the Hopf bifurcation shifts to the left (not shown). In this case, the corresponding Hopf bifurcation has shifted left of $P_{\text{min}} = 100\%$. The Hopf bifurcation is supercritical, which implies that a stable periodic orbit is born. This periodic orbit disappears before $P_{\text{min}} = 100\%$. Thus the neuron generates action potentials while it transits through the small parameter regime where the periodic orbit exists (Fig 3.6B.4). When $I_{\text{NKA}}^{\text{max}}$ reaches 100%, the periodic orbit disappears, and the membrane potential returns to baseline.

Pharmacological blockers

We simulate various scenarios observed experimentally where neurons and astrocytes in acute tissue slices of mouse brain were subjected to ED in the presence of an inhibitor of EAATs (TFB-TBOA) or NCX [191]. We first set $\alpha_e = 80\%$ and $P_{\min} = 50\%$, identical to Fig 3.5, and present four scenarios, illustrated in Fig 3.7B. First, we block EAAT transport (B.1) during the duration of ED, which blocks EAAT-mediated Na^+ influx into astrocytes. As a result, neurons and astrocytes depolarize before returning to baseline. Second, blocking NCX transport (B.2) has a stronger effect on membrane potentials, and both cells do not recover after restoring energy. During ED, NCX reverses, and thus mediates Na^+ efflux in low energy conditions, a phenomenon also suggested in experimental observations [191]. Blocking NCX transport promotes the cellular depolarization of the neuron and the astrocyte, driving them to the irreversible pathological state.

Third, motivated by experimental evidence [44] and modelling work [43], we explore the potential for recovery after blocking neuronal Na^+ influx pathways. We first simulate a short duration of ED ($P_{\min} = 50\%$) simultaneously blocking the voltage-gated Na^+ channel, upon which the neuron barely depolarizes (Fig 3.7B.3). Next, we consider the system after it has transited to a stable pathological state after longer ED, shown in (Fig 3.7B.4). Subsequently, we block the voltage-gated Na^+ channel of the neuron for 10 minutes. We observe that the neuron repolarizes and transits to the physiological resting state, with the restoration of all other ion concentrations and cell volume.

Motivated by this, we block neuronal K^+ efflux pathways to explore the potential for recovery. As before, we consider the system after it has transited to a stable pathological state, after longer ED. Blocking the voltage-gated K^+ channel for 10 minutes (Fig 3.7B.4), which is the major K^+ efflux pathway in the neuron, results in neuron and astrocyte repolarisation, and the entire system transits to the stable physiological resting state, as before ED.

In Fig 3.9, we demonstrate synaptic recovery after blocking the voltage-gated Na^+ channel and voltage-gated K^+ channel. We set $\alpha_e = 80\%$ and subject the neuron to ED for 15 minutes ($P_{\min} = 50\%$). Then, as the neuron has transited to the pathological state, between $t = 30$ and $t = 40$ minutes, we stimulate the cell with 25 pA current for 10 seconds, identical to Fig 3.4. Glutamate transients in the cleft during this period are shown in Fig 3.9A.1 (Na^+ channel) and Fig 3.9B.1. In both cases, the relative change in glutamate is about 10%, which is less than the change in glutamate transients in the physiological state (about 30%), shown in Fig 3.4A. Next, we block voltage-gated Na^+ and K^+ channels for 10 minutes (green region), bringing the system back to the physiological state. We then test synaptic recovery by applying the same stimulation to the neuron, 70 minutes after the block. The stimulation now induces a burst in the neuron and glutamate transients in the cleft, identical to Fig 3.4A, thereby demonstrating restoration of physiological synaptic function.

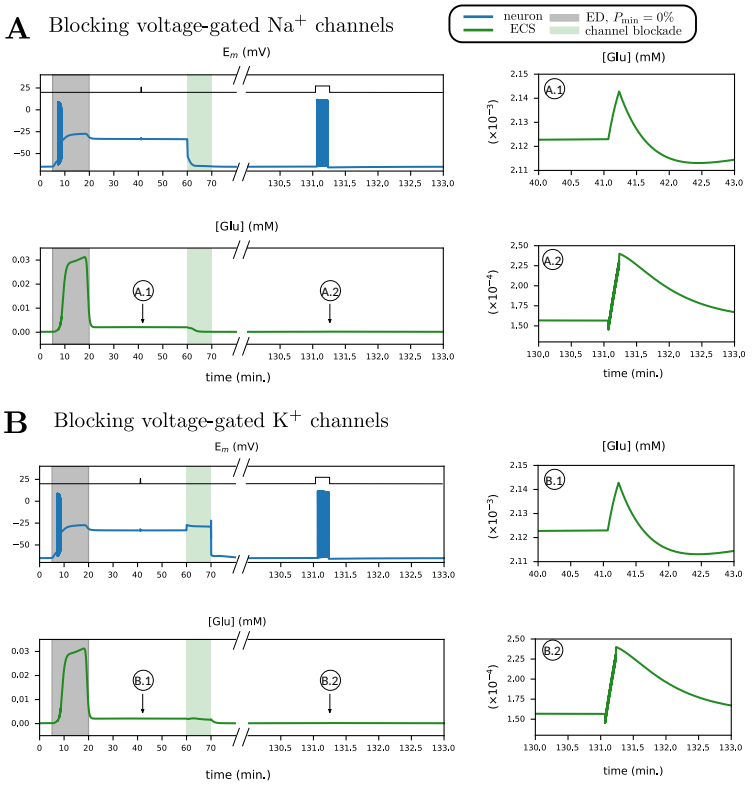

Figure 3.9: Neuronal stimulation upon recovery from ED shows different glutamate transients as compared to neuronal stimulation in a pathological state. Recovery from ED is achieved by blocking neuronal voltage-gated Na^+ channels (A) and blocking neuronal voltge-gated K^+ channels (B). Glutamate in the cleft (green trace) and neuronal membrane potential (blue trace) are shown, in response to neuronal excitation in physiological and pathological conditions. First, ED is simulated between $t = 5$ and $t = 20$ minutes ($P_{\min} = 50\%$, $\alpha_e = 80\%$). Then, neurons are subjected to 25 pA square wave input for 10 seconds, as indicated by the black trace. The system is then brought back to the physiological state by blocking voltage-gated Na^+ channels (shaded green area). After a little more than an hour, the neurons are subjected again, to 25 pA square wave input for 10 seconds.

Finally, we mention that, apart from neuronal Na^+ and K^+ voltage-gated channels, blocking any other ion channel did not assist in recovery from the pathological state, see Fig 3.14.

3.3.4 Glial chloride homeostasis under ischemia

In [12], fluorescence lifetime imaging microscopy (FLIM) was used, along with the chloride-sensitive dye MQAE to study glial Cl^- concentrations under both

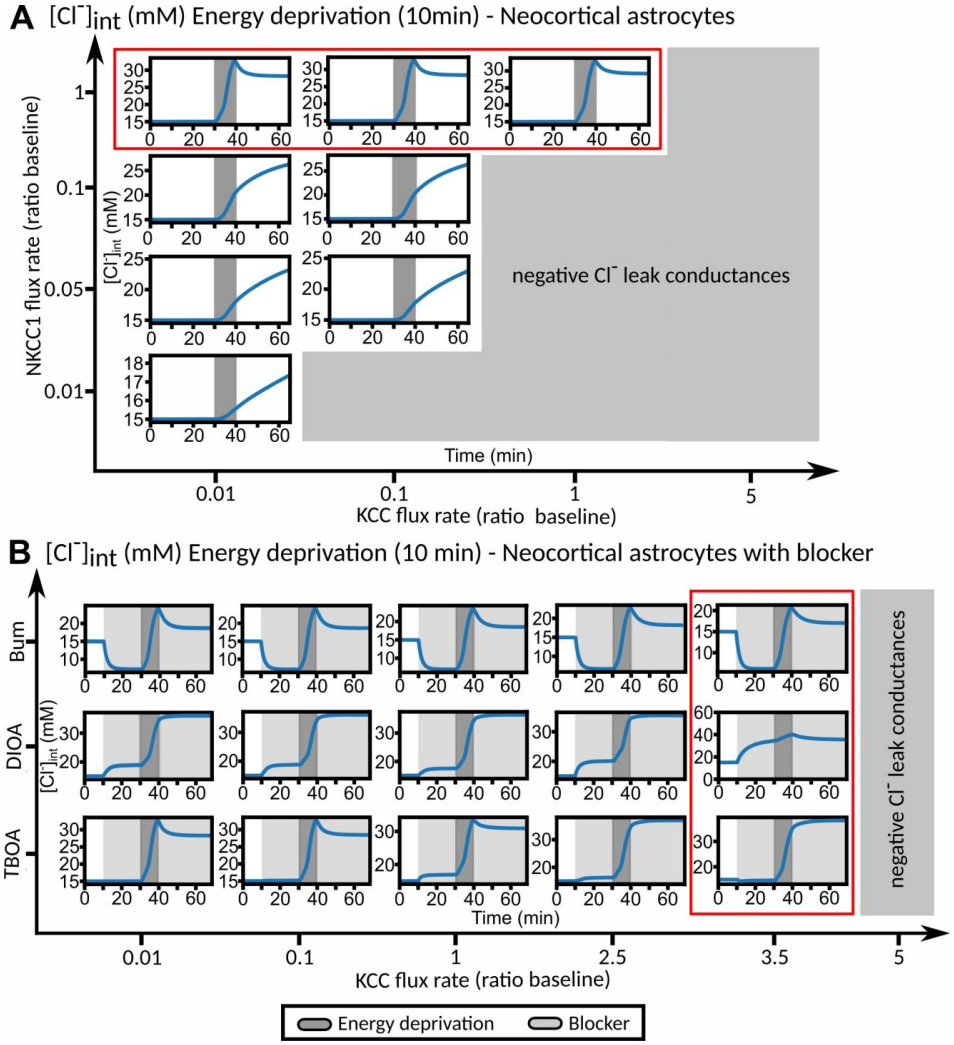

Figure 3.10: Iterative optimization of NKCC1 and KCC flux rates in neocortical astrocytes. (A) Predicted $[Cl^-]_a$ under resting conditions and changes during or after energy restriction for various normalized KCC and NKCC1 flux rates. NKCC1 flux rates P^a_{NKCC1} were varied between 1% and 100% of baseline values and the KCC flux rate P^a_{KCl} between 1% and 500% of baseline values. (B) Predicted changes in astrocytic $[Cl^-]_a$ under resting conditions, under blocking conditions (light gray block: bumetanide, R-(+)-DIOA or DL-TBOA) as well as during or after energy restriction for multiple KCC normalized flux rates (0.01-5) at fixed baseline P^a_{NKCC1}. At 20 min after the start of transport inhibition, transient ischemia (energy deprivation) was simulated by blocking neuronal and astrocyte NKA for 10 min (dark gray block), followed by energy restoration for 30 min in the presence of the mentioned blocker. For a KCC flux rate that is 3.5 times the baseline value, the predictions of the model are in best agreement with experimental results with blockers as well as with blockers under energy restriction. Red boxes show in (A) and (B) evaluated flux rates for neocortical astrocytes. Abbreviations: Bum: bumetanide; DIOA: R- (+)-DIOA; TBOA: DL-TBOA.

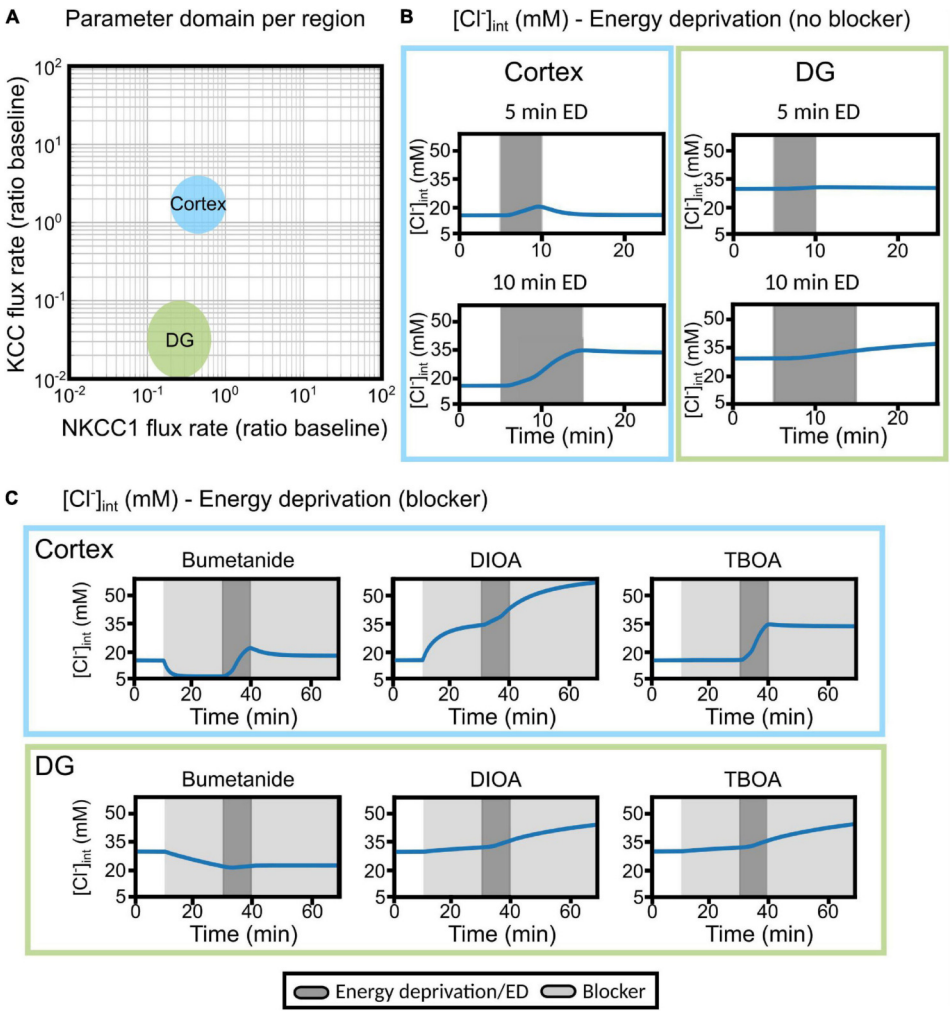

Figure 3.11: Differences in cortical and DG chloride homeostasis can be described by variation in glial KCC and NKCC1 expression levels in a mathematical model of the tripartite synapse. (A) Log–log plot of the KCC flux rate against the NKCC1 flux rate relative to baseline flux rates. Two distinct regions in this two-parameter space account for the results obtained with cortical (blue) or DG (green) $[Cl^-]_a$. The indicated regions correspond to parameter values with qualitative agreement with experimental traces. (B) Predicted changes in astrocytic $[Cl^-]_a$ without blocker under conditions used in experiments. Left panel, cortex; right panel; DG. (C) The model was subjected to block of a specific chloride transport system (light gray block: bumetanide, R-(+)-DIOA or DL-TBOA) for the first 30 min. At 20 min after the start of transport inhibition, transient ischemia (energy deprivation) was simulated by blocking neuronal and astrocyte NKA for 10 min (dark gray block), followed by energy restoration for 30 min in the presence of the mentioned blocker. Upper panel, cortex; lower panel, DG. Abbreviations: DG, dentate gyrus; ED, energy deprivation; DIOA, R-(+)-DIOA; TBOA, DL-TBOA.

control conditions and conditions that mimic ischemic energy restriction. The resting $[Cl^-]_a$ was determined in acute brain slices of four types of glial cells: hippocampal astrocytes in the dentate gyrus (DG) and cornu ammonis region 1 (CA1), hippocampal radial glialike (RGL) cells, and neocortical astrocytes. A marked regional heterogeneity was observed in glial ion concentration. Using specific blockers, the auhtors identified key chloride transport proteins that determine glial chloride homeostasis and assessed their contribution to $[Cl^-]_a$ and cell volume in the tested brain regions. Although chloride transport depends on processes that are affected during ischemia, only slight absolute changes in $[Cl^-]_a$ upon transient chemical ischemia.

In this section, we modify the current model to include the KCC transporter in the astrocyte in order to understand how changes in anion transporter activity shape the response to transient energy restriction. The model equations and conductance is set identical to the neuronal KCC transporter. Anion conductances generated by EAAT anion channels are represented as components of the astrocyte leak anion conductance. Since the Cl^-/HCO_3exchanger AE3, is not expressed in glial cells [220, 221], no HCO_3 transporter was integrated into the model.

In [12], it is shown that neocortical and DG astrocyte represent two extremes in both resting $[Cl^-]_a$ and changes in $[Cl^-]_a$ following the selective inhibition of anion transporters. As NKCC1 is the dominant Cl^- influx and KCC the dominant Cl^- efflux pathway in our model, we manipulated resting $[Cl^-]_a$ and changes of $[Cl^-]_a$ in response to energy restriction by varying the rates of these two transporters. With the exception of Cl^-, Na^+ and K^+leak conductances, all other parameters remained unchanged from the original model.

Fig. 3.10 illustrates the iterative approach we used in optimizing these two parameters for the example of neocortical astrocytes. We modify normalized NKCC1 flux rates (P^a_{NKCC1}) between 1 and 100% and normalized KCC flux rates between 1 and 500% of these baseline values. For each set of P^a_{KCl} and P^a_{NKCC1}, we calculate changes in neocortical $[Cl^-]_a$ under resting conditions, as well as during and after transient energy restriction. Variation of secondary active transporters requires adjustment of the leak conductances of the transported substrates to ensure that the sum of ion fluxes remains zero under resting conditions. For P^a_{NKCC1} between 0.01 and 0.1 of the starting values, tenfold or hundredfold decreased KCC rates require implausibly low Cl^- leak conductances that result in continuously increasing $[Cl^-]_a$ after energy restriction (Fig. 3.10-A) These predictions are in disagreement with experimental results in [12], and these parameter values are discarded. The initial test thus demonstrates that P^a_{NKCC1} must be around the starting values. The response of our model to energy restriction alone, however, does not suffice to restrain P^a_{KCl}. We thus test the effects of varying P^a_{KCl} at P^a_{NKCC1} fixed to the baseline value on the consequences of pharmacological block of glial anion transporters, see Fig. 3.10-B. 3.5-fold increased P^a_{KCl} flux rates predicts best the effect of the KCC blocker DIOA on astrocytic $[Cl^-]_a$ in neocortical astrocytes and was thus used

for further analyses.

Using this approach, we find two distinct parameter regions corresponding to $[Cl^-]_a$ measured in cortical and DG astrocytes, see Figs. 3.11-B,C. They are shown in a log–log plot of the NKCC1 and KCC flux rates in Fig. 3.11-A: cortical results are well described by higher numbers in functional KCCs (approximately 10 times) in astrocytes than in neurons; and results for DG astrocytes are well described by lower numbers in both functional NKCC1 (about 10 times lower than in the cortex) and KCCs (about 100 times lower than neuronal KCC). Within the tested parameter ranges, no bifurcations are observed in the two-parameter space. Astrocytic $[Cl^-]_a$ smoothly changes upon parameter variation, and simulation results are consistent with experiments in [12], also for large perturbations of the parameters. The effect of DL-TBOA is simulated by blocking both neuronal and astrocyte glutamate transport and partially blocking astrocytic Cl^- leak currents (Fig. 3.11-C). In the cortex, DL-TBOA causes a sharp increase in $[Cl^-]_a$, followed by a plateau (at +200% of baseline). In contrast, in the DG DL-TBOA causes a slow rise to +5% of baseline at the end of the ischemic block. The EAAT anion conductance is modeled as part of a glial resting anion conductance (leak conductance). Since the exact contribution of EAAT anion channels to the total resting anion conductance is unknown, we vary the degree of resting conductance blockade by DL-TBOA, but find no discernible differences.

Moderate transient ischemia is initially simulated by blocking the NKA in both neurons and astrocytes to 50% of baseline activity. In these simulations, astrocytes are subjected to energy deprivation for 5 or 10 min and then allowed to recover for 15 or 10 min, respectively (Fig. 3.11-B; gray shading). Additionally, astrocytes are treated with bumetanide (to block NKCC1), R-(+)-DIOA (to block astrocytic KCCs), or DL-TBOA (to block neuronal and astrocyte EAAT) for 20 min (light gray region), followed by energy deprivation for 10 min (dark gray block), and then another 30 min of transport block after energy restoration (Fig. 3.11-C). In response to transient ischemia for 5 min, $[Cl^-]_a$ in DG hippocampal astrocytes change only slightly, whereas cortical astrocytes undergo a transient increase in $[Cl^-]_a$ that is fully reversible by restoring NKA after 5 min of energy restriction (Figure 9B). In response to 10 min energy restrictions, simulated $[Cl^-]_a$ rises to a larger extent than observed in experiments, for cortical as well as for DG astrocytes. However, experimentally observed differences between the two classes of astrocytes are reproduced; cortical astrocytes reacts with larger chloride accumulation to ATP restriction than DG astrocytes (Fig. 3.9-B). In DG astrocytes, bumetanide triggers Cl^- efflux under control conditions, and additional chemical ischemia changes the effects only slightly (Fig. 3.11-C, lower panel). R-(+)-DIOA causes small increases in $[Cl^-]_a$ after chemical ischemia in DG astrocytes.

3.4 Discussion

We present a detailed biophysical model of energy-dependent ion fluxes in different compartments and of changes in cellular membrane potentials of the tripartite synapse to further our understanding of their dynamics in low energy conditions. We calibrate the model to Na^+ and K^+ concentration time-traces obtained from in-situ chemical ischemia experiments [191]. We demonstrate that astrocyte function is instrumental in maintaining physiological ion gradients for action potential generation and proper synaptic transmission. Crucially, the model indicates that surrounding extracellular volume size and baseline NKA pumping capability controls the ischemic vulnerability of the neuron-astrocyte interaction. Further, bifurcation analysis shows how the bistability depends on extracellular volume. Finally, we show that intervention through blocking voltage-gated Na^+ channels can revive the system from a pathological state.

3.4.1 Loss of synaptic function depends on the depth and duration of ischemia

In resting conditions, our model shows astrocyte and neuron membrane potentials close to the K^+ Nernst potential, similar to experimental observations. Loss of NKA-mediated Na^+ and K^+ transport results in intracellular Na^+ and extracellular K^+ accumulation and membrane depolarization, in accordance with experimental observations [15, 191] and previous simulations [43]. As expected [222], astrocytic dysfunction in our simulations also results in disruption of K^+ homeostasis and cessation of synaptic transmission, even in conditions with initially preserved neuronal function. However, upon neuronal stimulation, astrocytic Na^+ decreases. Earlier experimental work performed in brain tissue slices [217] has shown that most astrocytes undergo an increase in intracellular Na^+ during neuronal bursting activity. However, in about a third of cells, the increase was rather brief and was followed by an undershoot in $[Na^+]_i$. This undershoot could be mimicked by increasing extracellular K^+, indicating that it was due to activation of astrocyte NKA. Moreover, the combined addition of glutamate and high K^+ caused a biphasic increase-decrease in some cells, indicating that both processes - activation of NKA resulting in an export of Na^+ and activation of glutamate uptake resulting in an import of Na^+ - counteract each other. Notably in our model, NKA-induced export of Na^+ is higher than EAAT-mediated Na^+ uptake in astrocytes.

If the partial and transient ED is sufficiently long, no recovery occurs. During low energy conditions, glutamate in the cleft can rise to several hundred µM or even a few mM [223] and excitotoxic cell death will eventually follow [196]. The persistent increase in glutamate during the duration of ED is faithfully reproduced in our simulations (Fig 3.5B).

Our model simulations during low energy conditions also agree with the experimental findings from [15], shown in Fig 3.8: during oxygen-glucose

deprivation (OGD) neurons depolarize and cease firing action potentials after a short period of anoxic oscillations. We further show that the neuron can show bistable behaviour: even after cessation of OGD (simulated by restoring pump activity), the neuron can remain in a depolarized, pathological, state (Fig 3.8A).

3.4.2 Ischemic vulnerability depends on the extracellular volume fraction and baseline pump strength

Our simulations in Fig 3.6 show that a smaller ECS makes the neurons and astrocytes more likely to depolarize as the extracellular ion gradients will change faster; further, a smaller ECS makes it more likely that neurons and astrocytes remain in the pathological state, which is further illustrated by the bifurcation diagrams in Fig 3.7. We conclude that synapses surrounded by smaller ECS are more vulnerable to ED. For a larger ECS, the basins of attraction are farther apart in state space, making it less likely for the trajectory to escape from the physiological equilibrium to the pathological one. These simulations predict that synapses with smaller extracellular spaces are less likely to recover from ED. As the ECS size significantly declines with ageing [210, 207], this may aggravate ischemic damage to the aged brain [224].

We also simulated the recovery observed in magnocellular neurons by changing the baseline pump strength with the parameter $P_{\mathrm{NKA}}^{\mathrm{scale}}$ in Fig 3.8B. The neuron makes a few transient oscillations before returning to baseline, which was indeed observed in [15]. In this case, the Hopf bifurcation (inverted triangle) in Fig 3.7A shifts further to the left. Increasing baseline pump strength makes the physiological state the only stable resting state at baseline by moving the position of the Hopf bifurcation. The importance of baseline pump strength may also explain the experimental observation of Brisson and Andrew, showing that transient oxygen-glucose deprivation has differential effects on the potential for recovery of neurons in the hypothalamus and thalamus [15]. In similar experiments [225, 226], the difference in NKA activity due to varying α-isoform expression was highlighted as a possible governing factor for recovery.

We remark that our findings are at variance with an earlier modelling study, showing that smaller ECS size improves the recovery of neurons from transient ATP depletion [219]. In this model [219], that comprised Na^+, K^+ and Cl^- currents of a presynaptic neuron and the Na^+/K^+-ATPase, the role of glia was limited to K^+ buffering and passive extracellular K^+ diffusion. This modelling choice may underlie the divergent findings in our simulations, where an extended role for astrocytes together with ECS volume restrictions allows persistent K^+ accumulation in the ECS.

3.4.3 Neurons can be rescued from the pathological equilibrium state

In agreement with experimental observations [15], our simulations also show that a pathological state may persist after energy restoration. Phenomenologically, this persistence results from a persistent Na^+ current (the window current) at a membrane voltage near -30 mV [227, 43], that is too large to be counteracted by the Na^+/K^+ pump. The system can be rescued from this state, however, by a temporary blockage of voltage-gated Na^+ and K^+ currents, see Figs 3.7B and 3.9. We show that blocking Na^+ influx via voltage-gated Na^+ channels and K^+ efflux via voltage-gated K^+ channels serves to recover neuronal and astrocytic membrane potentials and Na^+/K^+ homeostasis. Moreover, in this recovered state, healthy synaptic function is resumed as demonstrated by exciting the neuron in Fig 3.9, where glutamate transients also return to the physiological range, identical to Fig 3.4A.
Our prediction regarding voltage-gated Na^+ channels agrees with previous modelling work, see [43]. While a study in rats after middle cerebral artery occlusion showed significantly improved neurological outcome after treatment with the Na^+ channel blocker valproic acid [228], to our knowledge, no experimental data have been reported that explicitly support this model prediction. Our prediction regarding voltage-gated K^+ channels is novel with respect to current modelling literature. An experimental study showed that using the K^+ channel blocker tetraethylammonium (TEA) was able to attenuate ischemia-triggered apoptosis in neurons [229]. However, to our knowledge, similar to the case with voltage-gated Na^+ channels, there is no experimental data that directly supports our prediction regarding K^+ channels.
Decrease in NKA activity in neurons and astrocytes creates an imbalance of Na^+ and K^+ gradients, causing net compartmental Na^+ influx and K^+ efflux. In that context, it is not too surprising that our model predicts that blocking major Na^+ and K^+ pathways in the neuron presents a potential pathway for recovery from the pathological state post ED. However this is not the case for astrocytes. Blocking any of the Na^+ or K^+ pathways post ED in the astrocyte (see supplementary figure 3.14) does not perturb the pathological state. This can be attributed to the fact that in our model, there is no astrocytic Na^+ influx or K^+ efflux process that contributes to large gradients, compared to the neuronal voltage-gated channels.

3.4.4 Differential Cl^- responses to ischemia

Our model predicts that the varying Cl^- responses to ischemia in different brain regions are attributed to the differential expression of the cotransporters KCC and NKCC1. In cortical astrocytes, the model predicts a bumetanide-mediated reduction of $[Cl^-]_a$ that is partially reversed by energy restriction. This prediction differs from experimental observations in [12], in which bumetanide

had only minor effects under control conditions, but decreased $[Cl^-]_a$ in combination with chemical ischemia. In simulations, R-(+)-DIOA causes massive Cl^- influx into the cortex (+300% of baseline), which is further enhanced by ischemic conditions and not reversed by energy restoration. This result is qualitatively, but not quantitatively similar to experiments in [12]. A possible explanation for the deviation between simulated and experimentally observed $[Cl^-]_a$ is provided in Fig. 3.15, in which changes in $[Cl^-]_a$ are compared for blocking NKA to 60% baseline pumping capacity with the results upon 50% reduction from Fig. 3.11. At higher remaining pump activity, the model predicts [Cl]int in DG astrocytes almost perfectly (Figure 10B). With less pronounced block of NKA, the model predicts fully reversible changes in $[Cl^-]_a$ for cortical astrocytes after 10 min of chemical ischemia. In cortical astrocytes (Fig. 3.15-A), the combination of chemical ischemia for 10 min with bumetanide reduces $[Cl^-]_a$ to 6 mM in model astrocytes, closely similar to experimental results in [12]. The effects of R-(+)-DIOA are comparable at 50 and 60% percentage remaining pump activity, and the TBOA effect is fully reversible at 60% rest activity. Pronounced differences in $[Cl^-]_a$ changes upon small variations in NKA activity (Fig. 3.15) are expected when simulating ion concentrations under ischemic conditions.

3.4.5 Relation to other computational models

This chapter extends the single-neuron formalism in [43] to a neuron-astrocyte interaction that describes biophysical processes in synaptic and somatic compartments. There have been several computational studies of neuronal dynamics in the context of energy failure [204, 203, 105, 173], while other studies have explicitly modelled astrocyte dynamics in the context of spreading depression, astrocyte Ca^{2+} signaling and physiological function [102, 94, 200]. To the best of our knowledge, however, no other computational study has explicitly modelled astrocyte dynamics nor did they include Na^+, K^+, Cl^-, Ca^{2+} and glutamate dynamics into a single model in the context of ED. In this chapter, we combine the dynamics of these five ions to provide a holistic description of ion and volume dysregulation during low energy conditions. Further, the model considers physical laws that arise in limiting cases, such as the Gibbs-Donnan equilibrium, which is reached when pump activity is absent. This provides a platform to extend the current formalism by introducing more ions, cellular compartments and transport mechanisms.

3.4.6 Modelling limitations

Our model has certain limitations, too. First, we assume spatially uniform compartments and ignores transmission delays, which is not the case in reality. We do not consider the diffusion of ions across the extracellular space, which extends to other synapses as well. Simulating in a finite volume may

cause exaggerated extracellular concentrations to appear, which speeds up the pathological effects of ED. However, this will not affect the bifurcation diagram structure, but only how tipping between the two basins of attraction occurs during short term ED. We also do not include astrocyte gap junctions which may change their permeability during low energy conditions and operate in the same timescale as membrane depolarization [230]. However, their role in mitigating extracellular K^+ uptake is debated.

3.4.7 Future directions

The current formulation of the model incorporates ion transients in synaptic and somatic compartments and predicts bistable behaviour in response to ischemia. Adding another neuron with a postsynaptic terminal will allow us to make predictions regarding synaptic transmission in ischemic conditions and to compare presynaptic versus postsynaptic vulnerability to such conditions. The first predictions from our model about glutamate transients can benefit from models such as [231] to include the glutamate-glutamine cycle, which is critical to the dynamics of neurotransmitter replenishment. Moreover, by introducing pH regulation, also the sodium-bicarbonate cotransporter (NBCe1) [232] and the sodium-proton exchanger (NHE) could be incorporated. These mechanisms will increase Na^+ transport into astrocytes, and might result in a net increase in astrocytic Na^+ with physiological stimulation, improving the current model.
We introduced a model of the tripartite synapse that describes ion and volume dynamics at synaptic and somatic levels. The model faithfully reproduces biological observations and identifies potential treatment targets to limit permanent synaptic failure in clinical conditions characterized by temporary energy failure. The model predicts that synapses surrounded by smaller extracellular spaces are more vulnerable to ischemia and that differential expression of baseline NKA may explain regional differences in ischemic vulnerability. Further, it predicts that blocking neuronal voltage-gated Na^+ and K^+ channels rescues the synapse from the pathological state post transient ED. Moreover, the model allows us to include additional processes and combine with more models from current literature to create a mathematical description of critical events concerning synaptic regulation in physiological and pathological conditions at the tripartite synapse.

3.5 Materials and methods

3.5.1 Ion concentrations and membrane potentials

The model describes the dynamics of molar amounts N_X^i of the ions Na^+, K^+, Cl^-, Ca^{2+} and glutamate, and compartmental volumes W_i, for $i = \{n, a\}$. The

corresponding membrane potentials follow from the relation,

$$V_i = \frac{\mathrm{F}}{\mathrm{C_i}} \sum_X z_X N_X^i, \tag{3.10}$$

where $i = \{n, a\}$ and z_X is the valence of the ion/species X. The ions X also include impermeable ions A^- and B^+ in each of the somatic compartments. This is necessary to maintain a non-zero resting membrane potential across the semi-permeable neuronal and astrocyte membranes. The molar quantities of these ions are unknown, we estimate them from baseline conditions in the section **Estimating parameters**. Assuming that $\mathrm{Na^+}$, $\mathrm{K^+}$ and $\mathrm{Cl^-}$ concentrations are the same in the somatic and synaptic compartments, we get

$$\begin{aligned} [X]_\mathrm{n} &= N_X / W_\mathrm{n} = [X]_\mathrm{ps}, \\ [X]_\mathrm{a} &= N_X / W_\mathrm{a} = [X]_\mathrm{pap}, \\ [X]_\mathrm{e} &= N_X / W_e = [X]_\mathrm{c}, \qquad\qquad X \in \{\mathrm{Na^+}, \mathrm{K^+}, \mathrm{Cl^-}\}. \end{aligned} \tag{3.11}$$

The volumes W_{ps}, W_c, W_{pap} are constant. We further assume that all glutamate and $\mathrm{Ca^{2+}}$ in the neurons and astrocytes are located in the synaptic compartments. Thus,

$$\begin{aligned} [Y]_\mathrm{n} &= N_Y / W_\mathrm{ps} = [Y]_\mathrm{ps}, \\ [Y]_\mathrm{a} &= N_Y / W_\mathrm{pap} = [Y]_\mathrm{pap}, \\ [Y]_\mathrm{e} &= N_Y / W_c = [Y]_\mathrm{c}, \qquad\qquad Y \in \{\mathrm{Ca^{2+}}, \mathrm{Glu}\ \}. \end{aligned} \tag{3.12}$$

In the following sections, we elaborate on how the dynamics of ion amounts N_X^i an volumes W_i are described in the model. The values of a few common parameters, such as fixed volumes and physical constants, are presented in Table 3.3.

3.5.2 Neuronal dynamics

The following currents/fluxes are used to describe neuronal somatic dynamics:

1. voltage-gated $\mathrm{Na^+}$, $\mathrm{K^+}$, $\mathrm{Cl^-}$ and $\mathrm{Ca^{2+}}$ channels,
2. $\mathrm{Na^+/K^+}$-ATPase (NKA),
3. $\mathrm{K^+}$-$\mathrm{Cl^-}$-cotransporter (KCC),
4. $\mathrm{Na^+/Ca^{2+}}$-exchanger (NCX), which is described in the section **Synaptic dynamics**;
5. and Excitatory Amino Acid Transporter (EAAT), which is described in the section **Synaptic dynamics**.

Parameters corresponding to all processes in the neuronal compartment can be found in Table 3.4.

Table 3.3: Common model parameters along with sources. Units are presented in the same manner as they are implemented in the Python code. All adjusted parameters are in the same order of magnitude as their original counterparts.

Constant	Value	Description
C_n, C_a	20 pF	Membrane capacitance [43]
F	96485.333 [C mol^{-1}]	Faraday's constant
R	8314.4598 [C(mV)(mol K)$^{-1}$]	Universal gas constant
T	310K	Room temperature [43]
W_{ps}	10^{-3} [1000µm^3]	Fixed presynaptic terminal volume [233]
W_c	10^{-3} [1000µm^3]	Fixed synaptic cleft volume (Empirical, chosen to be same as W_{ps})
W_{pap}	10^{-3} [1000µm^3]	Fixed perisynaptic astrocyte process volume (Empirical, chosen to be same as W_{ps})

3.5.3 Conservation laws

The model has constant total volume W_{tot}, i.e.

$$\sum_i W_i = W_{tot}. \tag{Cons.1}$$

As a consequence we get a conservation law for ionic molar amounts giving

$$\sum_i N_X^i = C_X, \tag{Cons.2}$$

where the sum is over all compartments, for each ion X. As the net charge in the system must be zero, we have, at all times

$$\sum_X z_X C_X + \sum_{Y,i} z_Y N_Y^i = 0, \tag{Cons.3}$$

where Y contains the impermeable cations and anions. The equations (Cons.1-Cons.3) give us the three conserved quantities. As a consequence, we can now describe extracellular dynamics from

$$\begin{aligned} W_e &= W_{tot} - W_n - W_a, \\ [X]_e &= \frac{1}{W_e}\left(C_X - \sum_{i\neq e} N_X^i\right). \end{aligned} \tag{3.13}$$

Voltage-gated currents and leak channels

The Goldman-Hodgkin-Katz (GHK) currents are solutions to the Nernst-Planck equations that describe the electrodiffusive flux of ions across a permeable

membrane when we assume membrane homogeneity and instantaneous and independent movement of ions. We use the GHK currents to model voltage-gated and leak currents [234]. The gating variables are from [211] and are similar to those in the Hodgkin-Huxley model. The currents are as follows,

$$\begin{aligned} I_G^{\mathrm{Na}^+,n} &= P_G^{\mathrm{Na}^+,n} m^3 h \mathrm{GHK}(V_n, [\mathrm{Na}^+]_n, [\mathrm{Na}^+]_e), \\ I_G^{\mathrm{K}^+,n} &= P_G^{\mathrm{K}^+,n} n^4 \mathrm{GHK}(V_n, [\mathrm{K}^+]_n, [\mathrm{K}^+]_e), \\ I_G^{\mathrm{Ca}^{2+},n} &= 4 P_G^{\mathrm{Ca}^{2+},n} m^2 h \mathrm{GHK}(V_n, [\mathrm{Ca}^{2+}]_n, [\mathrm{Ca}^{2+}]_e), \end{aligned} \tag{3.14}$$

where m, h and n are Hodgkin-Huxley gating variables. The expression for the calcium channel is obtained from [21]. The function $\mathrm{GHK}(V_y, [X]_y, [X]_e)$ is given by,

$$\mathrm{GHK}(V_y, [X]_y, [X]_e) = \frac{\mathrm{F}^2 V_y}{z_X^2 \mathrm{RT}} \frac{[X]_y - [X]_e \exp\left(-\frac{\mathrm{F}V_y}{z_X \mathrm{RT}}\right)}{1 - \exp\left(-\frac{\mathrm{F}V_y}{z_X \mathrm{RT}}\right)}. \tag{3.15}$$

The dynamical equations for q are given by Eq. (3.1) where $q = \{m, h, n\}$. The voltage-dependent expressions α_q and β_q are given by,

$$\begin{aligned} \alpha_m &= \frac{0.32(V+52)}{1-\exp(-(V+52)/4)}, \beta_m = \frac{0.28(V+25)}{\exp((V+25)/5)-1}, \\ \alpha_h &= 0.128\exp(-(V+53)/18), \beta_h = \frac{4}{1+\exp(-(V+30)/5)}, \\ \alpha_n &= \frac{0.016(V+35)}{1-\exp(-(V+35)/5)}, \beta_n = 0.25\exp\left(-\frac{V+50}{40}\right). \end{aligned} \tag{3.16}$$

Note that this is different from the subscript n, which refers to the neuronal somatic compartment. They have the same expressions as in [211]. For the Cl^- gated current, we adopt the choice from [43],

$$I_G^{\mathrm{Cl}^-,n} = \frac{P_G^{\mathrm{Cl}^-,n}}{1+\exp\left(-\frac{V_n+10}{10}\right)} \mathrm{GHK}(V_n, [\mathrm{Cl}^-]_n, [\mathrm{Cl}^-]_e). \tag{3.17}$$

All the leak currents are modelled as GHK currents

$$I_L^{X,n} = P_L^{X,n} \mathrm{GHK}(V_n, [X]_n, [X]_e). \tag{3.18}$$

Active transport across neuronal membrane: $\mathrm{Na}^+/\mathrm{K}^+$**-ATPase (NKA)**

The NKA exchanges three Na^+ for two K^+ by consuming one molecule of adenosine triphosphate (ATP). It is modelled as a function of intracellular Na^+

and extracellular K^+ as in [235] by the following flux,

$$I^n_{NKA}(t) = \left(\frac{I^{\max}_{\mathrm{NKA}}(t)}{100}\right) P^{\mathrm{scale}}_{\mathrm{NKA}} f_{\mathrm{NKA}} = \left(\frac{I^{\max}_{\mathrm{NKA}}(t)}{100}\right) P^{\mathrm{scale}}_{\mathrm{NKA}} g_{\mathrm{NKA}} \times \frac{[\mathrm{Na}^+]^{1.5}_n}{[\mathrm{Na}^+]^{1.5}_n + (\alpha^n_{NKA})^{1.5}} \frac{[\mathrm{K}^+]_e}{[\mathrm{K}^+]_e + (\beta^n_{NKA})}, \tag{3.19}$$

where

$$g_{\mathrm{NKA}} = \left(1 + 0.1245 \cdot \exp\left(-0.1\frac{FV_n}{RT}\right) + 0.0365 \cdot \sigma \cdot \exp\left(-\frac{FV}{RT}\right)\right), \tag{3.20}$$

and

$$\sigma = \frac{1}{7} \cdot \left(\exp\left(\frac{[\mathrm{Na}^+]_e}{67.3}\right) - 1\right), \tag{3.21}$$

where P^n_{NKA} is the NKA permeability or the pump strength. $P^{\mathrm{scale}}_{\mathrm{NKA}}$ is the scaling factor which we vary in simulations to scale the strength of NKA and the function $I^{\max}_{NKA}(t)$ is used to simulate energy derivation for some time period. They are also explained in the section **Simulations and model calibration**. The corresponding Na^+ and K^+ currents are given by

$$\begin{aligned} I^{\mathrm{Na}^+,n}_{\mathrm{NKA}} &= 3I^n_{\mathrm{NKA}}(t), \\ I^{\mathrm{K}^+,n}_{\mathrm{NKA}} &= -2I^n_{\mathrm{NKA}}(t). \end{aligned} \tag{3.22}$$

Secondary active transport across neuronal membrane: K^+-Cl^--cotransporter

The K^+-Cl^--cotransporter (KCC) is a symporter that allows one Cl^- ion and K^+ to leave the neuron, along its concentration gradient. It is the main extruder for Cl^- ions in the neuron, thereby providing a counterforce to the gated Cl^- channel, which mediates a massive influx of Cl^- after Na^+ loading in neurons [236, 42, 237, 238, 239]. We model the flux as the difference of the K^+ and Cl^- Nernst potentials as in [102],

$$J_{\mathrm{KCl}} = \frac{\mathrm{RT}}{\mathrm{F}} \ln\left(\frac{[\mathrm{K}^+]_e[\mathrm{Cl}^-]_e}{[\mathrm{K}^+]_n[\mathrm{Cl}^-]_n}\right). \tag{3.23}$$

The corresponding K^+ and Cl^- currents are given by

$$\begin{aligned} I^{\mathrm{K}^+,n}_{\mathrm{KCl}} &= \mathrm{F}J^n_{\mathrm{KCl}}, \\ I^{\mathrm{Cl}^-,n}_{\mathrm{KCl}} &= \mathrm{F}J^n_{\mathrm{KCl}}. \end{aligned} \tag{3.24}$$

3.5.4 Astrocyte soma

Astrocytes possess a wealth of membrane ion channels and transporters, which allow them to detect, respond and modulate neuronal activity. Major

tasks fulfilled by astrocytes at glutamatergic synapses are the regulation of extracellular K^+ homeostasis and the re-uptake of synaptically-released glutamate [240]. In this section, we describe the incorporated relevant ion channels/cotransporters that govern astrocyte dynamics during physiological conditions and in response to metabolic stress. We use the following currents/fluxes to describe astrocyte somatic dynamics:

1. Kir4.1 channel,
2. Na^+/K^+-ATPase (NKA),
3. Na^+-K^+-$2Cl^-$-cotransporter (NKCC1),
4. Na^+/Ca^{2+}-exchanger (NCX), which is described in the section **Synaptic dynamics**;
5. and Excitatory Amino Acid Transporter (EAAT), which is described in the section **Synaptic dynamics**.

Table 3.5 lists all parameters corresponding to astrocyte fluxes/currents.

Kir4.1 channel

The weakly inwardly rectifying K^+ channel Kir4.1 is highly expressed in astrocytes and maintains the resting membrane potential [48, 241], close to the K^+ reversal potential. We choose the model from [242], as it allows the current to vanish at the Gibbs-Donnan condition. This property is not present in recently published models on Kir4.1, such as [104]. The current is given by,

$$I_{Kir}^{K^+,a} = P_{Kir} m_\infty \frac{[K^+]_e}{[K^+]_e + 13}(V_a - E_{K^+}^a), \tag{3.25}$$

with

$$m_\infty = \left(2 + \exp\left(1.62\frac{F}{RT}(V_a - E_{K^+}^a)\right)\right)^{-1}, \tag{3.26}$$

where $E_{K^+}^a$ is the K^+ reversal potential in the astrocyte,

$$E_{K^+}^a = \frac{RT}{F}\log\frac{[K^+]_e}{[K^+]_a}. \tag{3.27}$$

Active transport: Na^+/K^+-ATPase

The NKA in the astrocyte follows the exact same model as that in the neuron, as in [102]. The NKA current in the astrocyte is given by,

$$I_{NKA}^a = \left(\frac{I_{NKA}^{max}(t)}{100}\right) P_{NKA}^{scale} f_{NKA} = \left(\frac{I_{NKA}^{max}(t)}{100}\right) P_{NKA}^{scale} g_{NKA} \times \frac{[Na^+]_a^{1.5}}{[Na^+]_a^{1.5} + (\alpha_{NKA}^a)^{1.5}} \frac{[K^+]_e}{[K^+]_e + (\beta_{NKA}^a)}, \tag{3.28}$$

where

$$g_{\mathrm{NKA}} = \left(1 + 0.1245 \cdot \exp\left(-0.1\frac{\mathrm{F}V_a}{\mathrm{RT}}\right) + 0.0365 \cdot \sigma \cdot \exp\left(-\frac{\mathrm{F}V_a}{\mathrm{RT}}\right)\right), \quad (3.29)$$

and

$$\sigma = \frac{1}{7} \cdot \left(\exp\left(\frac{[\mathrm{Na}^+]_e}{67.3}\right) - 1\right), \quad (3.30)$$

where P^a_{NKA} is the astrocyte NKA pump strength. Thus the corresponding Na^+ and K^+ currents are given by

$$\begin{aligned} I^{\mathrm{Na}^+,a}_{\mathrm{NKA}} &= 3I^a_{\mathrm{NKA}}(t), \\ I^{\mathrm{K}^+,a}_{\mathrm{NKA}} &= -2I^a_{\mathrm{NKA}}(t). \end{aligned} \quad (3.31)$$

Na^+-K^+-2Cl^--cotransporter (NKCC1)

The astrocyte K^+ removal mechanism is complemented by the inward Na^+-K^+-2Cl^--cotransporter (NKCC1), which is highly expressed in astrocytes [240]. NKCC1 is a symporter and transports one Na^+ , one K^+ and two Cl^- into the astrocyte. It is activated by high extracellular K^+ and plays a major role in astrocyte swelling [243, 244]. Astrocyte Cl^- regulation also crucially depends on NKCC1 [245, 246]. The flux is proportional to the difference of Nernst potentials of the respective ions as is done in [102] and is given by

$$J^a_{NKCC1} = P^a_{NKCC1}\frac{\mathrm{RT}}{\mathrm{F}}\log\left(\frac{[\mathrm{Na}^+]_e}{[\mathrm{Na}^+]_a}\frac{[\mathrm{K}^+]_e}{[\mathrm{K}^+]_a}\left(\frac{[\mathrm{Cl}^-]_e}{[\mathrm{Cl}^-]_a}\right)^2\right). \quad (3.32)$$

Thus the corresponding Na^+, K^+ and Cl^- currents are given by

$$\begin{aligned} I^{\mathrm{Na}^+,a}_{\mathrm{NKCC1}} &= -\mathrm{F}J^a_{\mathrm{NKCC1}}, \\ I^{\mathrm{K}^+,a}_{\mathrm{NKCC1}} &= -\mathrm{F}J^a_{\mathrm{NKCC1}}, \\ I^{\mathrm{Cl}^-,a}_{\mathrm{NKCC1}} &= 2\mathrm{F}J^a_{\mathrm{NKCC1}}. \end{aligned} \quad (3.33)$$

Leak currents

So far, we only have an inward NKCC1 flux to model movement of Cl^- in the astrocyte. We approximate the remaining fluxes as passive electrodiffusive currents via the Goldman-Hodgkin-Katz formula for ion currents,

$$I^{L,a}_X = P^{L,a}_X\,\mathrm{GHK}(V_a, [X]_a, [X]_e), \quad (3.34)$$

where the formula for $GHK(\cdot,\cdot,\cdot)$ is given by Eq. (3.15), and $X = \{\mathrm{Na}^+, \mathrm{K}^+, \mathrm{Cl}^-\}$.

3.5.5 Synaptic dynamics

This section describes the dynamics of Ca^{2+} and glutamate in the synaptic cleft and their coupling to the dynamics of Na^+, K^+ and Cl^- via the transporters NCX and EAAT. We assume that the volumes of these synaptic compartments remain small and fixed during the first few hours of metabolic stress. Note that, as previously introduced in Eq. (3.11) and (3.12), we assume that all of their ions are confined to the 'synaptic compartments' only, i.e., the presynaptic terminal, synaptic cleft and astrocyte process. We now describe the relevant channels/cotransporters acting in the synaptic compartments and the mechanism of glutamate recycling in the cleft.

Glutamate transport (EAAT)

The re-uptake of synaptically released glutamate is mediated by high-affinity, Na^+-dependent glutamate transporters (EAATs). EAATs are expressed by both presynaptic terminals and astrocytes, with astrocytes mediating about 90% of glutamate uptake in the CNS [50]. The cotransporter protein carries one glutamate molecule, three Na^+ and one H^+ into the cells in exchange for one K^+. The transport yields a net double positive charge influx. We model EAAT in the same way the KCC and NKCC1 cotransporters are modelled. Thus, the EAAT current is written as,

$$J^i_{EAAT} = P^i_{EAAT} \frac{RT}{F} \ln\left(\frac{[Na^+]^3_e}{[Na^+]^3_i}\frac{[K^+]_i}{[K^+]_e}\frac{[H^+]_c}{[H^+]_i}\frac{[Glu\,]_c}{[Glu\,]_i}\right). \tag{3.35}$$

The corresponding ion currents are

$$\begin{aligned} I^{Na^+,i}_{EAAT} &= -3FJ^i_{EAAT}, \\ I^{K^+,i}_{EAAT} &= FJ^i_{EAAT}, \\ I^{Glu\,,i}_{EAAT} &= FJ^i_{EAAT}. \end{aligned} \tag{3.36}$$

In our model, we do not model the dynamics of protons, but we keep the ratio $\frac{[H^+]_c}{[H^+]_a}$ constant [247]. The constant is chosen from modelling work done in [213], where EAAT forms a part of the biophysical description of ion homeostasis at the postsynaptic cradle.

Na^+/Ca^{2+}-exchanger (NCX)

The Na^+/Ca^{2+}-exchanger NCX allows Na^+ to flow along its concentration gradient into the neuron/astrocyte in exchange for Ca^{2+}. It is expressed across various cell types, including neurons and astrocytes. Thus, three Na^+ are imported in exchange for one Ca^{2+}, yielding a net positive charge to the

compartment. The notable aspect about NCX is that it reverses when $[Na^+]$ increases in the respective compartment [191].
We follow the model from [235], which describes the NCX current by

$$I^i_{NCX} = P^i_{NCX}\left(\frac{[Na^+]^3_e}{\alpha^3_{Na^+} + [Na^+]^3_e}\right)\left(\frac{[Ca^{2+}]_c}{\alpha_{Ca^{2+}} + [Ca^{2+}]_c}\right)\times \frac{\frac{[Na^+]^3_i}{[Na^+]^3_e}\exp\left(\frac{\eta F V_i}{RT}\right) - \frac{[Ca^{2+}]_i}{[Ca^{2+}]_c}\exp\left(\frac{(\eta-1)FV_i}{RT}\right)}{1 + k_{NCX}\exp\left(\frac{(\eta-1)FV_i}{RT}\right)}. \tag{3.37}$$

The corresponding Na^+ and Ca^{2+} currents are given by

$$\begin{aligned} I^{Na^+,i}_{NCX} &= 3I^i_{NCX}, \\ I^{Ca^{2+},i}_{NCX} &= -I^i_{NCX}. \end{aligned} \tag{3.38}$$

Vesicular recycling

In response to action potentials that reach the presynaptic terminal and consequent Ca^{2+} elevations, glutamate is released into the synaptic cleft. This process involves packing of the neurotransmitter into synaptic vesicles, which fuse with the presynaptic membrane following formation of the SNARE complex [248]. The packing of glutamate into vesicles by vesicular glutamate transporters (VGLUTs) depends on $[Cl^-]$ and on a proton gradient across the vesicular membrane, which is mediated by an ATP-dependent proton pump. It was suggested that VGLUT expression declines with age, although these ideas still remain inconclusive [249]. In this chapter, we assume that vesicular packing and recycling is not directly energy-dependent. This allows us to see what happens during partial ED when Na^+/K^+-ATPase is affected, but glutamate continues to be efficiently packed into vesicles.
To model vesicular recycling, we combine models from [215] and [216], see Fig 3.2. The model proposed by Walter et al. [216] describes the sequential slow-fast mechanism of packing glutamate into vesicles, depending on Ca^{2+} elevations. The sequence models the pathway of glutamate from a large storage pool (called depot) to the irreversible fused state, which is when glutamate is released into the synaptic cleft by the interaction of vesicles with SNARE proteins lined up on the presynaptic membrane. The cycle is then completed by plugging in the model by Tsodyks and Markram [215] which models glutamate recycling back into the depot. The equations for the inactive (I) and fused (F) state are then adjusted to include the uptake of glutamate via EAAT and electrodiffusive leak currents. This is done by removing the linear term for recruitment of glutamate from the fused state back into the inactive state, and replacing it with terms for EAAT and leak dynamics. The dynamical equations

for the various states of glutamate are given by,

$$\begin{cases} \frac{d}{dt}N_{\mathrm{I}} = \frac{d}{dt}N^{n}_{\mathrm{Glu}} = -\frac{1}{\tau_{\mathrm{rec}}}N_{\mathrm{I}}N_{\mathrm{D}} + \frac{1}{\mathrm{F}}\left(I^{\mathrm{Glu},n}_{\mathrm{EAAT}} + I^{\mathrm{Glu},n}_{L}\right), \\ \frac{d}{dt}N_{\mathrm{D}} = \frac{1}{\tau_{\mathrm{rec}}}N_{\mathrm{I}}N_{\mathrm{D}} - k_1 N_{\mathrm{D}} + k_{-1}N_{\mathrm{N}}, \\ \frac{d}{dt}N_{\mathrm{N}} = k_1 N_{\mathrm{D}} - (k_{-1}+k_2)N_{\mathrm{N}} + k_{-2}N_{\mathrm{R}}, \\ \frac{d}{dt}N_{\mathrm{R}} = k_2 N_{\mathrm{N}} - (k_{-2}+3k_3[\mathrm{Ca}^{2+}]_n)N_{\mathrm{R}} + k_{-3}N_{\mathrm{R}_1}, \\ \frac{d}{dt}N_{\mathrm{R}_1} = 3k_3[\mathrm{Ca}^{2+}]_n N_{\mathrm{R}} - (k_{-3}+2k_3[\mathrm{Ca}^{2+}]_n)N_{\mathrm{R}_1} + 2k_{-3}N_{\mathrm{R}_2}, \\ \frac{d}{dt}N_{\mathrm{R}_2} = 2k_3[\mathrm{Ca}^{2+}]_n N_{\mathrm{R}_1} - (2k_{-3}+k_3[\mathrm{Ca}^{2+}]_n)N_{\mathrm{R}_2} + 3k_{-3}N_{\mathrm{R}_3}, \\ \frac{d}{dt}N_{\mathrm{R}_3} = k_3[\mathrm{Ca}^{2+}]_n N_{\mathrm{R}_2} - (3k_{-3}+k_4)N_{\mathrm{R}_3}. \end{cases} \tag{Mod.1}$$

The coefficient k_1 is taken from [216]

$$k_1 = k_{1,\max}\frac{[\mathrm{Ca}^{2+}]_n}{[\mathrm{Ca}^{2+}]_n + K_{\mathrm{M}}} \tag{3.39}$$

where K_M is the half saturation Ca^{2+} concentration in the presynaptic terminal to recruit vesicles from the depot into the non-releasable pool. The coefficients k_2 and k_{-2} are taken from [216]

$$\begin{aligned} k_2(\mathrm{Ca}^{2+}) &= k_{20} + g(\mathrm{Ca}^{2+})k_{2\mathrm{cat}}, \\ k_{-2}(\mathrm{Ca}^{2+}) &= k_{-20} + g(\mathrm{Ca}^{2+})k_{-2\mathrm{cat}}, \end{aligned} \tag{3.40}$$

where the probability for a Ca^{2+}-bound catalyst $g(Ca^{2+})$ is given by [216]

$$g(\mathrm{Ca}^{2+}) = \frac{[\mathrm{Ca}^{2+}]}{[\mathrm{Ca}^{2+}] + K_{\mathrm{Dv}}}. \tag{3.41}$$

From the molar amounts of the various states of glutamate, we can define glutamate concentrations in the neuron and cleft. Thus,

$$[\mathrm{Glu}\,]_n = [\mathrm{Glu}\,]_{ps} = \frac{1}{W_{PreSyn}}N^{n}_{\mathrm{Glu}} = \frac{1}{W_{PreSyn}}(N_{\mathrm{I}}) \tag{3.42}$$

and

$$[\mathrm{Glu}\,]_c = \frac{1}{W_c}N^{c}_{\mathrm{Glu}} = \frac{1}{W_c}N_{\mathrm{F}}. \tag{3.43}$$

All parameters corresponding to vesicular recycling can be found in Table 3.6. The expression for N_F is derived from conservation laws, see section **Conservation laws**.

3.5.6 Volume dynamics

The exact channels for water movement between the extracellular space, neuron and astrocytes is are still debated today [250, 251]. In this chapter, we assume it to depend linearly on the osmotic pressure gradient across the membrane. We follow the model from [43] to model the volume compartmental volume W_i as

$$\frac{d}{dt}W_i = L^i_{H_2O}\Delta\pi_i, \tag{Mod.2}$$

where $\Delta\pi_i$ is the osmotic pressure gradient given by,

$$\Delta\pi_i = \mathrm{RT}\sum_X([X]_i - [X]_e), \tag{3.44}$$

for $X, Y \in \{\mathrm{Na}^+, \mathrm{K}^+, \mathrm{Cl}^-\}$ and $i \in \{n, a\}$. From Eq. (3.1), we then obtain the relation

$$\lambda_i = L^i_{H_2O}\mathrm{RT}. \tag{3.45}$$

3.5.7 Model equations

The dynamics of individual ion amounts based on the described ion currents is given by

$$\begin{cases}
\frac{d}{dt}N^n_{\mathrm{Na}^+} = -\frac{1}{\mathrm{F}}\left(I^{\mathrm{Na}^+,n}_{\mathrm{G}} + I^{\mathrm{Na}^+,n}_{\mathrm{NKA}} + I^{\mathrm{Na}^+,n}_{\mathrm{EAAT}} + I^{\mathrm{Na}^+,n}_{\mathrm{NCX}} + I^{\mathrm{Na}^+,n}_{\mathrm{L}}\right) + \frac{1}{F}I_{\mathrm{stim}}(t), \\
\frac{d}{dt}N^n_{\mathrm{K}^+} = -\frac{1}{\mathrm{F}}\left(I^{\mathrm{K}^+,n}_{\mathrm{G}} + I^{\mathrm{K}^+,n}_{\mathrm{NKA}} + I^{\mathrm{K}^+,n}_{\mathrm{EAAT}} + I^{\mathrm{K}^+,n}_{\mathrm{KCl}} + I^{\mathrm{K}^+,n}_{\mathrm{L}}\right), \\
\frac{d}{dt}N^n_{\mathrm{Cl}^-} = \frac{1}{\mathrm{F}}\left(I^{\mathrm{Cl}^-,n}_{\mathrm{G}} + I^{\mathrm{Cl}^-,n}_{\mathrm{KCl}} + I^{\mathrm{Cl}^-,n}_{\mathrm{L}}\right), \\
\frac{d}{dt}N^n_{\mathrm{Ca}^{2+}} = -\frac{1}{2\mathrm{F}}\left(I^{\mathrm{Ca}^{2+},n}_{\mathrm{G}} + I^{\mathrm{Ca}^{2+},n}_{\mathrm{NCX}} + I^{\mathrm{Ca}^{2+},n}_{\mathrm{L}}\right), \\
\frac{d}{dt}N^n_{\mathrm{Glu}} = \frac{1}{\mathrm{F}}\left(I^{\mathrm{Glu},n}_{\mathrm{EAAT}} + I^{\mathrm{Glu},n}_{L}\right), \\
\frac{d}{dt}N^a_{\mathrm{Na}^+} = -\frac{1}{\mathrm{F}}\left(I^{\mathrm{Na}^+,a}_{\mathrm{NKCC1}} + I^{\mathrm{Na}^+,a}_{\mathrm{NKA}} + I^{\mathrm{Na}^+,a}_{\mathrm{EAAT}} + I^{\mathrm{Na}^+,a}_{\mathrm{NCX}} + I^{\mathrm{Na}^+,a}_{\mathrm{L}}\right), \\
\frac{d}{dt}N^a_{\mathrm{K}^+} = -\frac{1}{\mathrm{F}}\left(I^{\mathrm{K}^+,a}_{\mathrm{NKCC1}} + I^{\mathrm{K}^+,a}_{\mathrm{NKA}} + I^{\mathrm{K}^+,a}_{\mathrm{EAAT}} + I^{\mathrm{K}^+,a}_{\mathrm{Kir}} + I^{\mathrm{K}^+,a}_{\mathrm{L}}\right), \\
\frac{d}{dt}N^a_{\mathrm{Cl}^-} = \frac{1}{\mathrm{F}}\left(I^{\mathrm{Cl}^-,a}_{\mathrm{NKCC1}} + I^{\mathrm{Cl}^-,a}_{\mathrm{L}}\right), \\
\frac{d}{dt}N^a_{\mathrm{Ca}^{2+}} = -\frac{1}{2\mathrm{F}}\left(I^{\mathrm{Ca}^{2+},a}_{\mathrm{NCX}} + I^{\mathrm{Ca}^{2+},a}_{\mathrm{L}}\right), \\
\frac{d}{dt}N^a_{\mathrm{Glu}} = \frac{1}{\mathrm{F}}\left(I^{\mathrm{Glu},a}_{\mathrm{EAAT}} + I^{\mathrm{Glu},a}_{L}\right),
\end{cases} \tag{Mod.3}$$

where $I_{\mathrm{stim}}(t)$ is a square-wave current used to stimulate the neuron when we perform neuronal stimulation experiments, such as in Fig 3.4. The equations

(Mod.1-Mod.3) together give the model. The initial values used, are shown in Tables 3.7 and 3.8. However, we have not described extracellular dynamics yet. These are obtained directly from conservation laws, which we describe in the following section.

3.5.8 Estimating parameters from conservation laws

In order to maintain physiological resting states, we incorporate impermeable ions in the system. Biophysically these correspond to large proteins that are unable to move across the cell membrane. We calculate them directly from conservation equations. At rest, the right-hand side of Eq. (Mod.2) must be equal to zero. From this, we get two rest conditions,

$$\begin{cases} \sum_X ([X]_n - [X]_e) &= 0, \\ \sum_X ([X]_a - [X]_e) &= 0, \end{cases} \tag{Rest.1}$$

where X accounts for all ions (including impermeable ones) in the system. At baseline conditions, Eq. (3.10) and (Cons.3) provide three more rest conditions,

$$\begin{cases} \sum_X z_X C_X + \sum_{Y,i} z_Y N_Y^i = 0, \\ V_n^0 = \dfrac{\mathrm{F}}{\mathrm{C_i}} \sum_X z_X [X]_n^0 W_n^0, \\ V_a^0 = \dfrac{\mathrm{F}}{\mathrm{C_i}} \sum_X z_X [X]_a^0 W_a^0, \end{cases} \tag{Rest.2}$$

where $Y = \{A^-, B^+\}$ are the impermeable ions. Using Eq. (Rest.1) and (Rest.2), we compute the constants $N_{A^-}^n$, $N_{A^-}^e$, $N_{B^+}^e$, $N_{A^-}^a$ and $N_{B^+}^a$.
We assume that total glutamate in the presynaptic terminal amounts to 2 mM. Thus,

$$\sum_Z N_Z^0 = 2 \times W_{ps}, \quad \text{where } Z \in \{I, N, D, R, R1, R2, R3\}. \tag{Rest.3}$$

Thus, from Eq. Rest.3 and by setting the right hand side of Eq. 3.2 to 0 at baseline conditions, we can compute all initial conditions corresponding to the various glutamate stages.
The leak permeabilities $P_L^{X,i}$ are computed by setting the dynamical equations of N_X^i from Eq. Mod.3 to zero at rest conditions. Note that for glutamate and Ca^{2+} dynamics, we assume constant volumes of the presynaptic terminal, synaptic cleft and perisynaptic astrocytes processes.
The various parameters estimated in this section are laid out in Table 3.9.

3.5.9 Python implementation

The code is implemented in Python and is available publicly at `github.com/mkalia94/TripartiteSynapse`. The simulations were made with the `CVode` solver, implemented in the Python package `assimulo`.

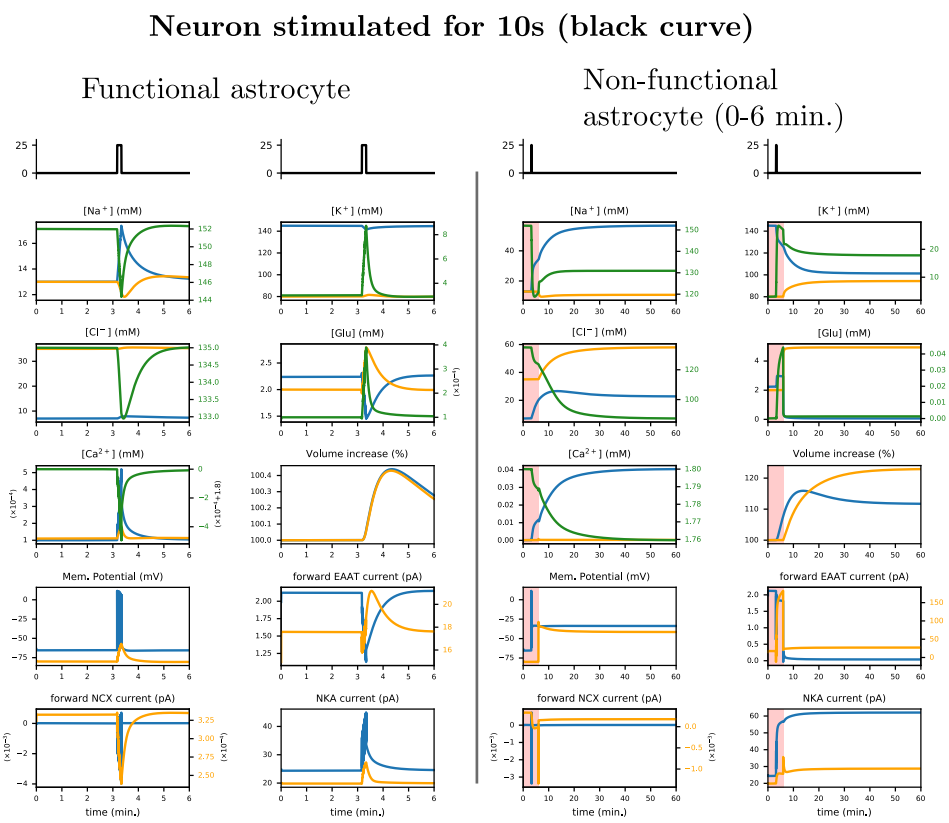

Figure 3.12: Extension of Fig 3.4 . Here, we further plot Cl^- and Ca^{2+} concentration profiles, along with important ion gradients. (B) shows that astrocytes are critical for maintaining ion homeostasis when Na^+/K^+-ATPase (NKA) is fully functional. Here, we plot neuronal (blue), astrocyte (orange) and extracellular (green) traces against time for several quantities. The initial extracellular volume ratio $\alpha_e = 20\%$. Shaded red area corresponds to periods during which ion transport across the astrocytic plasma membrane is blocked. Neurons are subjected to a 25 pA square wave input, as indicated by the black trace. The burst contains 475 action potentials. The green extracellular calcium trace has an offset of 1.8 mM.

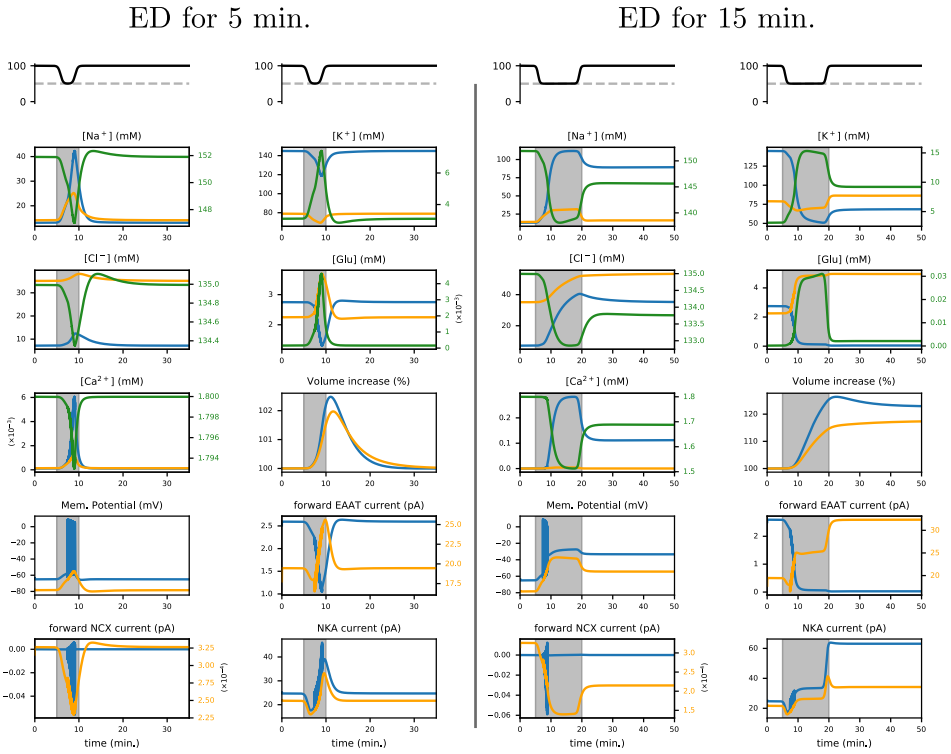

Figure 3.13: Extension of Fig 3.5. Here, we further plot Cl^- and Ca^{2+} concentration profiles, along with important ion gradients. We plot neuronal (blue), astrocyte (orange) and extracellular (green) traces against time. The initial extracellular volume ratio $\alpha_e = 80\%$ and minimal energy available $P_{\text{min}} = 50\%$. Shaded grey areas correspond to the period where Na^+/K^+-ATPase (NKA) activity is gradually reduced to P_{min} and restored to baseline after 5 minutes (left panel) or 15 minutes (right). This temporal profile is indicated in the upper panel.

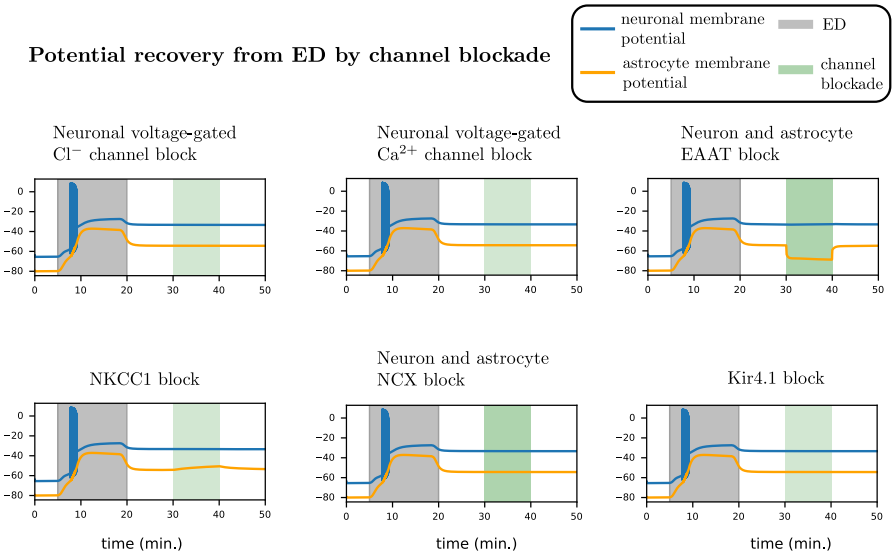

Figure 3.14: Extension of Fig 3.7B. We introduce pharmacological blockers post ED by blocking various ion channels/cotransporters to look for potential for recovery from the ED-induced pathological state. In all of the cases presented, the pathological state remains stable even after channel blockade. We plot neuronal (blue) and astrocyte (orange) membrane potentials against time. The initial extracellular volume ratio $\alpha_e = 80\%$ and minimal energy available $P_{\text{min}} = 0\%$. Shaded grey areas correspond to the period where Na^+/K^+-ATPase (NKA) activity is gradually reduced to P_{min} and restored to baseline after 15 minutes. The shaded light green area corresponds to channel blockade.

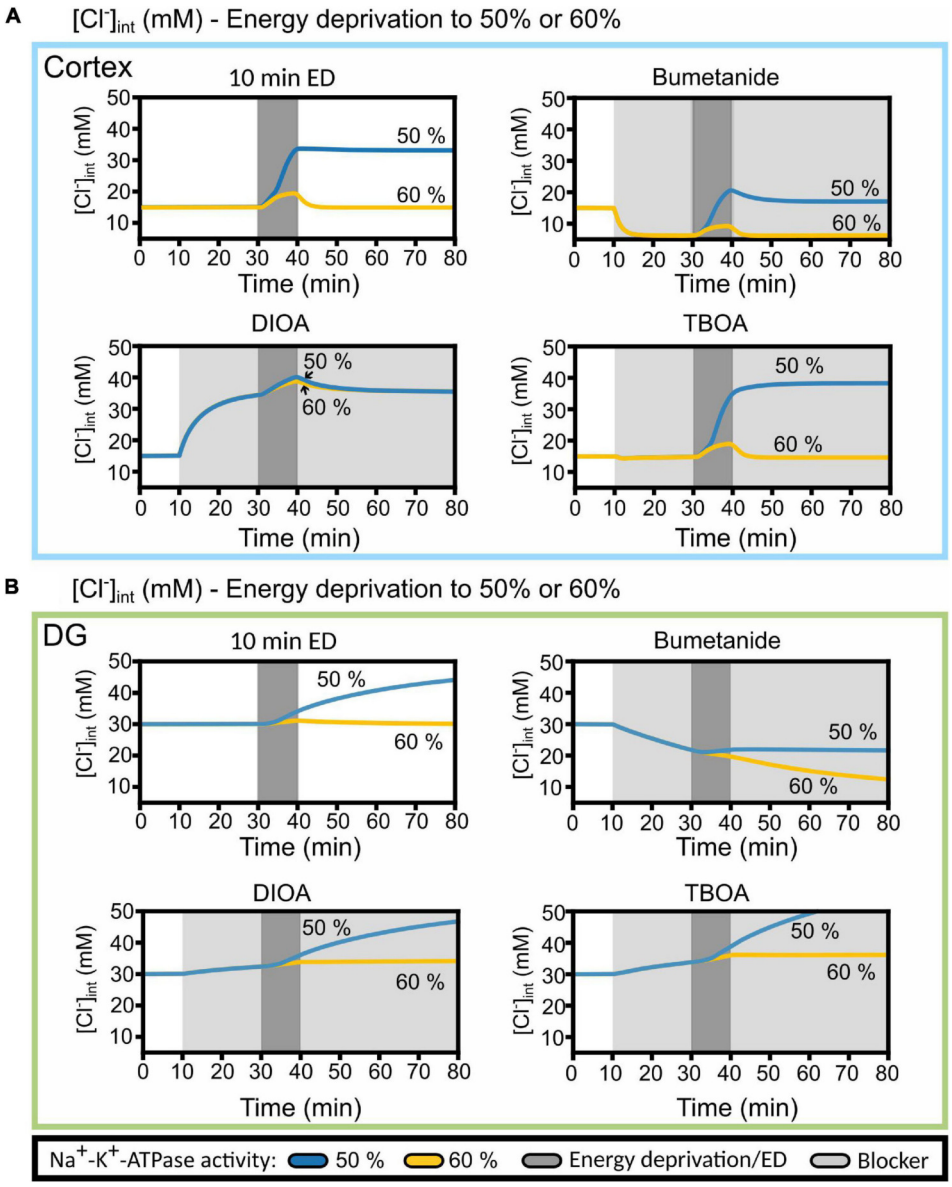

Figure 3.15: Predicted cortical and DG astrocyte chloride dynamics at NKA activity reduced to 50 or 60% of the baseline activity during chemical ischemia (energy deprivation). Time-dependent changes in $[Cl^-]_a$ for neocortical (A) and DG (B) astrocytes by reducing neuronal and astrocyte NKA activity for 10 min (dark gray block) to 50% (blue line) or to 60% (yellow line) of baseline. The model was subjected to block of a specific chloride transport system (light gray block: bumetanide, R-(+)-DIOA or DL-TBOA). At 20 min after the start of transport inhibition, transient ischemia was simulated followed by energy restoration for 40 min in the presence of the mentioned blocker. Abbreviations: DG, dentate gyrus; ED, energy deprivation; DIOA, R-(+)-DIOA; TBOA, DL-TBOA.

Table 3.4: **Model parameters for the neuronal compartment**, along with sources. Units are presented in the same manner as they are implemented in the Python code. All adjusted parameters are in the same order of magnitude as their original counterparts.

Constant	Value	Description
$P_{\mathrm{G}}^{\mathrm{Na}^+,n}$	8×10^{-4} [1000µm^3(ms)$^{-1}$]	Voltage-gated Na^+ channel permeability [43]
$P_{\mathrm{G}}^{\mathrm{K}^+,n}$	4×10^{-4} [1000µm^3(ms)$^{-1}$]	Voltage-gated K^+ channel permeability [43]
$P_{\mathrm{G}}^{\mathrm{Cl}^-,n}$	1.95×10^{-5} [1000µm^3(ms)$^{-1}$]	Voltage-gated Cl^- channel permeability [43]
$P_{\mathrm{G}}^{\mathrm{Ca}^{2+},n}$	1.5×10^{-5} [1000µm^3(ms)$^{-1}$]	Voltage-gated Ca^{2+} channel permeability [252]
P_{NKA}^{n}	86.4 [pA]	Maximal NKA current (Empirically scaled, of same magnitude as in [43])
$\alpha_{NKA}^{\mathrm{Na}^+}$	13 [mM]	NKA: Half-saturation concentration for intracellular Na^+(Empirical, adjusted from [235])
$\alpha_{NKA}^{\mathrm{K}^+}$	0.2 [mM]	NKA: Half-saturation concentration for extracellular K^+(Empirical, adjusted form [235])
P_{KCl}^{n}	1.3×10^{-6} [fmol (ms mV)$^{-1}$]	KCl cotransporter strength [43]
P_{NCX}^{n}	10.8 [pA]	NCX exchanger: scaling factor, identical to astrocyte
$\alpha_{\mathrm{NCX}}^{\mathrm{Na}^+}$	87.5 [mM]	NCX exchanger: half saturation concentration for Na^+[235]
$\alpha_{\mathrm{NCX}}^{\mathrm{Ca}^{2+}}$	1.38 [mM]	NCX exchanger: half saturation concentration for Ca^{2+}[235]
η_{NCX}	0.35 [dimensionless]	NCX exchanger: position of the energy barrier that controls voltage dependence of NCX current [235]
k_{NCX}	0.1 [dimensionless]	NCX exchanger saturation factor at very negative potentials [235]
P_{EAAT}^{n}	10^{-6} [fmol (ms mV)$^{-1}$]	Neuronal EAAT cotransporter strength, chosen to be of the same magnitude as KCl and NKCC1 cotransporters
$\alpha_{\mathrm{H}^+}^{n}$	0.66 [dimensionless]	Ratio of extracellular to intracellular proton concentration
$L_{H_2O}^{n}$	2×10^{-14} [1000 µm^3 mPa^{-1} ms^{-1}]	Neuronal membrane water permeability [43]

Table 3.5: **Model parameters for the astrocyte compartment**, along with sources. Units are presented in the same manner as they are implemented in the Python code.

Constant	Value	Description
P^a_{Kir}	0.286102 [nS]	Kir4.1 conductance, taken from [242] after multiplying with baseline surface area.
P^a_{NKCC1}	7.3215×10^{-7} [fmol (ms mV)$^{-1}$]	NKCC1 cotrasporter strength (taken from [102] after multipying with baseline surface area)
P^a_{EAAT}	2×10^{-5} [fmol (ms mV)$^{-1}$]	Astrocyte EAAT cotransporter strength, chosen to keep astrocyte to neuronal baseline EAAT current ratio at 9:1.
P^a_{NKA}	86.4 [pA]	Maximal NKA current (Empirically scaled to fit experimental data from [191], of same magnitude as in [43])
$\alpha^{\text{Na}^+}_{NKA}$	13 [mM]	NKA: Half-saturation concentration for intracellular Na^+[235]
$\alpha^{\text{K}^+}_{NKA}$	0.2 [mM]	NKA: Half-saturation concentration for extracellular K^+[235]
P^a_{NCX}	5.7 [pA]	NCX exchanger: Maximal NCX current, chosen in accordance with [214] as 1/15 of maximal NKA current.
$\alpha^{\text{Na}^+}_{\text{NCX}}$	87.5 [mM]	NCX exchanger: half saturation concentration for Na^+[235]
$\alpha^{\text{Ca}^{2+}}_{\text{NCX}}$	1.38 [mM]	NCX exchanger: half saturation concentration for Ca^{2+}[235]
η_{NCX}	0.35 [dimensionless]	NCX exchanger: position of the energy barrier that controls voltage dependence of NCX current [235]
k_{NCX}	0.1 [dimensionless]	NCX exchanger saturation factor at very negative potentials [235]
$\alpha^a_{\text{H}^+}$	0.66 [dimensionless]	Ratio of extracellular to intracellular proton concentration
$L^a_{H_2O}$	2×10^{-14} [1000 µm^3 mPa^{-1} ms^{-1}]	Astrocyte membrane water permeability [43]

Table 3.6: **Model parameters for glutamate recycling**, along with sources. Units are presented in the same manner as they are implemented in the Python code.

Constant	Value	Description
$k_1^{\max}$	1 [ms^{-1}]	Maximum forward reaction rate (Empirical)
K_M	2.3×10^{-3} [mM]	Ca^{2+} half-saturation concentration for forward reaction rate (Depot to Non Releasable Pool) [216]
K_{D_v}	1×10^{-4} [mM]	Half-saturation concentration for forward reaction rate (Non releasable pool to readily releasable pool) [216]
k_{20}	2.1×10^{-5} [ms^{-1}]	Uncatalysed forward reaction rate [216]
$k_{2_{\text{cat}}}$	2×10^{-2} [ms^{-1}]	Catalysed forward reaction rate [216]
k_{-20}	1.7×10^{-5} [ms^{-1}]	Uncatalysed backward reaction rate [216]
k_{-1}	5×10^{-5} [ms^{-1}]	Backward reaction rate [216]
k_3	4.4 [(mM ms)$^{-1}$]	Forward reaction rate [216]
k_{-3}	5.6×10^{-2} [ms^{-1}]	Backward reaction rate [216]
k_4	1.45 [ms^{-1}]	Fusion rate [216]
τ_{rec}	30 [ms (fmol)$^{-1}$]	Vesicle fusion factor (Empirical, adapted from [216])

Table 3.7: **Initial values for the various ion concentrations in the model.** These values correspond to 'baseline' conditions, and are used to estimate unknown parameters. Units are presented in the same manner as they are implemented in the Python code

Constant	Value	Description
V_i^0	-65.5 [mV]	Neuronal membrane potential at rest.
V_g^0	-80 [mV]	Astrocyte membrane potential at rest.
$[Na^+]_n^0$	13 [mM]	Taken from [191].
$[K^+]_n^0$	145 [mM]	Taken from [43].
$[Cl^-]_n^0$	7 [mM]	Taken from [43].
$[Ca^{2+}]_n^0$	1×10^{-4} [mM]	Rounded off from 73 nM [253].
$[Glu\ ]_n^0$	2.2385 [mM]	Free glutamate in the cytoplasm is about 2 mM [254]. See section **Estimating parameters**.
$[Na^+]_a^0$	13 [mM]	Obtained from experimental traces in [191].
$[K^+]_a^0$	80 [mM]	Obtained by setting K^+reversal potential to $\sim$-85 mV (here it is -87.7 mV).
$[Cl^-]_a^0$	35 [mM]	Obtained from Bergmann glia data in [255].
$[Ca^{2+}]_a^0$	1×10^{-4} [mM]	Chosen to be the same as in the presynaptic terminal (Empirical).
$[Glu\ ]_a^0$	2 [mM]	Chosen to be the same as in the presynaptic terminal (Empirical).

Table 3.8: **Initial values for gating variables, glutamate states and volumes.** These values correspond to 'baseline' conditions, and are used to estimate unknown parameters. Units are presented in the same manner as they are implemented in the Python code

Constant	Value	Description
m_0	1.33135×10^{-2}	Na^+activation gating variable. Estimated by setting right-hand side of the third equation of Eq. (3.1) to zero at resting conditions.
h_0	0.987298	Na^+inactivation gating variable. Estimated by setting right-hand side of the third equation of Eq. (3.1) to zero at resting conditions.
n_0	2.96946×10^{-3}	K^+activation gating variable. Estimated by setting right-hand side of the third equation of Eq. (3.1) to zero at resting conditions.
N_I^0	2.238×10^{-3} [fmol]	Baseline molar amount of free glutamate in the presynaptic terminal. Obtained from the relation $N_I^0 = [\text{Glu}\,]_n^0 \times W_{\text{PreSyn}}$.
N_D^0	4.04605×10^{-7} [fmol]	Baseline molar amount of vesicular glutamate in the depot of the presynaptic terminal. See section **Estimating parameters**.
N_N^0	3.36567×10^{-4} [fmol]	Baseline molar amount of non releasable vesicular glutamate in the presynaptic terminal. See section **Estimating parameters**.
N_R^0	4.14849×10^{-4} [fmol]	Baseline molar amount of readily releasable vesicular glutamate (not yet binded to Ca^{2+}) in the presynaptic terminal. See section **Estimating parameters**.
$N_{R_1}^0$	9.778061×10^{-6} [fmol]	Baseline molar amount of readily releasable vesicular glutamate (binded to one Ca^{2+}ion) in the presynaptic terminal. See section **Estimating parameters**.
$N_{R_2}^0$	7.655809×10^{-8} [fmol]	Baseline molar amount of readily releasable vesicular glutamate (binded to two Ca^{2+}ions) in the presynaptic terminal.
$N_{R_3}^0$	$2.08192593 \times 10^{-11}$ [fmol]	Baseline molar amount of readily releasable vesicular glutamate (not yet binded to three Ca^{2+}) in the presynaptic terminal.
W_n^0	2 [1000μm^3]	Baseline neuronal soma volume (taken from [43])
W_a^0	2 [1000μm^3]	Baseline astrocyte soma volume (Empirical, chosen to be the same as W_n^0)

Table 3.9: **Parameters estimated from baseline conditions.** Units are presented in the same manner as they are implemented in the Python code. See section 'Estimating parameters' for derivation.

Constant	Value	Description
$P_{\mathrm{L}}^{\mathrm{Na}^+,n}$	1.706×10^{-6} [1000µm^3(ms)$^{-1}$]	Neuronal Na^+ leak channel permeability.
$P_{\mathrm{L}}^{\mathrm{K}^+,n}$	1.771×10^{-5} [1000µm^3(ms)$^{-1}$]	Neuronal K^+ leak channel permeability.
$P_{\mathrm{L}}^{\mathrm{Cl}^-,n}$	2.494×10^{-6} [1000µm^3(ms)$^{-1}$]	Neuronal Cl^- leak channel permeability.
$P_{\mathrm{L}}^{\mathrm{Ca}^{2+},n}$	1.649×10^{-11} [1000µm^3(ms)$^{-1}$]	Neuronal Ca^{2+} leak channel permeability.
$P_{\mathrm{L}}^{\mathrm{Glu},n}$	3.662×10^{-6} [1000µm^3(ms)$^{-1}$]	Neuronal Glu leak channel permeability.
$P_{\mathrm{L}}^{\mathrm{Na}^+,a}$	1.054×10^{-7} [1000µm^3(ms)$^{-1}$]	Astrocytic Na^+ leak channel permeability.
$P_{\mathrm{L}}^{\mathrm{K}^+,a}$	7.877×10^{-5} [1000µm^3(ms)$^{-1}$]	Astrocytic K^+ leak channel permeability.
$P_{\mathrm{L}}^{\mathrm{Cl}^-,a}$	4.388×10^{-7} [1000µm^3(ms)$^{-1}$]	Astrocytic Cl^- leak channel permeability.
$P_{\mathrm{L}}^{\mathrm{Ca}^{2+},a}$	3.022×10^{-10} [1000µm^3(ms)$^{-1}$]	Astrocytic Ca^{2+} leak channel permeability.
$P_{\mathrm{L}}^{\mathrm{Glu},a}$	2.891×10^{-5} [1000µm^3(ms)$^{-1}$]	Astrocytic Glu leak channel permeability.
Volumes and amounts of ions (obtained after setting $\alpha_e = 20\%$)		
W_e^0	0.925 [1000µm^3]	Baseline extracellular volume.
$N_{\mathrm{A}^-}^n$	302.0105 [fmol]	Amount of impermeant anions in the neuronal soma.
$N_{\mathrm{B}^+}^e$	2.790 [fmol]	Amount of impermeant cations in the extracellular space.
$N_{\mathrm{A}^-}^e$	21.264 [fmol]	Amount of impermeant anions in the extracellular space.
$N_{\mathrm{B}^+}^a$	110.497 [fmol]	Amount of impermeant cations in the astrocyte soma.
$N_{\mathrm{A}^-}^a$	209.111 [fmol]	Amount of impermeant anions in the astrocyte soma.
C_{Na^+}	188.7 [fmol]	Total amount of Na^+ions in the system.
C_{K^+}	428.775 [fmol]	Total amount of K^+ions in the system.
C_{Cl^-}	198.375 [fmol]	Total amount of Cl^-ions in the system.
$C_{\mathrm{Ca}^{2+}}$	1.8×10^{-3} [fmol]	Total amount of Ca^{2+}ions in the system.
C_{Glu}	5×10^{-3} [fmol]	Total amount of Glu ions in the system.
W_{tot}	2.925 [1000µm^3]	Total volume of the system.

Chapter 4

A neural mass model for EEG in ischemia

M. Kalia, S. L. B. Ligtenstein, M.J.A.M. van Putten and H.G.E. Meijer, (*submitted*), 2022.

Abstract

Normal brain function depends on continuous cerebral blood flow for the supply of oxygen and glucose, and is quickly compromised in conditions where the metabolic demand cannot be met. Insufficient cerebral perfusion can result in ischemic stroke, with symptoms ranging from loss of motor or language function to coma, depending on the brain areas affected. Cerebral ischemia also results in changes in the electroencephalogram. Initially, a reduction of the frequency of the rhythms occurs. Depending on the depth and duration of energy deprivation, this eventually leads to the disappearance of all rhythmic activity. In this chapter, we study the relationship between electroencephalogram (EEG phenomenology and cellular biophysical principles using a model of interacting thalamic and cortical neural masses coupled with energy-dependent synaptic transmission. Our model faithfully reproduces the characteristic EEG phenomenology during acute cerebral ischemia and shows that synaptic arrest occurs before cell swelling and irreversible neuronal depolarisation. The early synaptic arrest is attributed to ion homeostatic failure due to dysfunctional Na^+/K^+-ATPase. Moreover, we also show that the excitatory input from relay cells to the cortex controls rhythmic behavior. In particular, low relay-interneuron interaction manifests in burst-like EEG behavior immediately prior to synaptic arrest. The model thus reconciles the implications of stroke on a cellular, synaptic and circuit level and provides a basis for exploring multi-scale therapeutic interventions.

4.1 Introduction

Stroke is one of the leading causes of death in the world today [256], with approximately 11% of global deaths, as per the World Health Organisation. ischemic stroke, in particular, accounts for 87% of all stroke cases and is caused by a blockage in blood supply to the brain. This blockage results in a lack of oxygen and glucose, compromising various energy-dependent processes, such as synaptic transmission and maintenance of membrane potentials [5]. In the core region of the affected area, cerebral blood flow (CBF) is less than $\approx$ 10 ml/100g/min, which leads to irreversible loss of function occurring within minutes. In the surrounding area, known as the penumbra, CBF is in the range of 10-40 ml/100g/min, and significant neuronal dysfunction exists with potential for recovery, depending on the depth and duration of the remaining perfusion [41]. In the penumbra, synaptic transmission failure is the main cause of loss of function.

Oxygen and glucose are essential for the synthesis of adenosine triphosphate (ATP) by the mitochondria, where the main consumer is the Na^+/K^+-ATPase (NKA). The NKA maintains ion homeostasis at the synapse by exchanging 3 Na^+ ions for 2 K^+ ions per ATP molecule consumed against their respective concentration gradients. At the synaptic level, the vesicular-ATPase (vATPase) consumes ATP to maintain the pH level of neurotransmitter-carrying vesicles. The proton gradient is vital to the efficient packing (endocytosis) and release (exocytosis) of these vesicles. Synaptic recycling is interrupted during mild ischemia in the form of limited endocytosis or exocytosis [257]. If energy is restored sufficiently fast, synaptic function recovers completely. However, persistent transmission failure is possible after prolonged ischemia [258]. We note that synaptic transmission failure can occur without changes in membrane potentials or baseline ion concentrations [41].

If the ATP depletion is more severe, resting membrane potentials will also change, as the NKA cannot compensate for the non-zero transmembrane ion currents. The resulting depolarization, in turn, causes further large fluxes of the ions Na^+, K^+ and Cl^- across the membrane along their concentration gradients, and a net intracellular increase in Na^+ and Cl^- occurs [43]. The increase in intracellular osmolarity will subsequently induce cytotoxic edema [259]. Changes in neuronal function resulting from ischemic stroke, in particular, are also reflected in the electroencephalogram if the cortex is involved (EEG) [14, 64, 137]. In the clinic, EEG monitoring is used in patients at risk for cerebral ischemia, for instance, during carotid endarterectomy [64, 260, 65] or to assess recovery in patients with a postanoxic encephalopathy after cardiac arrest [71, 261]. The EEG changes in acute ischemia are well characterized and depend on the depth and duration of the ischemia. Initially, higher frequencies are suppressed, subsequently followed by the emergence of slower rhythms in the delta range, and finally, all rhythms may disappear [262, 64]. However, the precise biological mechanisms that result in such changes in the EEG are not

well known.

In this chapter, we employ a biophysical approach to reconcile principles of EEG and cellular synaptic function. We propose a mathematical model of coupled neural masses, where the coupling is based on population-averaged synaptic behavior. Population-averaged ion dynamics of the neural masses result in a firing-rate function dependent on membrane and Nernst potentials. Subsequently, this firing rate is used to compute synaptic currents from one neural mass to another. Each neural mass is surrounded by a finite extracellular bath containing oxygen, and energy deprivation is modelled by transiently depriving the bath of oxygen. We use the model to explain the link between cellular synaptic inhibition and evolution of the EEG rhythms and explore the differential sensitivity of NKA and vATPase function to energy availability.

Neural mass models are widely used to describe population synaptic dynamics based on a population-averaged firing rate [119, 133, 111, 130]. Such models have been successfully applied to explain several neuropathologies such as epilepsy [263, 127, 112] neurodegenerative diseases [264, 265]. The Liley model [133] in particular is conductance-based and thus more biophysically interpretable. The model has been extended to produce EEG rhythms associated with postanoxic encephalopathy [137]. Spiking neuron models have also been used to model the effects of stroke on thalamocortical circuits [266]. On a cellular level, ion homeostasis in neurons, astrocytes and the tripartite synapse are modelled using biophysical principles, as done in Chapter 3 and [43, 22, 267]. In some of these works inhibition of Na^+/K^+-ATPase (NKA) is used to model consequences of energy deprivation [43, 268].

To our knowledge, there are no computational models that reconcile single-ion and neural mass approaches. Following work on single-ion dynamics in Chapter 3 and [43], we present for the first time a biophysical model of a neural mass that depends on ion dynamics of Na^+, K^+ and Cl^-. We obtain dynamics of ion concentrations, membrane potentials, cellular volumes and synaptic currents in one formalism. This approach allows us to extend the idea of bistability observed in our previous work to the synaptic context. In particular, we show corroboration with experimental literature by modelling mild ischemia by slow (de)activation of synapses. Moreover, we show that inhibiting the NKA and vATPase results in several phases of synaptic rhythms - from healthy to complete synaptic arrest and cellular depolarization.

We also explore the implication of stroke on neural circuitry in the context of functional reorganisation. In particular, we show that excitatory thalamic relay cells govern normal EEG behavior. For low relay-interneuron interaction, we show that the interface between rhythms and synaptic arrest is characterized by different types of mixed-mode oscillations [131], which are burst-like behaviors that arise from slow changes in cellular function.

4.2 Model description

The model scheme used in this chapter is shown in Fig. 4.1-A. We model two neural regions, cortex and thalamus. The thalamus is used to provide excitatory drive to the cortex and is not subjected to energy deprivation for all simulations shown in this chapter. For each neural region, we model two local populations, inhibitory and excitatory, that interact via synaptic connections. In the cortex, we model excitatory pyramidal neurons (P) and inhibitory interneurons (I). Similarly, we include excitatory reticular (R) and inhibitory relay (S) neurons for the thalamus. The model for each population is composed of two parts, averaged ion dynamics and the synaptic component. All four local populations are modelled as point neuronal compartments with averaged ion dynamics and embedded in a shared, finite extracellular space. Within these compartments, dynamics of Na^+, K^+ and Cl^- are modelled via the activity of ion channels and cotransporters. Passive osmotic diffusion enables the compartments to swell or shrink via the movement of water. Each population's ion dynamics produces a net population firing rate, which activates the AMPA (excitatory) or GABA (inhibitory) channels of other populations, leading to a cascade of excitation and inhibition in the system, see Fig. 4.1-B.

The single-neuron model from Dijkstra et al. [43] is used to model the averaged ion dynamics of every population. Additionally, the architecture of the neural mass network is chosen from [269]. The EEG signal is then assumed to emerge from the net synaptic current of the pyramidal population.

In the sections ahead, we explain the equations used to describe ion dynamics in a single neural region. The model contains two such neural regions - cortex and thalamus - for which the equations are identical except for parameter values.

4.2.1 Ion dynamics

For each neural region, ion homeostasis in the two populations is modelled based on the averaged behavior of single neuron ion dynamics. As a result the fast dynamics corresponding to action potential generation are averaged out, leaving slower dynamics such as ion homeostasis and EEG rhythms intact.

In particular, we describe the dynamics of the molar amounts N_Y^X of ions $Y \in \{Na^+, K^+, Cl^-\}$ in populations $X \in \{P, I, S, R\}$. The dynamics of population volumes W_X are described by the osmotic imbalance generated by concentrations $[X]_Y$ with respect to the extracellular space. As the total volume and number of ions are kept constant for each neural region, the extracellular volumes and concentrations are given by conservation laws. We fix constants C_Y and W_{tot} that refer to the total number of ions of type Y and total regional volume, respectively.

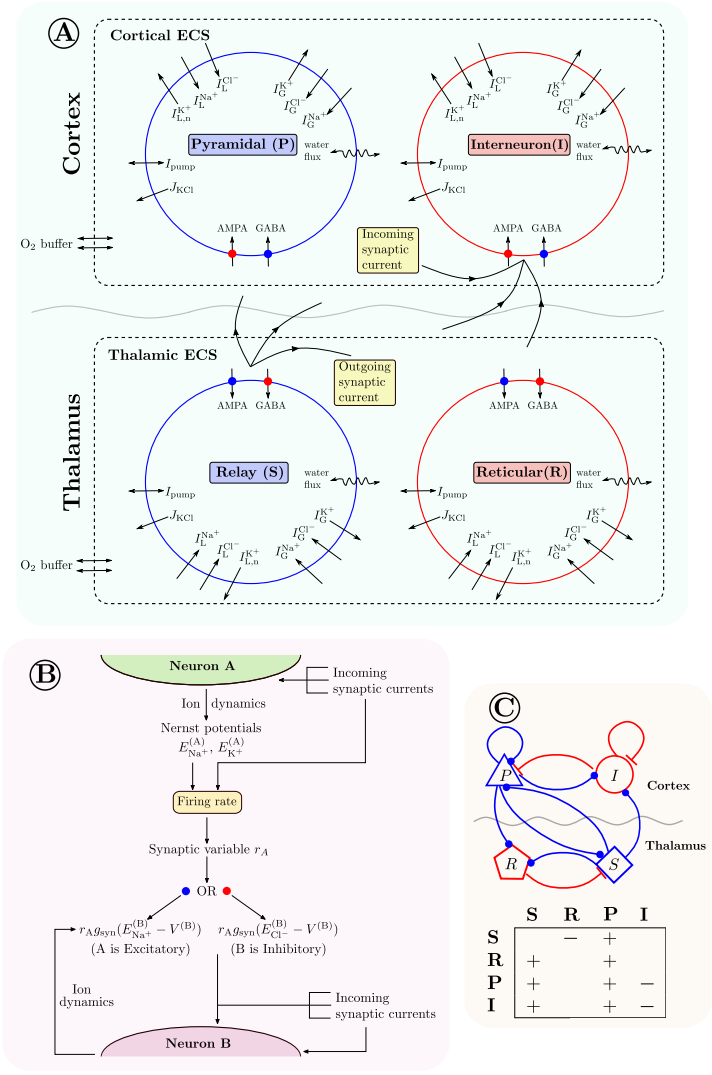

Figure 4.1: **A model of interacting neural populations with biophysical dynamics.** (A) The model consists of two neural regions: cortex and thalamus, each composed of two populations. Thus we model four populations, inhibitory interneurons (I), excitatory pyramidal neurons (P), thalamic relay neurons (S) and thalamic reticular neurons (R). The averaged ion dynamics of Na^+, $K^+$and Cl^- for each population are modelled with an averaged single-neuron formalism, where equations are chosen from [43]. Two populations from the same region are enclosed in a finite extracellular space, with an external bath of O_2. (B) The averaged ion dynamics produce population synaptic currents via a firing rate function which depends on incoming currents and Nernst potentials. (C) The populations are connected via synaptic currents; the network architecture is taken from [269]. Each mark in the table describes an excitatory (plus) or inhibitory (minus) connection from column population to row population.

Thus, the extracellular components are given by,

$$\begin{aligned} W_e &= W_{\text{tot}} - \sum_X W_X, \\ [Y]_e &= (C_Y - \sum_X N_Y^X)/W_e. \end{aligned} \tag{4.1}$$

The dynamics of the intracellular components of a population X are given by the following differential equations,

$$\begin{cases} \frac{d}{dt}N^X_{\text{Na}^+} = -\frac{1}{\text{F}}\left(I_{\text{G}}^{\text{Na}^+,X} + I_{\text{NKA}}^{\text{Na}^+,X} + I_{\text{L}}^{\text{Na}^+,X} + I_{\text{syn}}^{\text{Na}^+,X}\right), \\ \frac{d}{dt}N^X_{\text{K}^+} = -\frac{1}{\text{F}}\left(I_{\text{G}}^{\text{K}^+,X} + I_{\text{NKA}}^{\text{K}^+,X} + I_{\text{KCl}}^{\text{K}^+,X} + I_{\text{L}}^{\text{K}^+,X}\right), \\ \frac{d}{dt}N^X_{\text{Cl}^-} = \frac{1}{\text{F}}\left(I_{\text{G}}^{\text{Cl}^-,X} + I_{\text{KCl}}^{\text{Cl}^-,X} + I_{\text{L}}^{\text{Cl}^-,X} + I_{\text{syn}}^{\text{Cl}^-,X}\right), \\ \frac{d}{dt}W_X = L^X_{\text{H}_2\text{O}}\text{RT}\sum_Y([Y]_X - [Y]_e), \end{cases} \tag{4.2}$$

where F, R and T are Faraday's constant, the gas constant and fixed temperature, respectively. The subscript e indicates an extracellular quantity. $L^X_{H_2O}$ is the average water permeability of the intracellular compartments of population X. The various currents $I_Z^{Y,X}$ correspond to averaged ion currents of ion Y generated by ion channels and cotransporters Z in population X. Now, we briefly describe each ion current $I_Z^{Y,X}$. The synaptic currents $I_{\text{syn}}^{Y,X}$ are explained later.

Voltage-gated and leak channels

The voltage-gated channels $I_G^{Y,X}$ and leak channels $I_L^{Y,X}$ are formulated in the form of Goldman-Hodgkin-Katz (GHK) currents, as done in Chapter 3. The currents are given by,

$$\begin{aligned} I_G^{\text{Na}^+,X} &= P_G^{\text{Na}^+} m_\infty^3 h_\infty \text{GHK}(V_X, [\text{Na}^+]_X, [\text{Na}^+]_e), \\ I_G^{\text{K}^+,X} &= P_G^{\text{K}^+} n_\infty^4 \text{GHK}(V_X, [\text{K}^+]_X, [\text{K}^+]_e), \end{aligned} \tag{4.3}$$

where m, h and n are gating variables, P_G^Y are ion channel permeabilities and V_X is the averaged membrane potential of population X. The expression for V_X follows from [43],

$$V_X = \frac{F}{C}\left(N^X_{\text{Na}^+} + N^X_{\text{K}^+} - N^X_{\text{Cl}^-} - N^X_{\text{A}^-}\right),$$

where C is the averaged membrane capacitance of population X and A^- are large impermeant anions in the intracellular space of the population. The function $\text{GHK}(V_X, [Y]_X, [Y]_e)$ is given by,

$$\text{GHK}(V_X, [Y]_X, [Y]_e) = \frac{\text{F}^2 V_X}{z_X^2 \text{RT}} \frac{[Y]_X - [Y]_e \exp\left(-\frac{\text{F}V_X}{z_X \text{RT}}\right)}{1 - \exp\left(-\frac{\text{F}V_X}{z_X \text{RT}}\right)}, \tag{4.4}$$

where z_X is the valence of ion species X. The terms m_∞, h_∞ and n_∞ are given by,

$$\begin{aligned} m_\infty &= \alpha_m/(\alpha_m+\beta_m), \\ h_\infty &= \alpha_h/(\alpha_h+\beta_h), \\ n_\infty &= \alpha_n/(\alpha_n+\beta_n), \end{aligned}$$

where

$$\begin{aligned} \alpha_m &= \frac{0.32(V+52)}{1-\exp(-(V+52)/4)}, \beta_m = \frac{0.28(V+25)}{\exp((V+25)/5)-1}, \\ \alpha_h &= 0.128\exp(-(V+53)/18), \beta_h = \frac{4}{1+\exp(-(V+30)/5)}, \\ \alpha_n &= \frac{0.016(V+35)}{1-\exp(-(V+35)/5)}, \beta_n = 0.25\exp\left(-(V+50)/40\right), \end{aligned} \tag{4.5}$$

where the subscript was dropped from V for convenience. The expression for the voltage-gated Cl^- channel follows from [43] and is given by,

$$I_G^{Cl^-,X} = P_G^{Cl^-}\left(1+\exp\left(-\frac{V_X+10}{10}\right)\right)^{-1}\ \mathrm{GHK}(V_X,[Cl^-]_X,[Cl^-]_e), \tag{4.6}$$

and the leak currents are given by,

$$\begin{aligned} I_L^{Na^+,X} &= P_L^{Na^+}\mathrm{GHK}(V_X,[Na^+]_X,[Na^+]_e), \\ I_L^{K^+,X} &= P_L^{K^+}\mathrm{GHK}(V_X,[K^+]_X,[K^+]_e), \\ I_L^{Cl^-,X} &= P_L^{Cl^-}\mathrm{GHK}(V_X,[Cl^-]_X,[Cl^-]_e), \end{aligned} \tag{4.7}$$

with P_L the leak channel permeabilities.

KCl cotransporter

We model the flux as the difference of the K^+ and Cl^- Nernst potentials as in [102],

$$J_{KCl}^X = P_{KCl}\frac{RT}{F}\ln\left(\frac{[K^+]_e[Cl^-]_e}{[K^+]_X[Cl^-]_X}\right). \tag{4.8}$$

where P_{KCl} is the strength of the cotransporter. The corresponding K^+ and Cl^- currents are given by

$$\begin{aligned} I_{KCl}^{K^+,X} &= FJ_{KCl}^X, \\ I_{KCl}^{Cl^-,X} &= FJ_{KCl}^X. \end{aligned} \tag{4.9}$$

Na^+/K^+-ATPase (NKA)

The Na^+/K^+-ATPase is modeled as a function of intracellular Na^+, extracellular K^+, extracellular Na^+ and extracellular O_2. The current follows the model from [270] and is given by

$$I_{\mathrm{NKA}}^{X} = P_{\mathrm{NKA}} \left(\frac{1}{1+\exp\left(\gamma([\mathrm{O_2}]_{\mathrm{th}}^{\mathrm{NKA}} - [\mathrm{O_2}]_e)\right)} \right) \times \left(g_{\mathrm{NKA}} \frac{[\mathrm{Na^+}]_X^{1.5}}{[\mathrm{Na^+}]_X^{1.5} + (\alpha_{\mathrm{NKA}})^{1.5}} \cdot \frac{[\mathrm{K^+}]_e}{[\mathrm{K^+}]_e + \beta_{\mathrm{NKA}}} \right), \tag{4.10}$$

where $[\mathrm{O_2}]_{\mathrm{th}}^{\mathrm{NKA}}$ is the oxygen threshold for healthy activity. The functions g_{NKA} and σ are given by

$$g_{\mathrm{NKA}} = 1 + 0.1245 \cdot \exp\left(-0.1\frac{FV_X}{RT}\right) + 0.0365 \cdot \sigma \cdot \exp\left(-\frac{FV_X}{RT}\right), \tag{4.11}$$

and

$$\sigma = \frac{1}{7} \cdot \left(\exp\left(\frac{[\mathrm{Na^+}]_e}{67.3} \right) - 1 \right), \tag{4.12}$$

where P_{NKA} is the NKA permeability or the pump strength. The corresponding Na^+ and K^+ currents are given by

$$\begin{aligned} I_{\mathrm{NKA}}^{\mathrm{Na^+},X} &= 3I_{\mathrm{NKA}}^{X}, \\ I_{\mathrm{NKA}}^{\mathrm{K^+},X} &= -2I_{\mathrm{NKA}}^{X}. \end{aligned} \tag{4.13}$$

4.2.2 Synaptic dynamics

Next, for the two local populations we add synaptic currents, which describe the connections to each other and themselves, as shown in Fig. 4.1. Later on, we extend this to two regions. Synaptic currents depend on a firing rate function, which describes the firing frequency of the population as a function of membrane voltage and magnitude of external current. Usually, this is modelled as a sigmoidal function that depends on a membrane potential threshold. This chapter proposes a more realistic firing rate function that depends on incoming synaptic currents and Nernst potentials of Na^+ and K^+.

Biophysical firing rate function

The firing rate function is computed using numerical continuation data of a Hodgkin-Huxley model, which does not have the pump currents, the KCl cotransporter currents and the synaptic currents. From our biophysical setup,

the dynamics of the average population membrane potential V (subscript dropped for convenience) is given by,

$$\begin{aligned}\dot{V} &= \frac{F}{C}\sum_{Y} z_Y \dot{N}_Y \\ &= -\frac{1}{C}\sum_{Z,Y} I_Z^Y \\ &= -\frac{1}{C}\left(I_G^{\mathrm{Na}^+} + I_G^{\mathrm{K}^+} + I_G^{\mathrm{Cl}^-} + I_L - I_{\mathrm{NKA}} + I_{\mathrm{syn}}\right), \end{aligned} \tag{4.14}$$

where I_L is the averaged leak current and I_{syn} is the total synaptic current

$$I_{\mathrm{syn}} = -I_{\mathrm{syn}}^{\mathrm{Na}^+} - I_{\mathrm{syn}}^{\mathrm{Cl}^-}. \tag{4.15}$$

The Hodgkin-Huxley model is given by

$$\dot{V} = -\frac{1}{C}\left((I_G^{\mathrm{Na}^+} + I_G^{\mathrm{K}^+} + I_G^{\mathrm{Cl}^-} + I_L + I_{\mathrm{Ext}}\right), \tag{4.16}$$

where I_{Ext} is external input current. Comparing equations (4.14)-(4.16), we see that setting $I_{\mathrm{Ext}} = -I_{\mathrm{NKA}} + I_{\mathrm{syn}}$ in Eq. (4.16) gives our system Eq. (4.14). This property is exploited to compute a firing rate function that not only depends on external current, but also on the Nernst potentials of Na^+ and K^+. This is done in the following way:

- Perform continuation of the stable periodic orbit in the Hodgkin-Huxley model with respect to three parameters: $E_{\mathrm{K}^+}, E_{\mathrm{Na}^+}$ and I_{Ext}. The existence of the periodic orbit is in a compact domain, marked by two bifurcations on the boundary: a saddle-node of periodic orbits to the right, and a supercritical Hopf to the left, see Fig. 4.2 (left).
- Next, approximate a smooth function FR that describes the frequency of the computed periodic orbits in the previous step, as a function of $E_{\mathrm{K}^+}, E_{\mathrm{Na}^+}$ and I_{Ext}.
- Now, we set the input I to the firing rate function as $I_{\mathrm{Ext}} + I_{\mathrm{syn}} - I_{\mathrm{NKA}}$ instead, where I_{Ext} is the external current supplied to the population.

The firing rate function FR is thus expressed as

$$\mathrm{FR} \equiv \mathrm{FR}(E_{\mathrm{Na}^+}, E_{\mathrm{K}^+}, I) = \kappa\sqrt{I - \tilde{I}_1}\mathrm{H}(I - \tilde{I}_2), \tag{4.17}$$

where I refers to external input current, H is the standard Heaviside function and $\tilde{I}_{1,2}$ are Nernst potential-dependent thresholds. The functions κ and $\tilde{I}_{1,2}$ are

given by fitted cubic polynomial expansions as follows,

$$\kappa = \sum_{i,j=1}^{3} q_{ij}(E_{K^+})^i(E_{Na^+})^j,$$

$$\tilde{I}_1 = \sum_{i,j=1}^{3} p_{ij}(E_{K^+})^i(E_{Na^+})^j,$$

$$\tilde{I}_2 = \sum_{i,j=1}^{3} r_{ij}(E_{K^+})^i(E_{Na^+})^j,$$

where the fitting constants q_{ij}, p_{ij} and r_{ij} are given in Table 4.5.

Synaptic currents and mild ischemia

From the firing rate function FR, we compute the synaptic currents I^i_{syn} for a population i. First, we define the synaptic current $I^{j\to i}_{\text{syn}}$ as the current from population j to i. The net synaptic current for a population i is then given by,

$$I^i_{\text{syn}} = \sum_j I^{j\to i}_{\text{syn}}. \tag{4.18}$$

The current $I^{j\to i}_{\text{syn}}$ depends on the synaptic gating variable r_j and maximal current of population i. The current is modelled as a voltage-gated channel as follows,

$$I^{j\to i}_{\text{syn}} = \begin{cases} r_j \mathcal{g}^{j\to i}_{\text{syn}}(V_i - E^i_{Na^+}) & \text{(Excitatory AMPA)} \\ r_j \mathcal{g}^{j\to i}_{\text{syn}}(V_i - E^i_{Cl^-}) & \text{(Inhibitory GABA),} \end{cases} \tag{4.19}$$

where $g^{j\to i}_{\text{syn}}$ are connectivity constants. They are conductances that serve as network connection parameters. The dynamics of the synaptic variable r_j is given by a typical gating equation and depends on the firing rate FR_j of population j,

$$\dot{r_j} = \alpha_j(1 - r_j) - \beta_j r_j, \tag{4.20}$$

where

$$\alpha_j = \alpha_j^{\max}\frac{FR_j}{FR_j + FR_j^{\text{th}}}. \tag{4.21}$$

The threshold FR_j^{th} depends on the properties of the synaptic behavior of population j. For inhibitory populations, this threshold is kept higher than for excitatory populations. The currents $I^{Na^+,i}_{\text{syn}}$ and $I^{Cl^-,i}_{\text{syn}}$ are then given by,

$$I^{Na^+,i}_{\text{syn}} = \sum_j r_j(V_i - E^i_{Na^+}),$$

$$I^{Cl^-,i}_{\text{syn}} = \sum_k r_k(V_i - E^i_{Cl^-}),$$

where j and k span over excitatory (E,S) and inhibitory (I,R) populations, respectively. The proxy for EEG is computed as the pyramidal synaptic current I^E_{syn} that is run through a band-pass filter, filtering the signal to only show rhythms in the 0.1-40 Hz range.

4.2.3 Oxygen dynamics and simulating energy deprivation

We explicitly model oxygen dynamics as a way of performing transient energy deprivation. First, an infinitely large bath of oxygen is supplied to each neural region. This bath contains a constant concentration of oxygen $[O_2]_{\text{bath}} = 2$ mM. The diffusion of oxygen in the extracellular space happens via linear diffusion, where the baseline values is set at $[O_2]_e = 1.75$ mM, as per [89]. The influx of oxygen in the extracellular space is balanced by the consumption of NKA. The dynamics of $[O_2]_e$ are thus given by [89],

$$\frac{d}{dt}[O_2]_e = -\frac{\alpha\lambda}{F}\sum_j \frac{I^j_{\text{NKA}}}{W_j} + \epsilon_{O_2}\left([O_2]_{\text{bath}} - [O_2]_e\right), \tag{4.22}$$

where j runs over all populations from a single neural region. The constants α and λ are O_2 consumption rates from [89] and the constant ϵ_{O_2} is the O_2 diffusion constant. ischemia is simulated by transiently reducing the constant $[O_2]_{\text{bath}}$ to lower values before bringing it back to baseline, as done in [89]. For each population, we obtain four equations describing ion dynamics, given by Eq. (4.2) and the dynamics of its synaptic variable r, given by Eq. (4.20). Next, for each neural region, we obtain two equations for extracellular O_2 dynamics, given by Eq. (4.22). In this chapter, we model four populations of two neural regions, so in total, we have 22 differential equations for our working model.

4.2.4 Parameters and simulation

All the parameters used in the model equations are shown in Tables 4.1-5. Most of the parameters are chosen directly from previously published work, except the ones shown in tables 4.4 and 4.1. The parameters shown in Table 4.1 are estimated from baseline conditions by fixing state variables to their baseline values and setting the right-hand side of system equations to zero. The synaptic parameters, shown in Table 4.4, are empirically estimated such that α rhythms are produced following 20 pA external input current.
The parameters $g^{i\to j}$ are determined using the neural mass network architecture from [271, 269]. These parameters have to be adjusted from the original sources where they are fluxes (in units volt second) as in this chapter, they represent ion channel conductances (in units siemen). The parameters α_i and β_i are fixed in accordance with three assumptions. First, the deactivation constant β_i for inhibitory populations is kept at least a factor 10 lower than others to accommodate for the slowly deactivating $GABA_B$ receptor [272]. Second, the

parameters $g^{j\to i}$ for inhibitory populations j are kept a factor 10 higher than the rest, as resting Cl^- reversal potential is close to the resting membrane potential resulting in a small net GABA current. Finally, the parameters α_i and β_i are set to be a factor 10 lower than their cortical counterparts to ensure slow-wave input from the thalamus to cortex.
All simulations ahead are performed in `Julia`, and is available online at: `https://github.com/mkalia94/BioNeuralMass`. For continuation methods, we use Matcont [80].

Baseline behavior

We use the biophysical neural mass formulation to predict EEG behavior during mild ischemia and the effect of network heterogeneity on rhythmic behavior. The model is simulated by supplying the relay cell with an external input current of 20 pA. This stimulus excites the system and generates a robust α rhythm, which we define as baseline activity. This is shown in Fig. 4.2 (middle, top).
The choice of the input current is made by choosing a value that fits with the baseline α rhythm. In Fig. 4.2 (right), we plot resulting EEG frequencies against input current I_{Ext}, which shows a steady increase of frequencies after a threshold ($\approx$ 10 pA). We make the choice corresponding to an EEG frequency of $\approx$ 13 Hz.

4.3 Results

We use the biophysical neural mass formulation to predict EEG behavior during mild ischemia and the effect of network heterogeneity on rhythmic behavior. The model is simulated by supplying the relay cell with an external input current of 20 pA. This stimulus excites the system and generates a robust α rhythm, which we define as baseline activity. Baseline behavior is subjected to mild ischemia by transiently reducing Na^+/K^+-ATPase activity, which we perform explicitly via our oxygen model. Further, network heterogeneity is explored by varying parameters $g_{\text{syn}}^{j\to i}$.

4.3.1 δ rhythms emerge from slow (de)activation of synapses

Physiological EEG rhythms in the cortex are characterized by a dominant frequency in the α range (8-13 Hz). As a consequence of acute ischemia, these faster rhythms lose power, and slower (δ) rhythms emerge [64]. We demonstrate this behavior in Fig. 4.2. Here, the relay (excitatory thalamic) population is subjected to 20 pA of current, which provides an excitatory drive to the cortical populations. The synaptic currents of all populations then show synchronous rhythmic activity in the α range ($\approx$12 Hz). In Fig. 4.2 (middle, top), we plot the resulting synaptic current from the pyramidal cell (cortex, excitatory), which is used as a proxy for measuring EEG activity. Throughout this simulation,

the membrane potentials and ion concentrations do not deviate from baseline conditions.

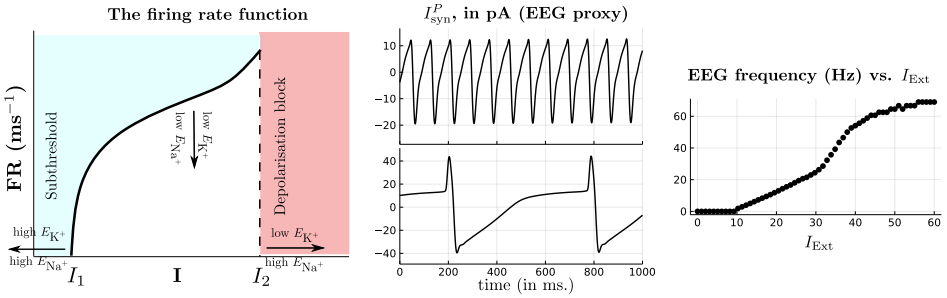

Figure 4.2: **Firing rate and signalling dynamics at baseline.** (Left) Plot of the biophysical firing rate function Eq. (4.17) against input current I for fixed E_{Na^+} and E_{K^+}. The firing rate is characterized by two thresholds of zero firing rate. The first corresponds to subthreshold behavior, and the latter signifies the depolarisation block, where averaged population membrane potentials saturate at pathological levels. (Middle) Plots of the net pyramidal synaptic current I^P_{syn} against time under two different conditions. The top trace corresponds to baseline parameters, which give rise to α oscillations ($\approx$12 Hz). In the bottom trace, the synaptic constants α_j^{max} and β_j are reduced to 10% of baseline values which gives rise to δ oscillations ($\approx$ 2 Hz). Note the increased amplitude of the δ oscillations. (Right) Frequency vs input current to the thalamic relay neurons I_{Ext}. Increasing input current past a threshold ($\approx$ 10 pA) substantially increases frequency. For the rest of the simulations, baseline input is set to 20 pA.

Next, we perform the same simulation but with mild ischemia. For this setting, we slow the synaptic activation and deactivation constants of the cortical populations, setting them to 10% of their baseline values. As before, we also subject the excitatory thalamic population to 20 pA constant current. The resulting simulation shows rhythmic behavior too, but much slower, i.e., in the δ range, see Fig. 4.2 (middle, bottom).
In our simulations, slowing the synaptic activation and deactivation constants of the cortex results in a α to δ transition, typical of mild ischemia. Based on this observation, we model the effect of the vesicular ATPase on synaptic dynamics, by changing Eq. (4.20) to

$$\dot{r_j} = f_{\text{vATP}}(\alpha_j(1 - r_j) - \beta_j r_j), \tag{4.23}$$

where f_{vATP} depends on extracellular O_2 and models the effect of the vesicular ATPase on the activation and deactivation of the synaptic variable. In the absence of O_2, it simulates mild ischemia by slowing down gating behavior. The term f_{vATP} is modelled as a sigmoid as follows,

$$f_{\text{vATP}} = [O_2]_{\text{min}} + (1 - [O_2]_{\text{min}}) \left(1 + \exp(\gamma([O_2]_{\text{th}}^{\text{vATP}} - [O_2]_e))\right). \tag{4.24}$$

The constant $[O_2]_{\text{min}}$ prevents synapses from completely slowing, and is set to 0.1, or 10% of baseline values. We assume that the vATPase consumes

extracellular O_2 in the same way as the NKA. Thus, Eq. (4.22) becomes,

$$\frac{d}{dt}[O_2]_e = -\frac{\alpha\lambda}{F}\sum_j \left(\frac{I^j_{\text{NKA}} + I^j_{\text{vATP}}}{W_j}\right) + \epsilon_{O_2}\left([\text{O}_2]_{\text{bath}} - [\text{O}_2]_e\right), \tag{4.25}$$

where I_{vATP} is the vATPase current associated with oxygen consumption, and is given by,

$$I^j_{\text{vATP}} = g_{\text{vATP}} f_{\text{vATP}}, \tag{4.26}$$

where the maximum current g_{vATP} converts the flux to a current and is computed from resting baseline conditions.

4.3.2 Mild ischemia leads to synaptic arrest via multiple phases

Next, we consider our extended model with the vATPase. We simulate energy deprivation in this case by transiently reducing $[\text{O}_2]_{\text{bath}}$. We show the result of such simulations in Fig. 4.3.

The extracellular oxygen concentration, $[\text{O}_2]_{\text{bath}}$, is reduced transiently to 80% of its baseline value between minutes 0.5 and 10. Meanwhile, 20 pA excitatory thalamic stimulation is provided for the full length of the simulation, as before. In Fig 4.3-top,right we plot the bath oxygen concentration $[\text{O}_2]_e$, which shows a characteristic transient profile of rapid initial decrease followed by slow recovery, as seen in previous work [89, 273].

Although the threshold $[\text{O}_2]^{\text{NKA}}_{\text{th}}$ is available in literature [89], the choice for the vATPase threshold $[\text{O}_2]^{\text{vATP}}_{\text{th}}$ is not clear. Given the high ATP demand of the NKA compared to endo/exocytosis [41] we assume that $[\text{O}_2]^{\text{vATP}}_{\text{th}} > [\text{O}_2]^{\text{NKA}}_{\text{th}}$. Thus we perform a parameter sweep by varying the two thresholds for various values between $[1.1, 1.6]$. For each parameter pair, we simulate energy deprivation as before while simultaneously providing excitatory thalamic input throughout the simulation. This setup allows us to observe transitions between several rhythmic patterns. The results of the parameter sweep are shown in Fig. 4.3-top, left. We observe three distinct behaviors of the EEG signal, and we plot an example for each case. Alongside the EEG, we plot a time-frequency plot of the signal, computed via a moving window for every time point. The first (square) corresponds to a recovery of the α rhythm after oxygen restoration. In this case, the EEG may slow down to the δ range during low-oxygen conditions. The presence of low-frequency rhythms is also accompanied by a significant increase in EEG amplitude. Recovery occurs for relatively low NKA thresholds. Upon increasing $[\text{O}_2]^{\text{NKA}}_{\text{th}}$ slightly, the EEG no longer recovers to the α range post oxygen restoration and remains flat (triangle and cross). In this scenario, two subcases are possible. First (triangle), the EEG stays flat after energy restoration, but membrane potentials and ion dynamics recover to baseline. The second (cross) case corresponds to a total loss of synaptic communication and

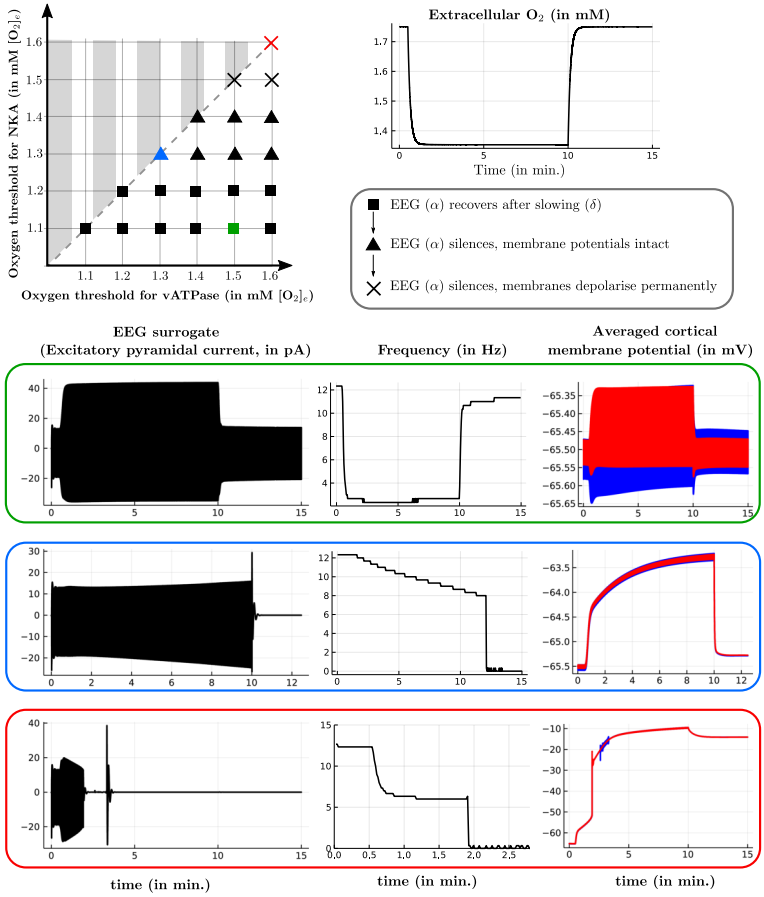

Figure 4.3: **Two-parameter sweep of the model with oxygen dynamics.** (Top, left) Two parameter plot of $[O_2]_{th}^{NKA}$ vs $[O_2]_{th}^{vATP}$ for several values between 1.1 and 1.6 mM. For each parameter pair, the oxygen bath supply $[O_2]_{bath}$ is reduced to 80% of its original capacity between minutes 0.5 and 10 while simultaneously stimulating the thalamic relay neuronal population with 20 pA for the whole duration of the simulation. This results in the extracellular oxygen trace (Top, right). For each parameter pair, we show the three possible cases (square, triangle, cross) corresponding to the transitional behavior of the EEG. The cases are ordered in pathological effect, and for each case, we plot the corresponding EEG signal behavior (Bottom, left solid black line). The green panel also shows that the α-δ transition is accompanied by increased amplitude during slow-wave activity. Alongside each EEG plot, we also show its frequency-time plot (Bottom, right), which shows the dominant frequency characteristics of the transitional behavior, and the corresponding averaged cortical membrane potentials. The red and blue trace correspond to interneurons and pyramidal cells respectively.

ion homeostasis - the EEG stays flat post energy restoration and the averaged neuronal membranes are permanently depolarised.
Moreover, varying $[O_2]_{th}^{vATP}$ while keeping $[O_2]_{th}^{NKA}$ fixed does not change the qualitative behavior of the EEG signal. Thus it suffices to keep these parameters identical.

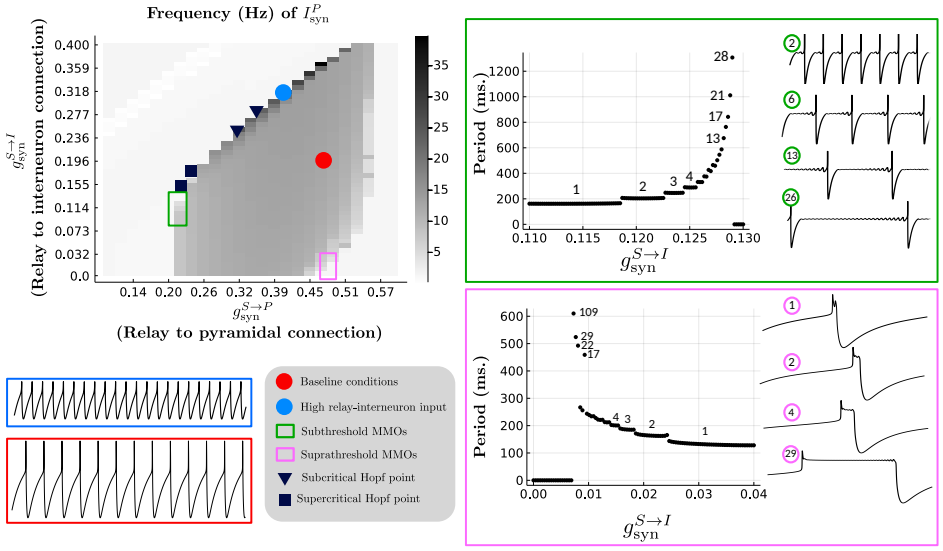

Figure 4.4: **The impact of relay neurons on cortical rhythms.** (Left, top) Plot of a two-parameter sweep with parameters $g_{syn}^{S\to P}$ and $g_{syn}^{S\to I}$, corresponding to relay input to pyramidal neuronal and interneuronal populations, respectively. For each parameter value, the frequency of the corresponding signal I_{syn}^P is shown. For a few cases, the corresponding I_{syn}^P is shown in pA (black trace). (Right) The two insets explore transitions involving mixed-mode oscillations (MMOs) (green and pink). In the green box, the period of I_{syn}^P is plotted (black dots) against parameter $g_{syn}^{S\to I}$ while $g_{syn}^{S\to P} = 0.225$, showing a period-adding sequence. The number on the black dots correspond to the number of subthreshold small amplitude oscillations (SAO). The onset of MMOs coincides with subcritical Hopf bifurcations nearby (black square), which transition to supercritical Hopf bifurcations (black inverted triangle) as $g_{syn}^{S\to I}$ is increased. Similar plots are shown in the pink box, where $g_{syn}^{S\to P} = 0.475$. Here the numbers correspond to the number of suprathreshold SAOs. (Left, bottom) Two simulations of regular rhythms are shown for baseline conditions (red) and the near-Hopf case (blue).

4.3.3 Relay cells control cortical rhythmic behavior

The global onset of cortical stroke may also have consequences on the thalamocortical circuit itself [77, 274, 275]. Our model contains four thalamocortical connections. These amount to the following parameters being nonzero: $g_{syn}^{P\to S}$, $g_{syn}^{P\to R}$, $g_{syn}^{S\to P}$ and $g_{syn}^{S\to I}$. We now vary these parameters to see the effect of sever-

ing thalamocortical contact on baseline signalling. First, we are able to immediately neglect two parameters: $g_{\text{syn}}^{P\to S}$ and $g_{\text{syn}}^{P\to R}$. These correspond to the excitatory input provided by cortical pyramidal cells to both thalamic populations. The parameter $g_{\text{syn}}^{P\to S}$ modulates the frequency of baseline behavior but does not drastically affect the signalling process. Further, setting the parameter $g_{\text{syn}}^{P\to R}$ to zero results in no change in qualitative behavior. Thus, we are left with two parameters $g_{\text{syn}}^{S\to P}$ and $g_{\text{syn}}^{S\to I}$, which control the excitatory thalamic input to the cortical populations. We perform a parameter sweep of these parameters in the two-parameter domain, see Fig. 4.4. Baseline α rhythms correspond to the parameter pair $(0.5, 0.2)$.

For each parameter, the resulting frequency of the total pyramidal synaptic current I_{syn}^{P} is plotted. For a few cases, corresponding traces of I_{syn}^{P} are shown. Several interesting behaviors emerge. We observe that rhythms exist for a small window of $g_{\text{syn}}^{S\to P}$. While keeping $g_{\text{syn}}^{S\to I}$ fixed, we see that there is a small window where rhythmic behavior exists. Increasing $g_{\text{syn}}^{S\to I}$ squeezes this window, till there are no more rhythms possible. Baseline α rhythms (red point) are structurally stable in a local neighbourhood and transit to silent behavior via three thresholds. For relatively low values of the parameter $g_{\text{syn}}^{S\to I}$ (less than 50% of baseline), two thresholds correspond to sequences of period-adding bifurcations (green and pink box). In both cases, the period-adding sequences are characterized by mixed-mode oscillations (MMOs) [276, 131], see traces in the green and pink box. For low values of $g_{\text{syn}}^{S\to P}$ (green box), the MMOs contain subthreshold small-amplitude oscillations (SAOs). For each jump in the period, a new subthreshold SAO is added to the signal. For higher values of $g_{\text{syn}}^{S\to P}$ (pink box), the sequence of MMOs contains suprathreshold SAOs. The last threshold (blue) corresponds to a supercritical Hopf bifurcation. Here, regular rhythms disappear while the frequency settles to a fixed high frequency and the amplitude decays.

The onset of MMOs coincides with nearby subcritical Hopf bifurcations, two examples of which are shown in the parameter sweep (black squares). Here, the silent EEG state loses stability without the emergence of stable periodic behavior. Upon increasing $g_{\text{syn}}^{S\to P}$, the Hopf bifurcations transition into a supercritical type (black inverted triangles). A small perturbation of the parameter $g_{\text{syn}}^{S\to I}$ at such a point results in the emergence of stable rhythmic behavior, with low amplitude. The Hopf points were computed via MatCont [80] using one-parameter continuation. It is natural to expect that these points form a continuous curve, where the transition from the supercritical to subcritical case is characterized by a generalized Hopf bifurcation. Due to the slow-fast and multi-scale nature of the system, continuation as a Hopf bifurcation curve was not feasible. However, upon detection of a Hopf point, MatCont also determines whether the Hopf bifurcation is sub- or super-critical. Our one-parameter continuations support the existence of codim 2 bifurcation.

4.4 Discussion

In this chapter, we have introduced a neural mass model to describe the pathophysiology of mild ischemia in the context of clinical stroke. The model is derived from biophysical principles and encapsulates the dynamical description of four populations in the cortex and thalamus.

4.4.1 Sequence of pathologies in low-oxygen conditions

Mild oxygen deprivation results in a smooth transition from α rhythms to the emergence of δ activity. In acute hemispheric strokes, the amount of asymmetry in δ-power is associated with the neurological status [64, 260, 14, 69, 277, 266]. The appearance of delta activity in acute ischemia is reversible if cerebral blood flow is restored sufficiently fast [64], but after 5-7 minutes of insufficient perfusion, irreversible neuronal damage can occur and EEG changes persist [66].

Synaptic transmission is metabolically demanding. At the presynaptic side, ATP is used on several types of ATPase, including the sodium/potassium pump, the Na^+/Ca^{2+} exchanger, the calcium-ATPase and the vesicular H^+-ATPase. Postsynaptically, ATP use is larger and primarily needed for restoring ion fluxes involved in synaptic currents [187]. The vATPase is an ATP-driven pump that ensures the necessary proton gradient across the vesicle membrane to allow efficient neurotransmitter secretion in the synaptic cleft [278]. Severe ischemia can result in excitotoxicity, characterized by neurotransmitter accumulation in the cleft and saturation of postsynaptic activity. Mild ischemia mainly affects vesicular endo- and exocytosis [257, 279], resulting in *presynaptic* transmission failure [258, 41].

We capture this phenomenon by modelling the vATPase by a sigmoidal factor that depends on extracellular oxygen. During low oxygen conditions, the vATPase slows down synaptic constants $\alpha_{\text{syn}}^{\max}$ and β_{syn}, thereby slowing resulting synaptic variables and EEG rhythms, see Figure 4.4. We found that varying vATPase affinity to available oxygen does not change the sequence of pathological behaviors associated with oxygen deprivation. Upon further reducing energy, EEG rhythms can disappear and remain absent even after energy restoration. Here, ion homeostasis in the population can either stay normal or settle at pathological behavior, see Figure 4.4. We observe that EEG silencing accompanied by normal ion homeostasis always precedes the case with depolarized populations, upon varying available oxygen or varying NKA/vATP oxygen thresholds. This is attributed to the failure of synaptic rhythmic generation in the model which precedes failure in ion homeostasis, concurrent with experimental literature on *in vivo* and *in vitro* models [280, 258, 41, 281].

4.4.2 Thalamic relay neurons control baseline activity

Our model contains four connections between the thalamus and cortex. We find that altering thalamocortical connections (connections from thalamic relay cells to interneurons and pyramidal cells) shows burst-like EEG oscillations at the interface between normal rhythms and silent EEG behavior. Cortical ischemic stroke not only causes damage to cortical neurons, but may also result in substantial loss of thalamocortical projection and generally dampens excitability in thalamocortical circuits [282, 77, 79, 283, 284, 285]. This behavior is replicated in the model. For low values of $g_{\text{syn}}^{S\to P}$, rhythmic activity is lost, see Fig. 4.4. Moreover, we hypothesize that rhythmic activity exists for a window of relay-pyramidal cell connections. The interface is marked either by fast, low-amplitude oscillations or burst-like behavior.

Mixed-mode oscillations characterize the burst-like behavior for weak relay-interneuron connectivities. MMOs are widely studied dynamical objects that arise in many computational neuroscience models [286, 132, 287, 288, 289, 290]. We observe MMOs of subthreshold and suprathreshold type as seen in previous literature [291], that occur at the border between normal and silent EEG activity. The suprathreshold MMOs are remarkably similar to generalized periodic discharge (GPD) behavior in EEGs, which are hypothesized to result from weak excitatory input to inhibitory interneurons [292, 71], which agrees with our model predictions, see Fig. 4.4. Moreover, GPDs are also hypothesized to be prevalent at the interface between normal and low-voltage EEG behavior [292]. These events may also be related to pathological burst suppression patterns, which are associated with poor neurological outcome following stroke [293, 137].

4.4.3 Model assumptions and limitations

Our model has several limitations. For instance, astrocytes are not included in the current model, while their role in ion homeostasis is undisputed, as shown in Chapter 3 and [259]. We also assumed that ischemia may affect thalamocortical projections, while preserving intrinsic neuronal function in the thalamus. While this is in agreement with reports on postmortem histopathology in patients with a postanoxic encephalopathy after cardiac arrest, showing that cortical neurons can be selectively affected [285], the involvement of the thalamus cannot be excluded. Several model parameters are empirically optimized to ensure baseline α activity. However, these choices - including network architecture - are not unique and their perturbation results in no qualitative change in the results shown. Despite these limitations, our simulations show similar EEG characteristics as clinically observed and provide candidate biophysical pathophysiological mechanisms for its generation.

4.4.4 Conclusion

In sum, we constructed a neural mass model based on biophysical principles of ion dynamics, which allows us to make predictions simultaneously about synaptic behavior and ion homeostasis. Our model makes several predictions for EEG rhythms following adapted neuronal activity due to mild ischemia or during post-stroke functional reorganisation. High amplitude δ rhythms emerge during mild ischemic connections, and bursting behavior via mixed-mode oscillations may manifest as a result of altering thalamocortical connections. The detailed behavior of the model makes it generalizable to other pathological behaviors such as epilepsy, and can be used to investigate network-based and neuronal pathologies simultaneously.

4.5 Appendix

Table 4.1: **Parameters estimated from baseline conditions.** Units are presented in the same manner as they are implemented in the Julia code.

Constant	Value	Description
$P_{\mathrm{L}}^{\mathrm{Na}^+}$	1.28×10^{-6} [1000 µm^3(ms)$^{-1}$]	Na^+ leak channel permeability.
$P_{\mathrm{L}}^{\mathrm{K}^+}$	1.252×10^{-5} [1000 µm^3(ms)$^{-1}$]	K^+ leak channel permeability.
$P_{\mathrm{L}}^{\mathrm{Cl}^-}$	2.812×10^{-6} [1000 µm^3(ms)$^{-1}$]	Cl^- leak channel permeability.
W_e	16 [1000 µm^3]	Baseline extracellular volume.
$N_{\mathrm{A}^-}^X$	302.0105 [fmol]	Amount of impermeant anions in a population soma.
$N_{\mathrm{A}^-}^e$	416.10 [fmol]	Amount of impermeant anions in the extracellular space.
C_{Na^+}	2484 [fmol]	Total amount of Na^+ions in a neural region.
C_{K^+}	628 [fmol]	Total amount of K^+ions in a neural region.
C_{Cl^-}	2192 [fmol]	Total amount of Cl^-ions in a neural region.
W_{tot}	20 [1000 µm^3]	Total volume of a neural region.
ϵ_{O_2}	1.1175×10^{-4} [ms^{-1}]	Oxygen diffusion constant
g_{vATP}	0.2409 [pA]	maximum vATPase current

Table 4.2: **Initial values for the various states in the model in all neural regions and populations** X**.** These values correspond to 'baseline' conditions, and are used to estimate unknown parameters. Units are presented in the same manner as they are implemented in the Julia code.

Constant	Value	Description
$[Na^+]_X$	13 [mM]	Taken from [11].
$[K^+]_X$	145 [mM]	Taken from [43].
$[Cl^-]_X$	7 [mM]	Taken from [43].
W_X	2 [1000 μm^3]	Baseline neuronal soma volume (taken from [43])
r_X	0	Initial synaptic variable
$[O_2]_e$	1.25 [mM]	Baseline oxygen concentration in the extracellular space [89]

Table 4.3: **Parameters associated with ion dynamics.** Units are presented in the same manner as they are implemented in the Julia code.

Constant	Value	Description
C	20 pF	Membrane capacitance [43]
F	96485.333 [C mol^{-1}]	Faraday's constant
R	8314.4598 [C(mV)(mol K)$^{-1}$]	Universal gas constant
T	310 K	Room temperature [43]
$P_G^{Na^+}$	8×10^{-4} [1000 μm^3(ms)$^{-1}$]	Voltage-gated Na^+ channel permeability [43]
$P_G^{K^+}$	4×10^{-4} [1000 μm^3(ms)$^{-1}$]	Voltage-gated K^+ channel permeability [43]
$P_G^{Cl^-}$	1.95×10^{-5} [1000 μm^3(ms)$^{-1}$]	Voltage-gated Cl^- channel permeability [43]
α_{NKA}	13 [mM]	NKA: Half-saturation concentration for intracellular Na^+, see Chapter 3
β_{NKA}	0.2 [mM]	NKA: Half-saturation concentration for extracellular K^+, see Chapter 3
P_{KCl}	1.3×10^{-6} [fmol (ms mV)$^{-1}$]	KCl cotransporter strength [43]
$L^X_{H_2O}$	2×10^{-14} [1000 μm^3 mPa^{-1} ms^{-1}]	Neuronal membrane water permeability [43]
α	0.1666	Conversion factor [89]
λ	1	Relative cell density [89]
$[O_2]_{bath}$	1.75 [mM]	Baseline bath oxygen concentration [89]
γ	20 [mM^{-1}]	Sigmoidal slope constant
$[O_2]^Y_{th}$	Varies, see Fig. 4.3 [mM]	Oxygen threshold for ATPase

Table 4.4: **Parameters associated with synaptic dynamics**. Parameters are empirically adjusted. Units are presented in the same manner as they are implemented in the Julia code.

Constant	Value	Description
$g^{S\to R}$	0.3 [nS]	Population connectivity
$g^{S\to E}$	0.5 [nS]	Population connectivity
$g^{S\to I}$	0.2 [nS]	Population connectivity
$g^{R\to S}$	2 [nS]	Population connectivity
$g^{E\to S}$	0.5 [nS]	Population connectivity
$g^{E\to R}$	0.1 [nS]	Population connectivity
$g^{E\to E}$	0.3 [nS]	Population connectivity
$g^{E\to I}$	0.5 [nS]	Population connectivity
$g^{I\to E}$	5 [nS]	Population connectivity
$g^{I\to I}$	2.5 [nS]	Population connectivity
$FR_S^{\text{th}}, FR_E^{\text{th}}$	0.2 [ms^{-1}]	Excitatory firing rate threshold
$FR_R^{\text{th}}, FR_I^{\text{th}}$	0.5 [ms^{-1}]	Inhibitory firing rate threshold
α_E	12.5 [ms^{-1}]	Pyramidal synaptic activation constant
α_I	5 [ms^{-1}]	Interneuron synaptic activation constant
α_S	1.25 [ms^{-1}]	Relay synaptic activation constant
α_R	0.5 [ms^{-1}]	Reticular nuclei synaptic activation constant
β_E	3 [ms^{-1}]	Pyramidal synaptic deactivation constant
β_I	0.03 [ms^{-1}]	Interneuron synaptic deactivation constant
β_S	0.3 [ms^{-1}]	Relay synaptic deactivation constant
β_R	0.003 [ms^{-1}]	Reticular nuclei synaptic deactivation constant

Table 4.5: **Coefficients of polynomials $\bar{I}_1$, κ and $\bar{I}_2$**

Coeff. ($\bar{I}_1$)	Value	Coeff.(κ)	Value	Coeff. ($\bar{I}_2$)	Value
p_{00}	-213.8	q_{00}	0.287	r_{00}	-185.9
p_{10}	-8.404	q_{10}	0.01094	r_{10}	-4.877
p_{01}	-3.007	q_{01}	0.001027	r_{01}	-3.674
p_{20}	-0.1111	q_{20}	0.0001692	r_{20}	-0.002785
p_{11}	-0.07862	q_{11}	-8.42e-6	r_{11}	-0.1044
p_{02}	-0.001213	q_{02}	-4.839e-5	r_{02}	0.01561
p_{30}	-0.0005002	q_{30}	8.167e-7	r_{30}	-1.17e-5
p_{21}	-0.0005221	q_{21}	-3.156e-7	r_{21}	1.897e-5
p_{12}	-1.483e-6	q_{12}	-4.421e-7	r_{12}	0.0006927
p_{03}	3.779e-5	q_{03}	2.764e-7	r_{03}	0.0001089

Chapter 5

Learning normal form autoencoders for data-driven discovery of universal, parameter-dependent governing equations

M. Kalia, S.L. Brunton, H.G.E. Meijer, C. Brune and J.N. Kutz, (*in review*), 2021.

Abstract

Complex systems manifest a small number of instabilities and bifurcations that are canonical in nature, resulting in universal pattern forming characteristics as a function of some parametric dependence. Such parametric instabilities are mathematically characterized by their universal unfoldings, or normal form dynamics, whereby a parsimonious model can be used to represent the dynamics. Although center-manifold theory guarantees the existence of such low-dimensional normal forms, finding them has remained a long standing challenge. In this chapter, we introduce deep learning autoencoders to discover coordinate transformations that capture the underlying parametric dependence of a dynamical system in terms of its canonical *normal form*, allowing for a simple representation of the parametric dependence and bifurcation structure. The autoencoder constrains the latent variable to adhere to a given normal form, thus allowing it to learn the appropriate coordinate transformation. We demonstrate the method on a number of example problems, showing that it can capture a diverse set of normal forms associated with Hopf, pitchfork, transcritical and/or saddle-node bifurcations. This method shows how normal forms can be leveraged as canonical and universal building blocks in deep learning approaches for model discovery and reduced-order modeling.

5.1 Introduction

Instabilities and bifurcations in dynamical systems are canonical in nature, taking on a small but distinct number of forms that dominate pattern formation across every field of physics, engineering, and biology [294]. For such bifurcations, local equations exist that describe the *universal unfolding* of the change in qualitative behavior arising from parametric dependencies [295]. These equations, called *normal forms*, are low-dimensional and depend on a minimal set of key parameters that modulate the dynamics. Current methods for characterizing such instabilities require knowledge of the governing equations and asymptotic approximations in local neighborhoods of the state and parameter space [294, 295]. However, modern data-driven approaches aim to quantify global behavior directly from measurements, including capturing representations of normal forms [296]. Physics-informed machine learning architectures [297, 298, 299, 300] leverage the flexibility and universal approximation capabilities of deep neural networks to learn characterizations of critical physics, including coordinate systems for the parsimonious representation of the dynamics [157, 301]. However, deep learning approaches have typically focused on a single parameter regime, and they have not resulted in explicit parameterizations of bifurcations and instabilities in the dynamics. In this chapter, we use deep learning to discover the low-dimensional coordinate system that encodes the underlying normal form dynamics and pattern-forming bifurcation structure of parameter-dependent high dimensional data, giving a data-driven, low-dimensional and universal representation of the dynamics.

Model discovery and model reduction methods aim to discover coordinate systems, or low-dimensional subspaces, in which high-dimensional data evolves. Modal decomposition techniques, such as *proper orthogonal decomposition* (POD) [302] and *dynamic mode decomposition* (DMD) [303], approximate *linear* subspaces using dominant correlations in spatio-temporal data [304]. Linear subspaces, however, are highly restrictive and ill-suited to handle parametric dependencies. Attempts to circumvent these shortcomings include using multiple linear subspaces covering different temporal or spatial domains, diffusion maps [296, 305, 306], or more recently, using deep learning to compute underlying nonlinear subspaces which are advantageous for the representation of the dynamics [157, 301, 307, 308]. Deep learning provides a flexible architecture for data representation, which has led to its significant integration into the physical and engineering sciences [297, 298]. Specifically, within such a framework, the *sparse identification of nonlinear dynamics* (SINDy) can uncover parsimonious nonlinear models [157, 309]. Building on the SINDy framework, the goal here is to capture the underlying normal form that encodes the parametric dependence of the data and its underlying bifurcation.

Despite the diverse and rapid advancement of deep learning methods, the model discovery process has not yet captured the often simple parameter-dependence of the high-dimensional data, except with brute force parametrization. We

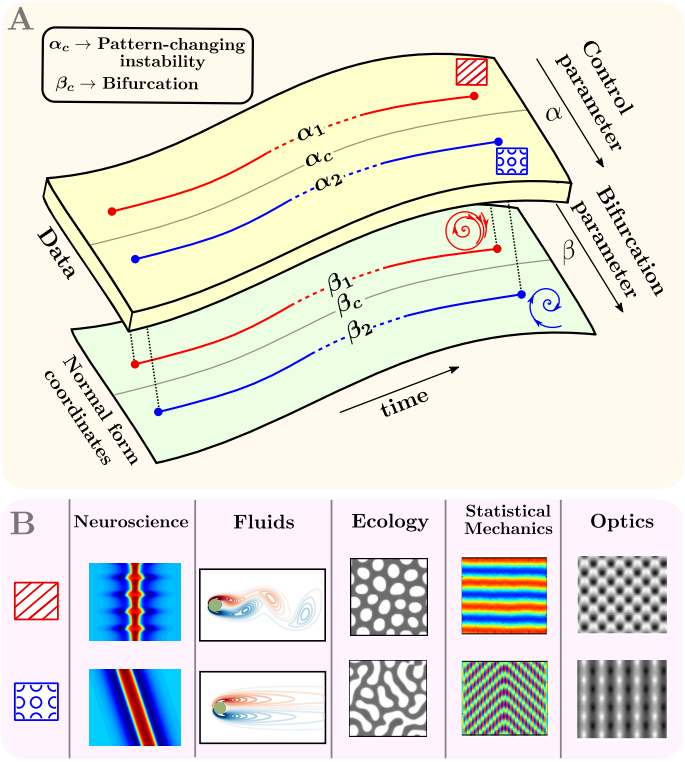

Figure 5.1: Instabilities, or bifurcations, lead to pattern formation in various physical systems that are characterized by underlying normal forms. Parameterized data across an instability is considered, which arises from a physical system with control parameter α (top). Such data is ubiquitous in the study of physical systems, for example, neuroscience [310], fluid physics, ecology [311], statistical physics [312] and optics [313] (bottom). Bottom panel figures are reproduced with permission.

highlight this issue in Fig. 5.1-A. Consider a bifurcation occurring within data at a critical parameter $\alpha = \alpha_c$. This instability induces a dramatic change in the behavior of the system, yielding different patterns for parameter values before and after the bifurcation. Such changes are ubiquitous in physical systems (Fig. 5.1-B) and present a challenge to cutting-edge model discovery methods. The different patterns are topologically inequivalent - they cannot be mapped onto each other by continuous, invertible transformations. Thus, observations from a single physical system yield irreconcilably different low-dimensional models, which is challenging for the aforementioned methods. Yet the underlying physics comes from a single model that simply walked through a bifurcation point.

In this chapter, we present a deep learning approach that extracts low-dimensional coordinates from high-dimensional parameter-varying temporal

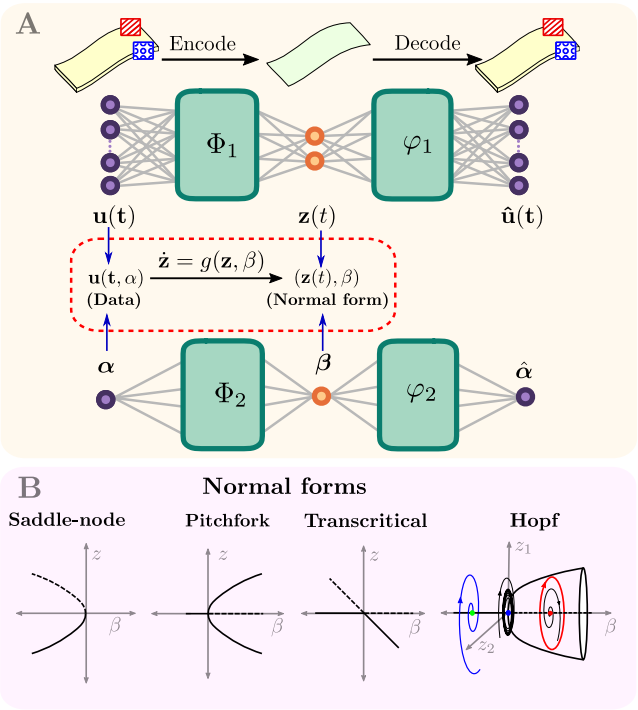

Figure 5.2: Normal for autoencoders to restrict parameterized data down to normal form coordinates. Parameterized data is collapsed down to the underlying normal form coordinates (z, β), with bifurcation parameter β using autoencoders (top). The dynamics on the reduced coordinates (z, β) are given by normal form equations. The different patterns from data are in one-to-one relation with the corresponding normal form patterns. Our novel approach uncovers a single parameterized equation (i.e., the normal form) that captures the parametric dependence across the data. This presents a plethora of normal forms to choose from, depending on the pattern changes observed in the data set (bottom).

data that exhibits instabilities. The coordinates and their parametric dependence are discovered using *autoencoders* that transform observations of states and parameters simultaneously while constraining the transformed variables to the corresponding normal form equations, as shown in Fig. 5.2-B. We demonstrate the method on various examples and instabilities: multiple bifurcations in a scalar ODE model, supercritical Hopf bifurcations in 1D partial differential equations (PDEs), and finally, a supercritical Hopf bifurcation in the 2D Navier-Stokes equations.

5.1.1 Normal Forms and Bifurcations.

The qualitative transitions in dynamics arising from bifurcations in temporal data are a cornerstone of dynamical systems analysis and *bifurcation* theory [295, 4].

Remarkably, there are only a small number of canonical instability types [294], allowing us to understand a diversity of instabilities manifesting in nature. For instance, the Hopf normal form is $\dot{z} = (\beta + i\omega)z + z|z|^2$, where the dot denotes time derivative. ω is the rotation frequency and β is the bifurcation parameter which characterizes the crossing of a pair of complex conjugate eigenvalues moving from the left to right half plane in a linear stability analysis [294]. Thus, growth of an oscillatory field is expected.

The Hopf bifurcation is only one of several bifurcations, with the simplest such bifurcations presented in Fig. 5.2-B. These bifurcations describe the interactions between multiple steady states upon perturbing the parameter. For a scalar system, there are only three possible bifurcations. A stable equilibrium could collide with an unstable one before disappearing (limit point) or split into two stable equilibria with an unstable one in between (pitchfork). Lastly, colliding equilibria can be followed by reemergence of the stable-unstable pair of equilibria, but switched in position (transcritical). One of the most commonly observed bifurcations, is the Hopf bifurcation requiring a minimum of two state dimensions. Hopf, pitchfork, transcritical and saddle-node bifurcations are the most commonly manifest instabilities of physical systems [294].

Dynamical systems theory and center manifold theorems [295] provide conditions for the existence of low-dimensional subspaces, or center manifolds, where the dynamics of the projection of the original dynamics, is given by the normal form. These theorems guarantee that a high-dimensional system $\dot{\boldsymbol{u}} = f(\boldsymbol{u}, \alpha), \boldsymbol{u} \in \mathbb{R}^n,\ n \gg 1$ depending on a parameter α exhibit generically a low dimensional model, typically one or two dimensional. Moreover, these theorems state that if $\boldsymbol{u}(\alpha)$ exhibits a saddle-node bifurcation, there exists a smooth invertible transformation φ such that the dynamics of $\varphi(\boldsymbol{u}(\alpha))$ are given by the saddle-node normal form. Thus center manifold theorems give guarantees that low-dimensional coordinates can be constructed using an appropriate normal form transformation φ.

5.1.2 Deep Learning of Normal Forms.

Consider a high-dimensional system $u(x, t; \alpha)$ parameterized by α where x denotes space, t denotes time. Discretizing u along n spatial locations x gives the vector $\boldsymbol{u}(t) \in \mathbb{R}^n$. Further discretizing along d timepoints gives the dataset $\boldsymbol{U} \in \mathbb{R}^{n \times d}$ composed of columns $\mathbf{u}(t)$ for $t = t_1, \ldots, t_d$. Note that the data set $\mathbf{U}$ is parameterized by the parameter α. The data measures a local instability at $\alpha = \alpha_c \in \mathbb{R}$. The objective is to extract low dimensional coordinates $\boldsymbol{z} \in \mathbb{R}^m,\ m \ll n$ and $\beta \in \mathbb{R}$ such that the dynamics of $\boldsymbol{z}$ are given by the

normal form of the instability,

$$\dot{\boldsymbol{z}} = g(\boldsymbol{z}(t), \beta). \tag{5.1}$$

The coordinates $\boldsymbol{z}$ are extracted by constructing smooth, invertible transformations φ_1 and φ_2 such that

$$\boldsymbol{z}(t) = \varphi_1 \boldsymbol{u}(t) \text{ and } \beta = \varphi_2 \alpha, \ \forall t. \tag{5.2}$$

We compute the functions φ_1 and φ_2 using deep learning. In particular, φ_1 and φ_2 are represented as fully connected neural networks. Further, we simultaneously compute neural networks ψ_1 and ψ_2 such that

$$\psi_1 \varphi_1(\boldsymbol{u}) \approx \boldsymbol{u} \text{ and } \psi_2 \varphi_2(\alpha) \approx \alpha \tag{5.3}$$

to make φ_j invertible. Such an approach is now standard in deep learning theory, and the pair (φ_j, ψ_j) is collectively referred to as an *autoencoder* [314].
Figure 5.2-A shows the two autoencoders (φ_j, ψ_j), $j = 1, 2$, corresponding to the state and parameter respectively. Combining equations (5.1) and (5.2) gives,

$$\dot{\boldsymbol{z}} = \mathrm{d}/\mathrm{dt}(\varphi_1 \boldsymbol{u}) = (\nabla_{\boldsymbol{u}} \varphi_1)\dot{\boldsymbol{u}} = g(\varphi_1 \boldsymbol{u}, \varphi_2 \alpha). \tag{5.4}$$

This relation is exploited to constrain the two autoencoders to the normal form (5.1). This is accomplished by computing minimizers of a loss function $\mathcal{L}$ that takes in the high-dimensional dataset $\boldsymbol{u}$, the neural networks φ_j, ψ_j and the parameter α,

$$\hat{\varphi}_j, \hat{\psi}_j = \arg\min_{\Theta} \mathcal{L}(\boldsymbol{u}, \alpha, \varphi_j, \psi_j) = \arg\min_{\Theta} \sum_k \mathcal{L}_k, \tag{5.5}$$

where Θ is the large set of parameters underlying the autoencoders (φ_j, ψ_j). The various terms $\mathcal{L}_k$ are outlined as follows. Terms $\mathcal{L}_{1,2}$ are the *autoencoder loss* terms that ensure φ_j and ψ_j are inverses of each other, enforcing Eq. (5.3):

$$\mathcal{L}_1 = \lambda_1 \|\boldsymbol{u} - \psi_1 \varphi_1 \boldsymbol{u}\|_2^2, \ \mathcal{L}_2 = \lambda_2 \|\alpha - \psi_2 \varphi_2 \alpha\|_2^2.$$

The *consistency loss* terms $\mathcal{L}_{3,4}$ constrain the autoencoders to the condition Eq. (5.5) and are given by,

$$\begin{aligned} \mathcal{L}_3 &= \lambda_3 \|\nabla_{\boldsymbol{u}} \dot{\boldsymbol{u}} - g(\varphi_1 \boldsymbol{u}, \varphi_2 \alpha)\|_2^2, \\ \mathcal{L}_4 &= \lambda_4 \|\dot{\boldsymbol{u}} - (\nabla_{\boldsymbol{z}} \psi_1) g(\varphi_1 \boldsymbol{u}, \varphi_2 \alpha)\|_2^2. \end{aligned}$$

Lastly, the *orientation loss* terms $\mathcal{L}_{5,6}$ ensure proper affine translation of the coordinates $(\boldsymbol{u}, \beta)$ with respect to the original coordinates $(\boldsymbol{u}, \alpha)$ and are given by,

$$\mathcal{L}_5 = \lambda_5 \|\mathbb{E}_t \varphi_1 \boldsymbol{u}\|_2^2, \ \mathcal{L}_6 = \lambda_6 \|\mathrm{sgn}(\alpha) \pm \mathrm{sgn}(\varphi_2 \alpha)\|_2^2,$$

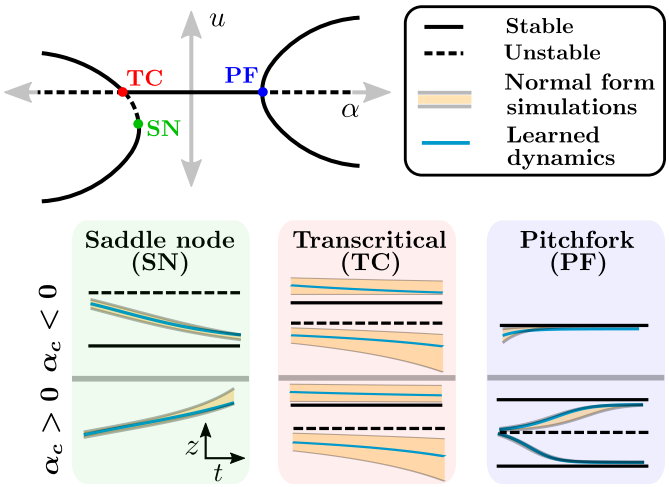

Figure 5.3: Learned normal form coordinates for the various bifurcations present in the 1D system Eq. 5.6. For each bifurcation, traces from learned test samples are plotted (in blue) against an ensemble of simulations of the underlying normal form (yellow).

where $\mathbb{E}_t$ denotes expectation over the entire time trace. The neural networks require training data in order to learn the autoencoder structure. The training data consists of dynamical trajectories where the initial conditions and parameters are chosen from a uniform distribution. They are shuffled and paired together and then used together to simulate trajectories. Once trajectories are computed, they are divided into training and testing datasets. The testing dataset is used to assess the performance of the autoencoder scheme, while training data is used to learn the neural networks. The neural networks φ_1 and ψ_1 require $\boldsymbol{u}$ and $\dot{\boldsymbol{u}}$ as input, while φ_2 and ψ_2 take α as input. They are then trained using the ADAM optimizer [315] for a fixed choice of parameters λ_i. For each of the examples presented ahead, details on training and validation, choice of neural networks, and regularization parameters λ_i can be found in the Appendix.

5.2 Results

In this section we demonstrate our method on four nonlinear dynamical systems: a scalar ODE, a neural field equation, the Lorenz96 equations and the Navier Stokes equation solved on a 2D spatial domain.

5.2.1 Scalar ODE system

The autoencoder scheme is first demonstrated on a system that exhibits the three scalar normal forms introduced in Figure 5.1-B. The system is characterized by

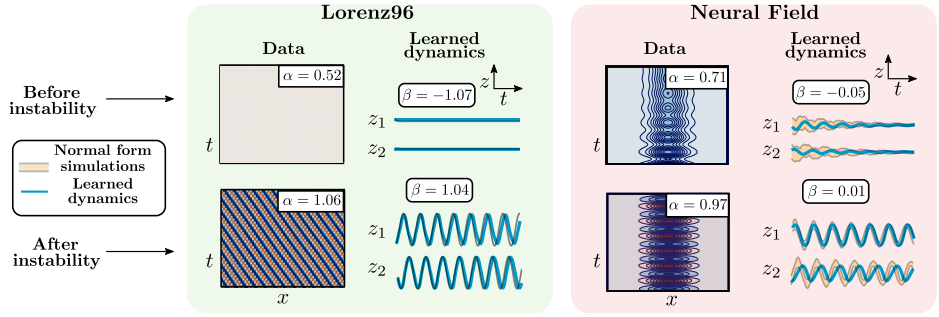

Figure 5.4: Learned Hopf normal form coordinates for the two high-dimensional systems, Lorenz96 (Eq.5.7) and Neural Field (Eq. 5.8), using test dataset samples. In both cases, imulations $(\boldsymbol{u}, \alpha)$ are shown alongside the learned normal form coordinates $(\boldsymbol{z}, \beta)$ (in blue) for values of α on both sides of the Hopf bifurcation point. For comparison, the Hopf normal form is simulated and plotted in the background (yellow).

a scalar ODE, given by

$$\dot{u} = \gamma u(\alpha - \alpha_{pf} - u^2)(\alpha - \alpha_{sn} + (u - u_{sn})^2), u \in \mathbb{R}, \tag{5.6}$$

where $\gamma = 0.01$, $u_{sn} = \alpha_{sn} = -6$ and $\alpha_{pf} = 6$. The bifurcation diagram of Eq. (5.6) in Fig. 5.3 shows how all the different scalar bifurcations are distributed in parameter space. Our objective is to use data generated from Eq. 5.6 and constrain it to each of the three individual normal forms. For each bifurcation scenario, data is collected from the neighborhood of a bifurcation and then constrained to the respective normal form using the autoencoder. A total of 500 initial conditions (u, α) are sampled per bifurcation scenario and used for training. Results are presented in Fig. 5.3. For each bifurcation, samples from test data are transformed to (z, β) coordinates using $\varphi_{1,2}$ and plotted against time (blue) for different α. An ensemble of simulations (in yellow) of the normal form are used for comparison. The learned coordinates (z, β) show remarkable agreement with the normal form, for each of the three bifurcation scenarios.
Next, we consider two 1D spatio-temporal systems, that exhibit supercritical Hopf bifurcations, the Lorenz96 equations [316] and the neural field equations [120]. Although the bifurcation is the same, the pattern formation is different. In the Lorenz96 case, the Hopf bifurcation manifests in a travelling wave pattern [317], while an oscillatory bump solution, called a 'breather', emerges in the neural field equation [318], see Fig. 5.4.

5.2.2 Lorenz96 system.

The Lorenz96 equations [316] are widely used in model discovery and data assimilation. The equations are given by

$$\dot{u}_j = -u_{j-1}(u_{j-2} - u_{j+1}) - u_j + \alpha, \; u \in \mathbb{R}^n \tag{5.7}$$

for $j = 1, 2, 3...n$ with boundary conditions $u_1 = u_n$ and $u_2 = u_{n-1}$. For $n = 64$, the trivial equilibrium $\boldsymbol{u} = \alpha$ undergoes a supercritical Hopf bifurcation with respect to α at $\alpha = \alpha_0 = 0.84975$ [317]. Across the bifurcation, a stationary solution transits to a moving stripe pattern, which is interpreted as a travelling wave solution. We sampled 10^3 initial conditions $(\boldsymbol{u}, \alpha)$ to train the neural networks. Results using test data are shown in Fig. 5.4. The learned coordinates $\boldsymbol{z}$ (in blue) are two-dimensional and match well with the simulated Hopf normal form (yellow) on both sides of the bifurcation.

5.2.3 Neural field equation.

The neural field equations describe the neuronal potential for a one-dimensional continuum of neural tissue [120, 119]. The dynamics due to an input inhomogeneity lead to a Hopf bifurcation of a stationary pattern leading to breathers when varying the input strength [318, 310]. The governing equations are

$$\dot{u} = -u - \kappa a + (w * f(u)) + I(x),\ \dot{a} = (u - a)/\tau_{nf}. \tag{5.8}$$

The operator $*$ represents a spatial convolution with $w(x) \equiv w(x - y) = w_e \exp(-((x - y)/\sigma_e)^2)$ the spatial connectivity kernel and $f(u)$ is a sigmoid given by $f(u) = \left(1 + \exp(\beta_{nf}(u - u_{thr}))\right)$ transforming the potential u into a firing rate. The spatially non-uniform input $I(x)$ is given by $I(x) = \alpha \exp(-(x/\sigma)^2)$ where $\kappa = 2.75, \tau_{nf} = 10, w_e = 1, \sigma_e = 1, \beta_{nf} = 6, u_{thr} = 0.375, \sigma = 1.2$.

A supercritical Hopf bifurcation with respect to a stationary bump response occurs at $\alpha = 0.8040$. In contrast to the Lorenz96 case, the stationary bump solution transits to an asymptotically stable periodic solution [310]. States (u, a) are discretized over a uniform spatial grid of size 64 each. Then, 10^3 initial conditions $(\boldsymbol{u}, \alpha)$ are used to generate training data. The normal form autoencoder results are presented in Fig. 5.4. Even though the pattern formation in this example is different from Lorenz96, the learned coordinates match the Hopf normal form behavior again.

The 1D PDEs considered are relatively low dimensional systems. For such systems, training fully connected neural network-based autoencoders is feasible. However, considering higher-dimensional PDEs leads to the so-called 'curse of dimensionality', and using fully connected neural networks is no longer feasible. In this situation, one has two options: use neural networks designed to assuage the curse of dimensionality, or reduce the dimension of data prior to training. In the next example, we choose the latter.

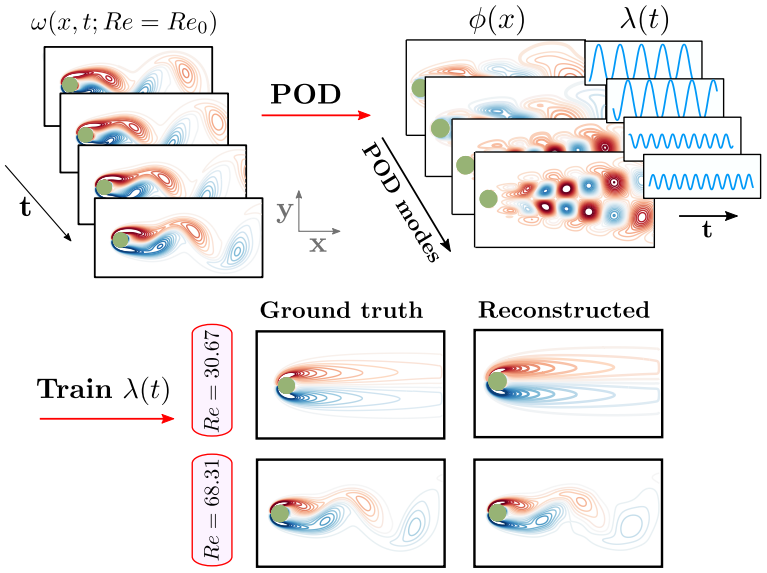

Figure 5.5: Training the normal form autoencoder over POD data generated from fluid flow past a cylinder. First, Eq. 5.9 is solved using 250 initial conditions (ω, Re) generated across the vortex shedding instability [319]. Then proper orthogonal decomposition is performed to obtain spatial modes $\phi(x)$ and their temporal coefficients $\lambda(t)$, which forms a low-dimensional dynamical system, which is used to train the normal form autoencoder.

5.2.4 Fluid flow in 2D.

As a more challenging example, we simulate the fluid flow past a circular cylinder with the two-dimensional, incompressible Navier-Stokes equations:

$$\nabla \cdot \boldsymbol{u} = 0, \quad \partial_t \boldsymbol{u} + (\boldsymbol{u} \cdot \nabla)\boldsymbol{u} = -\nabla p + \frac{1}{Re}\Delta \boldsymbol{u} \tag{5.9}$$

where $\boldsymbol{u}$ is the two-component flow velocity field in 2D and $\boldsymbol{p}$ is the pressure term. For Reynold's number $Re = Re_c \approx 47$, the fluid flow past a cylinder undergoes a supercritical Hopf bifurcation, where the steady flow for $Re < Re_c$ transitions to unsteady vortex shedding [319]. The unfolding of the transition gives the celebrated Stuart-Landau ODE, which is essentially the supercritical Hopf normal form written in complex coordinates, and this has resulted in accurate and efficient reduced-order models for this system [320, 321].
The scalar vorticity field $\omega \equiv \nabla \times \boldsymbol{u}$ is useful in reducing the complexity of the problem to a single component per grid point. The Hopf bifurcation persists in the vorticity field, and we use the vorticity field to construct datasets. Datasets are generated over a 2D spatial grid of 487×250 points across the domain $[-2, 10] \times [-3, 3]$. The discretization results in 121750 grid points, illustrating the aforementioned curse of dimensionality. This is mitigated by restricting the dataset to a lower dimension using proper orthogonal decomposition [297].

The normal form autoencoder provides a fundamentally different approach to characterizing the low-dimensional dynamics than Galerkin projection of the governing equations onto POD modes [320, 321, 302]. First, Eq. 5.9 is solved and the vorticity field $\omega(t, x)$ is computed. The reduced-order dynamical system $\lambda(t)$ is derived from the method of snapshots. Here, $\lambda \in \mathbb{R}^4$. This dynamical system characterizes the temporal evolution of spatial modes $\phi(x)$, that are kept aside. An example of spatial modes $\phi(x)$ and their temporal coefficients $\lambda(t)$ are presented in Fig. 5.5. The temporal coefficients $\lambda(t)$ are then used to train the neural networks. The training dataset is generated from 250 initial conditions (ω, Re). The learned coordinates (z, β) show agreement with the Hopf normal form dynamics (not shown). Further, the spatial modes $\phi(x)$ are used to project the learned coordinates (z, β) back to the vorticity field ω using the relation $\hat{\omega} \approx \bar{\omega} + \sum_j \phi_j(x)(\psi_1 \varphi_1 \lambda_j(t))$, where $\bar{\omega}$ is the time-averaged solution. The reconstructed vorticity field $\hat{\omega}$ shows remarkable agreement with ground truth for cases on either side of the bifurcation, demonstrating good agreement of the learned ψ_1 with the inverse of the encoder φ_1.

5.3 Conclusion

We demonstrated how to use deep learning to discover a coordinate transformation in which dynamics can be directly characterized in terms of universal normal form descriptions. Such embeddings of parameter-dependent dynamics automate many of the theoretical constructions used to characterize spatio-temporal pattern forming systems [294]. Indeed, the architecture leverages the vast body of knowledge concerning the small number of canonical instabilities that emerge in diverse models of physics, biology, and engineering. Our approach is currently limited by the vast state-parameter space required to be sampled to learn the whole phase space properly. Moreover, the approach currently requires a priori knowledge of the observed bifurcation, and this can perhaps be remedied with an offline detection step in the dataset. Model discovery techniques like SINDy [157] can then be leveraged to identify a bifurcation based on a library of normal forms.

Our approach has consequences for dynamical systems theory and data-driven model discovery alike. The approach can be extended to discover underlying low-dimensional, reduced-order models and center-manifold reductions using normal forms as the fundamental building blocks. Moreover, the method makes use of theoretical guarantees that allow such embeddings to exist. The flexibility of the autoencoder provides a modeling framework for finding the required coordinate transformations to the low-rank, universal unfolding of the dynamics.

All of the code used to produce the results presented in this chapter is available publicly on GitHub at:
`github.com/dynamicslab/NormalFormAE`.

5.4 Appendix

This appendix describes the data acquisition, preprocessing and neural network training for the normal form autoencoder approach.

Data acquisition for training

For each of the examples, datasets $\boldsymbol{U}, \dot{\boldsymbol{U}}$ and $\boldsymbol{\alpha}$ are constructed, which serve as inputs to the neural networks. These datasets are obtained by solving the corresponding governing equation. In this chapter, the governing equation is characterized by a parameterized, smooth, autonomous differential equation

$$\dot{u} = f(u, x; \alpha),\ u \in \mathbb{R}^n, n \geq 1. \tag{5.10}$$

The solution $\boldsymbol{u} \equiv [u(x_1, t), \ldots, u(x_N, t)]^T$ is defined on a finite spatiotemporal grid (x, t) using the initial value $(\boldsymbol{u}_0, \alpha_0)$. The datasets $\boldsymbol{U}, \dot{\boldsymbol{U}}$ and $\boldsymbol{\alpha}$ are constructed by concatenating several solutions $\boldsymbol{u}$ for a collection of initial values $(\boldsymbol{u}_0, \alpha_0)$. First, we define datasets

$$\begin{aligned}
\boldsymbol{U}^{(j)} \equiv \boldsymbol{U}(\alpha = \alpha^{(j)}) &= \begin{bmatrix} | & & | \\ \boldsymbol{u}_0^{(j)} & \ldots & \boldsymbol{u}_{t_f}^{(j)} \\ | & & | \end{bmatrix}, \\
\dot{\boldsymbol{U}}^{(j)} \equiv \dot{\boldsymbol{U}}(\alpha = \alpha^{(j)}) &= \begin{bmatrix} | & & | \\ \boldsymbol{f}(\boldsymbol{u}_0^{(j)}; \alpha^{(j)}) & \ldots & \boldsymbol{f}(\boldsymbol{u}_{t_f}^{(j)}; \alpha^{(j)}) \\ | & & | \end{bmatrix},
\end{aligned} \tag{5.11}$$

where t_f denotes the final time point. The function $\boldsymbol{f}(\boldsymbol{u}; \alpha)$ is defined by vectorizing f over the discrete spatial grid x,

$$\boldsymbol{f}(\boldsymbol{u}; \alpha) = \begin{bmatrix} | \\ f(\boldsymbol{u}, x_j) \\ | \end{bmatrix}. \tag{5.12}$$

The solution $\boldsymbol{U}^{(j)}$ may contain transients to the steady state solution, which are removed. Trimming off transients allows sampling of trajectories closer to steady state solutions, resulting in better conformity to normal form dynamics.

Next, N initial conditions $(\boldsymbol{u}_0^{(j)}, \alpha^{(j)})$ are stacked together to get the datasets $\boldsymbol{U}, \dot{\boldsymbol{U}}$ and $\boldsymbol{\alpha}$,

$$\boldsymbol{U} = \begin{bmatrix} \boldsymbol{U}^{(0)} & \ldots & \boldsymbol{U}^{(N)} \end{bmatrix}, \dot{\boldsymbol{U}} = \begin{bmatrix} \dot{\boldsymbol{U}}^{(0)} & \ldots & \dot{\boldsymbol{U}}^{(N)} \end{bmatrix} \text{ and } \boldsymbol{\alpha} = \begin{bmatrix} \alpha_0 & \ldots & \alpha_N \end{bmatrix} \tag{5.13}$$

Datasets

$$\begin{aligned}
\boldsymbol{X}_{train} &= \{\boldsymbol{U}^{(train)}, \dot{\boldsymbol{U}}^{(train)}, \alpha^{(train)}\}, \\
\boldsymbol{X}_{test} &= \{\boldsymbol{U}^{(test)}, \dot{\boldsymbol{U}}^{(test)}, \alpha^{(test)}\},
\end{aligned}$$

are constructed for training and validation, respectively. The results presented in the main manuscript are performed over validation sets for each example.

Choosing initial values $(\boldsymbol{u}_0, \alpha_0)$

The initial condition $(\boldsymbol{u}_0, \alpha_0)$ is sampled from a uniform distribution $\mathcal{U}$ based on the domain $[-1, 1]$ such that points from either side of the bifurcation parameter α_c are uniformly sampled. First, parameters σ_u and σ_α are fixed, such that

$$\begin{aligned} \boldsymbol{u}_0 &= \boldsymbol{u}_c + \sigma_u \mathcal{U}[-1, 1], \\ \alpha_0 &= \alpha_c + \sigma_\alpha \mathcal{U}[-1, 1] \end{aligned} \tag{5.14}$$

where $\boldsymbol{u} = \boldsymbol{u}_c$ is the steady state (equilibrium) at which the bifurcation occurs.

Training

The neural networks $\varphi_{1,2}, \psi_{1,2}$ are fully connected neural networks with a single activation function active in the hidden layers only. In this chapter, we use the hyperbolic tangent (tanh, for all Hopf examples) and exponential linear unit (elu, for scalar ODE examples) functions as activation, as they allow for the transformed data to be smoothly equivalent to the original dataset. This choice makes the corresponding encoder and decoder smooth. After training, $\psi \circ \varphi \approx I$, which makes φ approximately a diffeomorphism. Using center manifold theory [4], we thus obtain the existence of feasible solutions to the neural network problem.

The input to the normal form autoencoder is the set $\boldsymbol{X}_{train}$, as introduced earlier. In the latent space, we get

$$\begin{aligned} \boldsymbol{Z} &= \varphi_1 \boldsymbol{U}, \\ \boldsymbol{\beta} &= \varphi_2 \boldsymbol{\alpha}, \end{aligned} \tag{5.15}$$

where we drop the subscript $(train)$ for notational convenience. Passing the two latent variables through the decoder gives

$$\begin{aligned} \hat{\boldsymbol{U}} &= \psi_1 \boldsymbol{z}, \\ \hat{\boldsymbol{\alpha}} &= \psi_2 \boldsymbol{\beta}. \end{aligned} \tag{5.16}$$

We also compute $\dot{\hat{\boldsymbol{U}}}$ and $\dot{\boldsymbol{z}}$ in order to compute the consistency loss terms. This is done via the chain rule as follows

$$\begin{aligned} \dot{\boldsymbol{z}} &= \frac{\mathrm{d}}{\mathrm{d}x}(\varphi_1 \boldsymbol{U}) \\ &= (\nabla_{\boldsymbol{u}} \varphi_1) \dot{\boldsymbol{U}}. \end{aligned}$$

In order to compute $\dot{\hat{\boldsymbol{U}}}$, we first compute the time-derivative estimate of the latent variable, $\dot{\hat{\boldsymbol{z}}}$ which is given by

$$\dot{\hat{\boldsymbol{z}}} = g(\boldsymbol{z}, \boldsymbol{\beta}).$$

This gives $\dot{\hat{\boldsymbol{U}}}$ via the relation

$$\dot{\hat{\boldsymbol{U}}} = (\nabla_{\boldsymbol{z}} \psi_1)\dot{\hat{\boldsymbol{z}}}. \tag{5.17}$$

The loss function $\mathcal{L}$ is thus given by,

$$\mathcal{L} = \sum_j \mathcal{L}_j \tag{5.18}$$

where,

$$\begin{aligned}
\mathcal{L}_1 &= \lambda_1 \frac{1}{N t_f} \sum_k \|\boldsymbol{u}_k - \hat{\boldsymbol{u}}_k\|_2^2 = \lambda_1 \frac{1}{N t_f} \sum_k \|\boldsymbol{u}_k - \psi_1 \varphi_1 \boldsymbol{u}_k\|_2^2, \\
\mathcal{L}_2 &= \lambda_2 \frac{1}{N t_f} \sum_k \|\boldsymbol{\alpha}_k - \hat{\boldsymbol{\alpha}}_k\|_2^2 = \lambda_2 \frac{1}{N t_f} \sum_k \|\boldsymbol{\alpha}_k - \psi_2 \varphi_2 \boldsymbol{\alpha}_k\|_2^2, \\
\mathcal{L}_3 &= \lambda_3 \frac{1}{N t_f} \sum_k \|\dot{\hat{\boldsymbol{z}}}_k - \dot{\boldsymbol{z}}_k\|_2^2 = \lambda_3 \frac{1}{N t_f} \sum_k \|(\nabla_{\boldsymbol{u}} \varphi_1)\dot{u}_k - g(\varphi_1 \boldsymbol{u}_k, \varphi_2 \boldsymbol{\alpha}_k)\|_2^2, \\
\mathcal{L}_4 &= \lambda_4 \frac{1}{N t_f} \sum_k \|\dot{\hat{\boldsymbol{u}}}_k - \dot{\boldsymbol{u}}_k\|_2^2 = \lambda_4 \frac{1}{N t_f} \sum_k \|\dot{u}_k - (\nabla_{\boldsymbol{u}} \varphi_2) g(\varphi_1 \boldsymbol{u}_k, \varphi_2 \boldsymbol{\alpha}_k)\|_2^2, \\
\mathcal{L}_5 &= \lambda_5 \frac{1}{N} \left\| \frac{1}{t_f} \sum_k \boldsymbol{u}_k \right\|_1 = \lambda_5 \frac{1}{N} \|\mathbb{E}_t \boldsymbol{U}\|_1, \\
\mathcal{L}_6 &= \lambda_6 \frac{1}{N t_f} \|\mathrm{sgn}\alpha - \mathrm{sgn}\beta\|_1 = \lambda_6 \frac{1}{N t_f} \|\mathrm{sgn}\alpha - \mathrm{sgn}(\varphi_1 \alpha)\|_1.
\end{aligned}$$

Once the loss function is computed, the set of neural network parameters Θ, comprising both autoencoders, are simultaneously trained using the ADAM optimizer [322] with learning rate η, whose value depends on the example. For all examples, the `Flux.jl` package in the Julia language is used to train the neural networks. All code is available online at `github.com/dynamicslab/NormalFormAE`. For visualization, the latent dynamics $\boldsymbol{z}$ are plotted for all samples in the validation dataset. Using a uniform distribution of initial conditions centered around $(\boldsymbol{z}_0, \beta) = (\varphi_1 \boldsymbol{u}_0, \alpha)$, an ensemble of simulations of the normal form are generated and plotted in the background. The neural networks are trained repeatedly over the batches of data generated (called epochs) till the fit to the simulations in the latent space stabilizes.

Orientation loss terms $\mathcal{L}_{5,6}$

The loss terms $\mathcal{L}_{5,6}$ ensure that the latent variables $(\boldsymbol{z}, \beta)$ are properly oriented with respect to the normal form, and are hence called *orientation loss* terms.

Generically, the state variables in normal forms are scaled such that the bifurcation occurs at $(z, \beta) = (0, 0)$. Loss term $\mathcal{L}_5$ ensures that the time average of the latent space of a simulation is constrained to 0. This is pertinent specifically to the supercritical Hopf normal form, where the stable equilibrium for $\beta < 0$ is at $z = 0$, and the stable periodic orbit for $\beta > 0$ is centered around the now unstable equilibrium $z = 0$. The loss term $\mathcal{L}_6$ ensures that the direction of the bifurcation in the latent space is consistent with that of the normal form.

Choice of regularization constants λ_i

The choice of regularization parameters λ_j depends on the example in consideration. They remain fixed for the entire training procedure. However, parameters λ_3 and λ_4 are the most sensitive and generally require testing by training the architecture for short epochs before making a final choice. The parameter λ_3 controls the fit of the latent space to the normal form, while the parameter λ_4 makes sure that the reconstructed data $\hat{\boldsymbol{u}}$ fits up to the first-order time derivative. For large values of these two parameters, the training procedure prioritizes the latent space fit, which in practice results in the latent variables converging to the solution $\boldsymbol{z} = 0$. On the other hand, for very small values of λ_3 and λ_4, the latent space does not match well with the normal form simulations. As a rule of thumb, we choose $\lambda_{3,4}$ such that the corresponding loss terms $\mathcal{L}_{3,4}$ are a factor 10^{-2} of the autoencoder loss term $\mathcal{L}_1$. This choice prioritizes the term $\mathcal{L}_1$ slightly more, as done in [26], which is beneficial as the autoencoder fit for (φ_1, ψ_1) is typically the slowest moving loss term during training iterations. For large values of λ_5, the solution $\boldsymbol{z} = 0, \dot{\boldsymbol{z}} = 0$ is prioritized. In order to avoid this, λ_5 is kept low.

Scaling time with τ

this chapter deals with projecting dynamics $\boldsymbol{u}$ onto a low dimensional manifold such that the dynamics $\boldsymbol{u}$ on such a manifold obey a specific normal form equation. However, this introduces a time scale problem when dealing with finite time trajectories $\boldsymbol{u}$. Let us assume that data $\boldsymbol{U}$ corresponds to a Hopf bifurcation. For $\alpha > 0$ close to α_c, the period of the resulting periodic orbit is $T_\alpha \approx 2\pi/\omega_u$, where ω_u is the imaginary part of the center eigenvalue of the linearization of the dynamical system $\dot{u} = f$, at the α_c. Any diffeomorphism of such a signal will preserve the period if the periodic orbit persists. Thus the corresponding latent variable $\boldsymbol{Z}$ would also have period T_α. However, the period T_β corresponding to the Hopf normal form for $\beta = \varphi_2\alpha$ would be different, as $\omega_z \neq \omega_u$. Thus, we introduce a time scaling parameter τ to mitigate the difference in the period. This is done by introducing a new time t^* such that,

$$t^* = \tau^2 t, \tag{5.19}$$

which gives a scaled normal form equation

$$\frac{\mathrm{d}}{\mathrm{d}t^*}z = \frac{1}{\tau^2}g(z,\beta). \tag{5.20}$$

The time scaling parameter τ is included in the neural network parameter set Θ and learnt simultaneously. However, for the supercritical Hopf bifurcation examples, τ can be approximated theoretically and thus does not need to be trained. The value of τ is set to

$$\tau = \sqrt{T_\alpha / T_\beta}, \tag{5.21}$$

where T_α and T_β are estimates of the period approximated from data $\boldsymbol{U}$ and Hopf normal form simulations, respectively, for parameters close to the bifurcation value. These estimates are readily made using Fourier transforms of the simulated time traces after removing transients to the periodic steady state.

Data generation	
Normal Form	Hopf
u_c	$u = \alpha$
α_c	0.84975
σ_u	0.1
σ_α	0.5
Time domain	$[0, 80]$
Space domain	$[-32, 32]$, 64 points
t_{size}	500
Training set size	1000
Test set size	20
Trim	First 200 points

Training parameters	
λ_1	1
λ_2	10^{-2}
λ_3	10^{-3}
λ_4	10^{-3}
λ_5	0
λ_6	10^{-1}
Batchsize	100
$\boldsymbol{U}_{batch}$ dimension	64×30000
$\boldsymbol{Z}_{batch}$ dimension	2×30000
φ_1 hidden layers	[32,16]
ψ_1 hidden layers	[16,32]
φ_2 hidden layers	[16,16]
ψ_2 hidden layers	[16,16]
τ	0.825
η_{ADAM}	10^{-4}
Epochs	1000

Table 5.1: Data generation and training parameters for the Lorenz96 example.

Demonstrated systems

This section elaborates on the systems that were used to demonstrate the normal form autoencoder approach in the main manuscript and provides explicit training and validation details.

1D model

The scalar ODE explored is a toy model constructed to include all the major scalar bifurcations: saddle-node, pitchfork and transcritical. Data $\boldsymbol{X}_{train}$ is

Data generation	
Normal Form	Hopf
u_c	Not analytical
α_c	0.8040
σ_u	0.1
σ_α	0.5
Time domain	$[0, 100]$
Space domain	$[-6, 6]$, 64 points
t_{size}	250
Training set size	1000
Test set size	20
Trim	First 50 points

Training parameters	
λ_1	1
λ_2	10^{-2}
λ_3	10^{-4}
λ_4	0
λ_5	10^{-3}
λ_6	0
Batchsize	250
$\boldsymbol{U}_{batch}$ dimension	128×50000
$\boldsymbol{Z}_{batch}$ dimension	2×50000
φ_1 hidden layers	[64,32]
ψ_1 hidden layers	[32,64]
φ_2 hidden layers	[16,16]
ψ_2 hidden layers	[16,16]
τ	1.4
η_{ADAM}	10^{-4}
Epochs	2000

Table 5.2: Data generation and training parameters for the Neural Field example. As the critical equilibrium point is not analytical, this is computed by allowing the simulation to stabilize after $t \gg 1$.

Data generation	
Normal Form	Hopf
u_c	Not analytical
Re_c	44.6
σ_u	10^{-2}
Re domain	$[30, 70]$, 240 points
Time domain	$[0, 77]$
Space domain	$[-2, 10] \times [-3, 3]$, 487×250 points
t_{size}	6180
Training set size	220
Test set size	20
Trim	First 3250 points

Training parameters	
λ_1	1
λ_2	1
λ_3	10^{-4}
λ_4	10^{-4}
λ_5	0
λ_6	10^{-1}
Batchsize	110
$\boldsymbol{U}_{batch}$ dimension	4×32230
$\boldsymbol{Z}_{batch}$ dimension	2×32230
φ_1 hidden layers	[20,20,30]
ψ_1 hidden layers	[20,20,20]
φ_2 hidden layers	[10,10]
ψ_2 hidden layers	[10,10]
τ	0.6
η_{ADAM}	10^{-3}
Epochs	2700

Table 5.3: Data generation and training parameters for the Navier Stokes example.

collected from the vicinity of each of the bifurcation points and used to train the normal form autoencoder separately for each bifurcation scenario. The system is given by

$$\dot{u} = \gamma u(\alpha - \alpha_{pf} - u^2)(\alpha - \alpha_{sn} + (u - u_{sn})^2), u \in \mathbb{R}, \tag{5.22}$$

where $\gamma = 0.01$, $x_{sn} = \alpha_{sn} = -6$ and $\alpha_{pf} = 6$. The three bifurcations occur at:

- saddle-node: $(u, \alpha) = (u_{sn}, \alpha_{sn})$
- Pitchfork: $(u, \alpha) = (0, \alpha_{pf})$
- Transcritical: $(u, \alpha) = (0, \alpha_{sn} - u_{sn}^2)$

Before constructing the dataset $\boldsymbol{X}$, the system (5.22) is first translated such that the bifurcation in consideration occurs at $(u, \alpha) = (0, 0)$. For example, in the case of the pitchfork bifurcation, the translation $(u, \alpha) \mapsto (u, \alpha + \alpha_{pf})$ results in the new system,

$$\dot{u} = \gamma u(\alpha - u^2)(\alpha + \alpha_{pf} - \alpha_{sn} + (u - u_{sn})^2). \tag{5.23}$$

The third term in the above equation is positive for sufficiently small $|\alpha|$. Thus, equation (5.23) is smoothly equivalent to the pitchfork normal form $\dot{u} = u(\alpha - u^2)$ [4]. Smooth equivalence preserves orbits and the direction of time, but not the speed. We observe that the pitchfork normal form is scaled by a positive function $h(u, \alpha)$ given by,

$$h(u, \alpha) = \gamma(\alpha + \alpha_{pf} - \alpha_{sn} + (u - u_{sn})^2). \tag{5.24}$$

Thus,

$$\begin{aligned}
\dot{u} &= \gamma u(\alpha - u^2)(\alpha + \alpha_{pf} - \alpha_{sn} + (u - u_{sn})^2) \\
&= h(u, \alpha)u(\alpha - u^2) \\
&\approx \frac{1}{\tau^2} u(\alpha - u^2),\ \tau \neq 0 \text{ for } |u|, |\alpha| \text{ sufficiently small.}
\end{aligned}$$

This parameter τ is precisely the time scaling parameter introduced before, which we learn simultaneously with the neural network parameters while training. It can be shown for all other bifurcation scenarios that such a scaling would be necessary, and thus we learn the parameter τ for each case individually. Training results are shown in Fig. 5.6

Lorenz96

The Lorenz96 system [317, 316] is given by,

$$\dot{u}_j = -u_{j-1}(u_{j-2} - u_{j+1}) - u_j + \alpha,\ u \in \mathbb{R}^n, \tag{5.25}$$

for $j = 1, 2 \ldots n$ with boundary conditions $u_1 = u_n$ and $u_2 = u_{n-1}$. In this chapter, $n = 64$, for which a supercritical Hopf bifurcation occurs at the trivial

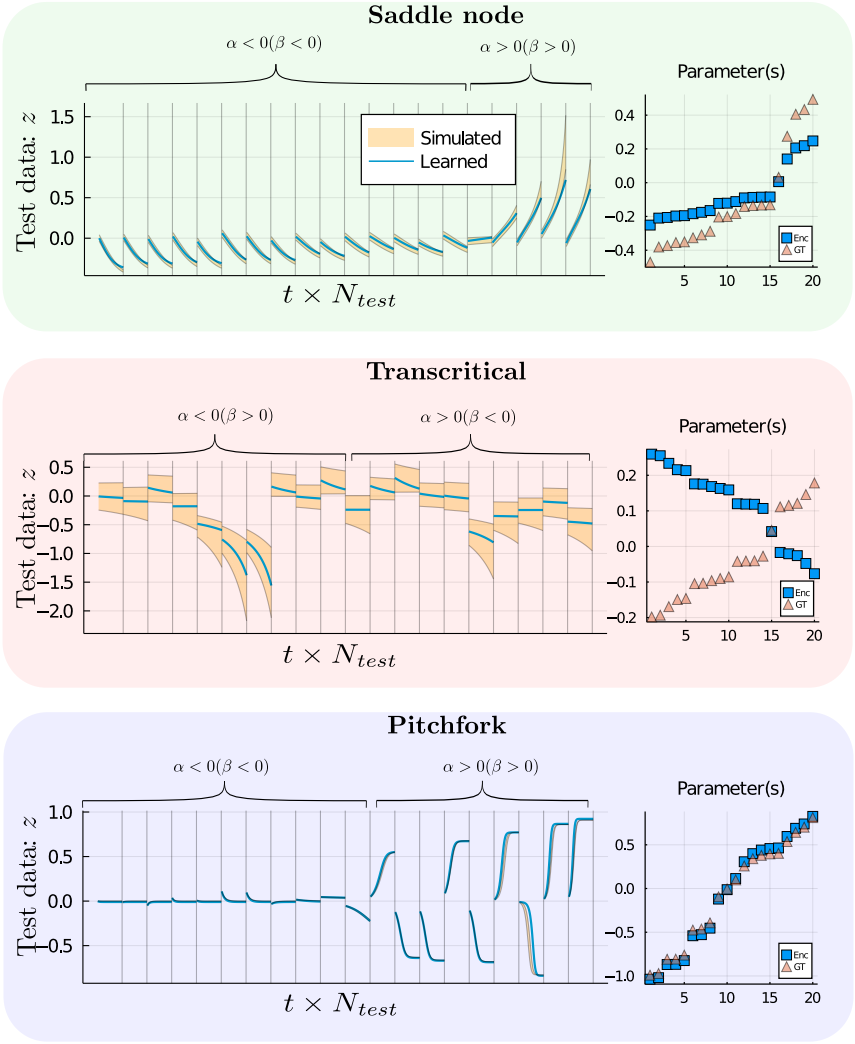

Figure 5.6: Validation results post-training for the scalar ODE example. The learned normal form coordinates computed via the formula $z = \varphi_1(\boldsymbol{U})$ is plotted against time t (in blue) for several simulations $N_{test} = 20$ in the validation set (test data). The different simulations are separated from each other by a vertical gray line. The simulation of the respective normal form is plotted in the background in yellow, which represents an ensemble of 20 trajectories with initial values chosen from a uniform distribution around the first time point $\varphi_1 \boldsymbol{u}_0$ and parameter $\beta = \varphi_2 \alpha$. For each example the corresponding ground truth parameters (α, in blue) and learned parameters (β, in orange) are also shown. Note that the parameter signs for the transcritical bifurcation are flipped as the direction of the bifurcation is in the reverse direction with respect to the normal form. For the transcritical case, the orientation term λ_6 is kept 0.

equilibrium $\boldsymbol{u} = \alpha$, for $\alpha = 0.84975$. As done in the previous section, the system is translated such that the bifurcation occurs at the origin. Moreover, for all choice of parameter α, it is made sure that the equilibrium occurs at the origin $\boldsymbol{u} = 0$. This is done via the translation $(\boldsymbol{u}, \alpha) \mapsto (\boldsymbol{u} + \alpha, \alpha + \alpha_c)$, where α_c is the bifurcation point $\alpha = 0.84975$.

The system is solved with 1000 initial conditions $(\boldsymbol{u}, \alpha)$ over a temporal domain $[0, 80]$, with 500 time points per simulation. The transients to the travelling wave pattern state are removed by neglecting the first 200 points of the simulation. The training set $\boldsymbol{X}_{train}$ thus comprises of 1000 simulations, giving rise to 3×10^5 training samples. For each training iteration, a batch of 100 simulations is used, giving rise to 10 training iterations per epoch. The system is trained for 1000 epochs or 10^4 training iterations.

Neural Field

The neural field equations [120, 119] are a system of integrodifferental equations that describe the dynamics of electrical activity in spatially continuous neural tissue. In this chapter, we consider a specific formulation of neural field equations with an input inhomogeneity that manifests in a Hopf bifurcation of a stationary pattern leading to breathers when varying the input strength [318, 310]. The governing equations are

$$\dot{u} = -u - \kappa a + (w * f(u)) + I(x), \quad \dot{a} = (u - a)/\tau_{nf}. \tag{5.26}$$

Here again, we translate the system such that the equilibrium and the bifurcation point both occur at the origin. However, in contrast to the Lorenz96 example, an analytical expression for the bifurcating equilibrium is absent. This is approximated from data. First, the parameter is translated to the bifurcation point $\alpha \mapsto \alpha + \alpha_c$, where $\alpha_c = 0.804$ is the bifurcation point. The system is then solved for several initial conditions $(\boldsymbol{u}, \alpha)$. Next, for $\alpha < 0$, the last point $\boldsymbol{u}_{t_f}$ of the simulation to be the equilibrium $\boldsymbol{u}_{eq}$ and for $\alpha > 0$, the time average of the simulation $\mathbb{E}_t \boldsymbol{U}^{(j)}$, after ignoring transients, is chosen as the equilibrium $\boldsymbol{u}_{eq}$. Then the translation $\boldsymbol{u} \mapsto \boldsymbol{u} + \boldsymbol{u}_{eq}$ is performed.

The system is solved with 1000 initial conditions $(\boldsymbol{u}, \alpha)$ over a temporal domain $[0, 100]$ with 250 time points per simulation. The first 50 points correspond to transients to the periodic breather solution and are removed. The training set thus comprises of 1000 simulations, giving rise to 2×10^5 training samples. A validation set of 20 simulations is constructed separately. A batch of 250 simulations is used for each training iteration, giving rise to 2 training iterations per epoch. The system is then trained for 2000 epochs on the training set, or 4000 training iterations. Training results for both Neural field and Lorenz96 cases are shown in Fig. 5.7.

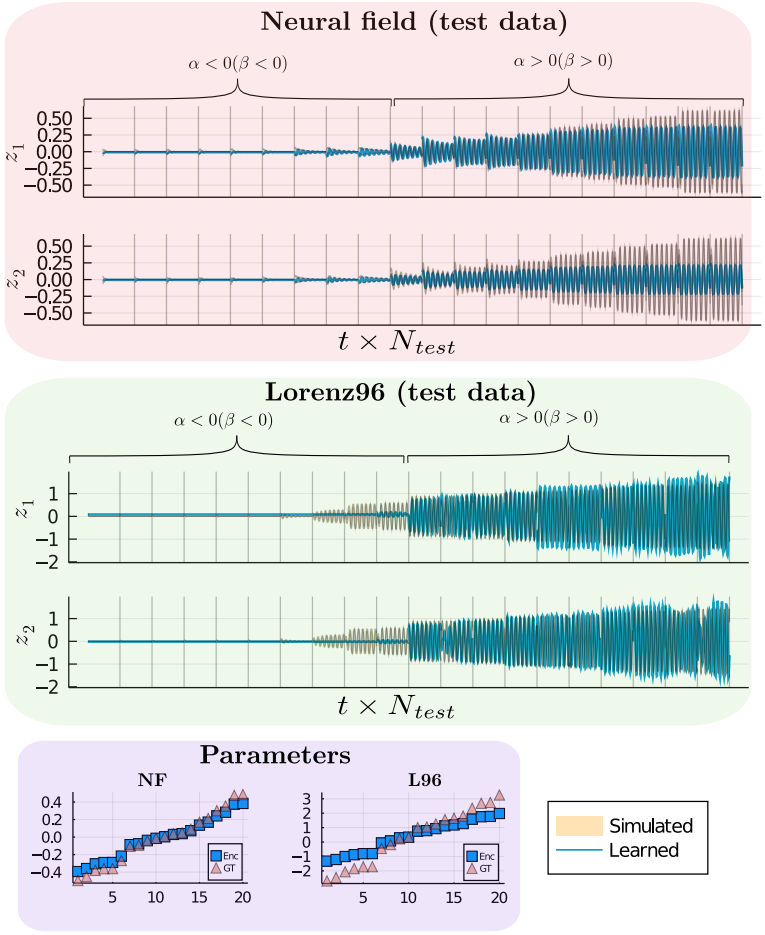

Figure 5.7: Validation results post-training for the neural field and Lorenz96 examples. The learned normal form coordinates computed via the formula $\boldsymbol{z} = \varphi_1(\boldsymbol{U})$ is plotted against time t (in blue) for several simulations $N_{test} = 20$ in the validation set (test data). The different simulations are separated from each other by a vertical gray line. The simulation of the respective normal form is plotted in the background in yellow, which represents an ensemble of 20 trajectories with initial values chosen from a uniform distribution around the first time point $\varphi_1 \boldsymbol{u}_0$ and parameter $\beta = \varphi_2 \alpha$. For each example the corresponding ground truth parameters (α, in blue) and learned parameters (β, in orange) are also shown. Note that the bifurcation parameter α_c is translated to 0 prior to training. In the Neural field example, the square root effect of the Hopf amplitude fades away for large $\alpha > 0$, possibly due to the original parameter α being far from the bifurcation point.

Fluid flow past a cylinder (Navier Stokes)

The final example leverages the model decomposition technique proper orthogonal decomposition (POD) on a high dimensional dataset of fluid flow past a cylinder constructed by solving the Navier Stokes PDE on a 2D domain, to obtain a reduced order dataset on which the normal form autoencoder is trained. The PDE is given by,

$$\nabla \cdot \boldsymbol{u} = 0, \quad \partial_t \boldsymbol{u} + (\boldsymbol{u} \cdot \nabla)\boldsymbol{u} = -\nabla p + \frac{1}{Re}\Delta \boldsymbol{u}, \tag{5.27}$$

where $\boldsymbol{u}$ is the two-component flow velocity field in 2D and $\boldsymbol{p}$ is the pressure term. For Reynold's number $Re = Re_c \approx 47$, the fluid flow past a cylinder undergoes a supercritical Hopf bifurcation, where the steady flow for $Re < Re_c$ transitions to unsteady vortex shedding [319]. We analyse the one component vorticity field $\boldsymbol{w}$ for the remainder of the chapter, given by,

$$\boldsymbol{w} = \nabla \times \boldsymbol{u}. \tag{5.28}$$

The training set is formulated in three steps:

- Simulate system (5.27) for several initial conditions $(\boldsymbol{u}, Re)$ and generate dataset $\boldsymbol{U}^{(j)}, j = 1, 2, \ldots$ and compute vorticity $\boldsymbol{W}$.
- For each simulation, obtain a reduced order dataset $\boldsymbol{\Lambda}$ by projecting the solution $\boldsymbol{U}^{(j)}$ onto finitely many POD modes.
- Perform a linear transformation of $\boldsymbol{\Lambda}$ to 'mix' the ordered set of harmonics $\boldsymbol{\Lambda}$.

Simulation. The Navier-Stokes PDE is solved for 250 initial values $(\boldsymbol{u}, Re)$ centered around the critical point $Re_c \approx 44.6$ on the spatial domain $x \times y = [-2, 10] \times [-3, 3]$ with 487×250 spatial grid points. The choice for $\Delta x, \Delta y$ and Δt is made by using the cell Reynold's number of 1.3 for $Re = 80$, and calculating the appropriate CFL condition after setting Δt. The temporal domain is $[0, 77]$ comprising of 6180 time steps per simulation. The cylinder is represented as a circle centered at $(x, y) = (-1, 1)$ with diameter 1. Equation (5.27) is solved in voriticity form using the immersed boundary projection method [304] which is implemented in the Julia package `ViscousFlow.jl`. This procedure gives us the dataset $\boldsymbol{W}^{(j)}$.

Projection onto POD modes. Proper orthogonal decomposition is a model decomposition technique that constructs a set of spatial basis functions in descending energy, from which a reduced order dataset can be created by projecting only onto a few high-energy modes [323]. Thus, a solution $\boldsymbol{w}(\boldsymbol{x}, t)$ is written as a Galerkin projection onto POD modes $\boldsymbol{\phi}(\boldsymbol{x})$ and their evolving temporal coefficients $\boldsymbol{\lambda}(t)$ as follows,

$$\boldsymbol{w}(\boldsymbol{x}, t) = \bar{\boldsymbol{w}} + \sum_k \sigma_k \boldsymbol{\phi}(\boldsymbol{x})_k \lambda_k(t), \tag{5.29}$$

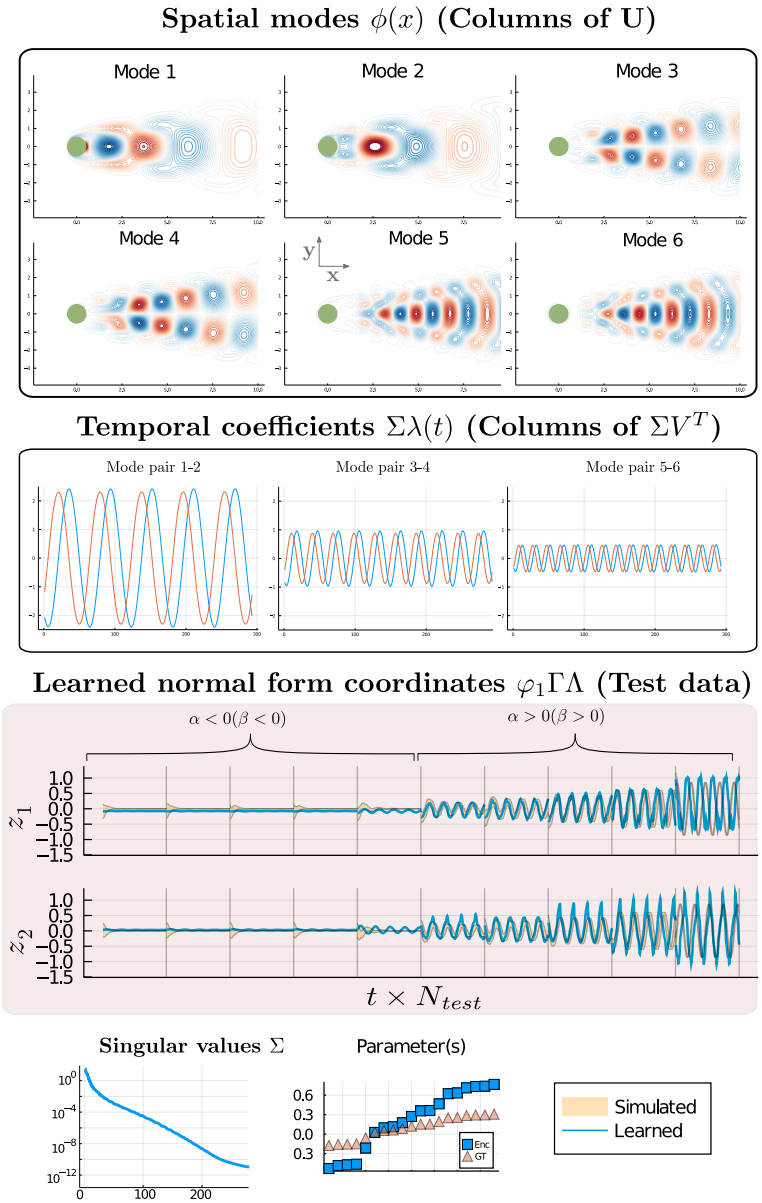

Figure 5.8: POD calculations and validation results post-training for the fluid flow example (Navier Stokes). In the top two rows, the POD spatial modes and their temporal coefficients are shown, as computed via SVD. Next, the learned normal form coordinates computed via the formula $\boldsymbol{z} = \varphi_1(\boldsymbol{\Gamma\Lambda})$ is plotted against time t (in blue) for several simulations $N_{test} = 10$ in the validation set (test data). The different simulations are separated from each other by a vertical gray line. The simulation of the respective normal form is plotted in the background in yellow, which represents an ensemble of 20 trajectories with initial values chosen from a uniform distribution around the first time point $\varphi_1 \boldsymbol{u}_0$ and parameter $\beta = \varphi_2 \alpha$. The corresponding ground truth parameters (α, in blue) and learned parameters (β, in orange) are also shown.

where $\bar{w}$ represents the mean flow $\mathbb{E}_t \boldsymbol{W}$. The coefficients σ_k form a descending sequence of singular values. In practice, the spatial modes are computed using the 'method of snapshots' [324] implemented by singular value decomposition (SVD). Thus, for a simulation $\boldsymbol{W}^{(j)}$, SVD yields unitary matrices U, V and a diagonal matrix Σ such that

$$\boldsymbol{W}^{(j)} = U\Sigma V^T. \tag{5.30}$$

The columns of matrix U represent the spatial modes, for which the columns of V give the temporally evolving coefficients. The matrix Σ is composed of t_f singular values in descending sequence, which is significantly smaller than the state space dimension (121750). Choosing the first m singular values generates an approximate reduced order model,

$$\boldsymbol{W}^{(j)} \approx U_m \Sigma_m V_m^T, \tag{5.31}$$

where U_m and V_m are truncated matrices composed of the first m columns of U and V, respectively. We work with $m = 4$, which gives a reduced-order model V of dimension 4. The SVD is performed in four steps:

- First the transients to the vortex shedding solution or the planar flow solution are trimmed off the first 3250 points.
- Next, the mean flow of the trimmed solution is computed and subtracted from the simulation.
- Finally, POD is permed via the method of snapshots, but on a dilated temporal scale, using $\Delta t \mapsto 10\Delta t$, as done in [325]. This yields matrices U, V and Σ, where V has dimension 293×293.
- The truncation above is performed on the matrices obtained via SVD, to obtain the dynamical system V with dimension 4×293.

The reduced order dynamical system $\boldsymbol{\Lambda}^{(j)}$ is then given by

$$\boldsymbol{\Lambda}^{(j)} = \Sigma_m^{(j)} (V^{(j)})^T, \tag{5.32}$$

where the superscript (j) indicates index of a specific simulation.

Linear transformation of $\boldsymbol{\Lambda}$. The resulting dynamical system Λ is composed of rows of pairwise harmonics that increase in frequency and decrease in amplitude for an increasing number of rows. Following suggestions from [320] on constraining Galerkin models to the Stuart-Landau expression (Hopf normal form), we introduce a linear transformation Γ of Λ, before training. This preserves the original frequency of the periodic orbit, but has the added disadvantage of introducing multiple timescale dynamics in the periodic orbit, which can be hard to remove in the latent space dynamics. Γ is chosen randomly, but in such a way that its condition number is close to 1. In other words,

we choose Γ to be unitary. This choice has the advantage of obtaining better reconstruction when projecting back into the original 2D space, as the higher-order harmonics in Λ are preserved. This is done by first generating a random matrix $\tilde{\Gamma}$, and obtaining Γ via SVD,

$$\tilde{\Gamma} = U\Sigma V^T,$$
$$\Gamma = UV^T.$$

In the results we show in the manuscript, this matrix Γ is given by,

$$\Gamma = \begin{bmatrix} 0.154739 & -0.523688 & 0.675546 & 0.495243 \\ 0.87244 & 0.298319 & 0.249166 & -0.29685 \\ -0.292797 & 0.785392 & 0.450626 & 0.30719 \\ 0.359894 & 0.141123 & -0.527721 & 0.756353 \end{bmatrix}. \tag{5.33}$$

Reconstruction post training. The dynamical system $\Gamma\Lambda^{(j)}$ is used for training the normal form autoencoder. The spatial modes $U_m^{(j)}$ and the mean solution $\bar{\boldsymbol{w}}^{(j)}$ are stored offline, and are used to reconstruct the full simulation $\hat{\boldsymbol{W}}^{(j)}$ via the relation

$$\hat{\boldsymbol{W}}^{(j)} = \bar{\boldsymbol{w}} + U^{(j)} \cdot \Gamma^T \hat{\boldsymbol{\Lambda}}^{(j)}, \tag{5.34}$$

where $\hat{\boldsymbol{\Lambda}}^{(j)}$ is the projection of the latent space onto the larger dimensional space via the state decoder ψ_1,

$$\hat{\boldsymbol{\Lambda}}^{(j)} = \psi_1(\varphi_1 \boldsymbol{\Gamma} \Lambda^{(j)}). \tag{5.35}$$

POD modes and their projections onto the normal form coordinates are shown in Fig. 5.8.

Chapter 6

Homoclinic saddle to saddle-focus transitions in 4D systems

M. Kalia, H.G.E. Meijer and Y.A. Kuznetsov, *Nonlinearity 32.6: 2024*, 2019.

Abstract

A saddle to saddle-focus homoclinic transition when the stable leading eigenspace is 3-dimensional (called the 3DL-bifurcation) is analyzed. Here a pair of complex eigenvalues and a real eigenvalue exchange their position relative to the imaginary axis, giving rise to a 3-dimensional stable leading eigenspace at the critical parameter values. This transition is different from the standard Belyakov bifurcation, where a double real eigenvalue splits either into a pair of complex-conjugate eigenvalues or two distinct real eigenvalues. In the wild case, we obtain sets of codimension 1 and 2 bifurcation curves and points that asymptotically approach the 3DL-bifurcation point and have a structure that differs from that of the standard Belyakov case. We give an example of this bifurcation in a perturbed Lorenz-Stenflo 4D ODE model.

6.1 Introduction

Homoclinic orbits play an important role in the analysis of ODEs depending on parameters

$$\dot{x} = F(x, \alpha), \quad x \in \mathbb{R}^n, \alpha \in \mathbb{R}^m, \tag{6.1}$$

where F is sufficiently smooth in both phase components and parameters. Orbits homoclinic to *hyperbolic equilibria* are of specific interest, as they are structurally unstable, and the corresponding parameter values generically belong to codim 1 manifolds in the parameter space $\mathbb{R}^m$. Bifurcations in generic one-parameter

families transverse to such manifolds depend crucially on the configuration of *leading eigenvalues* of the equilibrium, i.e. the stable eigenvalues with largest real part, and the unstable eigenvalues with smallest real part.

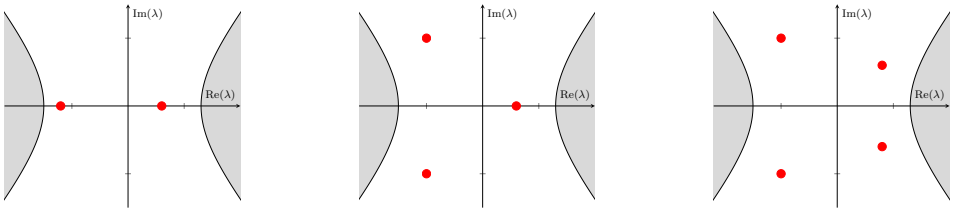

(a) Saddle (b) Saddle-focus (c) Focus-focus

Figure 6.1: Configurations of leading eigenvalues λ (red). Gray area contains all non-leading eigenvalues.

In µ 6.1, we see three configurations with simple leading eigenvalues, for which a detailed description of the bifurcations occurring near the homoclinic orbit is available (see, e.g. [326, 327, 328, 329]). For example, in the saddle case, a single periodic orbit appears generically. In the saddle-focus case, we can assume that the leading stable eigenvalues are complex by applying time-reversal if necessary. In this case, infinitely many periodic orbits exist if the *saddle quantity* σ_0, defined as the sum of the real part of the leading unstable and stable eigenvalues, is positive. This phenomenon is called *Shilnikov's homoclinic chaos* [330, 331]. On the contrary, if σ_0 is negative, then generically only one periodic orbit appears. Thus, the sign of σ_0 distinguishes *wild* and *tame* saddle-focus homoclinic cases. Note that in the wild case many other bifurcations occur nearby, including infinite sequences of fold (limit point, LP) and period-doubling (PD) bifurcations of periodic orbits, as well as secondary homoclinic bifurcations, which all accumulate on the primary homoclinic bifurcation manifold [332]. In the focus-focus case, which will not be considered in this chapter, infinitely many periodic orbits are always present.

Moving along the primary homoclinic manifold in the parameter space of (6.1), one may encounter a transition from the saddle case (a) to the saddle-focus case (b). This is a degenerate situation, and the corresponding homoclinic parameter values form generically a codim 2 sub-manifold in the parameter space. Nearby bifurcations should be studied using generic two-parameter families transverse to this codim 2 sub-manifold. We can therefore restrict ourselves to generic two-parameter ODEs ($m = 2$), where the primary homoclinic orbit exists along a smooth *homoclinic curve* in the parameter plane, while the saddle to saddle-focus transition happens at an isolated point on this curve. There are many more codim 2 homoclinic bifurcations, see [333, 328, 329].

As already noted in [333], at the simplest saddle to saddle-focus transition we

have either

(i) a *double* leading eigenvalue; or

(ii) *three simple* leading eigenvalues.

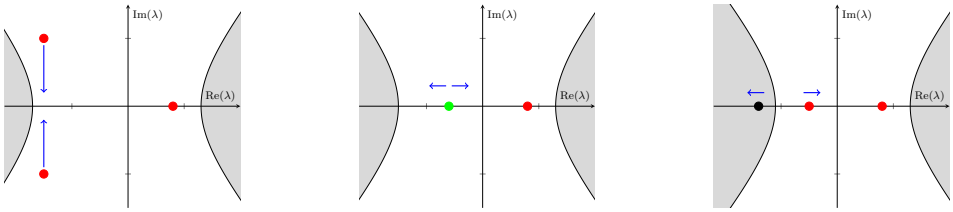

(a) $\alpha < 0$ (b) $\alpha = 0$ (c) $\alpha > 0$

Figure 6.2: Eigenvalue configurations of the saddle to saddle-focus transition in case (i); α is the parameter along the homoclinic curve and the bifurcation occurs at $\alpha = 0$. Arrows point in the direction of generic movement of eigenvalues. The green marker indicates a double real eigenvalue. The gray areas contain non-leading eigenvalues, leading eigenvalues are marked red and non-leading eigenvalues are marked black.

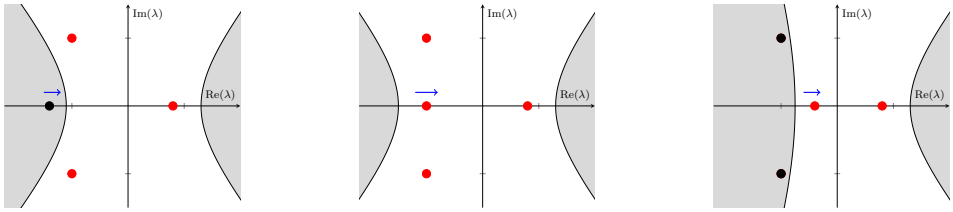

(a) $\alpha < 0$ (b) $\alpha = 0$ (c) $\alpha > 0$

Figure 6.3: Eigenvalue configurations of the saddle to saddle-focus transition in case (ii); the scalar bifurcation parameter along the homoclinic curve is α. Arrows point in the direction of possible movement of eigenvalues. There is a codimension 2 situation at $\alpha = 0$, where the leading stable eigenspace becomes 3-dimensional. Non-leading eigenvalues are contained in the gray area, leading eigenvalues are marked red and non-leading eigenvalues are marked black.

In case (i), see µ 6.2, the pair of leading complex eigenvalues approaches the real axis and splits into two distinct real eigenvalues. At the transition there is a double real eigenvalue and the leading eigenspace is two-dimensional. In case (ii), see µ 6.3, the real eigenvalue exchanges its position with the pair of complex-conjugate eigenvalues. At the transition there are two complex-conjugate eigenvalues and one real eigenvalue with the same real part. All leading eigenvalues are simple and the leading eigenspace is 3-dimensional.

Case (i) is a saddle to saddle-focus homoclinic transition that appears in various applications, e.g. in biophysics [334] and ecology [335]. Moreover, in these applications the transition corresponds to the wild case with $\sigma_0 > 0$. This

case was first studied analytically by Belyakov [336], who proved that the corresponding bifurcation diagram is complicated. We call this case the *standard Belyakov case*. In [336, 335] a description of the main features of the universal bifurcation diagram close to this transition for $n = 3$ in the wild case has been obtained:

1. There exists an infinite set of *limit point* (LP) and *period doubling* (PD) bifurcation curves.
2. There exists an infinite set of *secondary homoclinic* curves corresponding to homoclinic orbits making two global excursions and various numbers of local turns near the equilibrium.
3. Both sets have the same 'bunch' shape: The corresponding curves emanate from the codim 2 point and accumulate onto the branch of primary saddle-focus homoclinic orbits. The secondary homoclinics accumulate only from one side.

Case (ii) has recently been observed in [186] for a 4D system of ODEs arising from a study of traveling waves in a neural field model. We will revisit this model in Section 6.6, only noting here that the transition in this model is tame with $\sigma_0 < 0$. As in the standard Belyakov case, we expect a complicated bifurcation diagram in the wild case, i.e. when $\sigma_0 > 0$.

Our chapter is devoted to the theoretical analysis of the homoclinic saddle to saddle-focus transition for case (ii), when the leading stable eigenspace is three-dimensional. We call this transition the *3DL-transition* and mainly consider the *wild* case. To the best of our knowledge, no systematic analysis of this case is available in the literature, and it is one of a few remaining untreated codim 2 homoclinic bifurcations in ODEs, see [329] for a review. A possible reason for this gap is that case (ii) can only occur in (6.1) with $n \geq 4$, while case (i) happens already in three-dimensional ODEs. This leads to the study of a three-dimensional return map in case (ii), which is much more difficult to analyze than the planar return map in the standard Belyakov case (i).

By considering a generic 4D system with the 3DL-transition, we are able to obtain a two-parameter model 3D return map which describes the bifurcations occurring close to the transition. We will see that in the wild case $\sigma_0 > 0$, there exist infinitely many bifurcation curves. However, the shape of these bifurcation curves differs essentially from those in the standard Belyakov case (i):

1. There exist infinitely many PD, LP, torus (Neimark-Sacker, NS) and secondary homoclinic curves. These curves accumulate onto the curve of primary homoclinic orbits but do not emanate from the codim 2 point.
2. Each LP curve is a 'horn' composed of two branches. Close to the horn's tipping point LP and PD curves are organized via *spring* and *saddle areas*

[337]. Transitions between saddle and spring areas are observed. Each secondary homoclinic curve forms a 'horizontal parabola'.

3. Several codim 2 points exist on each of the LP, PD, and NS curves. We observe generalized period-doubling (GPD) and cusp (CP) points, as well as strong resonances.

Using the model map, we prove analytically that the cusp points asymptotically approach the wild 3DL transition point. The same is shown for the secondary homoclinic turning points. We present numerical evidence that all other mentioned codimension 2 points form sequences also converging to the 3DL transition point.

This chapter is organized as follows. In Section 6.2 we formulate the genericity assumptions on (6.1) with $n = 4$ and $m = 2$. Next, we derive a model 3D return map and its 1D simplification. In Section 6.3 we analyze the 1D model map to describe LP and PD bifurcations of the fixed points/periodic orbits. An essential part of the analysis of the 1D map is carried out analytically, while that of the full 3D model map in Section 6.4 employs advanced numerical continuation tools, except for the LP and PD bifurcations (reducible to the 1D return map studied in Section 6.3) and the secondary homoclinic bifurcations. In Section 6.5, implications for the dynamics of the original 4D ODE system are summarized. Finally, in Section 6.6, we give explicit examples of tame and wild 3DL-transitions in concrete models. The tame example is a system that describes traveling waves in a neural field. The wild example is a perturbed Lorenz-Stenflo model appearing in atmospheric studies. Various issues, including generalization to higher dimensions, are discussed in Section 6.7.

6.2 Derivation of the model maps

6.2.1 Assumptions

We make the following assumptions about the 3DL-transition at the critical parameter values, which we assume to be $\alpha_1 = \alpha_2 = 0$. Recall that we only consider $n = 4$ and $m = 2$.

(A.1) The eigenvalues of the linearisation at the critical 3DL equilibrium $x = 0$ are

$$\delta_0, \delta_0 \pm i\omega_0 \text{ and } \epsilon_0,$$

where $\delta_0 < 0, \omega_0 > 0$ and $\epsilon_0 > 0$.

(A.2) There exists a homoclinic orbit Γ_0 to this 3DL equilibrium, called the *primary homoclinic orbit*.

(A.3) The homoclinic orbit Γ_0 does not exhibit an additional orbit-flip: The normalized tangent vector to Γ_0 has nonzero projections to both the 1D eigenspace corresponding to the real eigenvalue δ_0 and to the 2D eigenspace corresponding to the complex eigenvalues $\delta_0 \pm i\omega_0$, when approaching the equilibrium.

Any system (6.1) with $(n, m) = (4, 2)$ and satisfying the assumptions **(A.1-3)**, can be transformed near the critical equilibrium via a translation, a linear transformation, a linear time scaling, and introducing new parameters $\mu = (\mu_1, \mu_2)$, to

$$\dot{x} = \Lambda(\mu)x + g(x, \mu), \qquad x \in \mathbb{R}^4,\ \mu \in \mathbb{R}^2, \tag{6.2}$$

where

$$\Lambda(\mu) = \begin{pmatrix} \gamma(\mu) & -1 & 0 & 0 \\ 1 & \gamma(\mu) & 0 & 0 \\ 0 & 0 & \gamma(\mu) - \mu_1 & 0 \\ 0 & 0 & 0 & \beta(\mu) \end{pmatrix}, \tag{6.3}$$

and the smooth vector-valued function $g(x, \mu)$ vanishes together with its derivative w.r.t. x at $x = 0$ for all $\mu \in \mathbb{R}^2$ sufficiently small, and

$$\gamma(0) = \frac{\delta_0}{\omega_0} \text{ and } \beta(0) = \frac{\epsilon_0}{\omega_0}. \tag{6.4}$$

Define

$$\nu(\mu) := -\frac{\gamma(\mu)}{\beta(\mu)} \tag{6.5}$$

and let $\gamma_0 := \gamma(0)$ and $\beta_0 := \beta(0)$. The number

$$\nu_0 = \nu(0) = -\frac{\gamma_0}{\beta_0} = -\frac{\delta_0}{\epsilon_0} \tag{6.6}$$

is called the *saddle index*. Note that the saddle quantity σ_0 introduced earlier is related to the saddle index (6.6) as follows:

$$\nu_0 < 1 \Longleftrightarrow \sigma_0 > 0,$$
$$\nu_0 > 1 \Longleftrightarrow \sigma_0 < 0.$$

We assume from now on that $\nu_0 < 1$, so that only the wild case $\sigma_0 > 0$ is considered.

In system (6.2), $\mu_2 = \mu_2(\alpha)$ is a 'splitting function' so that the primary homoclinic orbit to the equilibrium (saddle, 3DL, saddle-focus) exists along the curve $\mu_2 = 0$. The exact choice of μ_2 will be clarified later. The value $\mu_1(\alpha)$ controls which stable eigenvalue leads. For $\mu_1 > 0$, the stable leading eigenvalues are complex (saddle-focus case) and for $\mu_1 < 0$ the stable leading eigenvalue is real (saddle case).

Now we can formulate the final (transversality) assumption:

(A.4) The components of $\mu = (\mu_1, \mu_2)$ are small and the 3DL saddle exists at $\mu = 0$. Moreover, the mapping $\alpha \mapsto \mu(\alpha)$ is regular at $\alpha = 0$, i.e. $D\mu(0)$ is nonsingular.

6.2.2 Introducing cross-sections

Our next aim is to derive the model Poincaré map close to Γ_0 near the 3DL-transition, that we will use for the two-parameter perturbation study.

Using the Ovsyannikov-Shilnikov Theorem [338, 328] (see also [339, 340, 341]) and a time reparametrization, we can conclude that (6.2) is smoothly orbitally equivalent in a neighborhood of $x = 0$ to

$$\begin{cases} \dot{u} &= A(\mu)u + f(u, v, \mu)u, \\ \dot{v} &= \beta(\mu)v, \end{cases} \tag{6.7}$$

where $u = (u_1, u_2, u_3) \in \mathbb{R}^3, v \in \mathbb{R}$,

$$A(\mu) = \begin{pmatrix} \gamma(\mu) & -1 & 0 \\ 1 & \gamma(\mu) & 0 \\ 0 & 0 & \gamma(\mu) - \mu_1 \end{pmatrix}, \tag{6.8}$$

and, for all sufficiently small $\mu \in \mathbb{R}^2$, the (3×3)-matrix-valued function f vanishes at $u_1 = u_2 = u_3 = v = 0$ and, moreover, $f(u, 0, \mu) = 0$ for all $u \in \mathbb{R}^3$ with sufficiently small $\|u\|$, while $f(0, v, \mu) = 0$ for all sufficiently small $|v|$. Note that in general (6.7) is only C^{k-2}-smooth in (u, v, μ) even if the original system (6.2) is C^k.

µ 6.4 gives an impression of the homoclinic connection to a 3DL-saddle in the four-dimensional system (6.7). As we are interested in understanding the bifurcations close to the homoclinic orbit, we define two Poincaré cross-sections,

$$\Sigma_s = \{(u_1, u_2, u_3, v) | u_2 = 0\}, \tag{6.9}$$

$$\Sigma_u = \{(u_1, u_2, u_3, v) | v = d_u\}, \tag{6.10}$$

and assume that the homoclinic orbit passes through these cross-sections at $y_s = (d_s, 0, \tilde{d}_s, 0)$ and $y_u = (0, 0, 0, d_u)$, respectively, for all parameter values along the primary homoclinic curve, where $d_s, \tilde{d}_s$ and d_u are sufficiently small but positive. This is possible due to assumption **(A.3)**, which also guarantees that the primary homoclinic orbit does not exhibit an orbit-flip.

Clearly, both cross-sections are transversal to the flow and to the stable and unstable eigenspaces. Thus, by following orbits starting from Σ_s to Σ_u and returning back to Σ_s, we can define a three-dimensional map Π mapping (a subset of) Σ_s to itself. We will use this map to study both periodic orbits and

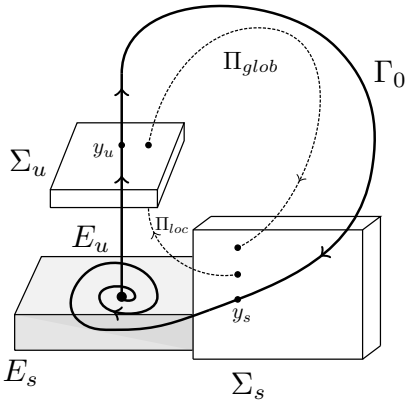

Figure 6.4: The choice of cross-sections close to the critical 3DL-saddle at $(0,0,0,0)$ and the homoclinic connection Γ_0, in order to obtain the map $\Pi : \Sigma_s \to \Sigma_s$. Here Σ_u is defined by the cross-section $v = d_u$ and Σ_s is the cross-section $u_2 = 0$. The homoclinic connection is assumed to pass through the points $y_s = (d_s, 0, \tilde{d_s}, 0)$ and $y_u = (0,0,0,d_u)$. The stable and unstable invariant manifolds locally coincide with the eigenspaces E_s and E_u, respectively.

secondary homoclinic orbits.

We shall construct the map Π by composing two maps, $\Pi_{loc} : \Sigma_s \to \Sigma_u$ and $\Pi_{glob} : \Sigma_u \to \Sigma_s$, i.e.

$$\Pi = \Pi_{glob} \circ \Pi_{loc}. \tag{6.11}$$

We want to construct a solution of (6.7) that starts at $t = 0$ from a point $x_0 \in \Sigma_s$ close to y_s and arrives at a point $x_\tau \in \Sigma_u$ close to y_u at some $t = \tau > 0$. This solution will be used to define the local map Π_{loc}.

6.2.3 Derivation of the return map

Following the classical approach by L.P. Shilnikov [338, 328], consider the integral equation on $[0, \tau]$:

$$\begin{cases} u(t) = e^{At}u_0 + \displaystyle\int_0^t e^{A(t-s)} f(u,v,\mu)u(s)ds, \\ v(t) = e^{-\beta(\tau-t)}v_\tau, \end{cases} \tag{6.12}$$

where $\tau > 0$ is some constant. Let $\epsilon > 0$ be sufficiently small, and let $\tau > 1/\epsilon$. Given any $(u_0, v_\tau) \in \mathbb{R}^4$ with $\|u_0\| + |v_\tau| < \epsilon$, a unique solution $(u(t), v(t))$ satisfying the above integral equation for $t \in [0, \tau]$ can be obtained by successive approximations. The resulting solution $x(t) = (u(t), v(t))$ satisfies (6.7) with $u(0) = u_0$ and $v(\tau) = v_\tau$, and depends (as smoothly as (6.7)) on τ, as well as on

(u_0, v_τ) and μ (see [338, 329]).

This solution will be used to define the local map Π_{loc} that sends $x_0 = (x_1^s, 0, x_3^s, x_4^s) \in \Sigma_s$ to a point $x_\tau = (x_1^u, x_2^u, x_3^u, d_u) \in \Sigma_u$, i.e. when $u_0 = (x_1^s, 0, x_3^s)$ and $v_\tau = d_u$. We now write $x^*(t)$ in a more explicit form.

First, by linearly scaling the phase variables, we transform (6.7) to

$$\begin{cases} \dot{x_1} = & \gamma(\mu)x_1 - x_2 + \dfrac{1}{d_s}\displaystyle\sum_{j=1}^{3} f_{1j}(\tilde{x},\mu)\tilde{x}_j, \\ \dot{x_2} = & x_1 + \gamma(\mu)x_2 + \dfrac{1}{d_s}\displaystyle\sum_{j=1}^{3} f_{2j}(\tilde{x},\mu)\tilde{x}_j, \\ \dot{x_3} = & (\gamma(\mu) - \mu_1)\, x_3 + \dfrac{1}{\tilde{d}_s}\displaystyle\sum_{j=1}^{3} f_{3j}(\tilde{x},\mu)\tilde{x}_j, \\ \dot{x_4} = & \beta(\mu)x_4, \end{cases} \tag{6.13}$$

where $\tilde{x} = (d_s x_1, d_s x_2, \tilde{d}_s x_3, d_u x_4)$. Note that the homoclinic orbit now passes through $y_s = (1, 0, 1, 0)$ and $y_u = (0, 0, 0, 1)$, since Σ_u is now characterized by $x_4 = 1$.

It follows from [338, 329] that the solution $x(t)$ of (6.13) can be written for sufficiently small $\|\mu\|$, as

$$x(t) = \begin{pmatrix} x_1^s e^{\gamma(\mu)t}\left[(1+\tilde{\varphi}_{11})\cos(t) + \tilde{\varphi}_{12}\sin(t) + o\left(e^{\gamma(\mu)t}\right)\right] \\ x_1^s e^{\gamma(\mu)t}\left[(1+\tilde{\varphi}_{21})\sin(t) + \tilde{\varphi}_{22}\cos(t) + o\left(e^{\gamma(\mu)t}\right)\right] \\ x_3^s e^{(\gamma(\mu)-\mu_1)t}\left[1 + \tilde{\varphi}_{31} + o(e^{\gamma(\mu)t})\right] \\ e^{-\beta(\mu)(\tau-t)} \end{pmatrix}. \tag{6.14}$$

The functions $\tilde{\varphi}_{ij}$ are smooth functions of $(t, x_0, \mu, d_s, \tilde{d}_s, d_u)$ and satisfy $\tilde{\varphi}_{ij} = O(d)$, where $d = \min\{d_s, \tilde{d}_s, d_u\}$. In general, these functions and the o-terms are only C^{k-2}-smooth when the scaled system (6.13) is C^k [340, 341].

Evaluating $x(t)$ at $t = \tau$, where

$$\tau = -\frac{1}{\beta}\ln(x_4^s), \tag{6.15}$$

we get the local map Π_{loc},

$$\Pi_{loc}: \begin{pmatrix} x_1^s \\ x_3^s \\ x_4^s \end{pmatrix} \mapsto \begin{pmatrix} x_1^s (x_4^s)^{\nu(\mu)} \left[(1+\varphi_{11})\cos(\tau) + \varphi_{12}\sin(\tau) + o\left((x_4^s)^\nu\right)\right] \\ x_1^s (x_4^s)^{\nu(\mu)} \left[(1+\varphi_{21})\sin(\tau) + \varphi_{22}\cos(\tau) + o\left((x_4^s)^\nu\right)\right] \\ x_3^s (x_4^s)^{\nu(\mu)+\mu_1/\beta(\mu)} \left[1 + \varphi_{31} + o\left((x_4^s)^\nu\right)\right] \end{pmatrix}, \tag{6.16}$$

where $\nu(\mu)$ is defined by (6.5) and φ_{ij} are smooth functions of $(x_1^s, x_3^s, x_4^s, \mu)$.

For the global return map $\Pi_{glob} : \Sigma_u \mapsto \Sigma_s$, we use a general smooth approximation of the flow of (6.13) from $(0,0,0,1)$ to $(1,0,1,\mu_2)$. Here μ_2 is the aforementioned splitting parameter. It controls the return of the orbit to the critical saddle. For $\mu_2 = 0$ only, we have a primary homoclinic connection.

Thus, the following representation of Π_{glob} can be used

$$\Pi_{glob}: \begin{pmatrix} x_1^u \\ x_2^u \\ x_3^u \end{pmatrix} \mapsto \begin{pmatrix} 1 \\ 1 \\ \mu_2 \end{pmatrix} + \begin{pmatrix} a_{11}(\mu) & a_{12}(\mu) & a_{13}(\mu) \\ a_{21}(\mu) & a_{22}(\mu) & a_{23}(\mu) \\ a_{31}(\mu) & a_{32}(\mu) & a_{33}(\mu) \end{pmatrix} \begin{pmatrix} x_1^u \\ x_2^u \\ x_3^u \end{pmatrix} + O(\|x^u\|^2), \tag{6.17}$$

where $x^u = (x_1^u, x_2^u, x_3^u)$. For $A_0 = [a_{ij}(0)]$, we also have $\det(A_0) \neq 0$ which follows from the invertibility of Π_{glob} for μ small enough.

Equations (6.16) and (6.17) together give us the full return map $\Pi = \Pi_{glob} \circ \Pi_{loc}$. Keeping the dependence of all coefficients on μ implicit, we can write Π as

$$\Pi: \begin{pmatrix} x_1^s \\ x_3^s \\ x_4^s \end{pmatrix} \mapsto \begin{pmatrix} 1 + b_1 x_1^s (x_4^s)^\nu \cos\left(-\frac{1}{\beta}\ln x_4^s + \theta_1\right) + b_2 x_3^s (x_4^s)^{\nu+\mu_1/\beta} \\ 1 + b_3 x_1^s (x_4^s)^\nu \sin\left(-\frac{1}{\beta}\ln x_4^s + \theta_2\right) + b_4 x_3^s (x_4^s)^{\nu+\mu_1/\beta} \\ \mu_2 + b_5 x_1^s (x_4^s)^\nu \sin\left(-\frac{1}{\beta}\ln x_4^s + \theta_3\right) + b_6 x_3^s (x_4^s)^{\nu+\mu_1/\beta} \end{pmatrix} + o(\|x^s\|^\nu), \tag{6.18}$$

where $x^s = (x_1^s, x_3^s, x_4^s)$ and

$$\begin{aligned} &\sin\theta_1 = -\frac{a_{12}}{\sqrt{a_{11}^2 + a_{12}^2}}, \quad \cos\theta_2 = \frac{a_{22}}{\sqrt{a_{21}^2 + a_{22}^2}}, \quad \cos\theta_3 = \frac{a_{32}}{\sqrt{a_{31}^2 + a_{32}^2}}, \\ &b_1 = \sqrt{a_{11}^2 + a_{12}^2}, \qquad b_3 = \sqrt{a_{21}^2 + a_{22}^2}, \qquad b_5 = \sqrt{a_{31}^2 + a_{32}^2}, \\ &b_2 = a_{13}, \qquad b_4 = a_{23}, \qquad \text{and} \quad b_6 = a_{33}. \end{aligned} \tag{6.19}$$

Following [332], we make the smooth invertible transformation $x_4^s \mapsto x_4^s \exp(\theta_3\beta)$ to eliminate θ_3. This gives

$$\Pi : \begin{pmatrix} x_1 \\ x_3 \\ x_4 \end{pmatrix} \mapsto \begin{pmatrix} 1 + \alpha_1 x_1 x_4^\nu \cos\left(-\frac{1}{\beta}\ln x_4 + \phi_1\right) + \alpha_2 x_3 x_4^{\nu+\mu_1/\beta} \\ 1 + \alpha_3 x_1 x_4^\nu \sin\left(-\frac{1}{\beta}\ln x_4 + \phi_2\right) + \alpha_4 x_3 x_4^{\nu+\mu_1/\beta} \\ \mu_2 + C_1 x_1 x_4^\nu \sin\left(-\frac{1}{\beta}\ln x_4\right) + C_2 x_3 x_4^{\nu+\mu_1/\beta} \end{pmatrix} + o(\|x\|^\nu), \tag{6.20}$$

where we have dropped the superscript 's' from the coordinates of $x = (x_1, x_3, x_4)$ for convenience, and where

$$\begin{array}{ll} \phi_1 = \theta_1 - \theta_3, & \phi_2 = \theta_2 - \theta_3, \\ \alpha_1 = b_1 \exp(\theta_3\beta\nu), & \alpha_2 = b_2 \exp((\nu + \mu_1/\beta)\theta_3\beta), \\ \alpha_3 = b_3 \exp(\theta_3\beta\nu), & \alpha_4 = b_4 \exp((\nu + \mu_1/\beta)\theta_3\beta), \\ C_1 = b_5 \exp(\theta_3\beta\nu), & C_2 = b_2 \exp((\nu + \mu_1/\beta)\theta_3\beta). \end{array} \tag{6.21}$$

Observe that α_j and C_k depend on μ and that $C_1 > 0$. Let us denote by α_j^0 and C_j^0 their critical values at $\mu = 0$.

Truncating the $o(\|x\|^\nu)$-terms in (6.20) and taking only the critical values of all coefficients, we define

$$G(x,\mu) := \begin{pmatrix} 1 + \alpha_1^0 x_1 x_4^{\nu_0} \cos\left(-\frac{1}{\beta_0}\ln x_4 + \phi_1^0\right) + \alpha_2^0 x_3 x_4^{\nu_0+\mu_1/\beta_0} \\ 1 + \alpha_3^0 x_1 x_4^{\nu_0} \sin\left(-\frac{1}{\beta_0}\ln x_4 + \phi_2^0\right) + \alpha_4^0 x_3 x_4^{\nu_0+\mu_1/\beta_0} \\ \mu_2 + C_1^0 x_1 x_4^{\nu_0} \sin\left(-\frac{1}{\beta_0}\ln x_4\right) + C_2^0 x_3 x_4^{\nu_0+\mu_1/\beta_0} \end{pmatrix}. \tag{6.22}$$

This map G is the final form of the *3D model return map* that we will use for the numerical analysis ahead.

Now, to analyze periodic orbits close to the homoclinic connection with respect to the critical 3DL-saddle, we look for fixed points of the map Π given by (6.20). These fixed points correspond to periodic orbits in the original ODE system. Bifurcations of these fixed points describe the various local bifurcations of the corresponding periodic orbits.

The fixed point condition for map (6.20) is

$$\begin{pmatrix} x_1 \\ x_3 \\ x_4 \end{pmatrix} = \begin{pmatrix} 1 + \alpha_1 x_1 x_4^\nu \cos\left(-\frac{1}{\beta}\ln x_4 + \phi_1\right) + \alpha_2 x_3 x_4^{\nu+\mu_1/\beta} \\ 1 + \alpha_3 x_1 x_4^\nu \sin\left(-\frac{1}{\beta}\ln x_4 + \phi_2\right) + \alpha_4 x_3 x_4^{\nu+\mu_1/\beta} \\ \mu_2 + C_1 x_1 x_4^\nu \sin\left(-\frac{1}{\beta}\ln x_4\right) + C_2 x_3 x_4^{\nu+\mu_1/\beta} \end{pmatrix} + o(\|x\|^\nu), \tag{6.23}$$

where all constants a_j and C_k still depend on μ. For non-degeneracy, we require that real constants C_1 and C_2 are nonzero. We justify this later. The coefficients C_1 and C_2 play the role of *separatrix values* (see [328]).

From (6.23), we get, using the Implicit Function Theorem, the following expressions for x_1 and x_3:

$$\begin{aligned} x_1 &= 1 + a_1 x_4^{\nu} \cos\left(-\tfrac{1}{\beta}\ln x_4 + \phi_1\right) + a_2 x_4^{\nu+\mu_1/\beta} + o(|x_4|^{\nu}),\\ x_3 &= 1 + a_3 x_4^{\nu} \sin\left(-\tfrac{1}{\beta}\ln x_4 + \phi_2\right) + a_4 x_4^{\nu+\mu_1/\beta} + o(|x_4|^{\nu}), \end{aligned}$$

which gives the condition for x_4

$$x_4 = \mu_2 + C_1 x_4^{\nu} \sin\left(-\frac{1}{\beta}\ln x_4\right) + C_2 x_4^{\nu+\mu_1/\beta} + o(|x_4|^{\nu}), \tag{6.24}$$

as a one-dimensional fixed point condition. As we are interested in the behavior close to $(1,0,1,0)$ on the cross-section Σ_s, we consider only the leading terms of (6.24) and introduce the following *scalar model map*:

$$x \mapsto F(x,\mu) := \mu_2 + C_1^0 x^{\nu_0} \sin\left(-\frac{1}{\beta_0}\ln x\right) + C_2^0 x^{\nu_0+\mu_1/\beta_0}. \tag{6.25}$$

The extra additive term $C_2^0 x^{\nu_0+\mu_1/\beta_0}$ is what makes this map different from the scalar model maps describing the codim 1 saddle-focus case.

If we were to set C_1^0 to zero, then we get the saddle case, where we obtain finitely many fixed points for all values of $\nu_0, \mu_1, \beta_0, \mu_2$ and C_2^0. If we set C_2^0 to zero, we get the codim 1 saddle-focus case.

Thus we assume

> **(A.5)** The homoclinic orbit Γ_0 does not exhibit an additional inclination-flip:
> $$C_1^0 C_2^0 \neq 0.$$

6.3 Analysis of the scalar model map

In this section, we study bifurcations of fixed points of the map (6.26). To stay close to the 3DL-bifurcation, we only work with small values of x and μ. To simplify notations, we rewrite the scalar model map (6.25) as

$$x \mapsto F(x,\mu) := \mu_2 + C_1 x^{\nu} \sin\left(-\frac{1}{\beta}\ln x\right) + C_2 x^{\nu+\mu_1/\beta}, \tag{6.26}$$

assuming that ν, β, and $C_{1,2}$ are fixed at their critical values.

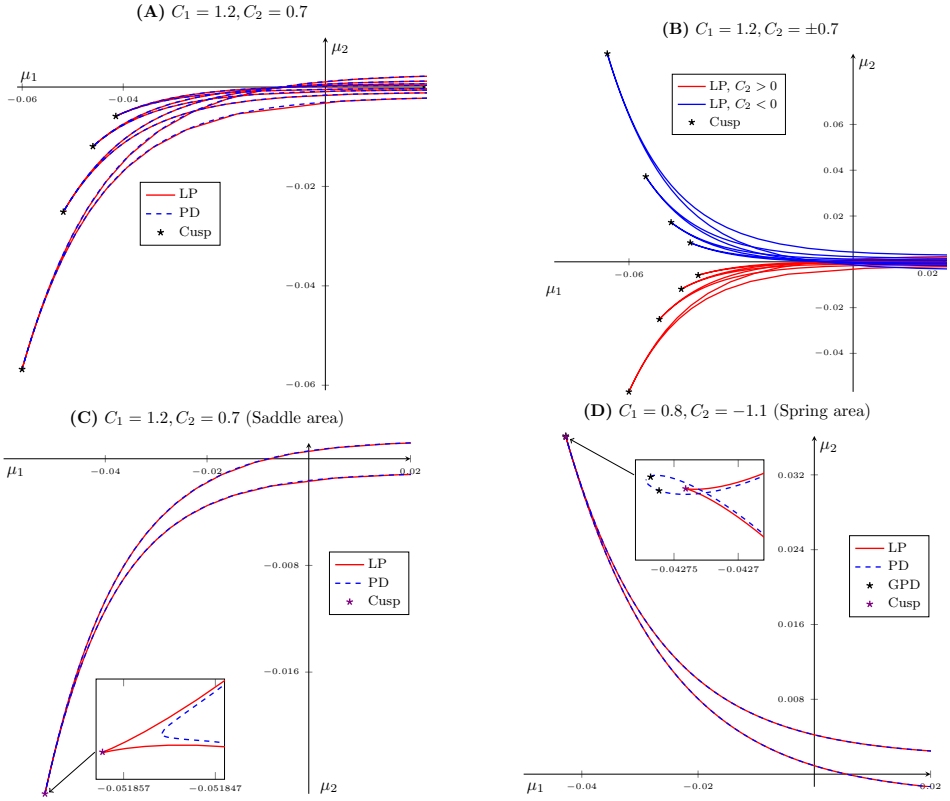

Figure 6.5: Primary LP and PD bifurcation curves obtained by numerical continuation, for the map (6.26) for some representative values of C_1 and C_2. We fix $\beta = 0.2$ and $\nu = 0.5$. In panel **(A)** we plot 4 pairs of these curves. All of them have the same global structure. There are two types of codimension 2 points that can be found along these curves: Cusp (on LP curves) and GPD (along PD curves). In panel **(B)** we see what happens when we switch the sign of C_2, the *horns* move from $\mu_2 > 0$ to $\mu_2 < 0$. In panel **(C)** and **(D)** we see examples of one PD and LP curve with the saddle area and spring area respectively (zoomed in). In the insets, μ_2 is scaled for visualization.

6.3.1 Numerical continuation results

Using the continuation package MATCONTM [342, 343], we obtained many LP and PD bifurcation curves, which form interesting structures. There is strong evidence that there exist infinitely many PD and LP curves in the (μ_1, μ_2)-parameter space. Several such curves can be seen in µ 6.5. We make the following observations:

1. The curves exhibit a repetitive behavior: two branches of one LP curve meet to form a *horn*. The sequence of these 'horns' in the parameter space appears to approach the half-axis $\mu_2 = 0 (\mu_1 > 0)$ asymptotically, which is the curve of primary homoclinic orbits. Also, the tips of the 'horns' are always located entirely in either the second, or third quadrant of the (μ_1, μ_2)-space.
2. The PD and LP curves appear to coincide on visual inspection, and there can exist GPD points in the vicinity of the tip of the LP horn.
3. The tip of each LP 'horn' is a cusp point. These cusps always exist, for all values of C_1 and C_2 and form a sequence that appears to approach the origin $\mu = 0$.
4. Upon closer inspection, we observe that there exists either of the two subtle structures near the top of every LP 'horn'. One is a *spring area*, where the PD curve loops around the cusp point. The other is a *saddle area*, where the PD curve makes a sharp turn close to the cusp, see the insets in µ 6.5. The spring area is accompanied by two GPD points along the PD loop. These points are absent in a saddle area. Mira et al. [337] discuss in detail the spring and saddle areas, including transitions from one case to the other and their genericity.
5. The global behavior of this set of curves depends on parameters C_1 and C_2. For example, by switching the sign of C_2, the set of curves can be moved from the second to the third quadrant of the μ-space, or vice-versa. The presence of saddle or spring areas depend on the parameters C_1 and C_2, but the exact conditions are not clear.

In the sections ahead, we support most of the observations by analytical asymptotics of the LP and PD bifurcation curves of (6.26).

6.3.2 Asymptotics

In this section we derive approximate solutions to the LP and PD conditions, and use them to justify numerical observations. As we are interested in solutions close to the 3DL bifurcation point $(\mu_1, \mu_2) = (0, 0)$ we assume that x, μ_1 and μ_2 are sufficiently small. As we investigate only the wild case we restrict ourselves to $\nu < 1$.

LP horns and cusp points

For the scalar model map (6.26) the fixed point condition is given by

$$\mu_2 + C_1 x^\nu \sin\left(-\frac{1}{\beta}\ln x\right) + C_2 x^{\nu+\mu_1/\beta} - x = 0. \tag{6.27}$$

Notice that x is a higher-order term compared to x^ν and $x^{\nu+\mu_1/\beta}$ for sufficiently small μ_1. Therefore, studying fixed points is asymptotically equivalent to studying zeros of $F(x,\mu)$. We introduce $\alpha := \min(1, 2\nu)$ and parametrize x using the following relation,

$$-\frac{1}{\beta}\ln x = 2\pi n + \theta, \tag{6.28}$$

for large $n \in \mathbb{N}$ and $\theta \in (0, 2\pi)$. Thus, (6.27) becomes

$$\mu_2 + C_1 e^{-\beta\nu(2\pi n+\theta)}\sin\theta + C_2 e^{-\beta(\nu+\mu_1/\beta)(2\pi n+\theta)} + O(e^{-\alpha\beta(2\pi n+\theta)}) = 0. \tag{6.29}$$

Let us define

$$\Phi(\theta,\mu_1,\mu_2) := \mu_2 + C_1 e^{-\beta\nu(2\pi n+\theta)}\sin\theta + C_2 e^{-\beta(\nu+\mu_1/\beta)(2\pi n+\theta)}. \tag{6.30}$$

Then

$$\Phi_\theta(\theta,\mu_1,\mu_2) = 0,$$

is the extra condition for an asymptotic LP point. Computing the derivative, we get

$$C_1\left(\beta\nu\sin\theta - \cos\theta\right) + C_2(\beta\nu+\mu_1)e^{-\mu_1(2\pi n+\theta)} = 0. \tag{6.31}$$

We now simultaneously solve (6.27) and (6.31) to obtain a sequence of functions $\mu_2^{(n)}(\mu_1)$ which describe the sequence of LP 'horns' already observed numerically. Thus, rewriting (6.31), we have

$$\begin{aligned}\beta\nu\sin\theta - \cos\theta &= -\tfrac{C_2}{C_1}\left(\beta\nu+\mu_1\right)e^{-\mu_1(2\pi n+\theta)}\\ &= -\tfrac{C_2}{C_1}\left(\beta\nu+\mu_1\right)e^{-2\pi\mu_1 n}\left[1-\mu_1\theta+O(\mu_1^2)\right]\\ &= -\tfrac{C_2}{C_1}e^{-2\pi\mu_1 n}\left[\beta\nu-(1-\beta\nu\theta)\mu_1+O(\mu_1^2)\right].\end{aligned} \tag{6.32}$$

Collecting trigonometric terms on the left we get

$$\sin(\theta-\phi) = -\frac{1}{\sqrt{1+\beta^2\nu^2}}\frac{C_2}{C_1}e^{-2\pi\mu_1 n}\left[\beta\nu-(1-\beta\nu\theta)\mu_1+O(\mu_1^2)\right], \tag{6.33}$$

where $\sin\phi = (1+\beta^2\nu^2)^{-1/2}$ and $\phi \in (0,\pi/2)$. Note that for large n and negative μ_1, the corresponding solution θ exists only for small $|\mu_1|$. Let

$$\theta_0^n := \arcsin\left(-\frac{\beta\nu}{\sqrt{1+\beta^2\nu^2}}\frac{C_2}{C_1}e^{-2\pi\mu_1 n}\right). \tag{6.34}$$

Then we have two solutions,

$$\begin{array}{l}\theta_1 = \phi + \theta_0^n + 2\pi\delta_{i1} + O(\mu_1),\\ \theta_2 = \phi + \pi - \theta_0^n + O(\mu_1),\end{array} \tag{6.35}$$

where $i = -\text{sign}(C_2)$ and δ_{ij} is the Kronecker delta.

For each n, we obtain two solutions $\theta = \theta_{1,2}$ given by (6.35). The corresponding functions $\mu_2^{(n)}(\mu_1)$ follow from (6.29),

$$\left\{\begin{array}{l}\mu_2^{(n,1)}(\mu_1) = -C_1 e^{-\beta\nu(2\pi n+\theta_1)}\sin\theta_1 - C_2 e^{-\beta(\nu+\mu_1/\beta)(2\pi n+\theta_1)},\\ \mu_2^{(n,2)}(\mu_1) = -C_1 e^{-\beta\nu(2\pi n+\theta_2)}\sin\theta_2 - C_2 e^{-\beta(\nu+\mu_1/\beta)(2\pi n+\theta_2)}.\end{array}\right. \tag{6.36}$$

On expanding $\sin\theta_1$ and $\sin\theta_2$ we get the expressions for two LP-branches forming the n-th 'horn'

$$\left\{\begin{array}{ll}\mu_2^{(n,1)}(\mu_1) & = -e^{-\beta\nu(\theta_0^n+\phi+2\pi\delta_{i1})}\frac{e^{-2\pi\beta\nu n}}{\sqrt{1+\beta^2\nu^2}}\left[C_1\left(1-\frac{\beta^2\nu^2}{1+\beta^2\nu^2}\frac{C_2^2}{C_1^2}e^{-4\pi\mu_1 n}\right)^{1/2}\right.\\ & \left.+\frac{C_2}{\sqrt{1+\beta^2\nu^2}}e^{-\mu_1(2\pi n+2\pi\delta_{i1}+\theta_0^n+\phi)}+O(\mu_1)\right],\\ \mu_2^{(n,2)}(\mu_1) & = -e^{-\beta\nu(\pi-\theta_0^n+\phi)}\frac{e^{-2\pi\beta\nu n}}{\sqrt{1+\beta^2\nu^2}}\left[-C_1\left(1-\frac{\beta^2\nu^2}{1+\beta^2\nu^2}\frac{C_2^2}{C_1^2}e^{-4\pi\mu_1 n}\right)^{1/2}\right.\\ & \left.+\frac{C_2}{\sqrt{1+\beta^2\nu^2}}e^{-\mu_1(2\pi n+\pi-\theta_0^n+\phi)}+O(\mu_1)\right].\end{array}\right. \tag{6.37}$$

Upon setting $\mu_2^{(n,j)}$ to zero, we get a sequence $\mu_1^{(n)}\big|_{\mu_2=0}$ of intersections of one of these branches with the axis $\mu_2 = 0$. Thus asymptotically

$$\mu_1^{(n)}\Big|_{\mu_2=0} = \frac{1}{4\pi n}\left[\ln\left(\frac{C_2^2}{C_1^2}\right) + O\left(\frac{1}{n}\right)\right]. \tag{6.38}$$

For genericity of the LP, we further require that the second derivative $\Phi_{\theta\theta} \neq 0$. Thus, the condition

$$\Phi_{\theta\theta} = 0,$$

determines a cusp point. We solve the following three conditions together

$$\left\{\begin{array}{l}\Phi(\theta,\mu_1,\mu_2) = 0,\\ \Phi_\theta(\theta,\mu_1,\mu_2) = 0,\\ \Phi_{\theta\theta}(\theta,\mu_1,\mu_2) = 0.\end{array}\right. \tag{6.39}$$

Taking derivative with respect to θ in (6.33) gives the third equation of (6.39),

$$\cos(\theta-\phi) + \frac{1}{\sqrt{1+\beta^2\nu^2}}\frac{C_2}{C_1}e^{-2\pi\mu_1 n}\left[\beta\nu\mu_1 + O(\mu_1^2)\right] = 0. \tag{6.40}$$

Using (6.33) and (6.40) we get

$$\frac{1}{(1+\beta^2\nu^2)}\frac{C_2^2}{C_1^2}e^{-4\pi\mu_1 n}\left[\beta^2\nu^2+O(\mu_1)\right]=1, \tag{6.41}$$

which gives the value of μ_1 at the cusp point,

$$\mu_1^n=\frac{1}{4\pi n}\left[\ln\left(\frac{\beta^2\nu^2}{(1+\beta^2\nu^2)}\frac{C_2^2}{C_1^2}\right)+O\left(\frac{1}{n}\right)\right]. \tag{6.42}$$

The corresponding value of μ_2 is obtained from (6.29). We get,

$$\mu_2^n=-e^{-\beta\nu(2\pi n+\theta_0+\phi)}\frac{\text{sign}(C_2)C_1}{\beta\nu\sqrt{1+\beta^2\nu^2}}a^{-(\theta_0+\phi)/4\pi n}+O\left(\frac{1}{\sqrt{n}}\right), \tag{6.43}$$

where θ_0 is the value of θ_0^n at the cusp point, that is

$$\theta_0=\begin{cases}\pi/2, & \text{if } C_2<0,\\ 3\pi/2, & \text{if } C_2>0,\end{cases} \tag{6.44}$$

and

$$a=\frac{\beta^2\nu^2}{1+\beta^2\nu^2}\frac{C_2^2}{C_1^2}. \tag{6.45}$$

Clearly, this cusp point is precisely where the two branches of a horn from (6.36) meet, i.e. when

$$\sin^2\theta_0^n=1.$$

PD curves

The formulas derived to describe the LP-'horns' also describe PD bifurcation curves away from the cusp points. Indeed, the asymptotic conditions for PD curves are

$$\begin{cases}\Phi(\theta,\mu_1,\mu_2) &= 0,\\ \Phi_\theta(\theta,\mu_1,\mu_2) &= 0,\end{cases} \tag{6.46}$$

which gives the same expressions (6.35) and (6.36) to describe PD curves.

6.3.3 Summarizing lemma for 1D model map

We summarize our findings in the following lemma.

Lemma 6.3.1. *In a neighborhood of the origin of the (μ_1,μ_2)-plane, the scalar model map (6.25) has an infinite number of fold curves for fixed points $LP_n^{(1)}, n\in\mathbb{N}$, accumulating to the half axis $\mu_2=0$ with $\mu_1\geq 0$.*

Each curve resembles a 'horn' with the following asymptotic representation of its two branches:

$$\begin{cases} \mu_2^{(n,1)}(\mu_1) &= -e^{-\beta_0\nu_0(\theta_0^n+\phi_0+2\pi\delta_{i1})}\frac{e^{-2\pi\beta_0\nu_0 n}}{\sqrt{1+\beta_0^2\nu_0^2}}\left[C_1^0\left(1-\frac{\beta_0^2\nu_0^2}{1+\beta_0^2\nu_0^2}\frac{(C_2^0)^2}{(C_1^0)^2}e^{-4\pi\mu_1 n}\right)^{1/2}\right. \\ &\quad \left. +\frac{C_2^0}{\sqrt{1+\beta_0^2\nu_0^2}}e^{-\mu_1(2\pi n+2\pi\delta_{i1}+\theta_0^n+\phi_0)}+O(\mu_1)\right], \\ \mu_2^{(n,2)}(\mu_1) &= -e^{-\beta_0\nu_0(\pi-\theta_0^n+\phi_0)}\frac{e^{-2\pi\beta_0\nu_0 n}}{\sqrt{1+\beta_0^2\nu_0^2}}\left[-C_1^0\left(1-\frac{\beta_0^2\nu_0^2}{1+\beta_0^2\nu_0^2}\frac{(C_2^0)^2}{(C_1^0)^2}e^{-4\pi\mu_1 n}\right)^{1/2}\right. \\ &\quad \left. +\frac{C_2^0}{\sqrt{1+\beta_0^2\nu_0^2}}e^{-\mu_1(2\pi n+\pi-\theta_0^n+\phi_0)}+O(\mu_1)\right]. \end{cases} \tag{6.47}$$

where

$$\phi_0 := \arcsin\left(\frac{1}{\sqrt{1+\beta_0^2\nu_0^2}}\right), \quad \theta_0^n := \arcsin\left(-\frac{\beta_0\nu_0}{\sqrt{1+\beta_0^2\nu_0^2}}\frac{C_2^0}{C_1^0}e^{-2\pi\mu_1 n}\right),$$

and δ_{ij} *is the Kronecker delta where* $i = -\mathrm{sign}(C_2^0)$.

The branches of each $LP_n^{(1)}$ *curve meet at a cusp point* $CP_n^{(1)}$ *with the following asymptotic representation*:

$$CP_n^{(1)} = \begin{pmatrix} \mu_1^n \\ \mu_2^n \end{pmatrix} = \begin{pmatrix} \frac{1}{4\pi n}\left[\ln(a)+O\left(\frac{1}{n}\right)\right] \\ -e^{-\beta_0\nu_0(2\pi n+\theta_0+\phi_0)}\frac{\mathrm{sign}(C_2^0)C_1^0}{\beta_0\nu_0\sqrt{1+\beta_0^2\nu_0^2}}a^{-(\theta_0+\phi_0)/4\pi n}+O\left(\frac{1}{\sqrt{n}}\right) \end{pmatrix}, \tag{6.48}$$

where

$$\theta_0 := \begin{cases} \pi/2, & \text{if } C_2^0 < 0, \\ 3\pi/2, & \text{if } C_2^0 > 0, \end{cases}$$

and

$$a := \frac{\beta_0^2\nu_0^2}{1+\beta_0^2\nu_0^2}\frac{(C_2^0)^2}{(C_1^0)^2}.$$

Moreover, there exists an infinite number of period-doubling curves $PD_n^{(1)}, n \in \mathbb{N}$, *which have – away from the cusp points* $CP_n^{(1)}$ *– the same asymptotic representation as the fold bifurcation curves* $LP_n^{(1)}$. *Depending on* (C_1^0, C_2^0), *the period-doubling curves could either be smooth or have self-intersections developing small loops around the corresponding cusp points.*

Figure 6.6 illustrates Lemma 6.3.1 by comparing the leading terms of the asymptotic expressions for LP curves with actual LP curves of the 1D model map (6.25) obtained by accurate numerical continuation.

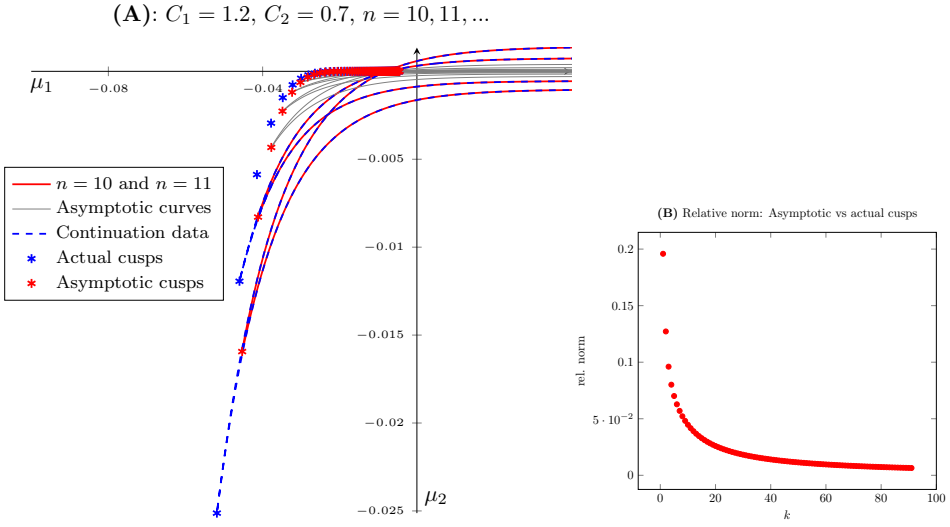

Figure 6.6: Plots of the truncated asymptotic curves and actual PD/LP curves obtained by numerical continuation. We fix $\beta = 0.2$ and $\nu = 0.5$. In **(A)** we see how successive asymptotic curves, indexed by n, approximate the set of PD/LP curves. Here, cusps are obtained by performing Newton iterations to the defining system of the cusp bifurcation with starting points as the asymptotic cusps. In **(B)**, convergence of the asymptotic cusps to the actual cusps is observed. The corresponding values of n in both plots are $n = 10, 11, ...90$.

6.4 Analysing the 3D model map

In this section we study the original 3D model map (6.22) that we restate here for convenience

$$G:\begin{pmatrix} x_1 \\ x_2 \\ x_4 \end{pmatrix} \mapsto \begin{pmatrix} 1+\alpha_1 x_1 x_4^{\nu}\cos\left(-\frac{1}{\beta}\ln x_4+\phi_1\right)+\alpha_2 x_2 x_4^{\nu+\mu_1/\beta} \\ 1+\alpha_3 x_1 x_4^{\nu}\sin\left(-\frac{1}{\beta}\ln x_4+\phi_2\right)+\alpha_4 x_2 x_4^{\nu+\mu_1/\beta} \\ \mu_2+C_1 x_1 x_4^{\nu}\sin\left(-\frac{1}{\beta}\ln x_4\right)+C_2 x_2 x_4^{\nu+\mu_1/\beta} \end{pmatrix}. \tag{6.49}$$

The analysis of fixed points of (6.49) leads to the same equation (6.24) for the x_4 coordinate. Thus, all conclusions about the existence and asymptotics of $LP_n^{(1)}$ and $PD_n^{(1)}$ curves, as well as $CP_n^{(1)}$ points in Lemma 6.3.1, remain valid. Indeed, taking into account the $O(|x|^{2\nu})$-term does not alter the leading terms in any expression.

6.4.1 Results of numerical continuation

We look for fixed points of map (6.49) and their various codim 1 curves. The results are similar to that of the scalar model map, except for higher dimensional codim 2 points that exist only in the 3D model map. In µ 6.7, we show the PD and LP curves obtained via numerical continuation in μ for a fixed set of parameters:

$$\begin{aligned} &\nu=0.5,\beta=0.2,C_1=0.8,C_2=1.2,\alpha_1=0.8,\\ &\alpha_2=1.3,\alpha_3=0.6,\alpha_4=1.1,\phi_1=\phi_2=\pi/6. \end{aligned} \tag{6.50}$$

We immediately see similarities with the scalar case. The global structure of these curves is the same as in the scalar case. They form sequences that accumulate onto the primary homoclinic curve asymptotically. The LP 'horns' have cusp points and are accompanied by PD curves with/without GPD points (depending on saddle or spring area). All this is expected as the scalar map is a correct asymptotic representation of the 3D model map.

There are however three main differences with respect to the scalar model map which can be attributed to the higher dimension of the 3D map:

1. Spring and saddle areas may occur differently for the 1D and 3D model maps for the same parameter values.
2. Between the PD and LP curves, there exist NS curves. The end points of each NS segment are *strong resonance* points.
3. Along the PD, LP and NS curves we observe many higher dimensional codimension 2 points. These points are R1 (resonance 1:1), R2 (resonance 1:2), LPPD (Fold-Flip), R3 (resonance 1:3), R4 (resonance 1:4).

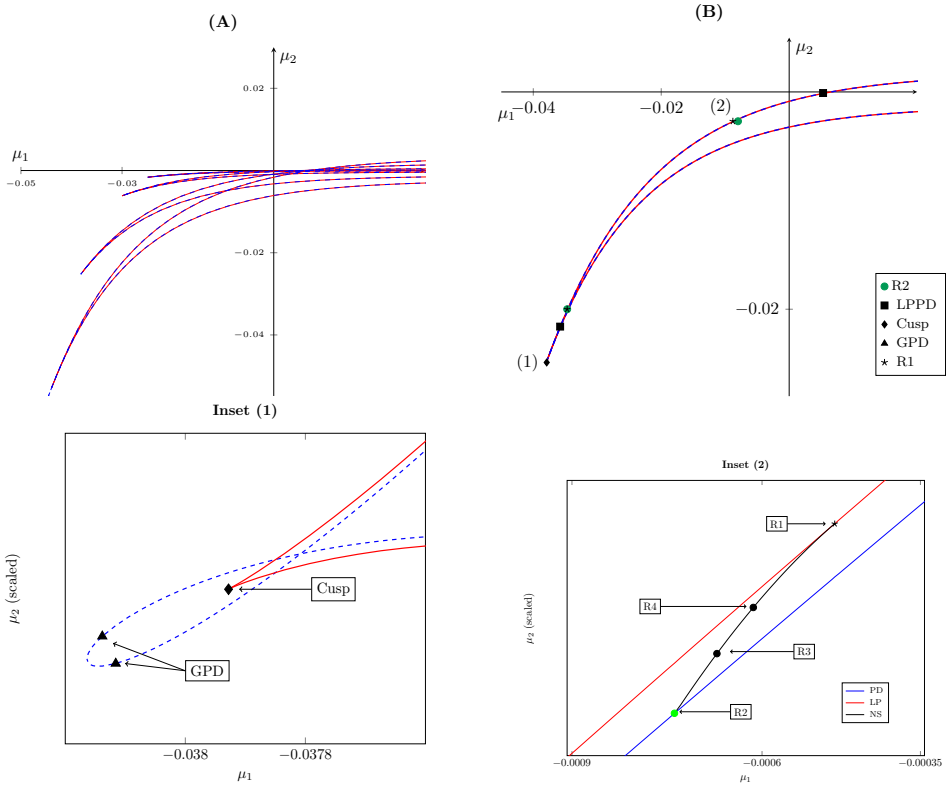

Figure 6.7: Primary LP (solid red) and PD (dashed blue) curves obtained by numerical continuation for the map (6.49) with parameters (6.50). The curves have almost the same global structure as for the 1D map, as can be seen in **(A)**. In **(B)** one such curve is presented, together with several codim 2 points found along it. In **Inset (1)** we see the previously described spring area made up by the PD and LP curves. Three codim 2 bifurcation points are observed, two corresponding to the generalised period doubling (GPD) bifurcation and one corresponding to the Cusp bifurcation. In **Inset (2)** we see the interaction between the 1:2 resonance (R2) point on the PD curve and the 1:1 resonance point (R1) on the LP curve, via the primary NS curve (solid black). On this curve we find two more codimension 2 bifurcation points: 1:3 resonance (R3) and 1:4 resonance (R4).

These points appear to numerically approach the origin $\mu = 0$ (3DL transition). The endpoints of the NS curve are points R1 and R2, as can be seen in µ 6.7 **(B)**. For a detailed discussion on the various codimension 2 points and their local bifurcation diagrams, see [4].

We did not see a significant difference in behavior of the PD/LP curves upon changing the coefficients α_i and ϕ_j. This can be attributed to the effect of the corresponding terms in (6.49) to the dynamics of x_4. These terms are $O(\|x\|^{2\nu})$ in the fixed point equation for x_4.

In Table 6.1 we present sequences of some of the codimension 2 points found on successive PD/LP curves of µ 6.7. These sequences are obtained via detection along PD/LP curves from continuation. GPD and CP points are not reported as they are generally hard to detect along continuations, due to large test function values and absolute gradients. GPD's are approximated in practice by noting where the sign of the corresponding test function changes. Note that codimension 2 points such as R1, R2 and LPPD were observed more than once on a single PD/LP curve. In Table 6.1 we show only one point per curve for each of the different bifurcation points.

LPPD (1)		R1 (1)		R2 (2)	
μ_1	μ_2	μ_1	μ_2	μ_1	μ_2
$5.9 \cdot 10^{-3}$	$-2.45 \cdot 10^{-4}$	$-9.9 \cdot 10^{-3}$	$-5.16 \cdot 10^{-3}$	$-4.02 \cdot 10^{-2}$	$-4.23 \cdot 10^{-2}$
$5.31 \cdot 10^{-3}$	$-1.38 \cdot 10^{-4}$	$-8.83 \cdot 10^{-3}$	$-2.74 \cdot 10^{-3}$	$-3.47 \cdot 10^{-2}$	$-2 \cdot 10^{-2}$
$4.39 \cdot 10^{-3}$	$-4.14 \cdot 10^{-5}$	$-7.27 \cdot 10^{-3}$	$-7.74 \cdot 10^{-4}$	$-2.74 \cdot 10^{-2}$	$-5.03 \cdot 10^{-3}$
$3.74 \cdot 10^{-3}$	$-1.21 \cdot 10^{-5}$	$-6.18 \cdot 10^{-3}$	$-2.19 \cdot 10^{-4}$	$-2.27 \cdot 10^{-2}$	$-1.34 \cdot 10^{-3}$
$3.25 \cdot 10^{-3}$	$-3.51 \cdot 10^{-6}$	$-5.38 \cdot 10^{-3}$	$-6.22 \cdot 10^{-5}$	$-1.95 \cdot 10^{-2}$	$-3.64 \cdot 10^{-4}$
$3.05 \cdot 10^{-3}$	$-1.89 \cdot 10^{-6}$	$-5.05 \cdot 10^{-3}$	$-3.31 \cdot 10^{-5}$	$-1.82 \cdot 10^{-2}$	$-1.91 \cdot 10^{-4}$
$2.88 \cdot 10^{-3}$	$-1.01 \cdot 10^{-6}$	$-4.76 \cdot 10^{-3}$	$-1.77 \cdot 10^{-5}$	$-1.6 \cdot 10^{-2}$	$-5.29 \cdot 10^{-5}$
$2.72 \cdot 10^{-3}$	$-5.44 \cdot 10^{-7}$	$-4.5 \cdot 10^{-3}$	$-9.41 \cdot 10^{-6}$	$-1.52 \cdot 10^{-2}$	$-2.79 \cdot 10^{-5}$
$2.34 \cdot 10^{-3}$	$-8.37 \cdot 10^{-8}$	$-3.87 \cdot 10^{-3}$	$-1.43 \cdot 10^{-6}$	$-1.36 \cdot 10^{-2}$	$-7.8 \cdot 10^{-6}$

Table 6.1: Cascades of codimension two points numerically obtained during continuation of limit point/period-doubling solutions of the 3D map (6.49). Other parameter values are as in µ 6.7.

For the scalar map we observed that transitions exist between spring and saddle areas. These transitions can be explained by observing the appearance and disappearance of GPD points, as they exist generically on the PD loop in a spring area, and do not exist in the case of a saddle area. In the 3D case too, we numerically observe such transitions. However, when there is a spring (saddle) area in the 3D case, it does not imply that the same structure would exist in the 1D map for the same choice of parameters C_1 and C_2. This is shown in µ 6.8.

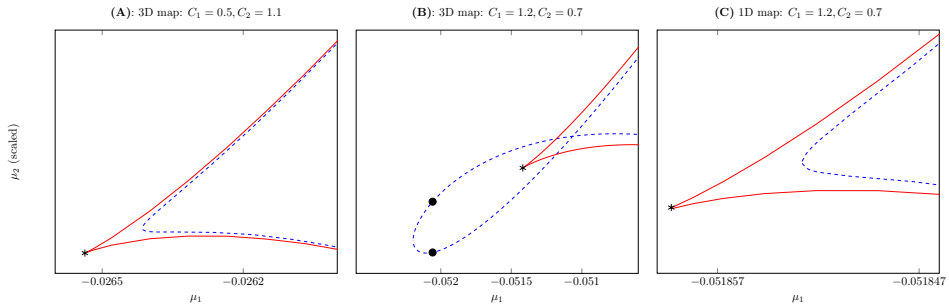

Figure 6.8: Plots of spring and saddle areas in the scalar map (6.26) and 3D map (6.22). We fix $\nu = 0.5, \beta = 0.2, \alpha_1 = 0.8, \alpha_2 = 1.3, \alpha_3 = 0.6, \alpha_4 = 1.1$ and $\phi_1 = \phi_2 = \pi/6$.In all plots μ_2 is scaled for convenience. In **(A)** we see that there exists a saddle area in the 3D case, where GPD points are absent. **(B)** and **(C)** are plotted for the same value of C_1 and C_2, but with respect to the 3D map (6.22) and 1D map (6.26) respectively. We see that the existence of the spring area in the 3D map does not imply the existence of the same in the 1D map. Other parameters fixed as in Figure 6.7.

6.4.2 Secondary homoclinic orbits

In this section we analyze a particular type of homoclinic orbits, i.e. *secondary* homoclinic orbits which – after leaving the saddle along the unstable manifold – make two global excursions before returning to the saddle.

We look at the existence of these homoclinic orbits close to the primary homoclinic orbit in (6.2), upon perturbing parameters μ_1 and μ_2. The existence of the orbits is a codim 1 situation and corresponds to a curve in the (μ_1, μ_2)-plane. As before, we look for these curves in the wild case, where $\nu < 1$. In the tame case $\nu > 1$, they do not exist.

Consider μ 6.9. The secondary homoclinic orbit Γ_1 in the scaled ODE (6.13) leaves the point $y_u = (0, 0, 0, 1) \in \Sigma_u$, along the unstable manifold and crosses Σ_s at $x = (x_1^s, 0, x_3^s, \mu_2)$. From this point, the orbit departs again and this time returns along the stable manifold, thus approaching the origin. The orbit crosses then Σ_s at $y_s = (1, 0, 1, 0)$. Using the 3D model map G defined by (6.49), the condition is

$$G \begin{pmatrix} 1 \\ 1 \\ \mu_2 \end{pmatrix} = \begin{pmatrix} 1 \\ 1 \\ 0 \end{pmatrix}, \tag{6.51}$$

which implies

$$\mu_2 + C_1 \mu_2^{\nu} \sin\left(-\frac{1}{\beta} \ln \mu_2\right) + C_2 \mu_2^{\nu + \mu_1/\beta} = 0. \tag{6.52}$$

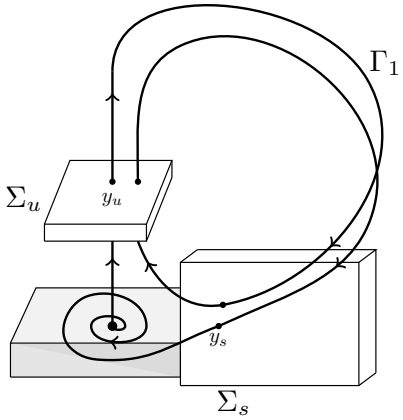

Figure 6.9: Poincaré map for the secondary homoclinic solution Γ_1. Upon leaving y_u along the unstable manifold, the corresponding orbit makes two global excursions and returns to the origin.

Let us define

$$H(\mu) := \mu_2 + C_1\mu_2^{\nu}\sin\left(-\frac{1}{\beta}\ln\mu_2\right) + C_2\mu_2^{\nu+\mu_1/\beta}. \tag{6.53}$$

Note that here μ_2 must be positive. The shape of $H(\mu) = 0$ is similar to the curve $F(x, \mu) = 0$ (from (6.26)). For positive μ_1, it is possible to obtain infinitely many solutions of (6.52) for μ_2 sufficiently small. That is not the case when $\mu_1 < 0$, as there are only finitely many or no non-trivial solutions for μ_2 sufficiently small.

In µ 6.10 the non-trivial solutions are continued with respect to the parameters μ_1 and μ_2 for two different sets of values of C_1 and C_2. We observe three things:

1. There are secondary homoclinic curves which form *horizontal parabolas* and these 'parabolas' approach the primary homoclinic curve $\mu_2 = 0$ asymptotically.
2. These 'parabolas' possess *turning* points where the two upper and lower secondary homoclinic branches merge. The sequence of turning points obtained from successive 'parabolas' appears to approach the origin asymptotically.
3. For different values of C_1 and C_2, the sequence of turning points is located strictly either in the first or second quadrant.

6.4.3 Asymptotics of secondary homoclinics

The observations above can be explained to some extent by asymptotic expressions for the parabolas and the corresponding turning points.

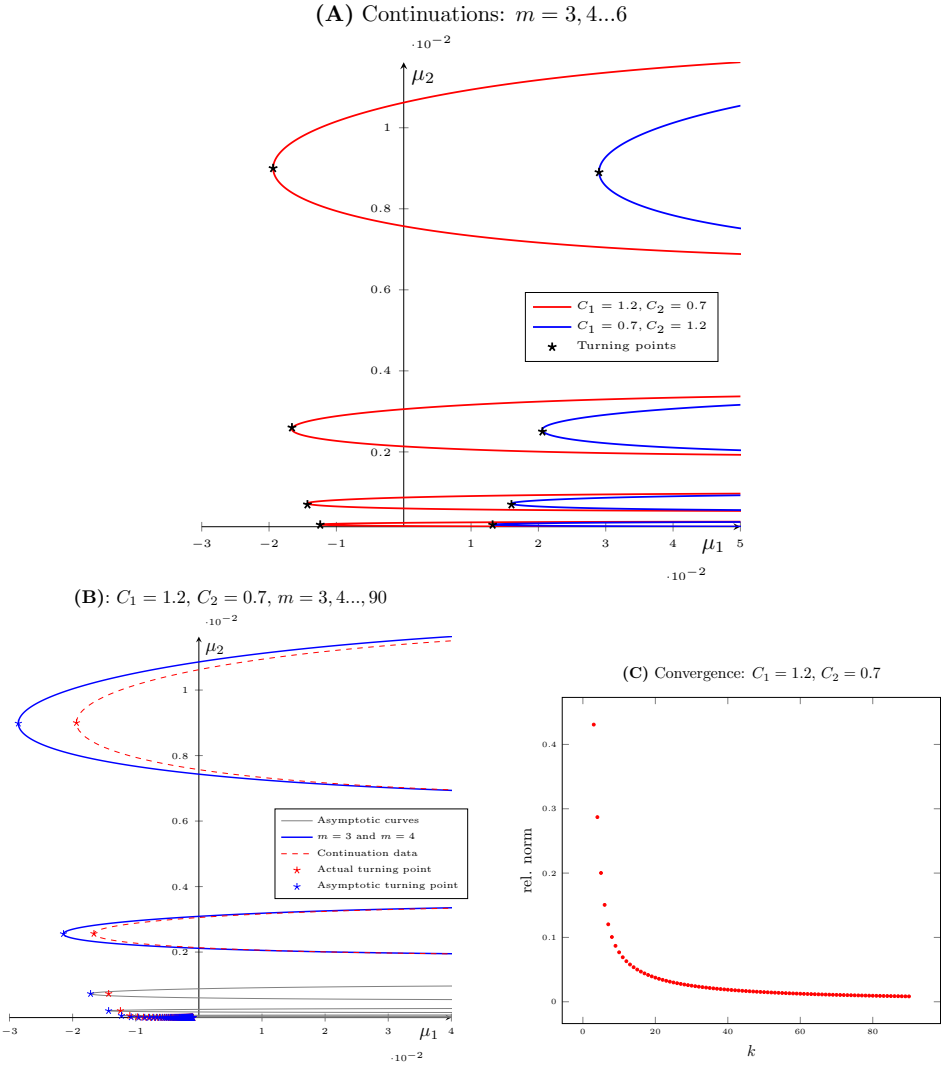

Figure 6.10: Solutions of (6.52) in (μ_1, μ_2)-space. We fix $\beta = 0.2$ and $\nu = 0.5$. In **(A)**, 'parabolas' are obtained via continuation in MATCONTB, for two sets of parameter values. The turning points (in black) are computed with high accuracy by Netwon iterations. In **(B)**, the computed curves are plotted together with asymptotic curves defined by the leading terms in (6.66). In **(C)**, we plot relative norm differences between asymptotic and numerically computed turning points.

Noticing $\mu_2 > 0$, let

$$-\frac{1}{\beta}\ln\mu_2 = 2\pi m + \theta, \tag{6.54}$$

for large $m \in \mathbb{N}$ and $\theta \in (0, 2\pi)$. On dividing both sides by $\mu_2^\nu \neq 0$ and using the above parametrization for μ_2, (6.52) becomes

$$e^{-\beta(1-\nu)(2\pi m+\theta)} + C_1\sin\theta + C_2 e^{-\mu_1(2\pi m+\theta)} = 0. \tag{6.55}$$

On simplifying, we get

$$\sin\theta = -\frac{C_2}{C_1}e^{-2\pi\mu_1 m}(1-\mu_1\theta + O(\mu_1^2)) + O(e^{-\alpha m}), \tag{6.56}$$

where $\alpha = 2\pi\beta(1-\nu)$. For large m and negative μ_1, a solution θ exists only for small $|\mu_1|$. Thus we get two solutions θ from (6.56),

$$\begin{aligned} \theta_1 &= \theta_0^m + 2\pi\delta_{i1} + O(1/m), \\ \theta_2 &= \pi - \theta_0^m + O(1/m), \end{aligned} \tag{6.57}$$

where

$$\theta_0^m := \arcsin\left(-\frac{C_2}{C_1}e^{-2\pi\mu_1 m}\right),$$

the index $i = -\text{sign}(C_2)$ and δ_{ij} is the Kronecker delta. Thus the expressions for two 'half-parabolas' are

$$\begin{cases} \mu_2^{(m,1)} = e^{-\beta(2\pi m+\theta_0^m+2\pi\delta_{i1}}(1+O(1/m)), \\ \mu_2^{(m,2)} = e^{-\beta(2\pi m+\pi-\theta_0^m)}(1+O(1/m)). \end{cases} \tag{6.58}$$

Taking derivative with respect to θ in (6.56) gives

$$\cos\theta = \frac{C_2}{C_1}e^{-2\pi\mu_1 m}(\mu_1 + O(\mu_1^2)) + O(e^{-\alpha m}). \tag{6.59}$$

Solving (6.56) and (6.59) together gives the condition for turning points. Using the two conditions gives,

$$\frac{C_2^2}{C_1^2}e^{-4\pi\mu_1 m}(1+O(\mu_1)) + O(e^{-\alpha m}) = 1. \tag{6.60}$$

From this we get μ_1,

$$\mu_1 = \frac{1}{4\pi m}\left[\ln\left(\frac{C_2^2}{C_1^2}\right) + O\left(\frac{1}{m}\right)\right], \tag{6.61}$$

which also follows from the condition

$$\sin^2\theta = 1. \tag{6.62}$$

Thus the sequence of turning points is given by

$$\begin{pmatrix} \mu_1^{(m)} \\ \mu_2^{(m)} \end{pmatrix} = \begin{pmatrix} \frac{1}{(4\pi m)}\left(\ln\left(\frac{C_2^2}{C_1^2}\right) + O\left(\frac{1}{m}\right)\right) \\ e^{-\beta(2\pi m+\theta_0)}\left(1+O\left(\frac{1}{m}\right)\right) \end{pmatrix}, \tag{6.63}$$

where

$$\theta_0 = \begin{cases} \pi/2, & \text{if } C_2 < 0, \\ 3\pi/2, & \text{if } C_2 > 0. \end{cases} \tag{6.64}$$

We summarize the results in the following lemma.

Lemma 6.4.1. *For the 3D model map G defined by* (6.22)*, the condition*

$$G\begin{pmatrix} 1 \\ 1 \\ \mu_2 \end{pmatrix} = \begin{pmatrix} 1 \\ 1 \\ 0 \end{pmatrix} \tag{6.65}$$

defines in a neighbourhood of the origin of the (μ_1, μ_2)-plane, an infinite sequence of 'parabolas' $Hom_m^{(2)}$, $m \in \mathbb{N}$, that accumulate onto the half axis $\mu_2 = 0$ with $\mu_1 \geq 0$. Each parabola is formed by two branches with the following asymptotic representation:

$$\begin{cases} \mu_2^{(m,1)} = e^{-\beta_0(2\pi m+\theta_0^m+2\pi\delta_{i1}}\left(1+O\left(\frac{1}{m}\right)\right), \\ \mu_2^{(m,2)} = e^{-\beta_0(2\pi m+\pi-\theta_0^m)}\left(1+O\left(\frac{1}{m}\right)\right), \end{cases} \tag{6.66}$$

where

$$\theta_0^m := \arcsin\left(-\frac{C_2^0}{C_1^0}e^{-2\pi\mu_1 m}\right).$$

These branches meet at a sequence of turning points $T_m^{(2)}$, which converges to the origin of the (μ_1, μ_2)-plane and is given by

$$T_m^{(2)} = \begin{pmatrix} \mu_1^{(m)} \\ \mu_2^{(m)} \end{pmatrix} = \begin{pmatrix} \frac{1}{(4\pi m)}\left(\ln\left[\frac{(C_2^0)^2}{(C_1^0)^2}\right] + O\left(\frac{1}{m}\right)\right) \\ e^{-\beta_0(\pi m+\theta_0)}\left(1+O\left(\frac{1}{m}\right)\right) \end{pmatrix}, \tag{6.67}$$

where

$$\theta_0 = \begin{cases} \pi/2, & \text{if } C_2 < 0, \\ 3\pi/2, & \text{if } C_2 > 0. \end{cases} \tag{6.68}$$

6.5 Interpretation for the original ODE system

Let us consider the original 4D system (6.2) in the linearizing coordinates near the equilibrium, the geometric construction in Figure 6.4 and the full 3D map Π defined by (6.20).

Fixed points of this map Π in Σ_s correspond to periodic orbits, thus period-doubling and fold bifurcations of these fixed points of this map correspond to the same bifurcations of periodic orbits in the original ODE system.

The second iterate of the map (6.20), for $\mu_2 > 0$, defines an orbit in the original system (6.2) which makes an extra global excursion before returning to Σ_u. Starting at a point in the unstable 1D manifold of the equilibrium and letting the third component of the image go to zero, implies that we consider an orbit of the ODE that departs along the unstable manifold and returns along the stable manifold back to the saddle. This orbit is therefore a secondary homoclinic orbit near the primary one.

Using Lemmas 6.3.1 and 6.4.1 we are now able to formulate our main results in terms of the original 4D ODE near the wild 3DL-homoclinic transition. It follows from the fact that taking into account the $o(\|x\|^\nu)$-term in (6.20) does not alter the leading terms in all expressions, which further implies that the given asymptotics are the same for the truncated map (6.49) and full 3D return map (6.20).

Theorem 6.5.1. *Consider a smooth 4D ODE system depending on two parameters*

$$\dot{x} = f(x, \alpha), \quad x \in \mathbb{R}^4, \ \alpha \in \mathbb{R}^2. \tag{6.69}$$

Suppose that at $\alpha = 0$ the system (6.69) satisfies the following assumptions:

> **(A.1)** *The eigenvalues of the linearisation at the critical 3DL equilibrium $x = 0$ are*
>
> $$\delta_0, \delta_0 \pm i\omega_0 \text{ and } \epsilon_0,$$
>
> *where $\delta_0 < 0, \omega_0 > 0$, $\epsilon_0 > 0$ and $\sigma_0 = \delta_0 + \epsilon_0 > 0$.*
>
> **(A.2)** *There exists a primary homoclinic orbit Γ_0 to this 3DL equilibrium.*

Then, in addition to the primary homoclinic curve $Hom^{(1)}$, the bifurcation set of (6.69) in a neighborhood of $\alpha = 0$ generically contains the following elements:

(i) *An infinite number of fold bifurcation curves $LP_n^{(1)}, n \in \mathbb{N}$, along which limit cycles with multiplier $+1$ exist making one global excursion and a number of small turns near the equilibrium. These curves accumulate to the saddle-focus part of the primary homoclinic curve. Each curve resembles a 'horn' consisting of two branches that meet at a cusp point $CP_n^{(1)}$. The sequence of cusp points converges to $\alpha = 0$.*

(ii) *An infinite number of period-doubling bifurcation curves* $PD_n^{(1)}, n \in \mathbb{N}$, *along which limit cycles with multiplier* -1 *exist making one global excursion and a number of small turns near the equilibrium. Away from the cusp points* $CP_n^{(1)}$, *these period-doubling curves have the same asymptotic properties as the fold bifurcation curves* $LP_n^{(1)}$. *These period-doubling curves could either be smooth or have self-intersections developing small loops around the corresponding cusp points.*

(iii) *An infinite number of secondary homoclinic curves* $Hom_m^{(2)}, m \in \mathbb{N}$, *along which the equilibrium has homoclinic orbits making two global excursions and a number of turns near the equilibrium after the first global excursion. These curves also accumulate to the saddle-focus part of the primary homoclinic curve. Each curve resembles a 'parabola' and the sequence of turning points converges to* $\alpha = 0$.

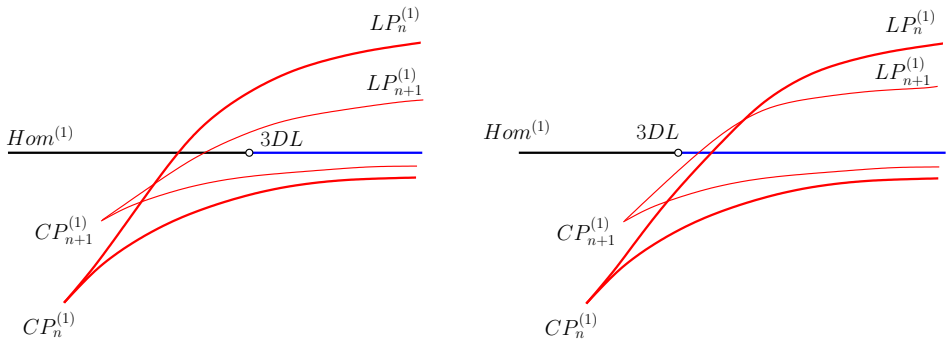

Figure 6.11: A sketch of two consecutive LP horns from Theorem 6.5.1. The saddle-focus part of $Hom^{(1)}$ branch is drawn in blue. The difference between cases **(a)** and **(b)** is explained in the text.

The genericity mentioned in the theorem means the nondegeneracy conditions **(A.3)-(A.5)**. Part (i) of Theorem 6.5.1 is illustrated in Figure 6.11. Notice that $LP_n^{(1)}$ curves can intersect the primary homoclinic branch $Hom^{(1)}$ either at saddle points (Figure 6.11(a)) or at saddle-focus points (Figure 6.11(b)). In terms of the 1D (or 3D) model map these cases correspond to $C_1^0 > |C_2^0|$ or $0 < C_1^0 < |C_2^0|$, respectively. See equation (6.38).

Part (iii) of Theorem 6.5.1 is illustrated in Figure 6.12. Notice that the turning points of the secondary homoclinic curves $Hom_m^{(2)}$ approach the 3DL-transition point on $Hom^{(1)}$ either along its saddle part (Figure 6.12(a)) or its saddle-focus part (Figure 6.12(b)). Note in case (a) we have an infinite sequence of pairs of secondary 3DL-transitions accumulating to the primary 3DL-transition. In terms of the 2D (or 3D) model map these cases also correspond to $C_1^0 > |C_2^0|$ or

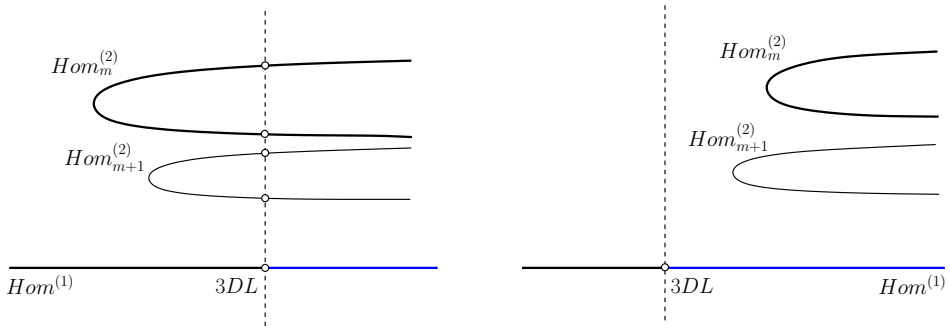

Figure 6.12: A sketch of two consecutive secondary homoclinic curves from Theorem 6.5.1. The saddle-focus part of $Hom^{(1)}$ branch is drawn in blue. The difference between cases **(a)** and **(b)** is explained in the text. The vertical dashed line indicates the saddle to saddle-focus transition. In case **(a)** the points where the secondary homoclinic curves intersect the dashed line correspond to secondary 3DL-transitions.

$C_1^0 < |C_2^0|$, respectively. See equation (6.61).

Our numerical analysis of the truncated model 3D map (6.22) also reveals NS curves in very small domains between the PD- and LP-curves. These curves correspond to *torus* bifurcation of cycles in the ODE system and do not exist for all combinations of (C_1^0, C_2^0). The end points of the NS segment are strong resonance points. There are other codimension 2 points, i.e. GPD and LPPD. All these points will also be present in the generic ODE system and should form sequences that converge to the 3DL-transition point.

6.6 Examples

In this section we study the presence of the 3DL-transition in two 4D ODE models.

6.6.1 Neural field model

In [186], a 3DL-transition was observed in a traveling wave system for a neural field equation. The corresponding ODE system is

$$\begin{cases} \dot{u} &= \dfrac{-u+\psi-a}{c}, \\ \dot{\phi} &= \phi, \\ \dot{\psi} &= \psi - f(u), \\ \dot{a} &= \dfrac{\kappa u - a}{c\tau}, \end{cases} \tag{6.70}$$

where $f(u) = (1 + \exp(\beta(u - \theta)))^{-1}$. The parameters $\beta = 20, \tau = 4.4, \theta = 0.3$ are fixed and κ, c are varied. The adaptation strength κ influences what wavespeeds c are admissible. Figure 6.13 (left) shows a part of the bifurcation diagram where the homoclinic orbit corresponding to a traveling wave is recomputed using MATCONTB [344, 345]. The upper part of this curve involves stable waves. On the homoclinic orbit we have detected two codim 2 bifurcation points. The first is the 3DL-point at $(\kappa, c) \approx (0.7413, 0.4213)$, while a neutral saddle (WT) occurs at $(\kappa, c) \approx (0.7415, 0.5232)$. The real part of the eigenvalues along the branch is shown in Figure 6.13 (right). At the 3DL-point we have eigenvalues $\lambda_1 = 0.9847, \lambda_2 = -1.2999, \lambda_{3,4} = -1.2999 \pm 0.058i$. So this concerns the *tame* case ($\nu_0 > 1$), while the saddle-focus switches from tame to wild at the neutral saddle (WT). Next we were able to locate two LPC-'horns' with corresponding cusps (using 120 mesh points with default tolerances). As predicted, we observe only finitely many 'horns' as this example exhibits the tame case. Note that CP^2 corresponds to a cycle with higher period than CP^1, and is further away from 3DL.

The significance of the two codim 2 points is as follows. As we start from $c = 0.4$ and increase c, we have a saddle-homoclinic orbit and move past the 3DL-point. We then have a tame saddle-focus homoclinic orbit. For nearby parameters, there are only finitely many periodic orbits. For the traveling waves, this implies the existence of a finite number of periodic pulses (*wave trains*), see [186] for more details. The additional wave trains appear from the limit point of cycle-bifurcations. Beyond the WT-point, there are infinitely many such waves.

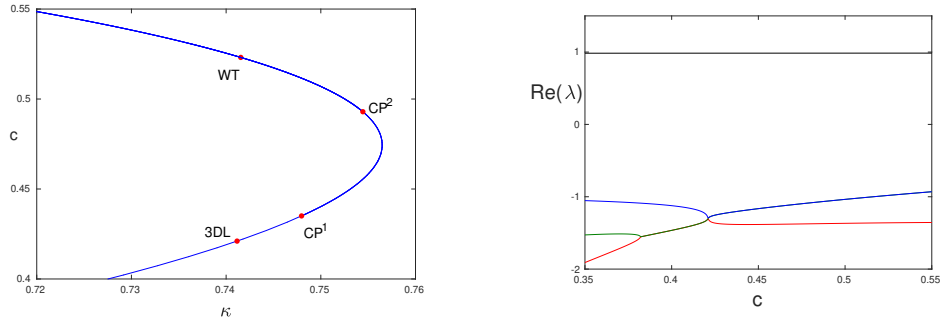

(a) Partial bifurcation diagram

(b) Real part of eigenvalues

Figure 6.13: Bifurcation diagram of system (6.70). (a) The homoclinic bifurcation curve exhibits two codim 2 points, 3DL and WT. Near the homoclinic bifurcation curve there are two more fold of cycle bifurcation curves. They are too close to the homoclinic to be resolved, but both fold curves exhibit a cusp bifurcation $\mathrm{CP}^{1,2}$. (b) Real part of eigenvalues of the saddle on the homoclinic bifurcation curve. At $c = 0.4213$, the three stable eigenvalues are distinct but have equal real parts. At $c = 0.5232$, the saddle quantity vanishes.

6.6.2 Lorenz-Stenflo model

As an example of a wild 3DL transition, we study the Lorenz-Stenflo (LS) equations. These equations are a generalization of the well-known Lorenz equations [346], that describe low-frequency, short-wavelength acoustic-gravity perturbations in the atmosphere with additional dependence on the earth's rotation. The LS equations are as follows:

$$\begin{cases} \dot{x} &= \sigma(y-x)+su, \\ \dot{y} &= rx-xz-y, \\ \dot{z} &= xy-bz, \\ \dot{u} &= -x-\sigma u, \end{cases} \tag{6.71}$$

where σ is the Prandtl number, r is a generalized Rayleigh parameter, b is a positive parameter and s is a new parameter dependent on the Earth's rotation [347]. Setting $s=0$ reduces the first three equations in (6.73) back to the original Lorenz model. The system (6.71) demonstrates chaotic dynamics and has a very complicated bifurcation diagram [348, 349, 350].

System (6.71) possesses the $\mathbb{Z}_2$-symmetry

$$(x,y,z,u) \mapsto (-x,-y,z,-u),$$

and has one or three equilibria (the trivial equilibrium exists always). The system exhibits a wild 3DL-transition of the primary homoclinic orbit to the trivial equilibrium at parameter values,

$$\sigma = 2,\ s = 203.47975,\ r = 126.43527,\ b = 6, \tag{6.72}$$

for which the eigenvalues are $\delta_0 \pm i\omega_0$, δ_0 and ϵ_0 with $\delta_0 = -6$, $\omega_0 \approx 2.5708$, and $\epsilon_0 \approx 7$, so that $\nu_0 < 1$ indeed. However, the corresponding PD and LP curves are difficult to resolve due to highly contractive properties close to the transition, caused by large real parts of the eigenvalues at the trivial equilibrium. Moreover, its bifurcation diagram will include additional bifurcation curves, e.g. related to (symmetric) cycles and heteroclinic orbits.

To overcome this, we perturb the system to get:

$$\begin{cases} \dot{x} &= \sigma(y-x)+su, \\ \dot{y} &= rx-xz-y+\boldsymbol{\epsilon_1 z}, \\ \dot{z} &= xy-bz, \\ \dot{u} &= -x-\sigma u+\boldsymbol{\epsilon_2 y}, \end{cases} \tag{6.73}$$

where the bold expressions are perturbation terms. This system is not $\mathbb{Z}_2$-symmetric anymore, but still has a trivial equilibrium for all parameter values. We are not aware of any physical interpretation of the added terms.

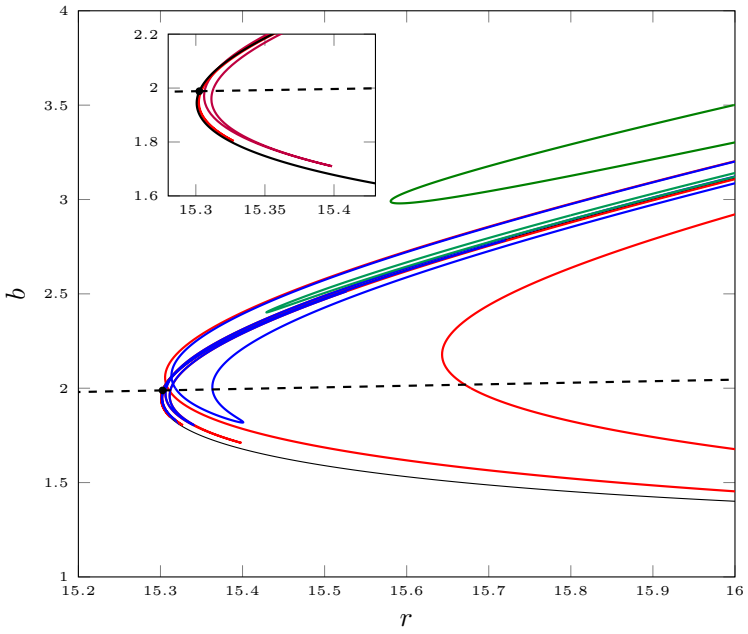

Figure 6.14: Bifurcation curves near a wild 3DL-transition in the (b, r)-plane: cyclic folds (red), period-doublings (blue), primary homoclinic (black), 3DL equilibrium transition (dashed black) and secondary homoclinics (green). For other parameter values, see (6.74).

The trivial equilibrium has homoclinic orbits, and in µ 6.14, we see a wild 3DL transition along the primary homoclinic curve (black) in the perturbed LS system (6.73) with

$$\sigma = 0.1,\ s = 33,\ \epsilon_1 = 0.1,\ \epsilon_2 = 0.3. \tag{6.74}$$

The 3DL-transition point is located at

$$(r, b) \approx (15.302531, 1.9884).$$

The corresponding eigenvalues are $\delta_0 \pm i\omega_0, \delta_0$, and ϵ_0 with $\delta_0 \approx -1.9884, \omega_0 \approx 6.2265, \epsilon_0 \approx 2.7769$, so that $\nu_0 < 1$ as well.

We clearly see PD (blue) and LP (red) curves accumulating onto the primary homoclinic curve according to the theory. The PD curve within each 'horn' forms a saddle area. The secondary homoclinic curves (green) form 'parabolas' on one side of the primary homoclinic curve as expected. The curve of trivial equilibria with a 3D stable eigenspace is shown as a dashed line. The cusp points on each LP horn form a sequence, and asymptotically approach the 3DL point at the intersection of the black curve with the dashed line. The inset shows only the LP horns. For this model the bifurcation curves have been computed using MATCONTB [344] also based on [351, 345]. There is, however, no stable

chaotic dynamics in the parameter range of μ 6.14.

We have also computed *kneading indices* [352, 353] to characterize the nature of attractors in parameter space in more detail. At each point in the parameter space, an orbit is computed starting from a phase point near the trivial equilibrium shifted in the unstable direction with x negative. Next, the number of extrema in the x-variable are indexed as follows. For the ith extremum at time t_i we have

$$c_i = \begin{cases} 1, & \text{if } x(t_i) < 0, \\ 0, & \text{if } x(t_i) > 0. \end{cases} \tag{6.75}$$

Next we compute the finite approximation of the *kneading index*,

$$K = \sum_{i=1}^{N} c_i q^i, \tag{6.76}$$

where q is chosen to be less than 1 and N is finite. The value of K itself bears no meaning, but a change in index may quantify the following events: either there is a homoclinic bifurcation, or one of the extrema of the time series passes zero. The latter is not a bifurcation as there is no structural change in the dynamics. It is difficult, however, to eliminate such false bifurcations automatically. In Figure 6.15 we overlay homoclinic bifurcation curves to find agreement between changes in kneading index and homoclinic bifurcation curves. The changes in color indicate where one may find a homoclinic bifurcation. Kneading indices are typically used for symmetric systems which allow a clear threshold to set c_i, but as a first inventory of homoclinic bifurcations prove rather useful here, e.g. the double and triple homoclinic bifurcation curves.

6.7 Discussion

We have studied bifurcation diagrams of 4D two-parameter ODEs having at some critical parameter values a homoclinic orbit to an hyperbolic equilibrium with one simple unstable eigenvalue and three simple stable eigenvalues (one real and a complex-conjugate pair). We demonstrated that this phenomenon occurs in two 4D ODE systems appearing in applications. We focused on the case where a transition from a saddle homoclinic orbit to Shilnikov's wild saddle-focus homoclinic orbit takes place at the critical parameter values. Similar to the 3D Belyakov's saddle to wild saddle-focus homoclinic transition, we found infinite sequences of codim 1 bifurcations curves related to limit cycles, i.e. folds and period-doublings, and secondary homoclinic orbits accumulating on the primary (wild) saddle-focus homoclinic branch. However, there is a striking difference between these two cases. While in the standard Belyakov case all bifurcation curves approach the codim 2 point in the parameter plane tangentially to the saddle-focus homoclinic curve (having actually tangency of infinite

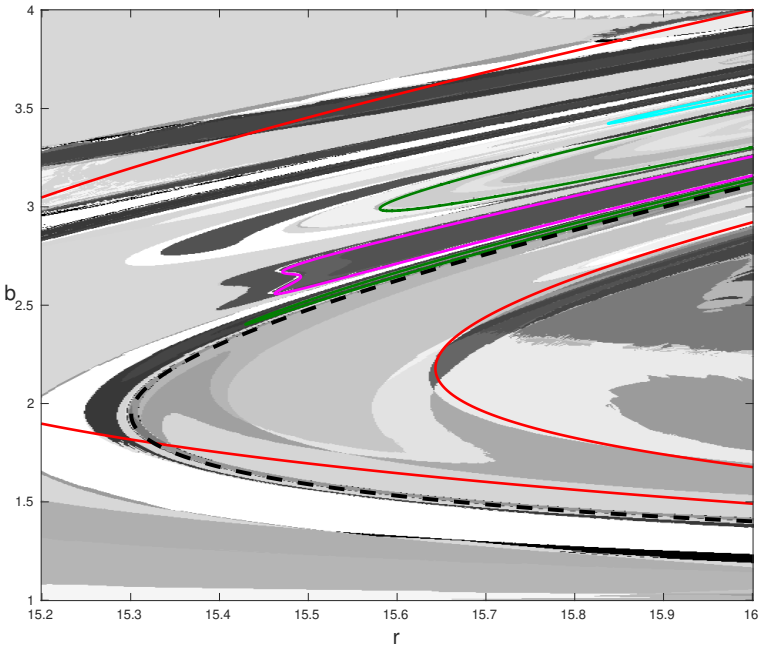

Figure 6.15: Kneading indices for the perturbed Lorenz-Stenflo model (6.73) in the (b, r)-plane for fixed parameters (6.74). Color codes in gray indicate domains with the same kneading index. The following bifurcation curves computed in MATCONT are overlaid: primary homoclinic (black,dashed), secondary homoclinic (green), tertiary homoclinic (pink), quadruple homoclinic (blue) and cyclic fold (red).

order) and form 'bunches', in the considered 3DL case none of them emanates from the codim 2 point. Instead, they form sequences of 'horns' with cusps and other codim 2 bifurcation points, or 'parabolas'. The sequences of codim 2 points and parabola tips indeed converge to the studied homoclinic 3DL point. In a sense, the bifurcation diagram for the considered 3DL-transition resembles more another codim 2 homoclinic bifurcation studied by Belyakov: A transition from tame to wild saddle-focus homoclinic orbit in 3D ODEs, when the saddle quantity vanishes [354]. In that case, fold bifurcation curves for cycles also have cusp points accumulating to the transition point, while the secondary homoclinic curves look like 'parabolas' with tips tending to the transition point. The exact source of this similarity remains a mystery but might be related to the simplicity of all eigenvalues in both cases.

One can employ the C^1-linearisation theorem by Belitskii [355, 326] to get the C^1-equivalence of the flow generated by (6.2) to that corresponding to its linear part, near the equilibrium $O = (0, 0, 0, 0)$:

$$\begin{cases} \dot{x_1} = & \gamma(\mu)x_1 - x_2, \\ \dot{x_2} = & x_1 + \gamma(\mu)x_2, \\ \dot{x_3} = & (\gamma(\mu) - \mu_1)\, x_3, \\ \dot{x_4} = & \beta(\mu)x_4. \end{cases} \tag{6.77}$$

This theorem is applicable, since

$$\text{Re } \lambda_i \neq \text{Re } \lambda_j + \text{Re } \lambda_k$$

for all eigenvalues of the saddle-focus at and near the 3DL homoclinic transition. This would allow one to easily obtain the Poincaré return map (6.20), but only permits to employ its first-order partial derivatives due to lack of smoothness. This would be sufficient to derive asymptotics for the fold and period-doubling bifurcations of the primary limit cycles, as well as those for the secondary homoclinic orbits. However, to verify nondegeneracy conditions for LP and PD bifurcations and to detect codim 2 points, one needs higher-order partial derivatives of the return map Π. Their existence can be granted by using the C^k-linearisation near the equilibrium with sufficiently big $k > 1$. This exists according to the C^k-linearisation theorem by Sternberg [356], if one imposes a finite number of low-order non-resonance conditions on the eigenvalues, i.e.

$$\lambda_i \neq \sum_{j=1}^{4} n_j \lambda_j,$$

where $n_j \geq 0$ and $2 \leq \sum_{j=1}^{4} n_j \leq N$ for some $N = N(k)$ (see also [357, 329]). However, our analysis shows that such extra conditions can be avoided, similar to other homoclinic bifurcation scenarios [328].

For n-dimensional systems, generically the analysis of homoclinic bifurcations can be restricted to the *Homoclinic Center Manifold*, a k-dimensional invariant finitely-smooth manifold that is tangent at the equilibrium to the eigenspace corresponding to the union of all *leading* eigenvalues [358, 338, 359, 360]. Thus, k is the number of all *leading* eigenvalues of the equilibrium, counting their multiplicities. For the considered 3DL saddle to saddle-focus homoclinic transition case, we have $k = 4$. Thus, our analysis of four-dimensional ODEs is sufficient to predict the main features of the bifurcation diagram near this transition in a generic n-dimensional situation. However, some 'gap' conditions should be imposed on the eigenvalues of the critical equilibrium to guarantee more than C^1-smoothness of the homoclinic center manifold that is needed for bifurcation analysis. Whether or not one can avoid using the homoclinic center manifold requires further analysis.

It will also be interesting to study n-homoclinic orbits with $n \geq 2$ near the considered bifurcation and, in particular, investigate whether they could be degenerate. Another challenge would be to prove analytically the existence of infinite sequences of generalized period-doubling points and strong resonances (see Figure 6.7), at least for the truncated 3D model map (6.22). An interesting research direction is also to study the homoclinic 3DL transition in volume-preserving 4D ODEs, where it is always wild and has codim 1.

Chapter 7

General Discussion

This thesis presents novel results surrounding the themes of *data, models* and *bifurcations* from a computational neuroscience perspective. The first part, Chapters 2 and 3, focuses on biophysical models that describe the pathophysiology of ischemic stroke at a local (synaptic) and global (population) level. Next, a data-driven model discovery method that generates parameter-dependent models is presented in Chapter 5. Lastly, Chapter 6 describes the unfolding of a novel homoclinic bifurcation, first observed in the traveling wave frame of a neural field model.

The challenges addressed and methods proposed reflects different approaches to mathematical modeling. On the one hand, in Chapters 3 and 4, the proposed models are biophysical and detailed. They are interpretable, corroborate to multiple isolated experiments and provide an *in silico* platform for exploring the effect of several interventions on physiological function. On the other hand, the models proposed in Chapter 5 and 6 arise from analyzing underlying bifurcations in physical phenomena. In this case, the models are desired to be compact - with as few nonlinear terms as possible - to be able to efficiently describe phenomena resulting from higher-dimensional dynamics. This dichotomy of bottom-up and top-down modeling and its consequences are highlighted in the following discussion.

In this chapter, the results of this thesis are discussed in the context of current challenges in the domains of ischemia, computational modeling and bifurcation analysis. Next, future work is proposed to extend the validity of the results shown.

7.1 Consequences of biophysical modeling

In Chapter 3, a novel biophysical model of the tripartite synapse is introduced, which explicitly describes ion dynamics in a presynaptic neuron, the synaptic

cleft and a perisynaptic astrocyte process. As part of the model, an elaborate glutamate recycling scheme is also proposed, that describes Ca^{2+}-catalyzed vesicular packing and glutamate transport mediated by excitatory amino acid transporters (EAATs). Thus for the first time, a mathematical formulation of ion transport of Na^+, K^+, Cl^-, Ca^{2+} and glutamate at the tripartite synapse is described in the context of ischemia. In Chapter 4, this formulation is extended to a population level. The proposed neural mass uses explicit ion dynamics to describe synaptic currents and the synaptic response, based on a novel firing rate function depending on ion concentrations and Nernst potentials, as done in [139].

In both chapters, the elaborate models contain descriptions of specific ion channels and additional properties such as cellular volume and inter-population network connectivities. Consequently, the models are subjected to differential sensitivity analysis with respect to these factors. The aim with such analyses is to understand how these neural systems adapt to varying conditions during ischemia, and corroborate the model to previously observed experimental data.

In Chapter 3, it is demonstrated that synapses with smaller extracellular spaces and weaker ATPases present higher vulnerability to low-energy conditions. Both these properties feature in adult brains and may explain the effect of aging on ischemic tolerance [207]. Varying extracellular sizes and ATPase strengths can also manifest in different brain regions, which can thus explain the selective survival of lower brainstem neurons during low-energy conditions [15, 225]. By blocking specific ion channels post energy-restoration, it was found that recovery from a depolarized state is possible by shutting down voltage-gated Na^+ and K^+ transport. These observations are consistent with previous experimental literature that suggest these therapeutic measures [228, 229]. Following novel experiments of Cl^- dynamics during ischemia [12], it was further shown that the differential behavior of Cl^- dynamics in different brain regions may be attributed to varying expressions of the cotransporters KCC and NKCC1.

On a population level, Chapter 4 focuses on the effect of neuronal Na^+/K^+-ATPase (NKA) and vesicular ATPase (vATP) inhibition, and network dysregulation on synaptic rhythms. It is shown that between the two ATPases, NKA behavior controls synaptic rhythms qualitatively, which is consistent with the ATP-greedy nature of NKA [41]. At a network level, examining the strength of thalamocortical connectivity shows that the interface of healthy rhythms and synaptic arrest is marked by low-voltage oscillations or burst-like behavior, similar to generalized periodic discharges (GPDs) [292]. These interface points are marked by either subcritical or supercritical Hopf bifurcations, and it is proposed that a generalized Hopf bifurcation controls the transition between the Hopf criticalities.

In both chapters, a bottom-up modeling approach is used to address biological and clinical challenges. These descriptions rely crucially on experimental data of low-energy dynamics at the synaptic and population level. The data is obtained from several isolated experiments on Na^+ and K^+ dynamics [11], membrane

potential changes [15] and EEG rhythms [262, 14]. However, the experimental observations do not constitute the entirety of the modeled state-space. For instance, time-traces of neuronal K^+ and volume changes remained unavailable during the modeling process and need to be modeled. Thus, ion homeostasis was described using biophysical models inspired by previously published work [102, 43, 89]. As a result, these models are robust formulations for detailed studies of ion dysregulation and synaptic reorganization during low-energy conditions or possibly other scenarios such as epilepsy and spreading depolarization.

7.2 Parameter-dependency in models

The second part of this thesis, Chapters 5 and 6, explores transitions in modeling from two different perspectives, data and analysis. In Chapter 5, the working assumption is that the characteristic behavior of the underlying bifurcations in data is known, and data-driven techniques are used to discover these bifurcations. However, in Chapter 6, the canonical dynamics of the underlying bifurcation are unknown, and its unfolding is described using a model map. In both cases, the underlying models are parameter-dependent and are required to be compact and simple - the model equations are described with as few nonlinear terms as possible.

Models constructed using biophysical principles can often result in complex descriptions with several parameters, of which not all can be inferred or estimated. Moreover, these models are not always 'feature-rich' - the complex descriptions do not necessarily manifest in rich qualitative features. For instance, the description of glutamate recycling in Chapter 3 amounts to 7 differential equations and 11 parameters. The bifurcation diagram of the full system results in two stable states of glutamate - baseline and pathological. A phenomenological model in place could replicate this bistable behavior in far fewer equations and parameters. Compact phenomenological representations of complex subsystems can be very useful when embedding them in spatial extensions and networks. However, model equations and predictions arising from such representations can be difficult to interpret.

The key element in feature-rich, compact phenomenological models is the presence of various bifurcations, that govern the transition between several desirable behavioral patterns. Current model discovery methods do not account for parameter variance and thus are only partially able to address this issue [27, 26]. In Chapter 5, normal forms are used as the low-dimensional models underlying high-dimensional parameter-varying data. The low-dimensional representation is achieved by using coupled autoencoders of state and parameter and forcing the latent space to be governed by the corresponding normal form equation. As a result, parameter-dependent low-dimensional models are discovered directly from data for the first time. The method is applied to several

pattern transitions arising in neuroscience and physics.
The idea of using data-driven methods in conjunction with normal forms and bifurcation theory is not entirely new. In [361] zigzag persistence homology is used to identify the presence of Hopf bifurcations in datasets. Diffusion maps have been used to identify the location of the time-trace in the corresponding bifurcation diagram [168]. However, the approach in Chapter 5 is the first of its kind to perform model discovery in the context of parameter-varying datasets - and provides tangible evolution equations. The method can also be interpreted as a data-driven center manifold reduction and is the first step in using normal form equations as building blocks for model discovery.
In Chapter 5, the *a priori* knowledge of canonical transitions in parameter-varying datasets are embedded in normal form equations, which are exploited to construct low-dimensional representations of high-dimensional datasets. However, it is common to come across bifurcations in models that are not associated with normal forms, but via *model maps*. These model maps are typically used to describe global bifurcations of homoclinic and heteroclinic orbits [169], where the corresponding Poincaré return map changes from system to system.
In Chapter 6, a novel homoclinic bifurcation dynamical in the traveling wave frame of a neural field model [186] is studied, and a model map is constructed to describe its unfolding. The bifurcation corresponds to a homoclinic saddle to saddle-focus transition, with a three-dimensional leading (3DL) stable eigenspace and a one-dimensional leading unstable eigenspace at the criticality. It is shown that in the wild case, the Shilnikov approach predicts a cascade of period-doubling, limit point, secondary homoclinic curves and even secondary 3DL points in the vicinity of the codimension two bifurcation point.
The unfolding of the bifurcation is remarkably different from the known Belyakov-type saddle to saddle-focus homoclinic transitions, particularly the existence of a cascade of secondary codimension two points in the vicinity of the bifurcation. The predictions of the bifurcation analysis for the wild case were confirmed only in a perturbed Lorenz-Stenflo model. Nevertheless, the consequences in the original neural field equation are interesting. The model map predicts the presence of a cascade of traveling pulses and waves close by, including pulse solutions with multiple bumps.

7.3 Future work and outlook

The scope of work covered in this thesis advances efforts in bottom-up and top-down approaches in the context of computational neuroscience. This section discusses possible extensions in the future points in these directions.
In Chapter 3, glutamate recycling is explicitly modeled, which describes changing glutamate concentrations in the synaptic cleft during low-energy conditions. Given the small and dynamic volume of the cleft, multiple

glutamate release sites and disparate glutamate measurements in literature [362], calibrating glutamate time traces from the model is challenging. Explicit modeling of a postsynaptic compartment would help perform this calibration and complete the *tripartite* synapse model. There is plentiful data on excitatory postsynaptic potentials (EPSPs) [363] in response to incoming activity from a presynaptic neuron, also in low-energy conditions [364, 365]. The postsynaptic potentials can be described by explicilty modeling AMPA and NMDA receptors in an extra neuronal compartment - as done in [97, 100, 252] - whose dynamics depend on extracellular glutamate concentration. Cleft glutamate accumulation during low-energy conditions can desensitize these receptors. Such an approach allows for possible explanation of early postsynaptic failure during low-energy conditions, where presynaptic function remains intact.

On the other hand, early synaptic arrest in excitatory synapses has also been attributed to presynaptic failure [13]. This phenomenon is exploited in the neural mass model in Chapter 4, but remains a challenge for the tripartite synapse model. This is due to the glutamate recycling scheme, that does not have a mechanism for glutamate replenishment in the presynaptic terminal. Model simulations show that persistent energy deprivation causes a an accumulation of extracellular glutamate and depletion of presynaptic glutamate storage. Consequently, all extracellular glutamate is absorbed by strong astrocyte EAAT activity following energy restoration. This behavior is accompanied by irreversible cellular depolarization and cell swelling of the full system. To study selective presynaptic failure, it is thus vital to model a more efficient glutamate recycling scheme in order to break this 'synchrony'. A candidate pathway is the glutamate-glutamine cycle as modeled, for instance, in [366], which allows astrocyte-driven replenishment of neuronal glutamate, resulting in a feedback mechanism. In Chapter 4, differential sensitivity of oxygen deprivation to the activity of the two ATPases: NKA and the vesicular ATPase (vATPase) is studied. The vATPase model is modeled simply as a sigmoidal function of extracellular oxygen concentration and helps to explain the selective presynaptic phenomenon in low-energy conditions. In conjunction with the postsynaptic compartment, the vATPase model can also be included in the tripartite synapse model in Chapter 3 to understand the differential effects of presynaptic and postsynaptic failure on synaptic communication during low-energy conditions.

In Chapter 4 a neural mass model is developed that depends on ion dynamics. The key modeling elements governing the pathophysiology of population rhythms are the firing-rate function and the interconnected synaptic currents. Both depend explicitly on ion concentrations. Recent experimental work on post-stroke therapy shows that optogenetically stimulation of thalamocortical and corticothalamic axons aids in restoring sensory function [77, 367]. The neural mass demonstrates the differential effects of altered thalamocortical projections on healthy rhythmic behavior, while altered corticothalamic projections do not disrupt healthy activity. The difference arises possibly due to the simple as-

sumptions in connectivities and functional differences between the populations. Modeling detailed synaptic currents, response functions and functional differences between all populations would permit a detailed study of stroke-mediated circuit rewiring and therapeutic measures.

The firing-rate function now explicitly depends on ion dynamics. This can be directly implemented in a neural field model coupled with extracellular ion diffusion and pointwise uptake. Using such a model, the onset and propagation of waves of ion dynamics and spreading depolarization can be studied, that are associated with early transient energy deprivation [368, 369, 11]. The multi-scale approach of combining biophysics, neural masses and neural fields have been explored in previous works such as [127, 370] and can reconcile local events such as ion dysregulation and presynaptic/postsynaptic failure with global events such as spreading depolarization and impairment in synaptic communication, during low-energy conditions.

The model discovery method introduced in Chapter 5 is the groundwork for building parsimonious, parameter-dependent models directly from data. The introduced method discovers transformations from datasets directly to the corresponding normal form equation. Several further steps are thus required to elevate the approach to perform generalizable model discovery. Consider for instance, the scalar ODE problem introduced in Chapter 5. Ideally the model discovery method should obtain the governing ODE directly from data, requiring several normal forms (limit point, pitchfork and transcritical) to be simultaneously discovered close to several bifurcation points. Two key challenges arise: choosing the right normal form, and its validity in state-parameter space.

The first challenge can be addressed by using a refinement-selection process while training the neural networks. This method was deployed for identifying the correct model terms in [26]. There, expansion coefficients for a candidate library of model terms were computed using SINDy. In the normal form autoencoder approach, the model terms are replaced by normal forms, and the refinement would have to be performed by eliminating worst fit (say in l_2) over several epochs. Next, the selected normal form would be valid in a small state-parameter neighborhood of the corresponding bifurcation point. Using SINDy [157], higher-order normal form terms can be computed to expand this neighborhood. However, another challenge arises at the intersection of two possible normal forms. SINDy may again be used to compute functions that mollify the intersecting domains.

Learning neural-network-based transformations to the center manifold results in several local minima, some of which are mitigated with the orientation loss terms introduced in Chapter 5. The normal form autoencoder approach learns mappings between state-parameter spaces of autonomous dynamical systems. It would thus be useful to introduce translational equivariance in the neural networks to accommodate for several local minima arising from translation in time. Convolutional neural networks naturally have translational equivariance

(if combined with max-pooling) [162], and are inherently suitable for multi-channel data, such as higher-dimensional PDEs. Multi-dimensional PDE data can also be systematically compressed using tensor network methods [371, 372]. From a theoretical viewpoint, it is vital to understand whether the discovered latent space defines the relevant center manifold as this has a direct consequence on the existence of solutions to the normal form autoencoder problem. The right choice of network architecture, regularizations and hyperparameters are a standard problem in deep learning theory. However, the solution to the existence problem places constraints on these choices and will provide a focused approach to performing data-driven center manifold reduction.

In Chapter 6, the model map describes the dynamics of the 3DL bifurcation on the homoclinic center manifold. The map contains two critical coefficients, C_1 and C_2, that govern the orientation of the various bifurcation curves around the codimension-two point, which are not explicitly computed for the examples shown. Classical numerical computation of the Poincaré map can reveal these coefficients, which would be useful especially to identify the case where a cascade of secondary 3DL points occur nearby. Recently, SINDy has also been used to compute these maps [373], which can be handy in domains with several saddle periodic orbits, such as with the 3DL bifurcation.

Another peculiar case arises in the traveling wave frame of the neural field model in [186], for $\kappa = 0.7, \theta = 0.3$ and $\tau \approx 4.5$. Varying the eigenvalues of the system with respect to parameter β shows a clear transition from the 3DL ($\tau < 4.5$) to Belyakov ($\tau > 4.5$) case. The transition point corresponds to hyperbolic triple-real leading eigenvalues, i.e., a possible codimension 3 point. As with the 3DL case, the transition occurs only in the tame case ($\nu > 1$), and no interesting behavior is observed nearby. An interesting question thus arises again regarding the unfolding of this codimension 3 point, in the wild case ($\nu < 1$).

Summary

This thesis is concerned with building and analyzing mathematical models in computational neuroscience using *bottom-up* and *top-down* approaches. Models are constructed using biophysical principles to understand the pathophysiology of cerebral ischemia at different spatial and temporal scales. Data-driven techniques in conjunction with machine learning are used to build compact parameter-dependent models from high-dimensional data. Finally, model maps are introduced to explain the generic unfolding of a newly observed bifurcation.

In Chapter 3, a comprehensive biophysical model of a glutamatergic synapse is developed, to identify key determinants of synaptic failure during energy deprivation. The model is based on fundamental biophysical principles, includes dynamics of the most relevant ions, i.e., Na^+, K^+, Ca^{2+}, Cl^- and glutamate, and is calibrated with experimental data. It confirms the critical role of the Na^+/K^+-ATPase in maintaining ion gradients, membrane potentials and cell volumes. The simulations demonstrate that the system exhibits two stable states, one physiological and one pathological. During energy deprivation, the physiological state may disappear, forcing a transit to the pathological state, which can be reverted when blocking voltage-gated Na^+ and K^+ channels. The model predicts that the transition to the pathological state is favoured if the extracellular space fraction is small. A reduction in the extracellular space volume fraction, as, e.g. observed with ageing, will thus promote the brain's susceptibility to ischemic damage. The work thus provides new insights into the brain's ability to recover from energy deprivation, with translational relevance for diagnosis and treatment of ischemic strokes.

In Chapter 4, the relationship between electroencephalogram (EEG phenomenology and cellular biophysical principles is studied using a model of interacting thalamic and cortical neural masses coupled with energy-dependent synaptic transmission. The model faithfully reproduces the characteristic EEG phenomenology during acute cerebral ischemia and shows that synaptic arrest occurs before cell swelling and irreversible neuronal depolarization. The early synaptic arrest is attributed to ion homeostatic failure due to dysfunctional

Na^+/K^+-ATPase. Moreover, it is also shown that the excitatory input from relay cells to the cortex controls rhythmic behavior. In particular, low relay-interneuron interaction manifests in burst-like EEG behavior immediately prior to synaptic arrest. The model thus reconciles the implications of stroke on a cellular, synaptic and circuit level and provides a basis for exploring multi-scale therapeutic interventions.

In Chapter 5, deep learning autoencoders are introduced to discover coordinate transformations that capture the underlying parametric dependence of a dynamical system in terms of its canonical *normal form*, allowing for a simple representation of the parametric dependence and bifurcation structure. The autoencoder constrains the latent variable to adhere to a given normal form, thus allowing it to learn the appropriate coordinate transformation. The method is demonstrated on a number of example problems, showing that it can capture a diverse set of normal forms associated with Hopf, pitchfork, transcritical and/or saddle node bifurcations. This method shows how normal forms can be leveraged as canonical and universal building blocks in deep learning approaches for model discovery and reduced-order modeling.

Finally, in Chapter 6, a saddle to saddle-focus homoclinic transition when the stable leading eigenspace is 3-dimensional (called the 3DL-bifurcation) is analyzed. Here a pair of complex eigenvalues and a real eigenvalue exchange their position relative to the imaginary axis, giving rise to a 3-dimensional stable leading eigenspace at the critical parameter values. This transition is different from the standard Belyakov bifurcation, where a double real eigenvalue splits either into a pair of complex-conjugate eigenvalues or two distinct real eigenvalues. In the wild case, sets of codimension 1 and 2 bifurcation curves are obtained, along with points that asymptotically approach the 3DL-bifurcation point and have a structure that differs from that of the standard Belyakov case. An example of this bifurcation is also provided in a perturbed Lorenz-Stenflo 4D ODE model.

References

[1] A. L. Hodgkin and A. F. Huxley, "A quantitative description of membrane current and its application to conduction and excitation in nerve," *The Journal of Physiology*, vol. 117, no. 4, pp. 500–544, 1952.

[2] B. Ermentrout and D. H. Terman, *Mathematical foundations of neuroscience*, vol. 35. Springer, 2010.

[3] J. Guckenheimer and P. Holmes, *Nonlinear oscillations, dynamical systems, and bifurcations of vector fields*, vol. 42. Springer Science & Business Media, 2013.

[4] Y. A. Kuznetsov, *Elements of Applied Bifurcation Theory*, vol. 112 of *Applied Mathematical Sciences*. Springer-Verlag, New York, third ed., 2004.

[5] E. H. Lo, T. Dalkara, and M. A. Moskowitz, "Mechanisms, challenges and opportunities in stroke," *Nature Reviews Neuroscience*, vol. 4, pp. 399–414, May 2003.

[6] M. D. Robert Teasell and N. Hussein, "Clinical consequences of stroke," *Evidence-Based Review of Stroke Rehabilitation. Ontario: Heart and Stroke Foundation and Canadian Stroke Network*, pp. 1–30, 2016.

[7] R. G. González, "Clinical MRI of acute ischemic stroke," *Journal of Magnetic Resonance Imaging*, vol. 36, pp. 259–271, July 2012.

[8] M. J. A. M. van Putten, *Dynamics of Neural Networks*. Springer Berlin Heidelberg, 2020.

[9] E. Neher and B. Sakmann, "Single-channel currents recorded from membrane of denervated frog muscle fibres," *Nature*, vol. 260, pp. 799–802, Apr. 1976.

[10] M. Y. Berezin and S. Achilefu, "Fluorescence lifetime measurements and biological imaging," *Chemical Reviews*, vol. 110, pp. 2641–2684, Mar. 2010.

[11] N. J. Gerkau, C. Rakers, S. Durry, G. C. Petzold, and C. R. Rose, "Reverse NCX attenuates cellular sodium loading in metabolically compromised cortex," *Cerebral Cortex*, vol. 28, pp. 4264–4280, Nov. 2017.

[12] M. Engels, M. Kalia, S. Rahmati, L. Petersilie, P. Kovermann, M. J. A. M. van Putten, C. R. Rose, H. G. E. Meijer, T. Gensch, and C. Fahlke, "Glial chloride homeostasis under transient ischemic stress," *Frontiers in Cellular Neuroscience*, vol. 15, Sept. 2021.

[13] S. Fedorovich, J. Hofmeijer, M. J. A. M. van Putten, and J. le Feber, "Reduced synaptic vesicle recycling during hypoxia in cultured cortical neurons," *Frontiers in Cellular Neuroscience*, vol. 11, Feb. 2017.

[14] S. Finnigan, A. Wong, and S. Read, "Defining abnormal slow EEG activity in acute ischaemic stroke: Delta/alpha ratio as an optimal QEEG index," *Clinical Neurophysiology*, vol. 127, pp. 1452–1459, Feb. 2016.

[15] C. D. Brisson and R. D. Andrew, "A neuronal population in hypothalamus that dramatically resists acute ischemic injury compared to neocortex," *Journal of Neurophysiology*, vol. 108, pp. 419–430, July 2012.

[16] H. R. Wilson and J. D. Cowan, "A mathematical theory of the functional dynamics of cortical and thalamic nervous tissue," *Kybernetik*, vol. 13, pp. 55–80, Sept. 1973.

[17] S.-I. Amari, "Homogeneous nets of neuron-like elements," *Biological Cybernetics*, vol. 17, pp. 211–220, Mar. 1975.

[18] F. H. L. da Silva, A. Hoeks, H. Smits, and L. H. Zetterberg, "Model of brain rhythmic activity," *Kybernetik*, vol. 15, no. 1, pp. 27–37, 1974.

[19] B. H. Jansen, G. Zouridakis, and M. E. Brandt, "A neurophysiologically-based mathematical model of flash visual evoked potentials," *Biological Cybernetics*, vol. 68, pp. 275–283, Jan. 1993.

[20] D. T. J. Liley and M. Walsh, "The mesoscopic modeling of burst suppression during anesthesia," *Frontiers in Computational Neuroscience*, vol. 7, 2013.

[21] C. Koch and I. Segev, eds., *Methods in Neuronal Modeling: From Synapses to Networks*. Cambridge, MA, USA: MIT Press, 1989.

[22] F. Oschmann, H. Berry, K. Obermayer, and K. Lenk, "From in silico astrocyte cell models to neuron-astrocyte network models: A review," *Brain Research Bulletin*, vol. 136, pp. 76–84, Jan. 2018.

[23] F. G. Donnan, "Theorie der membrangleichgewichte und membranpotentiale bei vorhandensein von nicht dialysierenden elektrolyten. ein beitrag zur physikalisch-chemischen physiologie.," *Zeitschrift für Elektrochemie und angewandte physikalische Chemie*, vol. 17, no. 14, pp. 572–581, 1911.

[24] B. W. Brunton and M. Beyeler, "Data-driven models in human neuroscience and neuroengineering," *Current Opinion in Neurobiology*, vol. 58, pp. 21–29, Oct. 2019.

[25] B. A. Richards, T. P. Lillicrap, P. Beaudoin, Y. Bengio, R. Bogacz, A. Christensen, C. Clopath, R. P. Costa, A. de Berker, S. Ganguli, C. J. Gillon, D. Hafner, A. Kepecs, N. Kriegeskorte, P. Latham, G. W. Lindsay, K. D. Miller, R. Naud, C. C. Pack, P. Poirazi, P. Roelfsema, J. Sacramento, A. Saxe, B. Scellier, A. C. Schapiro, W. Senn, G. Wayne, D. Yamins, F. Zenke, J. Zylberberg, D. Therien, and K. P. Kording, "A deep learning framework for neuroscience," *Nature Neuroscience*, vol. 22, pp. 1761–1770, Oct. 2019.

[26] K. Champion, B. Lusch, J. N. Kutz, and S. L. Brunton, "Data-driven discovery of coordinates and governing equations," *Proceedings of the National Academy of Sciences*, vol. 116, pp. 22445–22451, Oct. 2019.

[27] B. Lusch, J. N. Kutz, and S. L. Brunton, "Deep learning for universal linear embeddings of nonlinear dynamics," *Nature Communications*, vol. 9, Nov. 2018.

[28] J. W. Mink, R. J. Blumenschine, and D. B. Adams, "Ratio of central nervous system to body metabolism in vertebrates: its constancy and functional basis," *American Journal of Physiology-Regulatory, Integrative and Comparative Physiology*, vol. 241, no. 3, pp. R203–R212, 1981. PMID: 7282965.

[29] D. Attwell and S. B. Laughlin, "An energy budget for signaling in the grey matter of the brain," *Journal of Cerebral Blood Flow & Metabolism*, vol. 21, no. 10, pp. 1133–1145, 2001. PMID: 11598490.

[30] G. Yellen, "Fueling thought: Management of glycolysis and oxidative phosphorylation in neuronal metabolism," *Journal of Cell Biology*, vol. 217, pp. 2235–2246, 05 2018.

[31] G. W. Davis, "Not fade away: Mechanisms of neuronal atp homeostasis," *Neuron*, vol. 105, no. 4, pp. 591–593, 2020.

[32] G. Ashrafi and T. A. Ryan, "Glucose metabolism in nerve terminals," *Current Opinion in Neurobiology*, vol. 45, pp. 156–161, 2017. Molecular Neuroscience.

[33] C. R. Rose, "Dfg-research unit 2795: "synapses under stress: Early events induced by metabolic failure at glutamatergic synapses"," *Neuroforum*, vol. 25, no. 1, pp. 61–63, 2019.

[34] T. M. Mathiisen, K. P. Lehre, N. C. Danbolt, and O. P. Ottersen, "The perivascular astroglial sheath provides a complete covering of the brain microvessels: An electron microscopic 3d reconstruction," *Glia*, vol. 58, no. 9, pp. 1094–1103, 2010.

[35] J. W. Deitmer, S. M. Theparambil, I. Ruminot, S. I. Noor, and H. M. Becker, "Energy dynamics in the brain: Contributions of astrocytes to metabolism and ph homeostasis," *Frontiers in Neuroscience*, vol. 13, p. 1301, 2019.

[36] P. J. Magistretti and L. Pellerin, "Astrocytes couple synaptic activity to glucose utilization in the brain," *Physiology*, vol. 14, no. 5, pp. 177–182, 1999.

[37] P. Kofuji and E. A. Newman, "Potassium buffering in the central nervous system," *Neuroscience*, vol. 129, no. 4, pp. 1043–1054, 2004. Brain Water Homeostasis.

[38] H. K. Kimelberg and M. Nedergaard, "Functions of astrocytes and their potential as therapeutic targets," *Neurotherapeutics*, vol. 7, no. 4, pp. 338–353, 2010. Glial-Based Neurotherapeutics.

[39] M. M. Halassa, T. Fellin, and P. G. Haydon, "The tripartite synapse: roles for gliotransmission in health and disease," *Trends in Molecular Medicine*, vol. 13, no. 2, pp. 54–63, 2007.

[40] A. Araque, V. Parpura, R. P. Sanzgiri, and P. G. Haydon, "Tripartite synapses: glia, the unacknowledged partner," *Trends in Neurosciences*, vol. 22, pp. 208–215, May 1999.

[41] J. Hofmeijer and M. J. A. M. van Putten, "Ischemic cerebral damage - an appraisal of synaptic failure," *Stroke*, vol. 43, no. 2, pp. 607–615, 2012.

[42] K. T. Kahle, A. R. Khanna, S. L. Alper, N. C. Adragna, P. K. Lauf, D. Sun, and E. Delpire, "K-cl cotransporters, cell volume homeostasis, and neurological disease," *Trends in Molecular Medicine*, vol. 21, pp. 513–523, Aug 2015.

[43] K. Dijkstra, J. Hofmeijer, S. A. van Gils, and M. J. A. M. van Putten, "A biophysical model for cytotoxic cell swelling," *Journal of Neuroscience*, vol. 36, no. 47, pp. 11881–11890, 2016.

[44] R. Rungta, H. Choi, J. Tyson, A. Malik, L. Dissing-Olesen, P. C. Lin, S. Cain, P. Cullis, T. Snutch, and B. MacVicar, "The cellular mechanisms of neuronal swelling underlying cytotoxic edema," *Cell*, vol. 161, pp. 610–621, Apr 2015.

[45] N. MacAulay and T. Zeuthen, "Water transport between cns compartments: contributions of aquaporins and cotransporters," *Neuroscience*, vol. 168, no. 4, pp. 941–956, 2010. Aquaporins in the Brain and Spinal Cord.

[46] G. J. Augustine, E. M. Adler, M. P. Charlton, M. Hans, D. Swandulla, and K. Zipser, "Presynaptic calcium signals during neurotransmitter release: Detection with fluorescent indicators and other calcium chelators," *Journal of Physiology-Paris*, vol. 86, no. 1, pp. 129–134, 1992.

[47] D. Khananshvili, "Sodium-calcium exchangers (ncx): molecular hallmarks underlying the tissue-specific and systemic functions," *Pflügers Archiv - European Journal of Physiology*, vol. 466, pp. 43–60, Jan 2014.

[48] M. L. Olsen and H. Sontheimer, "Functional implications for kir4.1 channels in glial biology: from k+ buffering to cell differentiation," *Journal of Neurochemistry*, vol. 107, no. 3, pp. 589–601, 2008.

[49] B. R. Larsen, M. Assentoft, M. L. Cotrina, S. Z. Hua, M. Nedergaard, K. Kaila, J. Voipio, and N. MacAulay, "Contributions of the na+/k+-atpase, nkcc1, and kir4.1 to hippocampal k+ clearance and volume responses," *Glia*, vol. 62, no. 4, pp. 608–622, 2014.

[50] N. C. Danbolt, "Glutamate uptake," *Progress in Neurobiology*, vol. 65, pp. 1–105, Sept. 2001.

[51] N. J. Maragakis and J. D. Rothstein, "Glutamate transporters: animal models to neurologic disease," *Neurobiology of Disease*, vol. 15, no. 3, pp. 461–473, 2004.

[52] P. Marcaggi and D. Attwell, "Role of glial amino acid transporters in synaptic transmission and brain energetics," *Glia*, vol. 47, no. 3, pp. 217–225, 2004.

[53] B. K. Siesjö, "Calcium-mediated processes in neuronal degenerationa," *Annals of the New York Academy of Sciences*, vol. 747, pp. 140–161, Dec. 2006.

[54] C. R. Rose and C. Karus, "Two sides of the same coin: Sodium homeostasis and signaling in astrocytes under physiological and pathophysiological conditions," *Glia*, vol. 61, pp. 1191–1205, Apr. 2013.

[55] L. Hertz, N. J. Gerkau, J. Xu, S. Durry, D. Song, C. R. Rose, and L. Peng, "Roles of astrocytic na+, k+-ATPase and glycogenolysis for k+ homeostasis in mammalian brain," *Journal of Neuroscience Research*, vol. 93, pp. 1019–1030, Oct. 2014.

[56] B. R. Larsen, A. Stoica, and N. MacAulay, "Managing brain extracellular k+ during neuronal activity: The physiological role of the na+/k+-ATPase subunit isoforms," *Frontiers in Physiology*, vol. 7, Apr. 2016.

[57] D. Pietrobon and M. A. Moskowitz, "Chaos and commotion in the wake of cortical spreading depression and spreading depolarizations," *Nature Reviews Neuroscience*, vol. 15, pp. 379–393, May 2014.

[58] J. P. Dreier, "The role of spreading depression, spreading depolarization and spreading ischemia in neurological disease," *Nature Medicine*, vol. 17, pp. 439–447, Apr. 2011.

[59] M. Nedergaard and U. Dirnagl, "Role of glial cells in cerebral ischemia," *Glia*, vol. 50, no. 4, pp. 281–286, 2005.

[60] D. W. Choi and S. M. Rothman, "The role of glutamate neurotoxicity in hypoxic-ischemic neuronal death," *Annual Review of Neuroscience*, vol. 13, pp. 171–182, Mar. 1990.

[61] U. Dirnagl, C. Iadecola, and M. A. Moskowitz, "Pathobiology of ischaemic stroke: an integrated view," *Trends in Neurosciences*, vol. 22, pp. 391–397, Sept. 1999.

[62] B. Foreman and J. Claassen, "Quantitative EEG for the detection of brain ischemia," *Critical Care*, vol. 16, no. 2, p. 216, 2012.

[63] B. J. Kim, H. G. Kang, H.-J. Kim, S.-H. Ahn, N. Y. Kim, S. Warach, and D.-W. Kang, "Magnetic resonance imaging in acute ischemic stroke treatment," *Journal of Stroke*, vol. 16, no. 3, p. 131, 2014.

[64] M. J. A. M. van Putten, J. M. Peters, S. M. Mulder, J. A. M. de Haas, C. M. A. Bruijninckx, and D. L. J. Tavy, "A brain symmetry index (BSI) for online EEG monitoring in carotid endarterectomy," *Clinical Neurophysiology*, vol. 115, pp. 1189–1194, May 2004.

[65] M. J. A. M. van Putten, "Extended bsi for continuous eeg monitoring in carotid endarterectomy," *Clinical Neurophysiology*, vol. 117, no. 12, pp. 2661–2666, 2006.

[66] M. J. A. M. van Putten and J. Hofmeijer, "Invited Review. EEG Monitoring in Cerebral Ischemia: Basic Concepts and Clinical Applications," *J Clinical Neurophysiology*, vol. 33, no. 3, pp. 203–210, 2016.

[67] J. Szentágothai, "The 'module-concept' in cerebral cortex architecture," *Brain Research*, vol. 95, pp. 475–496, Sept. 1975.

[68] N. Spruston, "Pyramidal neurons: dendritic structure and synaptic integration," *Nature Reviews Neuroscience*, vol. 9, pp. 206–221, Mar. 2008.

[69] C. Fanciullacci, F. Bertolucci, G. Lamola, A. Panarese, F. Artoni, S. Micera, B. Rossi, and C. Chisari, "Delta power is higher and more symmetrical in ischemic stroke patients with cortical involvement," *Frontiers in Human Neuroscience*, vol. 11, July 2017.

[70] J. M. Cassidy, A. Wodeyar, J. Wu, K. Kaur, A. K. Masuda, R. Srinivasan, and S. C. Cramer, "Low-frequency oscillations are a biomarker of injury and recovery after stroke," *Stroke*, vol. 51, pp. 1442–1450, May 2020.

[71] M. C. Cloostermans, F. B. van Meulen, C. J. Eertman, H. W. Hom, and M. J. A. M. van Putten, "Continuous electroencephalography monitoring for early prediction of neurological outcome in postanoxic patients after cardiac arrest," *Critical Care Medicine*, vol. 40, pp. 2867–2875, Oct. 2012.

[72] J. Hofmeijer, T. M. J. Beernink, F. H. Bosch, A. Beishuizen, M. C. Tjepkema-Cloostermans, and M. J. A. M. van Putten, "Early EEG contributes to multimodal outcome prediction of postanoxic coma," *Neurology*, vol. 85, pp. 137–143, June 2015.

[73] J. Hofmeijer, M. C. Tjepkema-Cloostermans, and M. J. A. M. van Putten, "Burst-suppression with identical bursts: A distinct EEG pattern with poor outcome in postanoxic coma," *Clinical Neurophysiology*, vol. 125, pp. 947–954, May 2014.

[74] M. T. Joy and S. T. Carmichael, "Encouraging an excitable brain state: mechanisms of brain repair in stroke," *Nature Reviews Neuroscience*, vol. 22, pp. 38–53, Nov. 2020.

[75] S. T. Carmichael, L. Wei, C. M. Rovainen, and T. A. Woolsey, "New patterns of intracortical projections after focal cortical stroke," *Neurobiology of Disease*, vol. 8, pp. 910–922, Oct. 2001.

[76] C. E. Brown, P. Li, J. D. Boyd, K. R. Delaney, and T. H. Murphy, "Extensive turnover of dendritic spines and vascular remodeling in cortical tissues recovering from stroke," *Journal of Neuroscience*, vol. 27, pp. 4101–4109, Apr. 2007.

[77] K. A. Tennant, S. L. Taylor, E. R. White, and C. E. Brown, "Optogenetic rewiring of thalamocortical circuits to restore function in the stroke injured brain," *Nature Communications*, vol. 8, June 2017.

[78] J. T. Paz, C. A. Christian, I. Parada, D. A. Prince, and J. R. Huguenard, "Focal cortical infarcts alter intrinsic excitability and synaptic excitation in the reticular thalamic nucleus," *Journal of Neuroscience*, vol. 30, pp. 5465–5479, Apr. 2010.

[79] T. Tokuno, K. Kataoka, T. Asai, S. Chichibu, R. Kuroda, M. Ioku, K. Yamada, and T. Hayakawa, "Functional changes in thalamic relay neurons after focal cerebral infarct: A study of unit recordings from VPL neurons after MCA occlusion in rats," *Journal of Cerebral Blood Flow & Metabolism*, vol. 12, pp. 954–961, Nov. 1992.

[80] A. Dhooge, W. Govaerts, Y. A. Kuznetsov, H. G. E. Meijer, and B. Sautois, "New features of the software matcont for bifurcation analysis of dynamical systems," *Mathematical and Computer Modelling of Dynamical Systems*, vol. 14, no. 2, pp. 147–175, 2008.

[81] E. Izhikevich, *Dynamical systems in neuroscience : the geometry of excitability and bursting*. Cambridge, Mass: MIT Press, 2007.

[82] D. E. Goldman, "Potential, impedance, and rectification in membranes," *Journal of General Physiology*, vol. 27, pp. 37–60, Sept. 1943.

[83] A. L. Hodgkin and B. Katz, "The effect of sodium ions on the electrical activity of the giant axon of the squid," *The Journal of Physiology*, vol. 108, pp. 37–77, Mar. 1949.

[84] A. L. Hodgkin and B. Katz, "The effect of temperature on the electrical activity of the giant axon of the squid," *The Journal of Physiology*, vol. 109, pp. 240–249, Aug. 1949.

[85] H. Kager, W. J. Wadman, and G. G. Somjen, "Conditions for the triggering of spreading depression studied with computer simulations," *Journal of Neurophysiology*, vol. 88, pp. 2700–2712, Nov. 2002.

[86] H. Kager, W. J. Wadman, and G. G. Somjen, "Simulated seizures and spreading depression in a neuron model incorporating interstitial space and ion concentrations," *Journal of Neurophysiology*, vol. 84, pp. 495–512, July 2000.

[87] J. R. Cressman, G. Ullah, J. Ziburkus, S. J. Schiff, and E. Barreto, "The influence of sodium and potassium dynamics on excitability, seizures, and the stability of persistent states: I. single neuron dynamics," *Journal of Computational Neuroscience*, vol. 26, pp. 159–170, Jan. 2009.

[88] G. Ullah, J. R. C. Jr., E. Barreto, and S. J. Schiff, "The influence of sodium and potassium dynamics on excitability, seizures, and the stability of persistent states: II. network and glial dynamics," *Journal of Computational Neuroscience*, vol. 26, pp. 171–183, Dec. 2008.

[89] Y. Wei, G. Ullah, J. Ingram, and S. J. Schiff, "Oxygen and seizure dynamics: II. computational modeling," *Journal of Neurophysiology*, vol. 112, pp. 213–223, July 2014.

[90] Y.-X. Li and J. Rinzel, "Equations for InsP3 receptor-mediated $[Ca^{2+}]_i$ oscillations derived from a detailed kinetic model: A hodgkin-huxley like formalism," *Journal of Theoretical Biology*, vol. 166, pp. 461–473, Feb. 1994.

[91] G. W. D. Young and J. Keizer, "A single-pool inositol 1, 4, 5-trisphosphate-receptor-based model for agonist-stimulated oscillations in Ca^{2+} concentration.," *Proceedings of the National Academy of Sciences*, vol. 89, pp. 9895–9899, Oct. 1992.

[92] T. Höfer, L. Venance, and C. Giaume, "Control and plasticity of intercellular calcium waves in astrocytes: A modeling approach," *The Journal of Neuroscience*, vol. 22, pp. 4850–4859, June 2002.

[93] I. Goto, S. Kinoshita, and K. Natsume, "The model of glutamate-induced intracellular Ca^{2+} oscillation and intercellular Ca^{2+} wave in brain astrocytes," *Neurocomputing*, vol. 58-60, pp. 461–467, June 2004.

[94] M. D. Pittà, M. Goldberg, V. Volman, H. Berry, and E. Ben-Jacob, "Glutamate regulation of calcium and IP3 oscillating and pulsating dynamics in astrocytes," *Journal of Biological Physics*, vol. 35, pp. 383–411, June 2009.

[95] A. Volterra and J. Meldolesi, "Astrocytes, from brain glue to communication elements: the revolution continues," *Nature Reviews Neuroscience*, vol. 6, pp. 626–640, July 2005.

[96] N. Bazargani and D. Attwell, "Astrocyte calcium signaling: the third wave," *Nature Neuroscience*, vol. 19, pp. 182–189, Jan. 2016.

[97] S. Nadkarni and P. Jung, "Modeling synaptic transmission of the tripartite synapse," *Physical Biology*, vol. 4, pp. 1–9, Jan. 2007.

[98] D. E. Postnov, R. N. Koreshkov, N. A. Brazhe, A. R. Brazhe, and O. V. Sosnovtseva, "Dynamical patterns of calcium signaling in a functional model of neuron–astrocyte networks," *Journal of Biological Physics*, vol. 35, pp. 425–445, June 2009.

[99] L. P. Savtchenko, S. Sylantyev, and D. A. Rusakov, "Central synapses release a resource-efficient amount of glutamate," *Nature Neuroscience*, vol. 16, pp. 10–12, Dec. 2012.

[100] S. G. Tewari and K. K. Majumdar, "A mathematical model of the tripartite synapse: astrocyte-induced synaptic plasticity," *Journal of Biological Physics*, vol. 38, pp. 465–496, May 2012.

[101] M. D. Pittà and N. Brunel, "Modulation of synaptic plasticity by glutamatergic gliotransmission: A modeling study," *Neural Plasticity*, vol. 2016, pp. 1–30, 2016.

[102] I. Østby, L. Øyehaug, G. T. Einevoll, E. A. Nagelhus, E. Plahte, T. Zeuthen, C. M. Lloyd, O. P. Ottersen, and S. W. Omholt, "Astrocytic mechanisms explaining neural-activity-induced shrinkage of extraneuronal space," *PLoS Computational Biology*, vol. 5, p. e1000272, Jan. 2009.

[103] L. Øyehaug, I. Østby, C. M. Lloyd, S. W. Omholt, and G. T. Einevoll, "Dependence of spontaneous neuronal firing and depolarisation block on astroglial membrane transport mechanisms," *Journal of Computational Neuroscience*, vol. 32, pp. 147–165, June 2011.

[104] J. Sibille, K. D. Duc, D. Holcman, and N. Rouach, "The neuroglial potassium cycle during neurotransmission: Role of kir4.1 channels," *PLOS Computational Biology*, vol. 11, p. e1004137, Mar. 2015.

[105] N. Hübel and G. Ullah, "Anions govern cell volume: A case study of relative astrocytic and neuronal swelling in spreading depolarization," *PLOS ONE*, vol. 11, p. e0147060, Mar. 2016.

[106] M.-A. Dronne, E. Grenier, T. Dumont, M. Hommel, and J.-P. Boissel, "Role of astrocytes in grey matter during stroke: A modelling approach," *Brain Research*, vol. 1138, pp. 231–242, Mar. 2007.

[107] N. Hübel, M. S. Hosseini-Zare, J. Žiburkus, and G. Ullah, "The role of glutamate in neuronal ion homeostasis: A case study of spreading depolarization," *PLOS Computational Biology*, vol. 13, p. e1005804, Oct. 2017.

[108] B. Hille, *Ionic channels of excitable membranes*. Sunderland, Mass: Sinauer Associates, 1984.

[109] T. Manninen, R. Havela, and M.-L. Linne, "Computational models for calcium-mediated astrocyte functions," *Frontiers in Computational Neuroscience*, vol. 12, Apr. 2018.

[110] M. D. Pittà and H. Berry, eds., *Computational Glioscience*. Springer International Publishing, 2019.

[111] B. H. Jansen and V. G. Rit, "Electroencephalogram and visual evoked potential generation in a mathematical model of coupled cortical columns," *Biological Cybernetics*, vol. 73, pp. 357–366, Sept. 1995.

[112] A. Blenkinsop, A. Valentin, M. P. Richardson, and J. R. Terry, "The dynamic evolution of focal-onset epilepsies - combining theoretical and clinical observations," *European Journal of Neuroscience*, vol. 36, pp. 2188–2200, July 2012.

[113] M. Goodfellow, K. Schindler, and G. Baier, "Self-organised transients in a neural mass model of epileptogenic tissue dynamics," *NeuroImage*, vol. 59, pp. 2644–2660, Feb. 2012.

[114] T. Kameneva, T. Ying, B. Guo, and D. R. Freestone, "Neural mass models as a tool to investigate neural dynamics during seizures," *Journal of Computational Neuroscience*, vol. 42, pp. 203–215, Jan. 2017.

[115] P. J. Karoly, L. Kuhlmann, D. Soudry, D. B. Grayden, M. J. Cook, and D. R. Freestone, "Seizure pathways: A model-based investigation," *PLOS Computational Biology*, vol. 14, p. e1006403, Oct. 2018.

[116] P. Sanz-Leon, S. A. Knock, A. Spiegler, and V. K. Jirsa, "Mathematical framework for large-scale brain network modeling in the virtual brain," *NeuroImage*, vol. 111, pp. 385–430, May 2015.

[117] V. K. Jirsa, T. Proix, D. Perdikis, M. M. Woodman, H. Wang, J. Gonzalez-Martinez, C. Bernard, C. Bénar, M. Guye, P. Chauvel, and F. Bartolomei, "The virtual epileptic patient: Individualized whole-brain models of epilepsy spread," *NeuroImage*, vol. 145, pp. 377–388, Jan. 2017.

[118] R. L. Beurle, "Properties of a mass of cells capable of regenerating pulses," *Philosophical Transactions of the Royal Society of London. Series B, Biological Sciences*, vol. 240, no. 669, pp. 55–94, 1956.

[119] H. R. Wilson and J. D. Cowan, "Excitatory and inhibitory interactions in localized populations of model neurons," *Biophysical Journal*, vol. 12, pp. 1–24, Jan. 1972.

[120] S. ichi Amari, "Dynamics of pattern formation in lateral-inhibition type neural fields," *Biological Cybernetics*, vol. 27, no. 2, pp. 77–87, 1977.

[121] P. L. Nunez, "The brain wave equation: a model for the EEG," *Mathematical Biosciences*, vol. 21, pp. 279–297, Dec. 1974.

[122] S. Coombes, P. beim Graben, and R. Potthast, "Tutorial on neural field theory," in *Neural Fields*, pp. 1–43, Springer Berlin Heidelberg, 2014.

[123] P. Bressloff, *Waves in neural media : from single neurons to neural fields*. New York: Springer, 2014.

[124] P. A. Robinson, C. J. Rennie, D. L. Rowe, S. C. O'Connor, J. J. Wright, E. Gordon, and R. W. Whitehouse, "Neurophysical modeling of brain dynamics," *Neuropsychopharmacology*, vol. 28, pp. S74–S79, June 2003.

[125] J. S. Johnson, J. P. Spencer, S. J. Luck, and G. Schöner, "A dynamic neural field model of visual working memory and change detection," *Psychological Science*, vol. 20, pp. 568–577, May 2009.

[126] G. B. Ermentrout and J. D. Cowan, "A mathematical theory of visual hallucination patterns," *Biological Cybernetics*, vol. 34, no. 3, pp. 137–150, 1979.

[127] T. L. Eissa, K. Dijkstra, C. Brune, R. G. Emerson, M. J. A. M. van Putten, R. R. Goodman, G. M. McKhann, C. A. Schevon, W. van Drongelen, and S. A. van Gils, "Cross-scale effects of neural interactions during human neocortical seizure activity," *Proceedings of the National Academy of Sciences*, vol. 114, pp. 10761–10766, Sept. 2017.

[128] C. J. Rennie, P. A. Robinson, and J. J. Wright, "Unified neurophysical model of EEG spectra and evoked potentials," *Biological Cybernetics*, vol. 86, pp. 457–471, June 2002.

[129] M. Breakspear, J. A. Roberts, J. R. Terry, S. Rodrigues, N. Mahant, and P. A. Robinson, "A unifying explanation of primary generalized seizures through nonlinear brain modeling and bifurcation analysis," *Cerebral Cortex*, vol. 16, pp. 1296–1313, Nov. 2005.

[130] F. Wendling, F. Bartolomei, J. J. Bellanger, and P. Chauvel, "Epileptic fast activity can be explained by a model of impaired GABAergic dendritic inhibition," *European Journal of Neuroscience*, vol. 15, pp. 1499–1508, May 2002.

[131] M. Krupa, N. Popović, and N. Kopell, "Mixed-mode oscillations in three time-scale systems: a prototypical example," *SIAM Journal on Applied Dynamical Systems*, vol. 7, no. 2, pp. 361–420, 2008.

[132] R. Curtu and J. Rubin, "Interaction of canard and singular hopf mechanisms in a neural model," *SIAM Journal on Applied Dynamical Systems*, vol. 10, no. 4, pp. 1443–1479, 2011.

[133] D. T. J. Liley, P. J. Cadusch, and M. P. Dafilis, "A spatially continuous mean field theory of electrocortical activity," *Network: Computation in Neural Systems*, vol. 13, pp. 67–113, Jan. 2002.

[134] M. P. Dafilis, F. Frascoli, P. J. Cadusch, and D. T. J. Liley, "Chaos and generalised multistability in a mesoscopic model of the electroencephalogram," *Physica D: Nonlinear Phenomena*, vol. 238, pp. 1056–1060, June 2009.

[135] W. J. Freeman, "Tutorial on neurobiology: From single neurons to brain chaos," *International Journal of Bifurcation and Chaos*, vol. 02, pp. 451–482, Sept. 1992.

[136] I. Bojak, Z. V. Stoyanov, and D. T. J. Liley, "Emergence of spatially heterogeneous burst suppression in a neural field model of electrocortical activity," *Frontiers in Systems Neuroscience*, vol. 9, Feb. 2015.

[137] B. J. Ruijter, J. Hofmeijer, H. G. E. Meijer, and M. J. A. M. van Putten, "Synaptic damage underlies EEG abnormalities in postanoxic encephalopathy: A computational study," *Clinical Neurophysiology*, vol. 128, pp. 1682–1695, Sept. 2017.

[138] J. Baladron, D. Fasoli, O. Faugeras, and J. Touboul, "Mean-field description and propagation of chaos in networks of hodgkin-huxley and FitzHugh-nagumo neurons," *The Journal of Mathematical Neuroscience*, vol. 2, May 2012.

[139] B.-J. Zandt, S. Visser, M. J. A. M. van Putten, and B. ten Haken, "A neural mass model based on single cell dynamics to model pathophysiology," *Journal of Computational Neuroscience*, vol. 37, pp. 549–568, Aug. 2014.

[140] G. Ullah and S. J. Schiff, "Assimilating seizure dynamics," *PLoS Computational Biology*, vol. 6, p. e1000776, May 2010.

[141] L. Meng, M. A. Kramer, S. J. Middleton, M. A. Whittington, and U. T. Eden, "A unified approach to linking experimental, statistical and computational analysis of spike train data," *PLoS ONE*, vol. 9, p. e85269, Jan. 2014.

[142] M. J. Moye and C. O. Diekman, "Data assimilation methods for neuronal state and parameter estimation," *The Journal of Mathematical Neuroscience*, vol. 8, Aug. 2018.

[143] J. C. Quinn, P. H. Bryant, D. R. Creveling, S. R. Klein, and H. D. I. Abarbanel, "Parameter and state estimation of experimental chaotic systems using synchronization," *Physical Review E*, vol. 80, July 2009.

[144] H. D. I. Abarbanel, *Predicting the future : completing models of observed complex systems*. New York, NY: Springer, 2013.

[145] J. H. Tien and J. Guckenheimer, "Parameter estimation for bursting neural models," *Journal of Computational Neuroscience*, vol. 24, pp. 358–373, Nov. 2007.

[146] R. E. Kass, S.-I. Amari, K. Arai, E. N. Brown, C. O. Diekman, M. Diesmann, B. Doiron, U. T. Eden, A. L. Fairhall, G. M. Fiddyment, T. Fukai, S. Grün, M. T. Harrison, M. Helias, H. Nakahara, J. nosuke Teramae, P. J. Thomas, M. Reimers, J. Rodu, H. G. Rotstein, E. Shea-Brown, H. Shimazaki, S. Shinomoto, B. M. Yu, and M. A. Kramer, "Computational neuroscience: Mathematical and statistical perspectives," *Annual Review of Statistics and Its Application*, vol. 5, pp. 183–214, Mar. 2018.

[147] D. C. Knill and A. Pouget, "The bayesian brain: the role of uncertainty in neural coding and computation," *Trends in Neurosciences*, vol. 27, pp. 712–719, Dec. 2004.

[148] M. Colombo and P. Seriès, "Bayes in the brain—on bayesian modelling in neuroscience," *The British Journal for the Philosophy of Science*, vol. 63, pp. 697–723, Sept. 2012.

[149] H. Sohn and D. Narain, "Neural implementations of bayesian inference," *Current Opinion in Neurobiology*, vol. 70, pp. 121–129, Oct. 2021.

[150] L. Aitchison, J. Jegminat, J. A. Menendez, J.-P. Pfister, A. Pouget, and P. E. Latham, "Synaptic plasticity as bayesian inference," *Nature Neuroscience*, vol. 24, pp. 565–571, Mar. 2021.

[151] C. M. Sweeney-Reed and S. J. Nasuto, "A novel approach to the detection of synchronisation in EEG based on empirical mode decomposition," *Journal of Computational Neuroscience*, vol. 23, pp. 79–111, Feb. 2007.

[152] H. Liang, S. L. Bressler, R. Desimone, and P. Fries, "Empirical mode decomposition: a method for analyzing neural data," *Neurocomputing*, vol. 65-66, pp. 801–807, June 2005.

[153] J. H. Tu, , C. W. Rowley, D. M. Luchtenburg, S. L. Brunton, and J. N. K. and, "On dynamic mode decomposition: Theory and applications," *Journal of Computational Dynamics*, vol. 1, no. 2, pp. 391–421, 2014.

[154] N. Marrouch, J. Slawinska, D. Giannakis, and H. L. Read, "Data-driven koopman operator approach for computational neuroscience," *Annals of Mathematics and Artificial Intelligence*, vol. 88, pp. 1155–1173, Nov. 2019.

[155] B. W. Brunton, L. A. Johnson, J. G. Ojemann, and J. N. Kutz, "Extracting spatial–temporal coherent patterns in large-scale neural recordings using dynamic mode decomposition," *Journal of Neuroscience Methods*, vol. 258, pp. 1–15, Jan. 2016.

[156] W. Zhang, Y.-C. Yu, and J.-S. Li, "Dynamics reconstruction and classification via koopman features," *Data Mining and Knowledge Discovery*, vol. 33, pp. 1710–1735, June 2019.

[157] S. L. Brunton, J. L. Proctor, and J. N. Kutz, "Discovering governing equations from data by sparse identification of nonlinear dynamical systems," *Proceedings of the National Academy of Sciences*, vol. 113, pp. 3932–3937, Mar. 2016.

[158] N. M. Mangan, S. L. Brunton, J. L. Proctor, and J. N. Kutz, "Inferring biological networks by sparse identification of nonlinear dynamics," *IEEE Transactions on Molecular, Biological and Multi-Scale Communications*, vol. 2, pp. 52–63, June 2016.

[159] M. Hoffmann, C. Fröhner, and F. Noé, "Reactive SINDy: Discovering governing reactions from concentration data," *The Journal of Chemical Physics*, vol. 150, p. 025101, Jan. 2019.

[160] J.-C. Loiseau and S. L. Brunton, "Constrained sparse galerkin regression," *Journal of Fluid Mechanics*, vol. 838, pp. 42–67, Jan. 2018.

[161] E. Kaiser, J. N. Kutz, and S. L. Brunton, "Sparse identification of nonlinear dynamics for model predictive control in the low-data limit," *Proceedings of the Royal Society A: Mathematical, Physical and Engineering Sciences*, vol. 474, p. 20180335, Nov. 2018.

[162] I. Goodfellow, *Deep learning*. Cambridge, Massachusetts: The MIT Press, 2016.

[163] C. Aggarwal, *Neural networks and deep learning : a textbook*. Cham, Switzerland: Springer, 2018.

[164] F. Rosenblatt, *Principles of Neurodynamics: Perceptrons and the Theory of Brain Mechanisms*. Cornell Aeronautical Laboratory. Report no. VG-1196-G-8, Spartan Books, 1962.

[165] A. H. Marblestone, G. Wayne, and K. P. Kording, "Toward an integration of deep learning and neuroscience," *Frontiers in Computational Neuroscience*, vol. 10, Sept. 2016.

[166] T. C. Kietzmann, P. McClure, and N. Kriegeskorte, "Deep neural networks in computational neuroscience," Jan. 2019.

[167] S. E. Otto and C. W. Rowley, "Linearly recurrent autoencoder networks for learning dynamics," *SIAM Journal on Applied Dynamical Systems*, vol. 18, pp. 558–593, Jan. 2019.

[168] O. Yair, R. Talmon, R. R. Coifman, and I. G. Kevrekidis, "Reconstruction of normal forms by learning informed observation geometries from data," *Proceedings of the National Academy of Sciences*, vol. 114, pp. E7865–E7874, Aug. 2017.

[169] A. J. Homburg and B. Sandstede, "Homoclinic and heteroclinic bifurcations in vector fields," *Handbook of dynamical systems*, vol. 3, pp. 379–524, 2010.

[170] A. Roxin and A. Compte, "Oscillations in the bistable regime of neuronal networks," *Physical Review E*, vol. 94, July 2016.

[171] P. R. Protachevicz, F. S. Borges, E. L. Lameu, P. Ji, K. C. Iarosz, A. H. Kihara, I. L. Caldas, J. D. Szezech, M. S. Baptista, E. E. N. Macau, C. G. Antonopoulos, A. M. Batista, and J. Kurths, "Bistable firing pattern in a neural network model," *Frontiers in Computational Neuroscience*, vol. 13, Apr. 2019.

[172] S. Rich, H. M. Chameh, M. Rafiee, K. Ferguson, F. K. Skinner, and T. A. Valiante, "Inhibitory network bistability explains increased interneuronal activity prior to seizure onset," *Frontiers in Neural Circuits*, vol. 13, Jan. 2020.

[173] B.-J. Zandt, B. ten Haken, J. G. van Dijk, and M. J. A. M. van Putten, "Neural dynamics during anoxia and the "wave of death"," *PLoS ONE*, vol. 6, p. e22127, July 2011.

[174] P. Ashwin, S. Wieczorek, R. Vitolo, and P. Cox, "Tipping points in open systems: bifurcation, noise-induced and rate-dependent examples in the climate system," *Philosophical Transactions of the Royal Society A: Mathematical, Physical and Engineering Sciences*, vol. 370, pp. 1166–1184, Mar. 2012.

[175] U. Feudel, A. N. Pisarchik, and K. Showalter, "Multistability and tipping: From mathematics and physics to climate and brain—minireview and preface to the focus issue," *Chaos: An Interdisciplinary Journal of Nonlinear Science*, vol. 28, p. 033501, Mar. 2018.

[176] H. Korn and P. Faure, "Is there chaos in the brain? II. experimental evidence and related models," *Comptes Rendus Biologies*, vol. 326, pp. 787–840, Sept. 2003.

[177] J. Wojcik and A. Shilnikov, "Voltage interval mappings for activity transitions in neuron models for elliptic bursters," *Physica D: Nonlinear Phenomena*, vol. 240, pp. 1164–1180, July 2011.

[178] M. P. Dafilis, F. Frascoli, P. J. Cadusch, and D. T. J. Liley, "Four dimensional chaos and intermittency in a mesoscopic model of the electroencephalogram," *Chaos: An Interdisciplinary Journal of Nonlinear Science*, vol. 23, p. 023111, June 2013.

[179] J. Touboul, F. Wendling, P. Chauvel, and O. Faugeras, "Neural mass activity, bifurcations, and epilepsy," *Neural Computation*, vol. 23, pp. 3232–3286, Dec. 2011.

[180] S. Ahmadizadeh, P. J. Karoly, D. Nešić, D. B. Grayden, M. J. Cook, D. Soudry, and D. R. Freestone, "Bifurcation analysis of two coupled jansen-rit neural mass models," *PLOS ONE*, vol. 13, p. e0192842, Mar. 2018.

[181] K. E. Houssaini, C. Bernard, and V. K. Jirsa, "The epileptor model: A systematic mathematical analysis linked to the dynamics of seizures, refractory status epilepticus, and depolarization block," *eneuro*, vol. 7, pp. ENEURO.0485–18.2019, Feb. 2020.

[182] E. K. Ersöz and F. Wendling, "Canard solutions in neural mass models: consequences on critical regimes," *The Journal of Mathematical Neuroscience*, vol. 11, Sept. 2021.

[183] S. Coombes and P. C. Bressloff, *Bursting: the genesis of rhythm in the nervous system*. World Scientific, 2005.

[184] S. E. Folias and P. C. Bressloff, "Breathing pulses in an excitatory neural network," *SIAM Journal on Applied Dynamical Systems*, vol. 3, pp. 378–407, Jan. 2004.

[185] S. Coombes, P. beim Graben, R. Potthast, and J. Wright, eds., *Neural Fields*. Springer Berlin Heidelberg, 2014.

[186] H. G. E. Meijer and S. Coombes, "Travelling waves in models of neural tissue: from localised structures to periodic waves," *EPJ Nonlinear Biomedical Physics*, vol. 2, Mar. 2014.

[187] J. J. Harris, R. Jolivet, and D. Attwell, "Synaptic energy use and supply.," *Neuron*, vol. 75, pp. 762–77, sep 2012.

[188] M. Erecińska and I. A. Silver, "Ions and energy in mammalian brain," *Progress in Neurobiology*, vol. 43, no. 1, pp. 37 – 71, 1994.

[189] V. Dzhala, I. Khalilov, Y. Ben-Ari, and R. Khazipov, "Neuronal mechanisms of the anoxia-induced network oscillations in the rat hippocampus *in vitro*," *Journal of Physiology*, vol. 536, pp. 521–531, oct 2001.

[190] G. G. Somjen, *Ions in the brain : normal function, seizures, and stroke*. Oxford: Oxford University Press, 2004.

[191] N. J. Gerkau, C. Rakers, S. Durry, G. C. Petzold, and C. R. Rose, "Reverse NCX attenuates cellular sodium loading in metabolically compromised cortex," *Cerebral Cortex*, vol. 28, pp. 4264–4280, dec 2018.

[192] S. Song, L. Luo, B. Sun, and D. Sun, "Roles of glial ion transporters in brain diseases," *Glia*, vol. 68, no. 3, pp. 472–494, 2020.

[193] G. Pignataro, R. Sirabella, S. Anzilotti, G. Di Renzo, and L. Annunziato, "Does Na^+/Ca^{2+} exchanger, NCX, represent a new druggable target in stroke intervention?," *Translational Stroke Research*, vol. 5, pp. 145–155, Feb 2014.

[194] F. G. Donnan, "Theory of membrane equilibria and membrane potentials in the presence of non-dialysing electrolytes. a contribution to physical-chemical physiology," *Journal of Membrane Science*, vol. 100, no. 1, pp. 45 – 55, 1995.

[195] D. J. Rossi, J. D. Brady, and C. Mohr, "Astrocyte metabolism and signaling during brain ischemia," *Nature Neuroscience*, vol. 10, no. 11, pp. 1377–1386, 2007.

[196] M. A. Moskowitz, E. H. Lo, and C. Iadecola, "The science of stroke: mechanisms in search of treatments," *Neuron*, vol. 67, no. 2, pp. 181 – 198, 2010.

[197] W. Shou, C. T. Bergstrom, A. K. Chakraborty, and F. K. Skinner, "Research: theory, models and biology," *Elife*, vol. 4, p. e07158, jul 2015.

[198] F. Oschmann, H. Berry, K. Obermayer, and K. Lenk, "From in silico astrocyte cell models to neuron-astrocyte network models: A review," *Brain Research Bulletin*, vol. 136, pp. 76 – 84, 2018. Molecular mechanisms of astrocyte-neuron signalling.

[199] Y. X. Li and J. Rinzel, "Equations for InsP3 receptor-mediated $[Ca^{2+}]_i$ oscillations derived from a detailed kinetic model: a Hodgkin-Huxley like formalism," *Journal of Theoretical Biology*, vol. 166, no. 4, pp. 461 – 473, 1994.

[200] S. Nadkarni and P. Jung, "Modeling synaptic transmission of the tripartite synapse," *Physical Biology*, vol. 4, pp. 1–9, jan 2007.

[201] M. De Pittà, *Gliotransmitter exocytosis and Its Consequences on Synaptic Transmission*, ch. 10, pp. 245–287. Cham: Springer International Publishing, 2019.

[202] H. Kager, W. J. Wadman, and G. G. Somjen, "Seizure-like afterdischarges simulated in a model neuron," *Journal of Computational Neuroscience*, vol. 22, pp. 105–128, feb 2007.

[203] Y. Wei, G. Ullah, and S. Schiff, "Unification of neuronal spikes, seizures, and spreading depression," *Journal of Neuroscience*, vol. 34, no. 35, pp. 11733–11743, 2014.

[204] G. Ullah, Y. Wei, M. A. Dahlem, M. Wechselberger, and S. J. Schiff, "The role of cell volume in the dynamics of seizure, spreading depression, and anoxic depolarization," *PLoS Computational Biology*, vol. 11, p. e1004414, aug 2015.

[205] R. Schmidt-Kastner, "Genomic approach to selective vulnerability of the hippocampus in brain ischemia–hypoxia," *Neuroscience*, vol. 309, pp. 259 – 279, 2015.

[206] N. Tambasco, M. Romoli, and P. Calabresi, "Selective basal ganglia vulnerability to energy deprivation: Experimental and clinical evidences," *Progress in Neurobiology*, vol. 169, pp. 55 – 75, 2018.

[207] B. Schaller, "Influence of age on stroke and preconditioning-induced ischemic tolerance in the brain," *Experimental Neurology*, vol. 205, pp. 9–19, May 2007.

[208] P. F. Kinoshita, J. A. Leite, A. M. M. Orellana, A. R. Vasconcelos, L. E. M. Quintas, E. M. Kawamoto, and C. Scavone, "The influence of Na^+, K^+-ATPase on glutamate signaling in neurodegenerative diseases and senescence," *Frontiers in Physiology*, vol. 7, p. 195, 2016.

[209] A. Verkhratsky, R. Zorec, J. J. Rodríguez, and V. Parpura, "Astroglia dynamics in ageing and alzheimer's disease," *Current Opinion in Pharmacology*, vol. 26, pp. 74 – 79, 2016.

[210] E. Syková and C. Nicholson, "Diffusion in brain extracellular space," *Physiological Reviews*, vol. 88, no. 4, pp. 1277–1340, 2008.

[211] H. Kager, W. Wadman, and G. Somjen, "Simulated seizures and spreading depression in a neuron model incorporating interstitial space and ion concentrations," *Journal of Neurophysiology*, vol. 84, no. 1, pp. 495–512, 2000.

[212] M. J. Sætra, G. T. Einevoll, and G. Halnes, "An electrodiffusive, ion conserving pinsky-rinzel model with homeostatic mechanisms," *PLOS Computational Biology*, vol. 16, pp. 1–36, 04 2020.

[213] K. Breslin, J. J. Wade, K. Wong-Lin, J. Harkin, B. Flanagan, H. V. Zalinge, S. Hall, M. Walker, A. Verkhratsky, and L. McDaid, "Potassium and sodium microdomains in thin astroglial processes: A computational model study," *PLoS Computational Biology*, vol. 14, p. e1006151, may 2018.

[214] F. Oschmann, K. Mergenthaler, E. Jungnickel, and K. Obermayer, "Spatial separation of two different pathways accounting for the generation of calcium signals in astrocytes," *PLoS Computational Biology*, vol. 13, pp. 1–25, 02 2017.

[215] M. V. Tsodyks and H. Markram, "The neural code between neocortical pyramidal neurons depends on neurotransmitter release probability," *Proceedings of the National Academy of Sciences*, vol. 94, no. 2, pp. 719–723, 1997.

[216] A. Walter, P. Pinheiro, M. Verhage, and J. Sørensen, "A sequential vesicle pool model with a single release sensor and a Ca^{2+}-dependent priming catalyst effectively explains Ca^{2+}-dependent properties of neurosecretion," *PLoS Computational Biology*, vol. 9, pp. 1–15, 12 2013.

[217] C. Karus, M. A. Mondragão, D. Ziemens, and C. R. Rose, "Astrocytes restrict discharge duration and neuronal sodium loads during recurrent network activity," *Glia*, vol. 63, no. 6, pp. 936–957, 2015.

[218] P. Nelson, *Biological Physics. Energy, Information, Life.* New York: W.H. Freeman and Company, 2008.

[219] N. Hübel, R. D. Andrew, and G. Ullah, "Large extracellular space leads to neuronal susceptibility to ischemic injury in a Na^+/K^+ pumps–dependent manner," *Journal of Computational Neuroscience*, vol. 40, pp. 177–192, Apr 2016.

[220] R. R. Kopito, B. S. Lee, D. M. Simmons, A. E. Lindsey, C. W. Morgans, and K. Schneider, "Regulation of intracellular pH by a neuronal homolog of the erythrocyte anion exchanger," *Cell*, vol. 59, pp. 927–937, Dec. 1989.

[221] M. Hentschke, M. Wiemann, S. Hentschke, I. Kurth, I. Hermans-Borgmeyer, T. Seidenbecher, T. J. Jentsch, A. Gal, and C. A. Hubner, "Mice with a targeted disruption of the cl - /HCO 3 - exchanger AE3 display a reduced seizure threshold," *Molecular and Cellular Biology*, vol. 26, pp. 182–191, Jan. 2006.

[222] N. MacAulay, "Molecular mechanisms of K^+ clearance and extracellular space shrinkage—glia cells as the stars," *Glia*, vol. 68, no. 11, pp. 2192–2211, 2020.

[223] D. Attwell, B. Barbour, and M. Szatkowski, "Nonvesicular release of neurotransmitter," *Neuron*, vol. 11, no. 3, pp. 401 – 407, 1993.

[224] P. Hertelendy, D. Varga, A. Menyhárt, F. Bari, and E. Farkas, "Susceptibility of the cerebral cortex to spreading depolarization in neurological disease states: The impact of aging," *Neurochemistry International*, vol. 127, pp. 125 – 136, 2019. Special issue on Age and Sex Differences in Post-Ischemic Outcome and Therapy.

[225] C. D. Brisson, Y.-T. Hsieh, D. Kim, A. Y. Jin, and R. D. Andrew, "Brainstem neurons survive the identical ischemic stress that kills higher neurons: Insight to the persistent vegetative state," *PLoS ONE*, vol. 9, p. e96585, May 2014.

[226] R. D. Andrew, Y.-T. Hsieh, and C. D. Brisson, "Spreading depolarization triggered by elevated potassium is weak or absent in the rodent lower brain," *Journal of Cerebral Blood Flow & Metabolism*, vol. 37, no. 5, pp. 1735–1747, 2017.

[227] W. van Drongelen, H. Koch, F. P. Elsen, H. C. Lee, A. Mrejeru, E. Doren, C. J. Marcuccilli, M. Hereld, R. L. Stevens, and J. Ramirez, "Role of persistent sodium current in bursting activity of mouse neocortical networks in vitro," *J. Neurophysiol.*, vol. 96, pp. 2564–2577, 2006.

[228] X. S. Liu, M. Chopp, H. Kassis, L. F. Jia, A. Hozeska-Solgot, R. L. Zhang, C. Chen, Y. S. Cui, and Z. G. Zhang, "Valproic acid increases white matter repair and neurogenesis after stroke," *Neuroscience*, vol. 220, pp. 313–321, Sept. 2012.

[229] L. Wei, S. P. Yu, F. Gottron, B. J. Snider, G. J. Zipfel, and D. W. Choi, "Potassium channel blockers attenuate hypoxia- and ischemia-induced neuronal death in vitro and in vivo," *Stroke*, vol. 34, pp. 1281–1286, May 2003.

[230] M. L. Cotrina, J. Kang, J. H.-C. Lin, E. Bueno, T. W. Hansen, L. He, Y. Liu, and M. Nedergaard, "Astrocytic gap junctions remain open during ischemic conditions," *Journal of Neuroscience*, vol. 18, no. 7, pp. 2520–2537, 1998.

[231] R. Jolivet, J. S. Coggan, I. Allaman, and P. J. Magistretti, "Multi-timescale modeling of activity-dependent metabolic coupling in the neuron-glia-vasculature ensemble," *PLOS Computational Biology*, vol. 11, pp. 1–23, 02 2015.

[232] S. M. Theparambil, P. S. Hosford, I. Ruminot, O. Kopach, J. Reynolds, P. Y. Sandoval, D. A. Rusakov, L. F. Barros, and A. V. Gourine, "Astrocytes regulate brain extracellular ph via a neuronal activity-dependent bicarbonate shuttle," *Nature Communications*, vol. 11, p. 5073, Oct 2020.

[233] D. Jones and A. Cullen, "A quantitative investigation of some presynaptic terminal parameters during synaptogenesis," *Experimental Neurology*, vol. 64, no. 2, pp. 245 – 259, 1979.

[234] B. Hille, *Ion Channels of Excitable Membranes*. Oxford, UK: Oxford University Press, 2001.

[235] C. H. Luo and Y. Rudy, "A dynamic model of the cardiac ventricular action potential. ii. afterdepolarizations, triggered activity, and potentiation.," *Circulation Research*, vol. 74, no. 6, pp. 1097–1113, 1994.

[236] P. B. Dunham, "Oxygen sensing and K(+)-Cl(-) cotransport.," *The Journal of physiology*, vol. 526, p. 1, jul 2000.

[237] I. Chamma, Q. Chevy, J. C. Poncer, and S. Lévi, "Role of the neuronal K-Cl co-transporter KCC2 in inhibitory and excitatory neurotransmission.," *Frontiers in cellular neuroscience*, vol. 6, p. 5, 2012.

[238] J. R. Williams, J. W. Sharp, V. G. Kumari, M. Wilson, and J. A. Payne, "The neuron-specific K-Cl cotransporter, KCC2. Antibody development and initial characterization of the protein," *The Journal of biological chemistry*, vol. 274, pp. 12656–64, apr 1999.

[239] P. Uvarov, P. Pruunsild, T. Timmusk, and M. S. Airaksinen, "Neuronal K+/Cl- co-transporter (KCC2) transgenes lacking neurone restrictive silencer element recapitulate CNS neurone-specific expression and developmental up-regulation of endogenous KCC2 gene," *Journal of Neurochemistry*, vol. 95, pp. 1144–1155, nov 2005.

[240] A. Verkhratsky and M. Nedergaard, "Physiology of astroglia," *Physiological Reviews*, vol. 98, no. 1, pp. 239–389, 2018.

[241] M. L. Olsen, B. S. Khakh, S. N. Skatchkov, M. Zhou, C. J. Lee, and N. Rouach, "New insights on astrocyte ion channels: Critical for homeostasis and neuron-glia signaling," *Journal of Neuroscience*, vol. 35, no. 41, pp. 13827–13835, 2015.

[242] M.-A. Dronne, J.-P. Boissel, and E. Grenier, "A mathematical model of ion movements in grey matter during a stroke," *Journal of Theoretical Biology*, vol. 240, no. 4, pp. 599–615, 2006.

[243] B. A. Macvicar, D. Feighan, A. Brown, and B. Ransom, "Intrinsic optical signals in the rat optic nerve: Role for K^+ uptake via nkcc1 and swelling of astrocytes," *GLIA*, vol. 37, no. 2, pp. 114–123, 2002.

[244] G. Su, D. B. Kintner, M. Flagella, G. E. Shull, and D. Sun, "Astrocytes from na^+-k^+-cl^--cotransporter-null mice exhibit absence of swelling and decrease in eaa release," *American Journal of Physiology - Cell Physiology*, vol. 282, no. 5, pp. C1147–C1160, 2002.

[245] L. Annunziato, F. Boscia, and G. Pignataro, "Ionic transporter activity in astrocytes, microglia, and oligodendrocytes during brain ischemia.," *Journal of cerebral blood flow and metabolism*, vol. 33, pp. 969–82, jul 2013.

[246] S. N. Orlov, S. V. Koltsova, L. V. Kapilevich, S. V. Gusakova, and N. O. Dulin, "NKCC1 and NKCC2: The pathogenetic role of cation-chloride cotransporters in hypertension.," *Genes & diseases*, vol. 2, pp. 186–196, jun 2015.

[247] T. Leng, Y. Shi, Z.-G. Xiong, and D. Sun, "Proton-sensitive cation channels and ion exchangers in ischemic brain injury: New therapeutic targets for stroke?," *Progress in Neurobiology*, vol. 115, pp. 189 – 209, 2014. 2013 Pangu Meeting on Neurobiology of Stroke and CNS Injury: Progresses and Perspectives of Future.

[248] J. T. Hackett and T. Ueda, "Glutamate release," *Neurochemical Research*, vol. 40, pp. 2443–2460, Dec 2015.

[249] W. Krzyzanowska, B. Pomierny, M. Filip, and J. Pera, "Glutamate transporters in brain ischemia: to modulate or not?," *Acta Pharmacologica Sinica*, vol. 35, pp. 444–462, Mar 2014.

[250] T. Zeuthen, "How water molecules pass through aquaporins," *Trends in Biochemical Sciences*, vol. 26, pp. 77–79, 2001.

[251] T. Zeuthen, "Water-transporting proteins," *Journal of Membrane Biology*, vol. 234, pp. 57–73, 2010.

[252] C. Koch and I. Segev, *Methods in neuronal modeling: From synapses to networks*. Cambridge, MA, USA: MIT Press, 1991.

[253] R. C. Reyes, A. Verkhratsky, and V. Parpura, "Plasmalemmal na^+/ca^{2+} exchanger modulates ca^{2+}-dependent exocytotic release of glutamate from rat cortical astrocytes," *ASN Neuro*, vol. 4, no. 1, p. AN20110059, 2012.

[254] M.-C. Marx, D. Billups, and B. Billups, "Maintaining the presynaptic glutamate supply for excitatory neurotransmission," *Journal of Neuroscience Research*, vol. 93, no. 7, pp. 1031–1044, 2015.

[255] V. Untiet, P. Kovermann, N. J. Gerkau, T. Gensch, C. R. Rose, and C. Fahlke, "Glutamate transporter-associated anion channels adjust intracellular chloride concentrations during glial maturation," *GLIA*, vol. 65, pp. 388–400, nov 2016.

[256] E. S. Donkor, "Stroke in the 21st century: A snapshot of the burden, epidemiology, and quality of life," *Stroke Research and Treatment*, vol. 2018, p. 3238165, Nov 2018.

[257] S. Fedorovich, J. Hofmeijer, M. J. A. M. van Putten, and J. le Feber, "Reduced synaptic vesicle recycling during hypoxia in cultured cortical neurons," *Frontiers in Cellular Neuroscience*, vol. 11, p. 32, 2017.

[258] H. Bolay, Y. Gürsoy-Özdemir, Y. Sara, R. Onur, A. Can, and T. Dalkara, "Persistent defect in transmitter release and synapsin phosphorylation in cerebral cortex after transient moderate ischemic injury," *Stroke*, vol. 33, pp. 1369–1375, may 2002.

[259] M. J. A. M. van Putten, C. Fahlke, K. W. Kafitz, J. Hofmeijer, and C. R. Rose, "Dysregulation of astrocyte ion homeostasis and its relevance for stroke-induced brain damage," *International Journal of Molecular Sciences*, vol. 22, p. 5679, May 2021.

[260] M. J. A. M. van Putten and D. L. J. Tavy, "Continuous quantitative eeg monitoring in hemispheric stroke patients using the brain symmetry index," *Stroke*, vol. 35, no. 11, pp. 2489–2492, 2004.

[261] J. Hofmeijer and M. J. A. M. van Putten, "Eeg in postanoxic coma: Prognostic and diagnostic value," *Clinical Neurophysiology*, vol. 127, no. 4, pp. 2047–2055, 2016.

[262] K. Sainio, D. Stenberg, I. Keskimäki, A. Muuronen, and M. Kaste, "Visual and spectral EEG analysis in the evaluation of the outcome in patients with ischemic brain infarction," *Electroencephalography and Clinical Neurophysiology*, vol. 56, pp. 117–124, Aug. 1983.

[263] F. Wendling, A. Hernandez, J.-J. Bellanger, P. Chauvel, and F. Bartolomei, "Interictal to ictal transition in human temporal lobe epilepsy: insights from a computational model of intracerebral eeg," *Journal of Clinical Neurophysiology*, vol. 22, no. 5, p. 343, 2005.

[264] B. S. Bhattacharya, D. Coyle, and L. P. Maguire, "A thalamo–cortico–thalamic neural mass model to study alpha rhythms in alzheimer's disease," *Neural Networks*, vol. 24, pp. 631–645, Aug. 2011.

[265] F. Liu, J. Wang, C. Liu, H. Li, B. Deng, C. Fietkiewicz, and K. A. Loparo, "A neural mass model of basal ganglia nuclei simulates pathological beta rhythm in parkinson's disease," *Chaos: An Interdisciplinary Journal of Nonlinear Science*, vol. 26, p. 123113, Dec. 2016.

[266] J. B. G. van Wijngaarden, R. Zucca, S. Finnigan, and P. F. M. J. Verschure, "The impact of cortical lesions on thalamo-cortical network dynamics after acute ischaemic stroke: A combined experimental and theoretical study," *PLOS Computational Biology*, vol. 12, pp. 1–16, 08 2016.

[267] M. J. Sætra, G. T. Einevoll, and G. Halnes, "An electrodiffusive neuron-extracellular-glia model for exploring the genesis of slow potentials in the brain," *PLOS Computational Biology*, vol. 17, p. e1008143, July 2021.

[268] B.-J. Zandt, B. ten Haken, J. G. van Dijk, and M. J. A. M. van Putten, "Neural dynamics during anoxia and the "wave of death"," *PLOS ONE*, vol. 6, pp. 1–6, 07 2011.

[269] R. Hindriks, H. G. E. Meijer, S. A. van Gils, and M. J. A. M. van Putten, "Phase-locking of epileptic spikes to ongoing delta oscillations in non-convulsive status epilepticus," *Frontiers in Systems Neuroscience*, vol. 7, 2013.

[270] C. H. Luo and Y. Rudy, "A dynamic model of the cardiac ventricular action potential: I. Simulations of ionic currents and concentration changes," *Circulation Research*, vol. 74, no. 6, pp. 1071–1096, 1994.

[271] P. A. Robinson, C. J. Rennie, J. J. Wright, H. Bahramali, E. Gordon, and D. L. Rowe, "Prediction of electroencephalographic spectra from neurophysiology," *Phys. Rev. E*, vol. 63, p. 021903, Jan 2001.

[272] C. Koch, *Methods in neuronal modeling : from ions to networks*. Cambridge, Mass: MIT Press, 1998.

[273] P. Grube, C. Heuermann, A. Rozov, M. Both, A. Draguhn, and D. Hefter, "Transient oxygen-glucose deprivation causes region- and cell type-dependent functional deficits in the mouse hippocampus in vitro," *eNeuro*, vol. 8, no. 5, 2021.

[274] Z. Cao, S. S. Harvey, T. M. Bliss, M. Y. Cheng, and G. K. Steinberg, "Inflammatory responses in the secondary thalamic injury after cortical ischemic stroke," *Frontiers in Neurology*, vol. 11, p. 236, 2020.

[275] S. Chornyy, A. Das, J. A. Borovicka, D. Patel, H. H. Chan, J. K. Hermann, T. C. Jaramillo, A. G. Machado, K. B. Baker, and H. Dana, "Cellular-resolution monitoring of ischemic stroke pathologies in the rat cortex," *Biomed. Opt. Express*, vol. 12, pp. 4901–4919, Aug 2021.

[276] M. Desroches, J. Guckenheimer, B. Krauskopf, C. Kuehn, H. M. Osinga, and M. Wechselberger, "Mixed-mode oscillations with multiple time scales," *Siam Review*, vol. 54, no. 2, pp. 211–288, 2012.

[277] K. Laaksonen, L. Helle, L. Parkkonen, E. Kirveskari, J. P. Mäkelä, S. Mustanoja, T. Tatlisumak, M. Kaste, and N. Forss, "Alterations in spontaneous brain oscillations during stroke recovery," *PLOS ONE*, vol. 8, pp. 1–9, 04 2013.

[278] D. Wang and P. R. Hiesinger, "The vesicular ATPase: A missing link between acidification and exocytosis," *Journal of Cell Biology*, vol. 203, pp. 171–173, 10 2013.

[279] S. V. Fedorovich and T. V. Waseem, "Metabolic regulation of synaptic activity," *Reviews in the Neurosciences*, vol. 29, no. 8, pp. 825–835, 2018.

[280] M.-K. Sun, H. Xu, and D. L. Alkon, "Pharmacological protection of synaptic function, spatial learning, and memory from transient hypoxia in rats," *Journal of Pharmacology and Experimental Therapeutics*, vol. 300, no. 2, pp. 408–416, 2002.

[281] J. le Feber, S. Tzafi Pavlidou, N. Erkamp, M. J. A. M. van Putten, and J. Hofmeijer, "Progression of neuronal damage in an in vitro model of the ischemic penumbra," *PLOS ONE*, vol. 11, pp. 1–19, 02 2016.

[282] S. Thomas Carmichael, L. Wei, C. M. Rovainen, and T. A. Woolsey, "New patterns of intracortical projections after focal cortical stroke," *Neurobiology of Disease*, vol. 8, no. 5, pp. 910–922, 2001.

[283] H. Iizuka, K. Sakatani, and W. Young, "Neural damage in the rat thalamus after cortical infarcts.," *Stroke*, vol. 21, no. 5, pp. 790–794, 1990.

[284] M. J. A. M. van Putten, "The N20 in post-anoxic coma: Are you listening?," *Clinical Neurophysiology*, vol. 123, no. 7, pp. 1460–1464, 2012.

[285] M. J. A. M. van Putten, C. Jansen, M. C. Tjepkema-Cloostermans, T. J. Beernink, R. Koot, F. Bosch, A. Beishuizen, and J. Hofmeijer, "Postmortem histopathology of

electroencephalography and evoked potentials in postanoxic coma," *Resuscitation*, vol. 134, no. October 2018, pp. 26–32, 2018.

[286] R. Curtu, "Singular hopf bifurcations and mixed-mode oscillations in a two-cell inhibitory neural network," *Physica D: Nonlinear Phenomena*, vol. 239, no. 9, pp. 504–514, 2010. Mathematical Neuroscience.

[287] J. Rubin and M. Wechselberger, "The selection of mixed-mode oscillations in a hodgkin-huxley model with multiple timescales," *Chaos: An Interdisciplinary Journal of Nonlinear Science*, vol. 18, no. 1, p. 015105, 2008.

[288] I. Erchova and D. J. McGonigle, "Rhythms of the brain: An examination of mixed mode oscillation approaches to the analysis of neurophysiological data," *Chaos: An Interdisciplinary Journal of Nonlinear Science*, vol. 18, no. 1, p. 015115, 2008.

[289] M.-S. Abdelouahab, R. Lozi, and G. Chen, "Complex canard explosion in a fractional-order fitzhugh–nagumo model," *International Journal of Bifurcation and Chaos*, vol. 29, no. 08, p. 1950111, 2019.

[290] S. Ghosh, A. Mondal, P. Ji, A. Mishra, S. K. Dana, C. G. Antonopoulos, and C. Hens, "Emergence of mixed mode oscillations in random networks of diverse excitable neurons: The role of neighbors and electrical coupling," *Frontiers in Computational Neuroscience*, vol. 14, p. 49, 2020.

[291] B. V-Ghaffari, M. Kouhnavard, and S. M. Elbasiouny, "Mixed-mode oscillations in pyramidal neurons under antiepileptic drug conditions," *PLOS ONE*, vol. 12, pp. 1–20, 06 2017.

[292] M. C. Tjepkema-Cloostermans, R. Hindriks, J. Hofmeijer, and M. J. van Putten, "Generalized periodic discharges after acute cerebral ischemia: Reflection of selective synaptic failure?," *Clinical Neurophysiology*, vol. 125, pp. 255–262, Feb. 2014.

[293] J. Hofmeijer, M. C. Tjepkema-Cloostermans, and M. J. A. M. van Putten, "Burst-suppression with identical bursts: a distinct EEG pattern with poor outcome in postanoxic coma.," *Clinical neurophysiology : official journal of the International Federation of Clinical Neurophysiology*, vol. 125, pp. 947–54, may 2014.

[294] M. C. Cross and P. C. Hohenberg, "Pattern formation outside of equilibrium," *Reviews of modern physics*, vol. 65, no. 3, p. 851, 1993.

[295] J. Guckenheimer and P. Holmes, *Nonlinear oscillations, dynamical systems, and bifurcations of vector fields*, vol. 42. Springer Science & Business Media, 2013.

[296] O. Yair, R. Talmon, R. R. Coifman, and I. G. Kevrekidis, "Reconstruction of normal forms by learning informed observation geometries from data," *Proceedings of the National Academy of Sciences*, vol. 114, no. 38, pp. E7865–E7874, 2017.

[297] S. L. Brunton and J. N. Kutz, *Data-driven science and engineering: Machine learning, dynamical systems, and control*. Cambridge University Press, 2019.

[298] M. Raissi, P. Perdikaris, and G. E. Karniadakis, "Physics-informed neural networks: A deep learning framework for solving forward and inverse problems involving nonlinear partial differential equations," *Journal of Computational Physics*, vol. 378, pp. 686–707, 2019.

[299] F. Noé, S. Olsson, J. Köhler, and H. Wu, "Boltzmann generators: Sampling equilibrium states of many-body systems with deep learning," *Science*, vol. 365, no. 6457, p. eaaw1147, 2019.

[300] Y. Bar-Sinai, S. Hoyer, J. Hickey, and M. P. Brenner, "Learning data-driven discretizations for partial differential equations," *Proceedings of the National Academy of Sciences*, vol. 116, no. 31, pp. 15344–15349, 2019.

[301] K. Champion, B. Lusch, J. Kutz, and S. Brunton, "Data-driven discovery of coordinates and governing equations," *Proceedings of the National Academy of Sciences*, vol. 116, no. 45, pp. 22445–22451, 2019.

[302] P. Benner, S. Gugercin, and K. Willcox, "A Survey of Projection-Based Model Reduction Methods for Parametric Dynamical Systems," *SIAM Review*, vol. 57, pp. 483–531, jan 2015.

[303] P. J. Schmid, "Dynamic mode decomposition of numerical and experimental data," *Journal of fluid mechanics*, vol. 656, pp. 5–28, 2010.

[304] K. Taira and T. Colonius, "The immersed boundary method: A projection approach," *Journal of Computational Physics*, vol. 225, no. 2, pp. 2118–2137, 2007.

[305] F. Dietrich, M. Kooshkbaghi, E. M. Bollt, and I. G. Kevrekidis, "Manifold learning for organizing unstructured sets of process observations," *Chaos: An Interdisciplinary Journal of Nonlinear Science*, vol. 30, no. 4, p. 043108, 2020.

[306] A. Holiday, M. Kooshkbaghi, J. M. Bello-Rivas, C. W. Gear, A. Zagaris, and I. G. Kevrekidis, "Manifold learning for parameter reduction," *Journal of computational physics*, vol. 392, pp. 419–431, 2019.

[307] A. J. Linot and M. D. Graham, "Deep learning to discover and predict dynamics on an inertial manifold," *Physical Review E*, vol. 101, no. 6, p. 062209, 2020.

[308] K. Lee and K. T. Carlberg, "Model reduction of dynamical systems on nonlinear manifolds using deep convolutional autoencoders," *Journal of Computational Physics*, vol. 404, p. 108973, 2020.

[309] S. H. Rudy, S. L. Brunton, J. L. Proctor, and J. N. Kutz, "Data-driven discovery of partial differential equations," *Science Advances*, vol. 3, p. e1602614, apr 2017.

[310] S. Coombes and M. R. Owen, "Bumps, breathers, and waves in a neural network with spike frequency adaptation," *Phys. Rev. Lett.*, vol. 94, p. 148102, Apr 2005.

[311] E. Gilad, J. von Hardenberg, A. Provenzale, M. Shachak, and E. Meron, "Ecosystem engineers: From pattern formation to habitat creation," *Phys. Rev. Lett.*, vol. 93, p. 098105, Aug 2004.

[312] T. E. Lee and M. C. Cross, "Pattern formation with trapped ions," *Phys. Rev. Lett.*, vol. 106, p. 143001, Apr 2011.

[313] M. Tlidi, P. Mandel, and M. Haelterman, "Spatiotemporal patterns and localized structures in nonlinear optics," *Phys. Rev. E*, vol. 56, pp. 6524–6530, Dec 1997.

[314] G. E. Hinton and R. Zemel, "Autoencoders, minimum description length and helmholtz free energy," in *Advances in Neural Information Processing Systems* (J. Cowan, G. Tesauro, and J. Alspector, eds.), vol. 6, Morgan-Kaufmann, 1994.

[315] D. Kingma and J. Ba, "Adam: A method for stochastic optimization," 2017. arxiv,1412.6980.

[316] E. Lorenz, *Predictability – a problem partly solved*, p. 40–58. Cambridge University Press, 2006.

[317] D. van Kekem and A. Sterk, "Travelling waves and their bifurcations in the lorenz-96 model," *Physica D: Nonlinear Phenomena*, vol. 367, pp. 38 – 60, 2018.

[318] S. Folias, "Nonlinear analysis of breathing pulses in a synaptically coupled neural network," *SIAM Journal on Applied Dynamical Systems*, vol. 10, no. 2, pp. 744–787, 2011.

[319] P. Bearman, "On vortex shedding from a circular cylinder in the critical reynolds number regime," *Journal of Fluid Mechanics*, vol. 37, no. 3, pp. 577–585, 1969.

[320] B. Noack, K. Afanasiev, M. Morzyński, G. Tadmor, and F. Thiele, "A hierarchy of low-dimensional models for the transient and post-transient cylinder wake," *J. Fluid Mech.*, vol. 497, pp. 335–363, 2003.

[321] B. Noack, M. Morzynski, and G. Tadmor, *Reduced-order modelling for flow control*, vol. 528. Springer Science & Business Media, 2011.

[322] D. Kingma and J. Ba, "Adam: A method for stochastic optimization," 2017. Arxiv,1412.6980.

[323] C. Rowley, T. Colonius, and R. Murray, "Model reduction for compressible flows using pod and galerkin projection," *Physica D: Nonlinear Phenomena*, vol. 189, no. 1, pp. 115–129, 2004.

[324] L. Sirovich, "Turbulence and the dynamics of coherent structures part I: Coherent structures," *Quarterly of Applied Mathematics*, vol. 45, no. 3, pp. 561–571, 1987.

[325] J. Kutz, S. Brunton, B. Brunton, and J. Proctor, *Dynamic mode decomposition: data-driven modeling of complex systems*. SIAM, 2016.

[326] V. I. Arnold, V. S. Afrajmovich, Y. S. Il'yashenko, and L. P. Shil'nikov, *Dynamical Systems 5: Bifurcation Theory and Catastrophe Theory*. Springer-Verlag, Berlin, 1999.

[327] Y. Ilyashenko and W. Li, *Nonlocal Bifurcations*, vol. 66 of *Mathematical Surveys and Monographs*. American Mathematical Society, Providence, RI, 1999.

[328] L. P. Shilnikov, A. L. Shilnikov, D. Turaev, and L. O. Chua, *Methods of Qualitative Theory in Nonlinear Dynamics. Part II*, vol. 5 of *World Scientific Series on Nonlinear Science. Series A: Monographs and Treatises*. World Scientific Publishing Co., Inc., River Edge, NJ, 2001.

[329] A. Homburg and B. Sandstede, "Homoclinic and heteroclinic bifurcations in vector fields," in *Handbook of Dynamical Systems. Vol. 3* (H. W. Broer, B. Hasselblatt, and F. Takens, eds.), pp. 379–524, Elsevier/North-Holland, Amsterdam, 2010.

[330] L. P. Shil'nikov, "A case of the existence of a denumerable set of periodic motions," *Dokl. Akad. Nauk SSSR*, vol. 160, pp. 558–561, 1965.

[331] V. S. Afraimovich, S. V. Gonchenko, L. M. Lerman, A. L. Shil'nikov, and D. V. Turaev, "Scientific heritage of L. P. Shilnikov," *Regul. Chaotic Dyn.*, vol. 19, no. 4, pp. 435–460, 2014.

[332] S. V. Gonchenko, D. V. Turaev, P. Gaspard, and G. Nicolis, "Complexity in the bifurcation structure of homoclinic loops to a saddle-focus," *Nonlinearity*, vol. 10, no. 2, pp. 409–423, 1997.

[333] A. R. Champneys and Y. A. Kuznetsov, "Numerical detection and continuation of codimension-two homoclinic bifurcations," *Internat. J. Bifur. Chaos Appl. Sci. Engrg.*, vol. 4, no. 4, pp. 785–822, 1994.

[334] Y. A. Kuznetsov, "Impulses of a complicated form in models of nerve conduction," *Selecta Math.*, vol. 13, no. 2, pp. 127–142, 1994. [Translation from *Mathematics and Modeling*, Akad. Nauk SSSR, Nauchn. Tsentr Biol. Issled., Pushchino, 1990, pp. 208–222].

[335] Y. A. Kuznetsov, O. De Feo, and S. Rinaldi, "Belyakov homoclinic bifurcations in a tritrophic food chain model," *SIAM J. Appl. Math.*, vol. 62, no. 2, pp. 462–487, 2001.

[336] L. A. Belyakov, "The bifurcation set in a system with a homoclinic saddle curve," *Mat. Zametki*, vol. 28, no. 6, pp. 911–922, 962, 1980. [in Russian; English translation: *Math. Notes* 28(5-6): 910–916, 1981].

[337] C. Mira and J.-P. Carcassès, "On the "crossroad area–saddle area" and "crossroad area–spring area" transitions," *Internat. J. Bifur. Chaos Appl. Sci. Engrg.*, vol. 1, no. 3, pp. 641–655, 1991.

[338] L. P. Shilnikov, A. L. Shilnikov, D. V. Turaev, and L. O. Chua, *Methods of Qualitative Theory in Nonlinear Dynamics. Part I*, vol. 4 of *World Scientific Series on Nonlinear Science. Series A: Monographs and Treatises*. World Scientific Publishing Co., Inc., River Edge, NJ, 1998.

[339] B. Deng, "The Šil'nikov problem, exponential expansion, strong λ-lemma, C^1-linearization, and homoclinic bifurcation," *J. Differential Equations*, vol. 79, no. 2, pp. 189–231, 1989.

[340] B. Deng, "Exponential expansion with Šil'nikov's saddle-focus," *J. Differential Equations*, vol. 82, no. 1, pp. 156–173, 1989.

[341] B. Deng, "Exponential expansion with principal eigenvalues: Nonlinear dynamics, bifurcations and chaotic behavior," *Internat. J. Bifur. Chaos Appl. Sci. Engrg.*, vol. 6, no. 6, pp. 1161–1167, 1996.

[342] W. Govaerts, R. K. Ghaziani, Y. A. Kuznetsov, and H. G. E. Meijer, "Numerical methods for two-parameter local bifurcation analysis of maps," *SIAM Journal on Scientific Computing*, vol. 29, no. 6, pp. 2644–2667, 2007.

[343] N. Neirynck, B. Al-Hdaibat, W. Govaerts, Y. A. Kuznetsov, and H. Meijer, "Using MatContM in the study of a nonlinear map in economics," *Journal of Physics: Conference Series*, vol. 692, no. 1, p. 012013, 2016.

[344] A. Dhooge, W. Govaerts, and Y. A. Kuznetsov, "Matcont: A MATLAB package for numerical bifurcation analysis of ODEs," *ACM Trans. Math. Softw.*, vol. 29, pp. 141–164, June 2003.

[345] V. De Witte, W. Govaerts, Y. A. Kuznetsov, and M. Friedman, "Interactive initialization and continuation of homoclinic and heteroclinic orbits in MATLAB," *ACM Trans. Math. Software*, vol. 38, no. 3, pp. Art. 18, 34, 2012.

[346] E. N. Lorenz, "Deterministic nonperiodic flow," *Journal of the Atmospheric Sciences*, vol. 20, no. 2, pp. 130–141, 1963.

[347] L. Stenflo, "Generalized Lorenz equations for acoustic-gravity waves in the atmosphere," *Physica Scripta*, vol. 53, no. 1, p. 83, 1996.

[348] J. C. Xavier and P. C. Rech, "Regular and chaotic dynamics of the Lorenz-Stenflo system," *Internat. J. Bifur. Chaos Appl. Sci. Engrg.*, vol. 20, no. 1, pp. 145–152, 2010.

[349] R. A. Van Gorder, "Shil'nikov chaos in the 4D Lorenz-Stenflo system modeling the time evolution of nonlinear acoustic-gravity waves in a rotating atmosphere," *Nonlinear Dynam.*, vol. 72, no. 4, pp. 837–851, 2013.

[350] P. C. Rech, "Spiral organization of periodic structures in the Lorenz-Stenflo system," *Physica Scripta*, vol. 91, no. 7, p. 075201, 2016.

[351] A. R. Champneys, Y. A. Kuznetsov, and B. Sandstede, "A numerical toolbox for homoclinic bifurcation analysis," *Internat. J. Bifur. Chaos Appl. Sci. Engrg.*, vol. 6, no. 5, pp. 867–887, 1996.

[352] R. Barrio, A. Shilnikov, and L. Shilnikov, "Kneadings, symbolic dynamics and painting Lorenz chaos," *Internat. J. Bifur. Chaos Appl. Sci. Engrg.*, vol. 22, no. 4, pp. 1230016, 24, 2012.

[353] T. Xing, R. Barrio, and A. Shilnikov, "Symbolic quest into homoclinic chaos," *Internat. J. Bifur. Chaos Appl. Sci. Engrg.*, vol. 24, no. 8, pp. 1440004, 20, 2014.

[354] L. A. Belyakov, "Bifurcations of systems with a homoclinic curve of the saddle-focus with a zero saddle value," *Mat. Zametki*, vol. 36, no. 5, pp. 681–689, 798, 1984. [in Russian; English translation: *Math. Notes* 36(5-6): 838 - 843, 1985].

[355] G. R. Belitskii, *Normal Forms, Invariants, and Local Mappings*. Naukova Dumka, Kiev, 1979. [in Russian].

[356] S. Sternberg, "On the structure of local homeomorphisms of euclidean n-space. II," *Amer. J. Math.*, vol. 80, pp. 623–631, 1958.

[357] I. U. Bronstein and A. Y. Kopanskiĭ, *Smooth invariant manifolds and normal forms*, vol. 7 of *World Scientific Series on Nonlinear Science. Series A: Monographs and Treatises*. World Scientific Publishing Co., Inc., River Edge, NJ, 1994.

[358] A. J. Homburg, "Global aspects of homoclinic bifurcations of vector fields," *Mem. Amer. Math. Soc.*, vol. 121, no. 578, pp. viii+128, 1996.

[359] M. V. Shashkov and D. V. Turaev, "An existence theorem of smooth nonlocal center manifolds for systems close to a system with a homoclinic loop," *J. Nonlinear Sci.*, vol. 9, no. 5, pp. 525–573, 1999.

[360] B. Sandstede, "Center manifolds for homoclinic solutions," *J. Dynam. Differential Equations*, vol. 12, no. 3, pp. 449–510, 2000.

[361] S. Tymochko, E. Munch, and F. A. Khasawneh, "Using zigzag persistent homology to detect hopf bifurcations in dynamical systems," *Algorithms*, vol. 13, p. 278, Oct. 2020.

[362] K. Moussawi, A. Riegel, S. Nair, and P. W. Kalivas, "Extracellular glutamate: Functional compartments operate in different concentration ranges," *Frontiers in Systems Neuroscience*, vol. 5, 2011.

[363] R. E. Burke, "Composite nature of the monosynaptic excitatory postsynaptic potential.," *Journal of Neurophysiology*, vol. 30, pp. 1114–1137, Sept. 1967.

[364] T. M. Gao, W. A. Pulsinelli, and Z. C. Xu, "Prolonged enhancement and depression of synaptic transmission in CA1 pyramidal neurons induced by transient forebrain ischemia in vivo," *Neuroscience*, vol. 87, pp. 371–383, July 1998.

[365] H. Ye, S. Jalini, L. Zhang, M. Charlton, and P. L. Carlen, "Early ischemia enhances action potential-dependent, spontaneous glutamatergic responses in CA1 neurons," *Journal of Cerebral Blood Flow & Metabolism*, vol. 30, pp. 555–565, Oct. 2009.

[366] J. Shen, "Modeling the glutamate–glutamine neurotransmitter cycle," *Frontiers in Neuroenergetics*, vol. 5, 2013.

[367] S. Vahdat, A. V. Pendharkar, T. Chiang, S. Harvey, H. Uchino, Z. Cao, A. Kim, M. Choy, H. Chen, H. J. Lee, M. Y. Cheng, J. H. Lee, and G. K. Steinberg, "Brain-wide neural dynamics of poststroke recovery induced by optogenetic stimulation," *Science Advances*, vol. 7, Aug. 2021.

[368] C. Dohmen, O. W. Sakowitz, M. Fabricius, B. Bosche, T. Reithmeier, R.-I. Ernestus, G. Brinker, J. P. Dreier, J. Woitzik, A. J. Strong, and R. G. and, "Spreading depolarizations occur in human ischemic stroke with high incidence," *Annals of Neurology*, vol. 63, pp. 720–728, June 2008.

[369] C. Rakers and G. C. Petzold, "Astrocytic calcium release mediates peri-infarct depolarizations in a rodent stroke model," *Journal of Clinical Investigation*, vol. 127, pp. 511–516, Dec. 2016.

[370] J.-y. Liou, E. H. Smith, L. M. Bateman, S. L. Bruce, G. M. McKhann, R. R. Goodman, R. G. Emerson, C. A. Schevon, and L. Abbott, "A model for focal seizure onset, propagation, evolution, and progression," *eLife*, vol. 9, p. e50927, mar 2020.

[371] A. Cichocki, N. Lee, I. Oseledets, A.-H. Phan, Q. Zhao, and D. P. Mandic, "Tensor networks for dimensionality reduction and large-scale optimization: Part 1 low-rank tensor decompositions," *Foundations and Trends® in Machine Learning*, vol. 9, no. 4-5, pp. 249–429, 2016.

[372] E. Stoudenmire and D. J. Schwab, "Supervised learning with tensor networks," in *Advances in Neural Information Processing Systems* (D. Lee, M. Sugiyama, U. Luxburg, I. Guyon, and R. Garnett, eds.), vol. 29, Curran Associates, Inc., 2016.

[373] J. J. Bramburger and J. N. Kutz, "Poincaré maps for multiscale physics discovery and nonlinear floquet theory," *Physica D: Nonlinear Phenomena*, vol. 408, p. 132479, July 2020.

List of publications

Journal articles

1. **Homoclinic saddle to saddle-focus transitions in 4D systems**
   Manu Kalia, Hil G.E. Meijer and Yuri A. Kuznetsov
   Nonlinearity (2019) 32.6:2024
   preprint: arXiv 1712.03212
2. **Ion dynamics of the energy-deprived tripartite synapse**
   Manu Kalia, Hil G.E. Meijer, Stephan A. van Gils, Michel J.A.M. van Putten and Christine R. Rose
   PLoS Computational Biology (2021) 17(6): e1009019
   preprint: `https://www.biorxiv.org/content/10.1101/2021.03.19.436129v1`
3. **Glial chloride homeostasis under transient ischemic stress.**
   Miriam Engels, Manu Kalia, Sarah Rahmati, L. Petersilie, Peter Kovermann, Michel J.A.M. van Putten, Christine R. Rose, Hil G.E. Meijer, Thomas Gensch and Christoph Fahlke
   Frontiers in Cellular Neuroscience (2021) 15:735300
4. **A neural mass model for the EEG in ischemia**
   Manu Kalia, Sophie L.B. Ligtenstein, Hil G.E. Meijer and Michel J.A.M. van Putten
   submitted (2022)

5. **Learning normal form autoencoders for data-driven discovery of universal, parameter-dependent governing equations**
   Manu Kalia, Steven L. Brunton, Hil G.E. Meijer, Christoph Brune and J. Nathan Kutz
   submitted (2022)
   preprint: arXiv 2106.05102

Conference publications

1. **Deep learning of normal form autoencoders for universal, parameter-dependent dynamics**
   Manu Kalia, Steven L. Brunton, Hil G.E. Meijer, Christoph Brune and J. Nathan Kutz

1st NeurIPS workshop on Interpretable Inductive Biases and Physically Structured Learning (2020), virtual.

Conference presentations/posters

1. **Ion dynamics at the tripartite synapse**
   - *Bonn Brain 2019, Bonn, Germany* (Poster)
   - *The 5th International Conference on Mathematical NeuroScience 2019 (ICMNS), Copenhagen, Denmark* (Talk)
   - *28th Annual Computational Neuroscience Meeting 2019, Barcelona, Spain* (Poster, award)
   - *14th Göttingen Neuroscience Meeting 2021, virtual* (Poster)
   - *European Glial Meeting (GLIA) 2021, virtual* (Poster)
   - *Annual meeting of the Society for Mathematical Biology 2021, virtual* (Invited talk)
2. **Learning normal form autoencoders for data-driven discovery of universal,parameter-dependent governing equations**
   - *NeurIPS workshop on Interpretable Inductive Biases and Physically Structured Learning 2020, virtual* (Talk)
   - *SIAM conference on Applications of Dynamical Systems (DS20), virtual, held in 2021* (Talk)
3. **Estimating parameters from partial observations with neural networks**
   - *SIAM conference on Appliecations of Dynamical Systems 2019 (DS19), Snowbird, Utah, USA* (Poster)
   - *Lorentz Center Workshop on Data Science for Dynamical Systems 2019, Leiden, The Netherlands* (Invited talk)
   - *Inaugural SIAM conference on Mathematics of Data Science 2020, virtual* (Invited talk)

बंधा तूफान हूँ, चलना मना है
बँधी उद्याम निर्झर–धार हूँ मैं
कहूँ क्या कौन हूँ, क्या आग मेरी
बँधी है लेखनी, लाचार हूँ मैं।

परिचय – रामधारी सिंह "दिनकर"